Conception et optimisation multi-échelle de structures composites en intégrant une approche de modélisation global-local haute-fidelité

Giacinto Alberto Fiordilino

HESAM UNIVERSITÉ

Arts et Métiers Sciences et Technologies

ÉCOLE DOCTORALE SCIENCES DES MÉTIERS DE L'INGÉNIEUR
Institut de Mécanique et d'Ingénierie de Bordeaux (I2M)

Campus de Bordeaux-Talence

THÈSE

présentée par : **Giacinto Alberto FIORDILINO**

soutenue le : **11 janvier 2022**

pour obtenir le grade de : **Docteur d'HESAM Université**

préparée à : **École Nationale Supérieure d'Arts et Métiers**

Spécialité : **Conception**

Multi-scale design and optimisation of composite structures by integrating a high-fidelity global-local modelling approach

(Conception et optimisation multi-échelles de structures composites en intégrant une approche de modélisation globale-locale haute-fidélité)

THÈSE dirigée par :
M. MONTEMURRO Marco

et co-encadrée par :
M. CARRERA Erasmo et M. PAILHES Jérôme

Jury

M. Olivier POLIT, PU, Université Paris Nanterre, LEME	Rapporteur
M. YAO KOUTSAWA, Chercheur Senior HDR, LIST	Rapporteur
M. Marco GIGLIOTTI, PU, Université de Poitiers, Institut P'	Examinateur
Mme. Angela VINCENTI, MCF, Sorbonne Université, Institut JLRDA	Examinatrice
M. Marco MONTEMURRO, PU, Arts et Métiers Bordeaux-Talence, I2M	Examinateur
M. Erasmo CARRERA, PU, Politecnico di Torino, DIMEAS	Examinateur
Jérôme PAILHES, PU, Arts et Métiers Bordeaux-Talence, I2M	Examinateur

T H È S E

Abstract

This thesis focuses on the development of a suitable global-local modelling approach, based on higher-order theories, which is integrated into the multi-scale two-level optimisation strategy (MS2LOS) for the optimal design of composite structures developed by M. Montemurro and co-workers at the I2M laboratory in Bordeaux.
The development of an appropriate global-local modelling approach is a fundamental brick to be integrated into the MS2LOS in order to correctly capture (at each relevant scale) the effective mechanical response of the structure with a considerable reduction in computational time and cost. The global-local modelling approach aims to replace the equivalent single-layer approach with a layered approach based on higher-order theories within the framework of the Carrera Unified Formulation (CUF) for local optimisation of the composite. The extension of the MS2LOS in designing CSC stiffened panels is also addressed in this work. The MS2LOS, in fact, is applied to solve the least-weight design problem of a stiffened composite panel. At the macroscopic level, the structure is modelled as an equivalent single-layer plate and the goal is to find the optimum value of the design variables (geometrical and mechanical) to minimise the mass of the panel meeting the set of imposed design requirements (feasibility, manufacturing, stiffness, buckling, etc.) without introducing simplified hypothesis on the mechanical behaviour. At the mesoscopic scale, the aim is to find at least one stacking sequence that meets the optimum design variables resulting from the structural optimisation carried out at the macroscopic scale. Then, the MS2LOS is applied to the optimisation of VSCs. In particular, the first-level problem of the MS2LOS is solved to maximise the first buckling load of the VSC structure determining the optimal distribution of the VSC stiffness properties at the macroscopic scale and satisfying the requirements of the problem. In this optimisation, a deterministic algorithm is used to find the optimum using the gradient analytically determined by exploiting the properties of the polar formalism and of the B-spline surfaces which are used in the framework of the MS2LOS.
Lastly, the integration of the global-local modelling approach based on layer-wise higher-order theories in the MS2LOS is provided. The objective is to identify and isolate the regions of the model which require more precise investigations during the first optimisation step of the MS2LOS and to analyse these regions of interest using the global-local approach developed in the CUF framework. To this end, two FE models are developed and interfaced. The first one is a low-fidelity FE (LF-FE) model generated by means of commercial software. In the context of the LF-FE model, each laminate constituting the structure is modelled as an equivalent single-layer plate, whose macroscopic behaviour is described in the PPs space. The most critical regions of the LF-FE model, i.e. the so-called zones of interest (ZOIs), are identified by means of a suitable criterion formulated in the PPs space. Then, a high-fidelity FE (HF-FE) model based on layer-wise theories is generated for the critical ZOI to assess the local structural responses which are integrated into the problem formulation.

Résumé

La thèse porte sur le développement d'une approche de modélisation globale-locale appropriée, basée sur des théories d'ordre supérieur, qui est intégrée dans la stratégie d'optimisation multi-échelle à deux niveaux (MS2LOS) pour la conception optimale des structures composites, développée par M. Montemurro et ses collaborateurs au laboratoire I2M de Bordeaux. Le développement d'une approche de modélisation globale-locale appropriée est une brique fondamentale à intégrer dans la MS2LOS afin de capturer correctement (à chaque échelle du problème) la réponse mécanique effective de la structure avec une réduction considérable du temps et du coût de calcul. L'approche de modélisation globale-locale vise à remplacer l'approche monocouche équivalente par une approche en couches basée sur des théories d'ordre supérieur dans le cadre de la Formulation Unifiée de Carrera (CUF) pour l'optimisation locale du composite. L'application de la MS2LOS à la conception multi-échelle de panneaux renforcés CSC est également abordée dans ce travail. En fait, le MS2LOS est appliquée pour résoudre le problème de conception optimale d'un panneau raidi soumis à divers contraintes de conception. Au niveau macroscopique, la structure est modélisée comme une plaque monocouche équivalente et le but est de trouver la valeur optimale des variables de conception (géométriques et mécaniques) pour minimiser la masse du panneau répondant à l'ensemble des exigences de conception imposées (faisabilité, fabrication, rigidité, flambement, etc.) sans introduire d'hypothèse simplificatrice sur le comportement mécanique. À l'échelle mésoscopique, l'objectif est de trouver au moins une séquence d'empilement qui satisfait aux variables de conception optimales résultant de l'optimisation structurelle effectuée à l'échelle macroscopique. Ensuite, la MS2LOS est appliquée à l'optimisation des VSCs. En particulier, le problème de premier niveau est résolu pour maximiser la première charge de flambage de la structure du VSC en déterminant la distribution optimale des propriétés de rigidité du VSC à l'échelle macroscopique et en satisfaisant les contraintes du problème. Dans cette méthode, un algorithme déterministe est utilisé pour trouver l'optimum en utilisant le gradient analytique de la charge critique de flambage en exploitant les propriétés du formalisme polaire et des surfaces B-splines qui sont utilisées dans le cadre de la MS2LOS. Enfin, l'intégration de l'approche de modélisation globale-locale basée sur des théories d'ordre supérieur en couches dans la méthode MS2LOS est présentée. L'objectif est d'identifier et d'isoler les régions du modèle qui nécessitent des investigations plus précises lors de la première étape d'optimisation de MS2LOS et d'analyser ces régions d'intérêt en utilisant l'approche globale-locale développée dans le cadre de la CUF. À cette fin, deux modèles FE sont développés et interfacés. Le premier est un modèle EF de basse fidélité (LF-FE) généré au moyen d'un logiciel commercial. Dans le contexte du modèle LF-FE, chaque stratifié constituant la structure est modélisé comme une plaque monocouche équivalente, dont le comportement macroscopique est décrit dans l'espace des paramètres polaires. Les régions les plus critiques du modèle LF-FE, c'est-à-dire les zones d'intérêt (ZOI), sont identifiées au moyen d'un critère approprié formulé dans l'espace des PPs. Ensuite, un modèle FE

haute-fidélité (HF-FE) basé sur des théories d'ordre supérieur est généré pour la ZOI critique afin d'évaluer les réponses structurelles locales qui sont intégrées dans la formulation du problème.

Fundings

The work carried out in this Thesis has been funded in the framework of the SMART-COMPOSITE project by Nouvelle-Aquitaine Region.

List of Acronyms

AFP = Automated Fibre Placement
ADP = Automatic Dynamic Penalisation
AM = Additive Manufacturing
BCs = Boundary Conditions
CEs = Constraint Equations
CFF = Continuous Filament Fabrication
CG = Centre of Gravity
CLT = Classical Lamination Theory
CNLPP = Constrained Non-Linear Programming Problem
CP = Control Point
CSCs = Constant Stiffness Composites
CUF = Carrera Unified Formulation
DA = Deterministic Algorithm
DOFs = Degrees Of Freedom
ERASMUS = EvolutionaRy Algorithm for optimiSation of ModUlar Systems
DRs = Design Regions
ESL = Equivalent Single-Layer
FE = Finite Element
FLP = First-Level Problem
FN = Fundamental Nucleus
FSDT = First-order Shear Deformation Theory
FFF = Fused Filament Fabrication
GA = Genetic Algorithm
GFEM = Global FE Model
HESLT = Higher-order Equivalent Single Layer Theory
HF-FE = Hight Fidelity - Finite Element
LE = Lagrange-Expansion
LF-FE = Low Fidelity - Finite Element
LFEM = Local FE Model
LFI = Laminate Failure Index
LPs = Lamination Parameters
LW = Layer-Wise
MLOS = Multi-Level Optimisation Strategy
MS2LOS = Multi-Scale Two-Level Optimisation Strategy
MPC = Multi Point Constraint
NDRs = Non-Design Regions
NLPP = Non-Linear Programming Problem
NURBS = Non-Uniform Rational B-Spline
PBCs = Periodic BCs

PPs = Polar Parameters
PVD = Principle of Virtual Displacements
QH = Quasi-Homogeneous
QT = Quasi-Trivial
RU = Repetitive Unit
RVE = Representative Volume Element
SIMP = Solid Isotropic Material with Penalisation
SLOS = Single-Level Optimisation Strategy
SLP = Second-Level Problem
SLSQP = Sequential Least Square Quadratic Programming
SS = Stacking Sequence
TE = Taylor-Expansion
UNLPP = Unconstrained NLPP
VAT = Variable Angle Tow
VISION = VarI-able Stiffness composItes Optimisation based on NURBS
VSCs = Variable Stiffness Composites
XFEM = eXtended Finite Element Method
ZOI = Zone Of Interest

Contents

Chapter 1

Introduction

1.1 The Thesis Context and the SMART-COMPOSITE Project

The design and production of lightweight structures that are less expensive and more efficient are essential for advanced industrial sectors. In the last 30 years, composite materials have been widely used, and their potential is far from being exhausted in today industry because new challenges are emerging year by year. The aeronautics and space sectors remain the main domains in the composite materials market, among the advanced industrial fields. The program of the Boeing 787 Dreamliner is one of the most striking examples in this sense. The Boeing 787 has been the first commercial aircraft with a percentage of structural parts in composite material higher than the aluminium alloys counterpart. Fig. 1.1 shows the different materials used in the Boeing 787 structure.

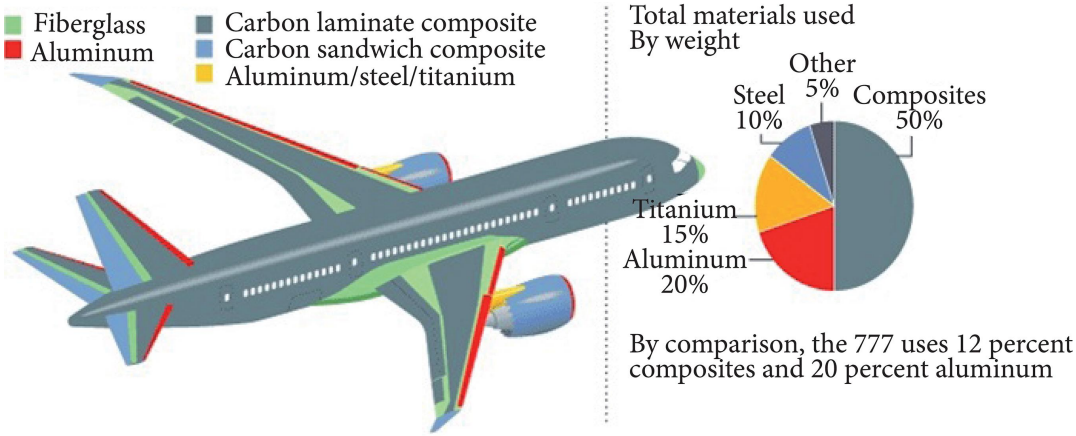

Figure 1.1: Materials used in the Boeing 787 Dreamliner body from [1]

Other areas of interest in the use of composite materials, whose demand is constantly growing, are the automotive sector and, in the renewable energy sector, wind turbines. The success of this class of materials is related to the outstanding properties in terms of lightness, stiffness, static and fatigue resistance that are appealing when compared to their self-constituent materials. They can also be moulded into complex shapes in a easier way than other materials. They are excellent insulators and can resist the corrosion

caused by the weather. All these excellent properties explain the aerospace sector is among the pioneeristic sectors using these materials. Taking the example of the Boeing 787 Dreamliner again, the use of more than 50% carbon fibre results in a 20% reduction in weight, as shown in [1], leading to a decrease of the fuel consumption and consequently to an increase the aircraft operating distance.

For the sake of clarity, the composite structures discussed so far are in the form of multilayer plates or shells consisting of an assembly (or stacking sequence) of bonded layers. The typical individual layer of the laminate composite for aerospace purposes consist of high-strength and high-stiffness fibres reinforcing a polymeric matrix material. The most common types of fibres are glass fibres, carbon fibres, and kevlar. In general, the single-layer has orthotropic or transversely isotropic behaviour. Depending on the stacking sequence, the laminate may have anisotropic, orthotropic or quasi-isotropic properties behaviour at the macroscopic scale regarding membrane, bending and membrane/bending coupling responses.
The mechanical behaviour of the constant stiffness composites (CSCs) reinforced through long fibres, i.e. those composites showing a strong anisotropic behaviour at the macroscopic scale, which can be described using a given set of suitable mechanical variables, is studied in this work. These "suitable" mechanical variables are chosen is such a way to represent a sort of mathematical descriptor of the laminate anisotropic behaviour at the macroscopic scale.
The problem of the multi-scale optimisation of structures made of CSC is usually formulated using numerous simplifying hypotheses that often have no physical and/or technological justification. In fact, designers often use such hypotheses to guarantee a priori the achievement of certain elastic properties that are difficult to obtain (membrane/bending uncoupling, membrane orthotropy, etc.) and particularly difficult to be mathematically formalised in the context of an optimal design problem of composite structures. These simplifying hypotheses are often translated in the introduction of design rules on the laminate stacking sequence, whose main consequence is an unnecessary limitation of the design space extent. A further limitation is about the choice of the set of possible orientations, often limited to the values of $0°, \pm 45°, 90°$: this is a choice of a technological nature which, with modern manufacturing processes, is no longer necessarily justified and which is extremely restrictive in the context of the design process.

In addition, the development of new composite manufacturing technologies makes it possible to go beyond the traditional rules used in the design of composites and thus to design new, high-performance original solutions. One of these innovative solutions, which belongs to the class of variable stiffness composites (VSC), is the variable angle tow (VAT) composite, wherein the tow is steered along pertinent (possibly optimised) trajectories to enhance the macroscopic physical properties of the composite structure. VSC solutions have gained an increasing attention thanks to the development of new manufacturing process, e.g. automated fibre placement (AFP) machines or recent additive manufacturing (AM) technologies, like Fused Filament Fabrication (FFF) and Continuous Filament Fabrication (CFF) processes.
The major advantages of VSCs are superior performances with respect to CSC with a significant weight saving. On the other hand, they present some critical issues, like a complex design/optimisation process at each pertinent problem scale, the damage mechanisms of VSCs are unknown, no damage tolerance criteria exist for this class of composite materials. Indeed, regardless of the application or the typology of composite material (CSC or VSC) considered, the use of composite materials considerably com-

plicates the process of designing a product. This is essentially due to the nature of composites, i.e. on the one hand, the heterogeneity that occurs at the microscopic scale (that of the constituents, in particular fibre and matrix) and, on the other hand, the anisotropy occurring at the mesoscopic (ply-level) and macroscopic (laminate-level) scales. Both heterogeneity and anisotropy introduce specific challenges that must be correctly addressed in order to formulate and solve the multi-scale design/optimisation problem of composite structures in the most general sense. Accordingly, the problem of the optimum design of a composite structure is essentially a multi-scale design problem requiring a correct and complete formalisation since the preliminary design stage. In addition, given the complexity of the mechanical responses of the material and given the large number of design variables involved at each scale (fibre volume fraction, fibre material properties and matrix, number, orientation, thickness and position of plies, geometric parameters of the structure, etc.), an optimisation of the system is mandatory. The multi-scale design of both CSC and VSC structures is faced in this work.

It is in this scenario, and to expand the current state of knowledge on VSC, that the SMARTCOMPOSITE project was born. This project is funded by the Nouvelle-Aquitaine region. The first goal of this project is to increase the impact of the scientific and industrial sectors of the Nouvelle-Aquitaine region within the community of composite materials and structures at both national and european levels. The second goal is to prove that, with current technological and computer capabilities, it is possible to develop an original and effective methodology for the study, design and multi-scale optimisation of complex-shaped VSC structures by integrating, from the early phases of the design process, the technological constraints linked to the manufacturing process to guarantee that the optimised configurations are also manufacturable. To this end, the project is articulated in two complementary research activities:

- The first one focuses on the study of the mechanical response of VSCs at different scales, with an emphasis on the development of laws and analytical/numerical models to describe the failure mechanisms in VSCs;
- The second one focuses on the development of a multi-scale design and optimisation strategy for VSC structures integrating a global-local modelling strategy based on higher-order theories to correctly describe the physical responses involved at each problem scale.

To achieve this ambitious objective, it is essential to:

1. Understand the potential and the limitations characterising the manufacturing process as well as its influence on the mechanical properties of the resulting structure;
2. Develop multi-scale models (micro, meso and macro) of the material to understand the damage phenomena occurring at different scales;
3. Validate the analytical/numerical models via a dedicated experimental campaign;
4. Formulate the design problem in a very general way and develop a strategy for multi-scale optimisation able of taking into account the manufacturing constraints linked to the process;
5. Validating the design process by creating a physical demonstrator to show the relevance of the models and the manufacturability of this type of solutions.

The partners of the project are: I2M Laboratory (Coordinator), Politecnico di Torino, Universitá di Pisa and ESTIA/Compositadour. Two theses are funded within the SMART-COMPOSITE project and this Thesis is one of them. The other one is the Ph.D. of T. Garulli [2].

1.2 Thesis objectives

This thesis gives an original contribution to the second part of the research activity of the SMARTCOMPOSITE project. It focuses on the development of a suitable global-local modelling approach, based on higher-order theories, which is integrated into the multi-scale two-level optimisation strategy (MS2LOS) for the optimal design of composite structures developed by M. Montemurro and co-workers at the I2M laboratory in Bordeaux.
The first goal of the work is to correctly catch (at each relevant scale) the mechanical responses of the composite structure with a considerable reduction in terms of computational costs while keeping a good level of accuracy. To do so, an appropriate global-local modelling approach based on higher-order layer-wise theories developed in the framework of the Carrera Unified Formulation (CUF) is proposed. This modelling strategy allows to correctly describe the stress state in the most critical regions of the composite structure and, consequently, allows correctly capturing the failure phenomena that cannot be detected through standard finite element (FE) formulation approaches, i.e. the equivalent single-layer approaches.
The second goal is to extend the MS2LOS in designing CSC stiffened panels. The effectiveness of the MS2LOS is firstly tested on a meaningful problem representative of thin-walled structures of the aerospace sector: the least-weight design problem of a stiffened composite panel (typical of aircraft structures), without introducing simplified hypothesis on the mechanical behaviour and considering the whole set of geometrical and mechanical design variables which are defined at both macroscopic and mesoscopic scales of the laminate. On the one hand, at the macroscopic scale where each laminate composing the structure is modelled as an equivalent single-layer plate, the goal is to find the optimum value of the design variables (geometrical and mechanical) to minimise the mass of the panel meeting the set of imposed design requirements (feasibility, manufacturing, stiffness, buckling, etc.). On the other hand, at the mesoscopic scale, the aim is to find at least one stacking sequence that meets the optimum design variables resulting from the structural optimisation carried out at the macroscopic scale.
The multi-scale optimisation of VSCs is also addressed in this work. In particular, the first-level problem of the MS2LOS is solved to determine the optimal distribution of the VSC stiffness properties at the macroscopic scale satisfying the requirements of the problem formulated as optimisation constraints. In this phase, the VSC laminate is modelled as an equivalent homogeneous anisotropic plate whose behaviour is described in terms of polar parameters (PP), which vary locally on the structure. FSDT (First-order Shear Deformation Theory) is used to take into account the influence of transverse shear stiffness on the mechanical response of the VSC and B-spline surfaces are used to represent the PPs fields over the structure. In this context, the expression of the gradient of the buckling factor is determined analytically by exploiting the properties of the polar formalism and of the B-spline surfaces in order to speed up the optimisation process.
The integration of the global-local modeling approach based on layer-wise higher-order theories in the MS2LOS is the final goal of this Thesis. The objective is to identify and isolate the regions of the model which require more precise investigations during the first

optimisation step of the MS2LOS and to analyse these regions of interest using the global - local approach developed in the CUF framework. To this end, two FE models are developed and interfaced. The first one is a low-fidelity FE (LF-FE) model generated by means of a commercial software. In the context of the LF-FE model, each laminate constituting the structure is modelled as an equivalent single-layer plate, whose macroscopic behaviour is described in the PPs space. The most critical regions of the LF-FE model, i.e. the so-called zones of interest (ZOIs), are identified by means of a suitable criterion formulated in the PPs space. Then, a high-fidelity FE (HF-FE) model based on layer-wise theories is generated for the critical ZOI to assess the local structural responses which are integrated in the problem formulation.

1.3 Thesis structure

The Thesis outline is provided here below.
Chapter 2 presents the state of the art on the main topics of the manuscript: the design methods for CSC and VSC structures and global-local modelling approaches for composites. In Chapter 3, the global-local modelling approach in the CUF framework is presented. The Chapter is devoted to the fundamentals of the 1D higher-order models based on CUF and to the description of the global-local methodology developed in this work.
Chapter 4 deals with the fundamentals of the polar method and composite laminate mechanics. These aspects are preparatory for better understand the MS2LOS used in this work for the design of CSC and VSC structures. The first part of the chapter shows the fundamentals of the polar method for plane elasticity and the application to the framework of the FSDT, respectively. The second part of the chapter presents the polar descriptions of the laminate strength tensors and the class of the quasi-trivial stacking sequences.
In Chapter 5, the least-weight design problem of a stiffened composite panel is presented. The chapter is characterised by the mathematical formulation of the first-level problem which provides the optimum set of design variables at the macroscopic scale, which satisfies the constraints of the problem, and of the second-level problem, which aims at finding the stacking sequence of the composite material that fulfil the optimal value of the design variables resulting from the first-level problem.
Chapter 6 presents the general iso-geometric polar approach for the optimisation of VSC structures applied to the eigenvalue buckling problem. Firstly, the mathematical formulation of the first-level problem is discussed with a preliminary introduction of the B-spline surface framework that is used to describe the point-wise variation of the mechanical properties of the VSC plate. The problem of the maximisation of the first buckling load is presented with particular emphasis on the derivation of the analytical expression of the gradient of each physical response in terms of design variables involved in the definitions of B-spline surfaces.
The integration of the global-local modelling approach based on CUF into the MS2LOS for the design of CSC structures is the object of Chapter 7. In particular, the description of the algorithm to deal with the least-weight design problem of a simplified wing-box is presented. The crucial aspects of interfacing the CUF-based global-local modelling approach with the MS2LOS are highlighted.
Finally, Chapter 8 concludes the Thesis with some meaningful comments and prospects.

Chapter 2

State of the art

2.1 Design methods for constant stiffness composite structures

CSCs, like fibre-reinforced composite materials, are widely used in different industrial fields thanks to their outstanding performances, e.g. high stiffness-to-weight and strength-to-weight ratios, which lead to a substantial weight saving when compared to metallic alloys. Nevertheless, the design of CSCs requires the formulation of a complex multi-scale problem involving a huge amount of design variables and a variety of phenomena intervening at the different scales (see [3–10]). In the case of multilayer plates, the problem scales are, at least, three, as shown in Fig. 2.1: (1) the microscopic scale (that of the constitutive phases), (2) the mesoscopic scale (that of the constitutive lamina) and (3) the macroscopic scale (that of the laminate).

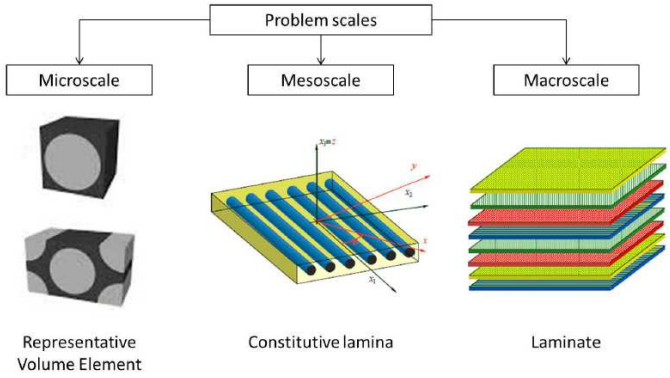

Figure 2.1: The different scales involved in the design problem of multilayer structures [5].

Furthermore, the designer has to deal with design variables of different nature depending on the considered scale. At the microscopic scale, for instance, the design variable set includes the material properties of constitutive phases (fibres, matrix, additives, etc.), their volume fraction and the spatial distribution of each phase, i.e. the topology of the representative volume element (RVE). At the mesoscopic scale, the design variables are the material properties, the thickness and the orientation angle of the single lamina. At the macroscopic scale, the composite is often modelled as an equivalent homogeneous anisotropic medium whose mechanical behaviour is described in terms of a set of constitutive matrices, which depend on the choice of the kinematic model. The design variables at

different scales are related, and the relationship among the problem scales is not bijective, see [11]. For instance, consider the mesoscopic-macroscopic scale transition: for a given stacking sequence one can determine a unique set of constitutive matrices describing the behaviour of the composite at the macroscopic scale; conversely, a given set of laminate constitutive matrices can be related to different SSs. Furthermore, the heterogeneity and the anisotropy, which are characteristic properties of composite materials, intervene at different scales of the material, thus further complicating the design of the CSCs [5].
Many researchers have faced the challenge of developing suitable strategies and algorithms for the design of CSCs. Nevertheless, the research is still ongoing.
The optimisation strategies of CSCs can be classified according to the criteria proposed in [5], which are:

1. Optimisation algorithm used to perform the solution search
2. Problem formulation

The most commonly used optimisation algorithms for the optimisation of CSCs can, in turn, be divided into the following groups:

- Deterministic algorithms. The gradient of the physical responses can be provided either in closed form or calculated numerically (through finite differences). The advantage of these algorithms lies in the speed of convergence of the optimisation problem, while the disadvantages are mainly related to the calculation of the gradient itself (when the analytical form is not available the computational cost to calculate it can be prohibitive) and to the possibility of determining only a local optimum.

- Meta-heuristic algorithms: unlike deterministic algorithms, they do not require the explicit calculation of the derivatives of the objective function and the constraints on the design variables. They have a weaker convergence than deterministic algorithms and the computational cost required for large-size problem is prohibitive, but, by exploiting the values of the objective function calculated in the previous steps, they can easily find a pseudo-optimal solution located near the global optimum. Moreover, at the end of the optimisation process, many solutions are available, which can be conveniently exploited for design purposes.

In the literature, it is possible to find several works on deterministic [12–17] and meta-heuristic [18–26] algorithms in the optimisation of CSCs. In this work, the meta-heuristic algorithm implemented in ERASMUS [5] will be used for the optimisation of CSCs at the macro-scale and meso-scale. For more details on the various differences between these algorithms, the reader is addressed to [5].
On the other hand, the formulation of the problem for searching the optimal stack in CSCs can also be decisive. The work of Ghiasi [27] exhaustively summarises the possible optimisation strategies by dividing them into two categories: single-level optimisation strategies (SLOS) and multi-level optimisation strategies (MLOS).

2.1.1 Single-Level Optimisation Strategies for CSCs

The single-level optimisation approaches are usually formulated by involving design variables at the laminate mesoscopic scale (ply-level). In fact, the main design variables are the number of layers, thickness, orientation angles and sometimes material properties. In this context, the objective function and the optimisation constraints are strongly non-convex

functions, thus a particular attention must be paid in the resolution of the related constrained non-linear programming problem (NLPP). To deal with such NLPPs, engineers make use of simplifying hypothesis and design guidelines to search for a feasible optimised solution. In the literature the most frequently used design assumptions are the following:

- Symmetric stack: a sufficient condition to ensure membrane/bending uncoupling.
- Balanced stack: a sufficient condition to ensure a membrane orthotropic behaviour.
- Orientation angles: the value of the generic ply orientation angle is genearlly limited to the following canonical set: $0°, \pm 45°, 90°$.

Together with the above simplifying hypotheses a set of design rules is often introduced when searching for an optimum SS: percentage rule, contiguity rule, disorientation rule, grouping rule, etc. [28]. These rules represent a sort of best practice in designing conventional stacks, which are the result of the experience collected in the last 50 years in the aerospace sector. If such rules make it possible to simplify the design problem of a composite structure, their systematic use has an important consequence: the extent of the design space is extremely reduced and the number of potential optimal solutions is, thus, decreased. In the literature, it is possible to find a huge amount of works dealing with the optimisation of CSCs through the SLOS. Without any ambition of exhaustiveness, only some works focusing on the buckling and post-buckling strength/stiffness optimisation will be quoted in the following. A rather exhaustive literature survey on the application of SLOS for the optimal design of CSCs is available in [27]. The SLOS is usually employed to solve the pre-buckling strength/stiffness and the post-buckling stiffness maximisation problem of simply supported biaxially loaded laminated plates using pre-set symmetrical angle-ply stacking sequences, as reported in [27, 29].
The maximisation of the first buckling load of a bi-material multilayer plate is faced in [30]. A genetic algorithm (GA) is used to solve the problem of maximising the first buckling load of a multilayer plate with a given number of plies in [31], whilst the Ant Colony Optimisation method is used in [32] showing better performances, in terms of computational cost, than the GA. Two examples of multi-objective optimisation (least-weight design and first buckling load maximisation) problem are proposed in [33, 34]. The US Department of Defense has also provided guidelines for optimizing CSCs [35].
As mentioned beforehand, all the works cited above share the use of simplifying assumptions to find a feasible optimal solution to the design problem of a CSC structure. In particular, the use of a pre-defined set of orientation angles is a major limitation because modern technologies (e.g. AFP) are able to orient the fibres with an accuracy of at least 1°. The same remark holds for the use of symmetrical stacks to guarantee the membrane/bending decoupling of the laminate. This is only a sufficient condition that undoubtedly shrinks the design domain and reduce the number of design variables to be optimised (only half of the layers orientations are optimised). As discussed in [36–38] , symmetric stacks constitute only a small sub-set of a larger class of sequences called *quasi-trivial stacking sequences*. Finally, the balanced stack hypothesis represents only a sufficient condition to ensure an orthotropic membrane behaviour of the laminate when a balanced stack is used the bending stiffness tensor is completely anisotropic, except for cross-ply laminates. The anisotropy of the bending stiffness tensor, unfortunately, has harmful effects, especially when symmetrical and balanced stacks are used for thin-walled structures, because they induce buckling and flexural vibration phenomena, and for this reason, such laminates are not the best choice [6, 39]. In this scenario, MLOS represent a suitable alternative to SLOS.

2.1.2 Multi-Level Optimisation Strategies for CSCs

Generally, the design problem of a composite structure is subdivided into two or more sub-problems in the framework of MLOS. However, such sub-division of the problem is possible if and only if the characteristic scales of the problem can be separated and if particular conditions are satisfied. The first step (or level) of a multi-scale optimisation strategy is formulated using macroscopic geometric and mechanical design variables. At this level, the laminate is modelled as a homogeneous and anisotropic continuum, and the mechanical and geometrical properties of the composite structure are optimised. The objective of the second step is, instead, to find at least one optimal stack matching the optimised mechanical properties found during the first optimisation step.
Such MLOS have the advantage of greatly reducing the number of design variables to be optimised in the first optimisation step. Moreover, the non-convexity characterising the constrained non-linear programming problem (CNLPP) is strongly relaxed during the first step. As far as the disadvantages are concerned, one of the main problems is to correctly formulate design requirements that actually intervene at lower scales, such as manufacturability constraints and constraints related to the failure of the material, in terms of equivalent constraint to be imposed on the macroscopic design variables involved at the first step. In the literature, the main difference that can be observed between the works focusing on the use of MLOS concerns the mathematical representation used to describe the macroscopic behaviour of the laminate. In this regard, the main multi-scale optimisation approaches can be divided into two categories: approaches based on the use of lamination parameters (LPs) and those based on the use of polar parameters (PPs).

Lamination parameters

The most common MLOS make use of the LPs combined with Tsao-Pagano parameters [11] to describe the laminate constitutive tensors at the macroscopic scale. Diaconu *et al.* presented two works [40, 41] on the LPs. In the first one, a method to determine the feasible region in the LPs space is presented. The second work shows the maximisation of the first natural frequency of a thick laminate through a MLOS. The optimisation of the flexural LPs is the goal of the work by Liu *et al* [42] to maximise the first buckling load of a multi-layered plate. In this case, only the optimal value of the flexural LPs is determined at the macroscopic scale, while there is no information on the second step of the procedure, i.e. the determination of an optimal lay-up corresponding to the values of the flexural LPs resulting from the first step of the procedure. A very interesting multiscale optimisation approach is presented in [43], where they solved the problem of the mass minimisation of a simply supported laminated plate by means of a two-step optimisation strategy taking into account failure and buckling constraints. This work also extended to the canonical set of orientation angles by adding the values: $\pm 30°$ and $\pm 60°$. The weight minimisation of composite panels with T-shaped stiffeners is the goal of the work of Herencia *et al.* [44]. Using a MLOS, in the first step the optimal value of the LPs satisfying strength, buckling and technological design requirements is determined. In the second step, the authors searched for stacks meeting the optimum LPs found at the first step. Another important work is the one presented by IJsselmuiden *et al.* [45]. Using the phenomenological failure criterion by Tsai and Wu [46], they created a conservative failure envelope to ensure a failure-free region in the LPs space. Recently, Bramsiepe *et al.* [47] presented an LPs-based approach for the least-weight design problem of a lifting system structure. This structure consists of symmetric laminates and the authors took into account blending, buckling and failure constraints in their multi-scale approach. The

reader is addressed to the review article [48] to find further interesting works on the topic of the optimisation of CSCs using LPs.
In conclusion, the mathematical representation based on LPs has the advantage of reducing the design variables of the problem during the first step of the MLOS. In fact, there are at most 12 design variables to be optimised to characterise the anisotropic behaviour of the CSC structure at the macroscopic scale using the classical lamination theory (CLT). Nevertheless, LPs are not tensor-invariant quantities. In fact, although some of Tsai-Pagano parameters are invariants, the remaining LPs are integrals of trigonometric functions that depend on the lamina angle and thickness.

Polar Parameters

A sound alternative to represent the macroscopic behaviour of a CSC structure is represented by the polar method. The polar method was introduced by Verchery [49], and allows representing a generic n-order plane tensor by means of tensor invariants, i.e. PPs. This method has been subsequently refined by Vannucci [50–52]. In particular, in [52], the analytical expression of the bounds of the feasible domain of the PPs space is provided. It is noteworthy that, recently, Picchi Scardaoni and Montemurro [53] rigorously proved that the feasible domain of a laminate made of identical plies (i.e. same thickness and material) is non-convex either in the LPs space or in the PPs space.
The possibility of describing the mechanical behaviour through tensor invariants and the fact that these parameters have a physical meaning related to the tensor symmetries explains why the polar method is particularly attractive in the study and optimisation of composite materials. In the work by Catapano *et al.* [54] the polar method is used for the formulation of common failure criteria for orthotropic laminates while in the work of Montemurro et al. [55] the mathematical representation through PPs is investigated for the design of the elastic properties of a generic laminate with the least number of plies. In the beginning, the polar method studied by Vannucci in [50] was developed in the CLT framework. Subsequently, in [56–58] Montemurro extended the polar method to Higher-order Equivalent Single Layer Theories (HESLTs), thus making it possible to study and optimise the mechanical behaviour of thick laminates. Catapano *et al.* in [59] proposed a unified formulation of the most common failure criteria of laminates using the polar method in the framework of the CLT. This work has been later extended by Catapano and Montemurro in [60] to the FSDT framework by proving that stiffness and strength tensors of the laminate are strictly related. Moreover, in this work, closed-form expressions of the stiffness and strength tensors of the laminate as a function of PPs are derived.
The MS2LOS presented by Montemurro *et al.* in [61] is devoted to the design and optimisation of composite structures. The basis of the MS2LOS is the polar method, which allows the description of the behaviour of the laminate at the macroscopic scale, during the first level of the optimisation process, without introducing simplifying hypotheses on the SS nature and by including in the problem formulation technological requirements at the lower scale by means of pertinent constraints on the laminate PPs. The effectiveness of the MS2LOS has been shown on several applications dealing with the optimum design of lightweight composite structures, like the least-weight design of a simplified wing box subject to requirements on the laminate feasibility and on the first buckling load in [61, 62], or the multi-scale optimisation of sandwich panels with honeycomb core [63, 64]. In [39], the strategy was further generalised by using Non-Uniform Rational B-Spline (NURBS) curves to describe the shape of the RVE constituting the honeycomb core of the sandwich panel. Further successful applications of the MS2LOS related to the design of CSC structures include: optimal design of the damping capability of hybrid laminates [65] and of compos-

ite structures equipped by viscoelastic patches [66], optimal design of composite stiffened panels [6] and of simplified wing-box architectures including blending constraints [67–69], multi-scale optimal design of real-world complex engineering structures like fuselage barrels [7]. In all of the aforementioned works the MS2LOS makes use of either standard deterministic algorithms or a special genetic algorithm, called ERASMUS (EvolutionaRy Algorithm for optimiSation of ModUlar Systems) [5], which is capable of solving CNLPPs defined over a space of changing dimension (i.e. CNLPPs characterised by a variable number of design variables). The MS2LOS, initially introduced by Montemurro *et al.* in [61, 62], has been extended in this Thesis, on the one hand, by generalising the use of quasi-trivial solutions during the second-level problem (Chapter 7) and, on the other hand, by integrating the global-local modelling strategy based on Carrera's Unified formulation to precisely describe the characteristic phenomena involved at the lower scale (ply-level) of the composite (Chapter 7).

2.2 Design methods for variable stiffness composite structures

The permanent need for more efficient structures and the constant technological progress in manufacturing processes led researchers to focus on new technological solutions for composite structures, as discussed in [70]. These innovative solutions, known as *Variable Stiffness Composites* (VSC), are characterised by properties (mechanical, thermal, etc.) that vary point-wise over the structure. The point-wise variation of properties confers, on the one hand, better performance compared to the CSCs counterpart but, on the other hand, significantly complicates the design/optimisation process, as discussed in the review work by Ghiasi *et al.* [71].
VSCs can be manufactured in a variety of ways: among the different classes of VSCs, only one particular family of solutions is investigated in this Thesis, i.e. the so-called variable angle tow (VAT) composites. This solution is characterised by fibres assembled into tows that are placed along a curvilinear path within the generic lamina in such a way to get a point-wise variation of physical properties (e.g. stiffness, strength, conductivity, etc.). VAT composites can be manufactured by means of two technologies: the automated fibre placement (AFP) or the additive manufacturing technology obtained by combining the Fused Filament Fabrication (FFF) process with the Continuous Filament Fabrication (CFF) one [72]. On the one hand, the AFP technology is, undoubtedly, the most widespread process to produce VAT composites because it provides great flexibility in making structures of large size. However, through the AFP technology, it is not possible to fabricate structural parts of complex geometry (only plate-like or shell-like structures can be tailored) and the manufactured parts are highly sensitive to manufacturing defects as discussed [73, 74]. In particular, the influence of the most common defects related to the AFP process, i.e. gaps and overlaps, are investigated by Nik *et al.* [75] on the buckling load and in-plane stiffness of VAT laminates. In Fig. 2.2 an example of AFP machine with its main components is shown. On the other hand, the FFF + CFF process allows manufacturing VAT composites of intricate shapes, however the quality of the employed materials is poor and the manufacturing process is characterized by different kinds of imperfections (porosities, geometric limitations on tow curvature, tow width, rich resin regions, etc.) which are strongly related to the set of multiple parameters tuning the process behaviour. The process features and the correlation between process parameters and material properties is currently under investigation in the framework of several research

projects [5].

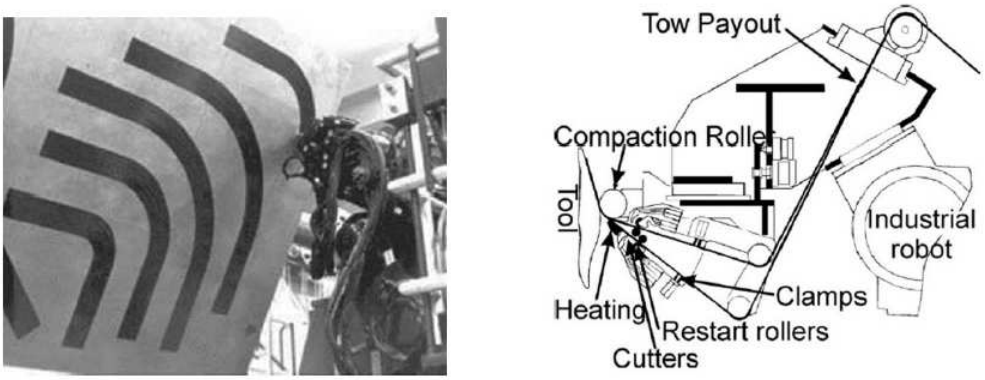

(a) A typical AFP machine (taken from [76]).

(b) Main elements constituting an AFP machine (taken from [77]).

Figure 2.2: The AFP manufacturing process.

The design/optimisation process of VAT composites is much more complicated than the one of CSCs and a huge number of design variables is necessary to properly describe the characteristic fields and to describe the mechanical behaviour at each relevant scale, as explained by Setoodeh *et al.* in [9, 10]. In addition, the lack of knowledge about damage mechanisms and the lack of dedicated failure criteria to be integrated in the design process of these materials represent open problems not yet fully resolved by the scientific literature. As discussed in [78], these issues are always related to two intrinsic properties of composite materials, i.e heterogeneity and anisotropy, that occur at different scales of the structure and vary point-wise in the case of VAT composites.
Up to now, no general rules are available in the literature for the multi-scale design of VAT composites. As in the case of CSC structures, two approaches are used in the literature to design/optimise VAT composites [71]: the SLOS and the MLOS.

2.2.1 Single-Level Optimisation Strategies for VSCs

In the context of the SLOS, the parameters tuning the shape of the fibres-path are considered as design variables: a large number of works carried out in the last thirty years can be found in literature on this topic. One of the first examples in this sense is the work by Hyer and Lee [79], wherein the authors underline the advantages of VAT composites over conventional CSCs by maximising the first buckling load of a plate with a hole in the centre. Hyer and Charette [80] understood that locally aligning the main orthotropy axis of the material to the principal stress and/or strain direction can lead to an increase of the failure load of open hole plates under tension. In particular, they made use of an iterative procedure to align the fibres-path with the principal stress direction. Another interesting work on VSCs is the one by Gürdal and Olmedo [81], wherein a closed-form solution of the plane elasticity problem of a symmetric laminated composite panel is presented. In this work, the local orientation angle of the fibres is described by means of a linear function.
A first attempt dealing with a general formulation of the fibres-path was proposed by Nagendra *et al.* [82]. In this work, the authors implemented a shape optimisation approach to determine an optimised fibres-path taking into account manufacturing

requirements. Jegley *et al.* [83] highlighted the effectiveness of stiffness tailoring using curvilinear fibres-paths. The authors succeed in demonstrating the efficiency of VAT composites in decreasing the stress concentration near geometric discontinuities (like holes) and in improving the load capacity of the plate. A SLOS was applied by Gürdal *et al.* [84] who dealt with the effects of the stiffness variation on the in-plane and buckling response in flat rectangular VAT laminates employing simplified fibres-path definitions based on 1-D functions [84]. Wu *et al.* in [85] dealt with the buckling load maximisation of a VAT composite plate under uni-axial load with mixed boundary conditions (mechanical and geometric) proposing a non-linear variation of the fibre-path. The buckling problem is solved by a modified version of the Rayleight Ritz method while a GA is used to find the optimal fibre-path by maximising the first buckling load. A differential quadrature methodology based on the Airy's stress function was developed to study the pre-buckling and post-buckling behaviours of VAT laminates subject to axial compression and mixed boundary conditions (BCs) in [86, 87]. Coburn *et al.* [88] proposed an analytical model for the buckling analysis of stiffened VAT panels. The results provided by this model are in good agreement with those resulting from a FE analysis.

2.2.2 Multi-Level Optimisation Strategies for VSCs

In the framework of the MLOS, the optimum design of a VSC structure is split in two sub-problems. In analogy with the case of CSCs, at the macroscopic scale the VSC is represented as an equivalent single layer plate and its mechanical response is described by a set of parameters, related to the VSC stiffness matrices, which constitute the design variables. At the mesoscopic scale (i.e. the lamina level) the goal is to determine the optimum fibres-path, in each lamina, satisfying the optimum distribution of the macroscopic mechanical variables.
As in the case of CSCs, the MLOS available in the literature can be divided in two groups, depending on the mathematical representation used to describe the VSC structure anisotropy at the macroscopic scale, i.e. LPs and PPs.

Lamination parameters

A review article on the MLOS for VSCs making use of lamination parameters (LPs) has recently been presented in [89].
Setoodeh *et al.* [10] presented a generalised reciprocal approximation for the design of VSC panels for maximum buckling load. In this formulation, the buckling load is approximated using a first-order Taylor series expansion in terms of the point-wise compliance tensors. The related maximisation problem is reduced to a simple local optimisation at any discretisation point. An approximation scheme for the evaluation of the buckling load is presented by IJsselmuiden *et al.* [90] in the LPs space. In this work, the LPs are the design variables of the problem, which are defined for each element constituting the mesh of the VSC structure FE model. The formulation based on the LPs proposed in this work approximates the buckling load as a convex function of the LPs and the adjoint method is used to compute its gradient. However, as discussed in [53] and as shown in Chapter 6, the buckling function is not convex neither in the LPs space nor in the PPs space. On the other hand, the need of refined FE models to better describe the distribution of the LPs field lead to a significant computational cost.
Khani *et al.* [91] showed quite interesting improvements on the failure load of a VSC plate with a central hole under tensile load. In their analysis, the authors employed the

laminate-level failure criterion introduced in [45] and a deterministic algorithm (DA) to maximise the failure load.
A two-level optimisation procedure is proposed by Wu *et al.* [92] in the LPs space. The design problem was formulated as the maximisation of the first buckling factor subject to feasibility constraints on LPs and the B-Spline surfaces are used to represent the LPs fields over the VAT laminate. A multilevel approach to optimise the fibres-path at each node of a FE model is presented in [93]. In the first level optimisation, the LPs are used to describe the mechanical response of the VAT laminate, while in the second step the Gauss-Newton quadratic approximation is used to retrieve the optimised fibres-path corresponding to the optimum LPs found during the first step. In this case, the manufacturing requirement is imposed through a constraint on the gradient of the fibre angle between nodes, even if in this way there is no warranty to find optimum fibres-paths satisfying both the manufacturing constraints and the optimised LPs distribution resulting from the first step.
As for the CSCs, the use of LPs in the VSCs is systematically associated to the use of simplifying hypotheses, like the use of symmetric stacks to obtain membrane-bending uncoupling or the use of balanced sequences to get membrane orthotropy, to solve the design optimisation problem. As discussed in [3, 4, 78, 94, 95], the use of these hypothesis systematically leads to a misleading solution (e.g. a symmetric balanced stack is totally anisotropic in bending) and extremely shrinks the design space.

Polar parameters

The work by Jibawy *et al.* [96] represents the first application of the MLOS based on the polar method to the optimal design of VSCs. The optimisation problem dealt with the minimisation of the compliance. In the first-level problem an iterative procedure is used to compute optimal value of the anisotropic polar moduli, while the main orthotropy axis is aligned to the direction of the principal stress after carrying out a FE analysis. In the second step, the fibres-path in each lamina is determined, althouhg continuity of the fibres-path and other manufacturing constraints are not ensured.
Catapano *et al.* [59] dealt with the problem of optimising the anisotropy distribution of a laminated structure maximising simultaneously its stiffness and strength. Polar formalism has been used to represent both the stiffness and strength tensors and a two-step hierarchical strategy is used to solve the optimisation problem. The first step aims to find the best distribution of the stiffness and strength anisotropic tensors while in the second one the lay-up satisfying the optimal properties obtained as a result of the first step is determined by a GA for each element of the FE model. No continuity constraints are applied in this work and many infeasible solutions were detected consequently. Moreover, the study was conducted under the hypothesis of mutual independence of the elastic and strength properties of the laminate. This hypothesis was proven wrong in a later work by Catapano and Montemurro [60]. An enhanced version of the MS2LOS was presented by Montemurro and Catapano in [94]. The use of the B-spline surfaces to describe the distribution of the PPs over the structure ensures the continuity and smoothness of the PPs fields describing the anisotropy of the VAT laminate at the macroscopic scale. Furthermore, the definition of the design variables is unrelated to the FE model of the structure. The latter is an important milestone because it significantly reduces the number of design variables and the computational cost without degrading the accuracy of the structural responses evaluation. In a subsequent work [4], the approach was enhanced by integrating, into the first-level problem formulation, an equivalent constraint in the PPs space (imposed on the gradient

of the main orthotropy axis) to ensure the fulfillment of the manufacturability requirement on the maximum admissible curvature of the tow at the ply-level.
In a recent work, Catapano and Montemurro [95] dealt with the problem of designing VSCs against failure. They used the MS2LOS to minimise, at the first level, the Laminate Failure Index (LFI), introduced by the same authors in [60], and to search the optimal fibre-path in the second-level problem. In the first-level problem, the GA ERASMUS is used to perform the solution search and the feasibility and the maximum tow curvature constraints are formulated in the PPs space. In the second level optimisation, the analytical method proposed by Miki and Sugiyamat [97] coupled with the use of quasi-trivial stacking sequences [36, 37] are applied to find the optimal fibres-path (within each ply) meeting the optimum set of PPs resulting from the first-level problem. A further check is done a posteriori to assess the local failure index for each ply.
The problem of the compliance minimisation was presented by Montemurro and Catapano in [78]. In this work, the analytical expressions of the gradient of the strain energy of the VAT laminate and the feasibility constraints were derived by exploiting the properties of the B-spline entities. The closed-form expressions allow speeding up the solution search for the first-level problem by using a suitable DA. Finally, in a recent work by Izzi *et al.* [98], the MLOS based on the polar method, on the B-spline surfaces and on the use of DA to solve the optimisation problem has been enhanced by integrating the laminate failure index, a new narrower (and more conservative) formulation of the maximum tow curvature requirement in the PPs space and by introducing an efficient variable transformation to automatically satisfy the feasibility constraint on the PPs. Of course, the gradient of each function was analytically derived by exploiting the properties of the B-spline surfaces.
As it can be inferred from the above works, the MS2LOS reveals to be an effective methodology to optimise VSC structures. Nevertheless, this approach needs to be improved to deal with design problems of increased complexity.
Chapter 6 is devoted to the application of the MS2LOS to maximise the first buckling load of a VAT laminate subject to feasibility constraint. The main contribution of this work is about the derivation of the analytical expression of the buckling factor gradient in the most general case (in-plane and out-of-plane loads) in the PPs space by exploiting the properties of the B-spline surfaces.

2.3 Global-local modelling strategies for composite structures

The design and analysis of aerospace structures require a detailed evaluation of stresses. Nevertheless, the complexity of large structures and the use of composite materials can significantly increase the computational costs of the numerical models. Typical FE models of aircraft structures in the preliminary design phase are characterised by the combination of 1D and 2D elements, which are appropriately selected to simulate stringers, panels, ribs and other components. This discretisation is, obviously, a simplification of reality but it is necessary because it allows the designer to have an idea of the distribution of stresses on the structure, even if affected by the simplifying assumptions due to the application of classical theories associated with the 1D/2D elements used by commercial software, and of the general mechanical response of the structure. However, 3D stress fields should be taken into account when geometric discontinuities of the structure are present, e.g. holes, joints and free edges and above all if composite materials are used. To accurately capture these localised 3D stress fields, the classical theories (CLT and FSDT

in the case of composites) cannot be used for this task and solid models or high-order theories are often necessary. However, using a full 3D FE model or a FE model composed of elements based on high-order kinematic models for a large-size structure is prohibitive from a computational perspective. To make the model more efficient, i.e. to find a good balance between computational cost and results accuracy, global-local approaches are often employed. Three main approaches are available in the literature to deal with a global-local analysis:

1. refining the mesh or the shape functions wherein critical regions [99–103];
2. formulating multi-model methods, in which different subregions of the structure are analysed with different mathematical models [104–111];
3. using models based on the Static Condensation also known as "Super-elements Methods" [112, 113].

The first class of methodologies listed above mainly address convergence problems in those regions where singularities occur. Adaptive techniques are often used to couple coarse and fine sub-regions of a structure. Among these techniques it is possible to make a further differentiation: *h*, *p* and *hp*-adaptation methods. The *h*-adaption method [99] is used when the structure subregions differ in mesh size, whereas the *p*-adaption method [100] can be applied when the subregions differ in the polynomial order of the shape functions. Moreover, the *hp*-adaption [101] can allow the implementation of subregions differing in both mesh size and shape functions. Other techniques allowing for the coupling of different meshes are, for instance, the multi-grid method [102], and the extended finite element method (XFEM) [103]. All these methodologies are considered here as single-model methods. Conversely, when it is necessary to verify the compatibility of displacements and the balance of stresses at the interface between kinematically incompatible elements, multi-models methodologies can be conveniently employed. These are characterised by the use of different mathematical models to describe the mechanical response within ZOI of the structure. The *s*-version of the FE method [104, 105] increases the resolution by superimposing additional mesh(es) of higher-order hierarchical elements in the ZOIs. This method is a valid alternative to the previous stated *h*, *p* and *hp*-adaptation single-model methods. The continuity of the displacement field is ensured by imposing homogeneous BCs at the ZOI boundary. The superimposed additional meshes can be of arbitrary shape, unlimited by the problem geometry, boundary conditions and the underlying mesh topography. A very interesting strategy is the one used by Shim *et al.* [106], wherein multipoint constraint equations are used to couple 1D and 2D elements with 3D solid by equating the work done on both sides of the dimensional interface. Blanco *et al.* [107] proposed an extended variational framework aiming at properly coupling structural models with different dimensionalities. The coupling conditions are obtained from the governing variational principle formulated at the continuous level. Ben Dhia [109] made use of the Arlequin method, which allows the superimposition of various mechanical models for structural analysis and computation. In particular, the author highlighted the potentialities of its method in the modelling of multi-scale mechanical problems showing the effectiveness of this new approach through a numerical test for the multi-scale problem of the cantilever beam. The Arlequin method was employed by Hu *et al.* [110] for the linear analysis of sandwich beams modelled via 1D and 2D finite elements.
Among the multiple-model methods, there are the so-called "Multi-steps methods" wherein the analysis of the ZOI is conducted in a second time. In other words, a preliminary global analysis is done on the whole structure, and once the critical region is identified, a local

analysis is set just on the ZOI. The BCs at the interface level are extracted from the analysis on the global structure and are imposed on the local model (provided a suitable transition region is preliminary defined).
One of the most representative multi-step methods is the one proposed by Mao and Sun [108]. The authors presented a global-local approach where, in the first step, a coarse mesh was used to analyse the entire structure to obtain the nodal displacements, which were subsequently used as BCs for the refined local analysis in the subsequent second step. A very interesting point related to the BCs of the ZOI was highlighted in that work. The BCs application always introduces some detrimental effects in the local analysis of the ZOI. To minimise the effects of such errors, the local analysis generally requires a region larger than the critical region where accurate stress fields are to be evaluated. Another interesting work on the global-local method sense is the one presented by Ransom and Knight [114]. They performed a global-local stress analysis making use of spline interpolation functions which satisfy the linear plate bending equation to determine displacements and rotations for the global-local coupling. The local analysis of the ZOI is totally independent of the global one. This methodology allows the use of refined local models to determine detailed stress states for specific structural regions reducing the computational cost.
The Ritz method for the computations of the kinematic BCs of the ZOI and the standard finite element method for the local analysis of the ZOI is employed in the two-step global-local methodology proposed by Haryadi *et al.* works [115, 116]. In this article, the global-local approach is used to compute the static response of a simply supported composite plate with cutouts [115] and small cracks [116]. The effectiveness of the methodology in the accurate prediction of stresses is numerically proven by showing a great reduction of computational costs.
The work of Thompson and Griffin [117] is one of the first examples of a multi-step global-local analysis for laminate composites coupling a 2D global model to the 3D local one. In the first step, a 2D global model of the laminate composite plate is realised and a zooming technique to refine the mesh in the proximity of the hole. The effect of the hole size is studied considering three different hole diameters and three different types of stacks: $[0^\circ_n, 90^\circ_2]_s$, $[90^\circ_n, 0^\circ_n]_s$ and $[0^\circ_{n/2}, 90^\circ_{n/2}, 0^\circ_{n/2}, 90^\circ_{n/2}]_s$. The global-local methodology has been successfully used in the interlaminar stress detection with reasonably computational cost compared to a fully 3D finite element analysis. Other interesting works on the multi-steps global-local methodologies are developed for ad-hoc applications, usually for the assessment of complex non-linear phenomena (e.g. crack propagation [118], progressive delamination [119] deep post-buckling [120]). Recently, the global-local modelling approach based on the *sub-modelling* technique has been integrated in the MS2LOS for the optimisation of large-size composite structures (fuselage barrel and wing-box structures) resulting in unconventional and very efficient structural solutions as discussed in [7, 8, 68, 121, 122]
The CUF, in the recent past, has been generalised by including global-local modelling strategies. The first example is the work by Biscani *et al.* [111], where the formulation of the Arlequin method in the context of the CUF and its application to the 1D finite element analysis using a different approximation order of the displacement field for the local ZOIs are shown. The Arlequin method was used for merging the global and local subdomains in order to solve the mechanical problem. Subsequently, further investigations were performed by coupling models with different kinematics by using point-wise Lagrange multipliers by Carrera *et al.* [123]. The main difference between the Arlequin-based and the Lagrange multipliers-based variable kinematic models is that the former includes an overlapping region, in which two solutions coexist which is a non-physical condition. Nev-

ertheless, both methods are suitable for building variable kinematic models. Recently, CUF has been extended by Zappino *et al.* [124] to deal with the global-local analysis of laminates by employing a node-dependent kinematics with high numerical efficiency.
A different approach is the one based on the super-element method. This methodology consists of dividing a large structure into many small ones (super-elements) which are then processed individually. The handling of each super-element results in a reduced set of matrices that represent the properties of the super-element accounting for the connections to adjacent structures. These matrices are computed by the Guyan's method [112, 113]. The super-element methodology is implemented in commercial FE software due to its robustness.
In Chapter 3 of this Thesis, a multi-step global-local modelling approach is presented. The proposed approach consists of a two-step procedure where the first step is devoted to the static analysis of a global model of the structure. It could be done by commercial software using 1D/2D elements. A criterion is established to identify the most critical region, which is subsequently analysed in the second step by using high-order models in the framework of CUF to obtain accurate stress fields. The framework of the high-order 1D models is the CUF, which has been demonstrated to be very efficient and effective for evaluating complex strain/stress fields of composite structures [125, 126] and also successful in the elastoplastic and progressive failure analyses [127, 128] over the last few years. The proposed methodology has the advantage of obtaining a detailed description of the stress field using high-order beam theories in the CUF framework in the critical region of the structure at reduced computational costs. Recently, the global-local methodology has been extended to the elastoplastic analysis of compact and thin-walled structures via refined models [129]. Finally, in Chapter 7, the global-local modelling approach base on CUF has been integrated in the MS2LOS to solve a meaninguful design problem: the least-weight design of a simplified wing-box structures subject to requirements of different nature assessed either on the global FE model or on the local one.

2.4 Conclusions

This literature survey has allowed to picture the state of the art of design procedures for CSC and VSC structures. In the case of CSC, the definition of the problem design variables is usually characterised by the use of rules and design guidelines that nowadays can be considered outdated. On the one hand, the use of these simplification rules allow simplifying the optimisation problem but, on the other hand, the design space is extremely shrunk and, consequently, the solution search cannot converge toward true global optima. To overcome this limitation, MLOS are adopted to find more general optimal solutions. Through the MLOS the optimisation of the macroscopic mechanical and geometrical characteristics of the CSC structures is carried out during the first-level problem, whilst the optimal lay-up is determined in the second step of the strategy. This formulation allows a relaxation of the non-convexity and brings a strong reduction of the number of design variables, without introducing simplifying hypotheses on the nature of the stacking sequences. In the literature, the main difference that can be observed between the various MLOS is about the mathematical representation of the laminate anisotropy at the macroscopic scale. Two representations are available: the one based on LPs and the one based on PPs. Nevertheless, MLOS based on LPs make a systematic use of the aforementioned simplifying rules with a detrimental effect on the design space. Furthermore, even if the optimisation problem of the first step is reduced in optimising only 12 LPs, these last are not invariant and do not have a physical meaning. Conversely, the representation PPs are

tensor invariants, which have a physical meaning directly related to the elastic symmetries. Through the polar method, not only simplifying hypotheses on the stacking sequence nature can be avoided, but it is also possible to optimise the laminate elastic symmetries at the macroscopic scale.
The permanent need for more efficient structures and the constant technological progress in manufacturing processes has led researchers to focus on new solutions which are characterised by the point-wise variation of their mechanical and thermal properties. These solutions, known as VCSs, presents better performance compared to the CSC counterparts. The same considerations of CSCs can be done for VCSs in the case of the design/optimisation problem, keeping in mind that the point-wise variation of the properties significantly complicates the resolution of the problem.
Lastly, a state of the art on the global-local modelling approaches has been carried out. Global-local modelling approaches are used to make models more efficient when detailed analysis is needed in a reduced time. The use of such methodologies increases the ability of models to determine much more accurate results while reducing computational costs and their application is particularly relevant in the design and certification process of aerospace structures. In these processes, detailed stress characterisation is often mandatory and the FE models used in the preliminary design phases are not always able to provide these results efficiently. FE models of structures such as wing and fuselage are essentially constructed by combining 1D and 2D elements that discretise the mathematical domains of reinforcements, panels, ribs, and other components. Such discretisation is obviously a simplification of reality and does not allow obtaining an accurate description of the 3D stress field that is of capital importance in some ZOIs of the models, e.g. the wing-fuselage intersection, engine-pylons, etc.
Detailed stress characterisation becomes even more important when composite materials are used for such structures due to the peculiar failure mechanisms related to composite materials. The failure mechanisms of composite materials are still being studied by the scientific community. Certainly, the use of 1D/2D FE models are unable to detect such failure mechanisms and, hence, in the preliminary design phase, it is usual to use high safety margins and consequently reducing all the advantages related to composite materials (high strength to weight ratio and high stiffness to weight ratio). To obtain a 3D description of the stress field, solid elements or element based on high-order theories are usually employed. Nevertheless, the generation of FE models of complex structures, like a wing or a fuselage, composed exclusively such elements, is unfeasible, from a computational perspective. In fact, in these cases, global-local modelling approaches reveals to be of paramount importance in the analysis of the structural responses. To conclude, this literature survey allows to identify the main advantages and disadvantages in the design and optimisation of CSC and VSC structures. The work that will be presented in the following chapters aims at giving a contribution to the multi-scale design and optimisation of composite structuresby integrating a multi-step global-local modelling strategy based on high-order kinematic models.

Chapter 3

Global-local approach in the framework of CUF

3.1 Introduction

Global-local finite element approaches are used to make models more efficient when detailed analysis is needed. The use of such methodologies increases the ability of models to determine much more accurate results while reducing computational costs. The application of global-local approaches is of particular relevance for example in the design and certification process of aerospace structure and system. In these processes, detailed stress characterisation is required and the FE models used in these phases are not always able to deliver these results efficiently. FE models of structures such as wing and fuselage are essentially constructed by combining 1D and 2D elements that discretise the mathematical domains of reinforcements, panels, ribs, and other components. Such discretisation is obviously a simplification of reality and does not allow a 3D description of the stress that is of capital importance in some ZOIs of the models, for example the wing-fuselage intersection, engine-pylons, etc.
Detailed stress characterization becomes even more important when composite materials are used for such structures. The failure mechanisms of composite materials are still being studied by the scientific community. Certainly, the use of 1D/2D FE models are unable to detect such failure mechanisms and, therefore, in the preliminary design phase, it is usual to use high safety margins by adding weight and consequently reducing all the advantages of using composite materials (high strength to weight ratio and high stiffness to weight ratio). To obtain a 3D description of the stress field, solid elements or element models based on high order theories are usually employed. Nevertheless, the generation of FE models of complex structures, like a wing or a fuselage, composed of such elements, is not a strategy feasible, from a computational perspective. In fact, in these cases, global-local modelling approaches reveals to be of paramount importance in the analysis of the structural responses.

In this Chapter, a global-local methodology based on a two-step procedure is developed to accurately assess the stress field in the ZOI of the structures. In this methodology, the first step is dedicated to the static analysis of the global FE model (GFEM). The GFEM is made of classical 1D/2D elements and is generated by means of a commercial software. In this phase a criterion is established to isolate the most critical ZOIs of the GFEM that will be analysed in the second step using high order 1D theories to describe in detail the stress field. The refined local FE model (LFEM) used in the second step is implemented in the CUF framework. In particular, CUF has proven to be very effective and efficient in

evaluating complex stress and deformation states in composite structures [125, 126] and also successful in elastoplastic and progressive failure analysis [127, 128]. CUF provides 1D and 2D theories that overcome the classical theories (Euler, Timoshenko, Kirchoff, Reissner-Midlin, Love) by expressing the displacement field on cross-section (1D case) and along the thickness (2D case) in terms of basic functions whose shapes and order are chosen by the user. The capability, in terms of accuracy and description of stress and deformation states, of such 1D/2D models based on CUF is comparable with those obtained from 3D FE models but with a lower computational cost.

The novelty of the global-local methodology described here is to exploit the potential of CUF to study the stress/strain fields within the ZOI of the GFEM. The objective is to have a tool able to correctly describe these fields within the LFEM in the preliminary design phase of the structure paying attention to the free-edge effects, failure modes, delamination, etc.

This Chapter is organized as follows: Section 3.2 shows the main features of the 1D higher-order models based on CUF, while the global-local methodology is described in Section 3.3. Section 3.4 is devoted to numerical results. In particular, the first part of the section is dedicated to benchmarks of metal and composite structures to validate the methodology. The second part shows typical benchmarks for the study of the free-edge phenomenon in composite structures. Finally, Section 3.5 is devoted to the concluding remarks.

Publication related to this chapter: The methodology and the results presented in this Chapter have been published in [130].

3.2 1D higher-order models based on CUF

Consider a generic beam-like structure whose longitudinal axis, with respect to a Cartesian coordinate system, is oriented along y axis and its cross-section is defined on the xz-plane, as shown in Fig. 3.1. The cross-section of the structure is denoted by Ω, and the beam boundaries along y are $0 \leq y \leq L$. The transposed displacement vector is reported as

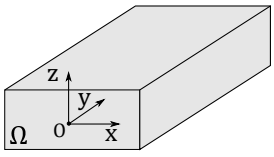

Figure 3.1: Coordinate frame of the beam model.

follows:

$$\mathbf{u}^T(x,y,z) = \{u_x(x,y,z), u_y(x,y,z), u_z(x,y,z)\}, \tag{3.1}$$

while the strain $\boldsymbol{\epsilon}$ and stress $\boldsymbol{\sigma}$ components, arranged according to the Voigt's notation reads as:

$$\begin{aligned} \boldsymbol{\epsilon}^T &= \left\{\epsilon_{xx} \quad \epsilon_{yy} \quad \epsilon_{zz} \quad \epsilon_{yz} \quad \epsilon_{xz} \quad \epsilon_{xy}\right\}, \\ \boldsymbol{\sigma}^T &= \left\{\sigma_{xx} \quad \sigma_{yy} \quad \sigma_{zz} \quad \sigma_{yz} \quad \sigma_{xz} \quad \sigma_{xy}\right\}. \end{aligned} \tag{3.2}$$

In the case of small displacements, the strain - displacement relation is

$$\boldsymbol{\epsilon} = \mathbf{D}\mathbf{u}, \tag{3.3}$$

where $\mathbf{D}$ is the linear differential operator expressed as:

$$\mathbf{D} = \begin{bmatrix} \frac{\partial}{\partial x} & 0 & 0 \\ 0 & \frac{\partial}{\partial y} & 0 \\ 0 & 0 & \frac{\partial}{\partial z} \\ 0 & \frac{\partial}{\partial z} & \frac{\partial}{\partial y} \\ \frac{\partial}{\partial z} & 0 & \frac{\partial}{\partial x} \\ \frac{\partial}{\partial y} & \frac{\partial}{\partial x} & 0 \end{bmatrix} . \tag{3.4}$$

The stress components can be attained by means of the Hooke's law

$$\sigma = \mathbf{C}\epsilon, \tag{3.5}$$

where $\mathbf{C}$ is the stiffness matrix of the material. For the sake of brevity, the expression of matrix $\mathbf{C}$ is not reported here, but it can be easily found in [131].
In the framework of CUF, the displacement field over the cross-section can be expressed as:

$$\mathbf{u}(x, y, z) = F_\tau(x, z)\mathbf{u}_\tau(y), \qquad \tau = 1, 2, ..., M \ , \tag{3.6}$$

where F_τ are functions which vary over the cross-section. In Eq. (3.6), $\mathbf{u}_\tau$ is the generalized displacement vector and M stands for the number of terms of the expansion where the repeated subscript, τ, indicates summation.
The choice of the expansion class F_τ determines the 1D CUF model that has to be adopted. Taylor-Expansion (TE) and Lagrange-Expansion (LE) classes are described in the following.

Taylor-Expansion class

TE 1D models make use of 2D classical polynomials in the form $x^i z^j$ $(i, j = 0, \ldots, N$ where N is the order of the expansion) as $F_\tau(x, z)$. For example, the second-order model, $N = 2$, leads to the following displacement field:

$$\begin{aligned} u_x &= u_{x_1} + x\ u_{x_2} + z\ u_{x_3} + x^2\ u_{x_4} + xz\ u_{x_5} + z^2\ u_{x_6}, \\ u_y &= u_{y_1} + x\ u_{y_2} + z\ u_{y_3} + x^2\ u_{y_4} + xz\ u_{y_5} + z^2\ u_{y_6}, \\ u_z &= u_{z_1} + x\ u_{z_2} + z\ u_{z_3} + x^2\ u_{z_4} + xz\ u_{z_5} + z^2\ u_{z_6}. \end{aligned} \tag{3.7}$$

The kinematic model described in Eq.(3.7) is characterised by three constants, six linear and nine quadratic terms, which are the unknowns of the problem at hand.
The possibility of easily enriching the displacement field of the 1D model allows dealing with a wide variety of problems without using ad-hoc formulations. Non-classical effects (e.g., shear effects, warping, in-plane deformations, bending-torsion couplings) can be studied by opportunely varying the order of the adopted model. Furthermore, the kinematic fields of the classical beam theories (Euler and Timoshenko) can be defined as particular cases of the first order TE model (N=1), which includes just the constant and the linear terms of Eq. (3.7). A more detailed description of TE models can be found in [126].

Lagrange-Expansion class

The LE 1D models are based on the use of Lagrange polynomials as generic functions above the cross-section. The cross-section of the beam is divided into a number of local

expansion sub-domains, whose polynomial degree depends on the type of Lagrange Expansion employed. Three-node linear L3, four-node bilinear L4, nine-node cubic L9, and sixteen-node quartic L16 polynomials can be used to formulate refined beam theories. LE allows for taking into account arbitrary section geometries.

Point	α_τ	β_τ
1	-1	-1
2	0	-1
3	$+1$	-1
4	$+1$	0
5	$+1$	$+1$
6	0	$+1$
7	-1	$+1$
8	-1	0
9	0	0

Table 3.1: L9 cross-section element point natural coordinates

Fig. 3.2 shows the node locations of one L9 sub-domain and Table 3.1 reports the node natural coordinates. In the case of a L9 element the interpolation functions are given by:

$$\begin{array}{rl} F_\tau = \frac{1}{4}(\alpha^2+\alpha\alpha_\tau)(\beta^2+\beta\beta_\tau), & \tau = 1,3,5,7\ , \\ F_\tau = \frac{1}{2}\beta_\tau^2(\beta^2+\beta\beta_\tau)(1-\alpha^2) + \frac{1}{2}\alpha_\tau^2(\alpha^2+\alpha\alpha_\tau)(1-\beta^2), & \tau = 2,4,6,8\ , \\ F_\tau = (1-\alpha^2)(1-\beta^2), & \tau = 9\ , \end{array} \tag{3.8}$$

where α and β vary between -1 and $+1$. In the case of L9 polynomials, the displacement field reads:

$$\begin{aligned} u_x &= F_1 u_{x1} + F_2 u_{x2} + \ldots + F_9 u_{x9}, \\ u_y &= F_1 u_{y1} + F_2 u_{y2} + \ldots + F_9 u_{y9}, \\ u_z &= F_1 u_{z1} + F_2 u_{z2} + \ldots + F_9 u_{z9}. \end{aligned} \tag{3.9}$$

Refined beam models can be obtained by adopting higher-order Lagrange polynomials

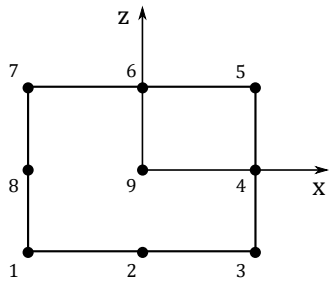

Figure 3.2: L9 expansion on the beam cross-section.

or by using a combination of Lagrange polynomials on multi-domain cross-sections, e.g. in Fig. 3.3 three assembled L9 polynomial expansion sub-domains are represented. More details about Lagrange-class models can be found in [126, 131]

3.2.1 Implementation by using the finite element method

The FE method is used to discretise the structure along the y-axis. The discretisation process is conducted via a classical 1D FE model, where the generalized displacement

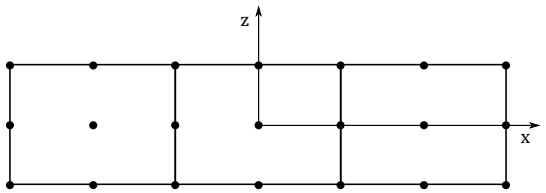

Figure 3.3: Three assembled L9 expansions.

vector $\mathbf{u}_\tau(y)$ can be approximated by the nodal shape functions $N_i(y)$.

$$\mathbf{u}(x,y,z) = N_i(y)F_\tau(x,z)\mathbf{u}_{i\tau}, \qquad \tau = 1,...,M, \qquad i = 1,...,n_n, \tag{3.10}$$

where $N_i(y)$ stands for the $i-th$ shape function, n_n is the number of nodes in one element and $\mathbf{u}_{i\tau}$ is the vector of nodal unknowns. For the sake of brevity, the shape functions are not reported here. They can be found in classical books like [101]. 1D elements with four nodes (B4) are considered here: in this way a cubic approximation of the displacement fields along the y-axis is assumed. The correspondent virtual variation of the displacement reads:

$$\delta\mathbf{u}(x,y,z) = N_j(y)F_s(x,z)\delta\mathbf{u}_{js}, \qquad s = 1,...,M, \qquad j = 1,...,n_n. \tag{3.11}$$

The governing equations are derived by applying the Principle of Virtual Displacements (PVD). For a static problem:

$$\delta L_{int} = \delta L_{ext}, \tag{3.12}$$

where δL_{int} stands for the virtual variation internal work, δL_{ext} is the virtual variation of work done by the external loads. The virtual variation of the internal work can be expressed as:

$$\delta L_{int} = \int_V \delta\epsilon^T \sigma dV. \tag{3.13}$$

By using Eqs. (3.3), (3.5) and (3.10) the previous expression simplifies to:

$$\delta L_{int} = \delta\mathbf{u}_{js}^T \mathbf{K}^{ij\tau s}\mathbf{u}_{i\tau}, \tag{3.14}$$

where $V = \Omega \cdot L$ is the volume of the beam and $\mathbf{K}^{ij\tau s}$ is the stiffness matrix in the form of a 3×3 fundamental nucleus (FN). The derivation FN is not reported here, but the interested reader can find more details in [126]. However, the terms $K_{xx}^{ij\tau s}$ and $K_{xy}^{ij\tau s}$ are given for clarity purpose.

$$\begin{aligned} K_{xx}^{ij\tau s} = \; & (\lambda + 2G)\int_L N_i N_j\, dy \int_\Omega F_{\tau,x}F_{s,x}\, d\Omega + G\int_L N_i N_j\, dy \int_\Omega F_{\tau,z}F_{s,z}\, d\Omega + \\ & + G\int_L N_{i,y}N_{j,y}\, dy \int_\Omega F_\tau F_s\, d\Omega, \\ K_{xy}^{ij\tau s} = \; & \lambda\int_L N_{i,y}N_{j,y}\, dy \int_\Omega F_\tau F_{s,x}\, d\Omega + G\int_L N_i N_j\, dy \int_\Omega F_{\tau,x}F_s\, d\Omega, \end{aligned} \tag{3.15}$$

where G and λ are the Lamé's parameters and comma denotes partial derivatives. It can be proven that all the components of $\mathbf{K}^{ij\tau s}$ can be derived from Eq.(3.15) by permutations. Furthermore, it should be noted that the formal expressions of the components of the fundamental nucleus $\mathbf{K}^{ij\tau s}$ of the stiffness matrix do not depend on the choice of the cross-sectional functions F_τ, which determine the theory of structure, and shape functions N_i, which determine the numerical accuracy of the FE model approximation. This means that any classical or higher-order beam element can be automatically formulated by opportunely expanding the fundamental nuclei according to the indices τ, s, i, and j.
The formal expression of the load vector coherent to the considered model and theory can be found in [131].

Application of 1D CUF elements to multi-layer structures

In the case of composite laminated structures, the CUF provides a method to model laminates, matrices, and fibers using 1D elements on the longitudinal direction and its expansion classes on the cross-section of the beam. This concept is clearly depicted in Fig. 3.4, where a three-layer laminated beam is modelled in the framework of CUF.

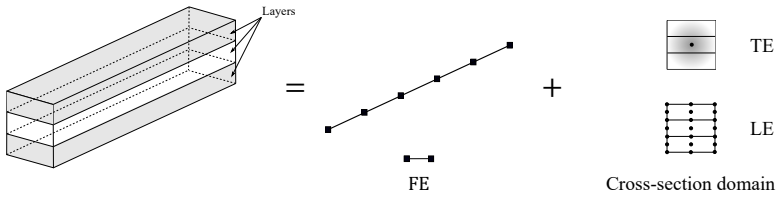

Figure 3.4: Differences between TE and LE classes in 1D CUF finite elements.

The Equivalent Single-Layer (ESL) approach and the Layer-Wise (LW) approach can be easily used to study 1D multi-layer structures in the framework of CUF.

- In the ESL approach, the multi-layer configuration is modelled as a single-layer having a set of variables assumed for the entire cross-section. This is obtained by homogenising the properties of the different layers composing the laminate into a single layer. In this way, during the assembly phase of the stiffness matrix, the contributions of the individual layers are added together. This homogenisation process of the layers however, causes an incorrect evaluation of some intrinsic quantities of each layer and their interfaces. The ESL can be formulated through the use of any 1D model (e.g TE and LE) in the CUF framework.

- In the LW approach, all layers are individually modelled and the continuity of the displacement solutions on the interfaces between layers is ensured by the correspondence of the shared sides of the cross-section expansion domains. In this regard, Fig. 3.5 shows the assembly procedure of the stiffness matrix in both approaches. For this approach, the LE class is more suitable than the TE because of its multi-domain nature. In the LE class, in fact, each layer can be modelled considering one or more local expansions. The addition of multiple local expansions per layer improves model accuracy and may be necessary for the study of higher-order effects. LW can be also obtained by means of TE, but special attention must be given to the interface conditions in this case, see [123, 132].

Both the approaches are widely discussed in [133] and their applications in the framework of CUF are given in [126, 134]. In this thesis, the LE class is used for higher-order local 1D models. The possibility to implement LW theories, which are fundamental for the description of 3D stress in laminate structures and the possibility to easily transfer the geometrical BCs from the GFEM to the LFEM were crucial in the choice of this class. This last aspect is described in the following section.

3.3 Global-local modelling in the CUF framework

Global-local modelling strategy can be really determinant in the preliminary design phase of a structure, as it allows to properly assess complex and localized 3D stress field. This evaluation, carried out with limited computational costs, allows the designer to intervene by making the necessary modifications to the structural model.

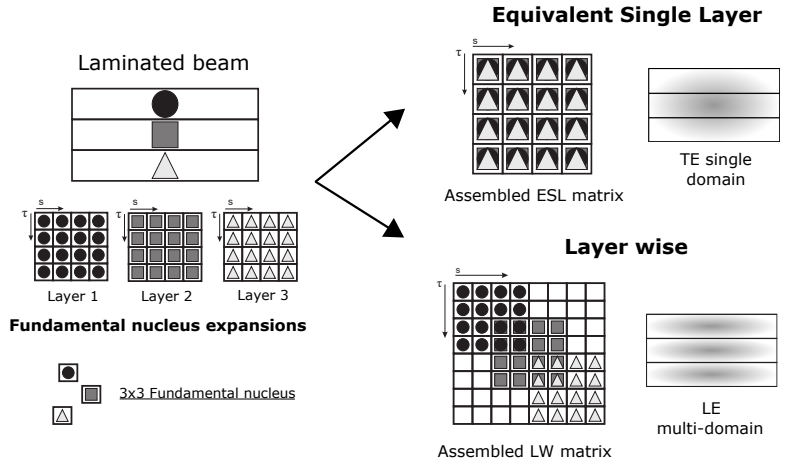

Figure 3.5: Assembly procedure of the stiffness matrix through ESL and LW approaches, [134]

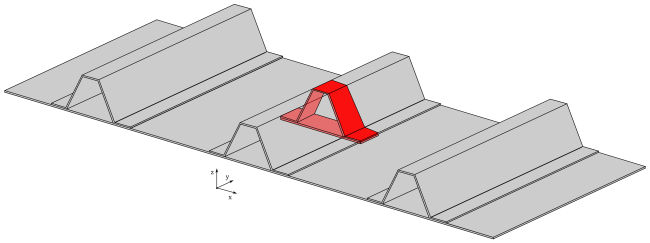

(a) Stiffened plate with an highlighted ZOI.

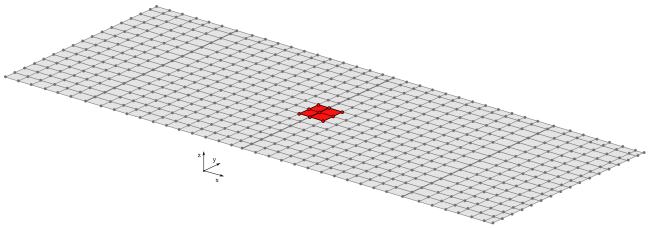

(b) Global 2D/1D FE model of the stiffened plate with the highlighted ZOI elements.

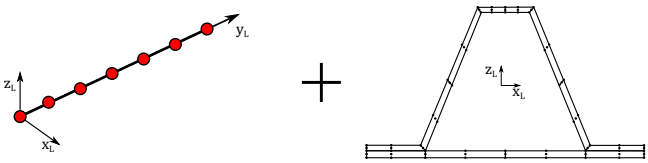

(c) Local refined 1D CUF model of the ZOI

Figure 3.6: Stiffened plate with highlighted ZOI and global and local FE models.

In this study, the GFEM is always made of classical 1D and 2D elements (or a combination of them) available in with commercial software. In general, such models are *low-fidelity* models, because they required a low computational cost but are not able to describe complex stress states (for example out-plane stresses). This is due to the basic assumptions related to the kinematic field of the element. The global-local approach pre-

sented in this Chapter is based on the idea of identifying critical regions of the GFEM, i.e. the ZOIs, isolating them and build a *high-fidelity* LFEM made of higher-order CUF 1D elements capable of describing complex stress states within the ZOI with great accuracy and low computational cost.
The proposed global-local modelling strategy is essentially based on two steps. The first step is devoted to the analysis of the GFEM to identify the critical ZOIs. The identification of such ZOIs is carried out by means of a criterion established by the user and is crucial for the appropriate extraction of BCs that will then be applied to the local CUF model. At this stage, two important issues arise:

1. What kind of BCs should be transferred from the GFEM to the LFEM? Two types of BCs will be discussed in the following sections: Mechanical-BCs and Geometrical-BCs.

2. How to couple the GFEM realized with commercial software with the LFEM realized in the CUF framework? This issue is related to the kinematics of higher-order 1D elements, which is different and not compatible with the low-fidelity elements of GFEM.

The above points will be discussed with in the following sections.
The second step of the global-local modelling strategy is dedicated to the setting of the LFEM in CUF framework and the corresponding static analysis for the evaluation of the 3D stress field in the ZOI.

For instance, Fig. 3.6 shows a stiffened plate with the highlighted ZOI, the GFEM of the structure and the LFEM of the ZOI.

3.3.1 Application of the BCs - Mechanical vs Geometrical BCs

The coupling between GFEM and LFEM can be made by applying two types of BCs, i.e. *Mechanical BCs* and *Geometrical BCs*.

- *Mechanical BCs*
  The application of forces and moments at the interface makes the FE static problem indeterminate. The structure is unconstrained, and consequently, its stiffness matrix is singular. These kinds of problems are frequent in the aerospace field and they are solved by making use of a procedure known in the literature as *Inertia relief*, [135–138]. This procedure, implemented by commercial software as *MSc-Nastran* and *Abaqus CAE*, allows to simulate unconstrained structures in static and dynamic analysis. In fact, taking into account the rigid-body motions of the structure, it removes the singularity of the stiffness matrix so the final algebraic system could be solved. For a deeper insight into the matter, the interested reader is addressed to [136, 137].

- *Geometrical BCs*
  The application of displacements and rotations at interface does not require further procedures because the system is constrained, resulting in a determinate problem that can be solved. This is the reason for the prevalence of *Geometrical BCs* in the majority of global-local approaches found in the literature, see [108, 114, 117].

There are no particular differences between the BC types from the point of view of the accuracy of the results, but from a purely numerical perspective, it is much easier to automate the application of *Geometrical - BCs* on the LFEM boundary than the mechanical ones. In fact, the application of the *Inertia relief* requires a further mathematical model that is not necessary for applying geometrical BCs. For the aforementioned reasons, *Geometrical - BCs* are used as BCs for the LFEM implemented within the CUF framework.
Figure 3.7 shows a 2D model of a hat-stringer to be analysed with the global-local modelling approach. The static analysis of the entire structure is done by a commercial software, and the displacements and rotations at the interface nodes are known. For the sake of simplicity, consider two structural nodes A and B, located at the interface between the GFEM and the critical region, as shown in Fig. 3.7(a). Exploiting the displacements and rotations of nodes A and B and using linear shape functions, it is possible to determine, for all the middle plane nodes of the CUF LFEM located between nodes A and B, the value of both displacements and rotations, as illustrated in Fig. 3.7(b). A linear interpolation function is used to keep conformity with the kinematics of the GFEM. Furthermore, such interpolation procedures allow the use of the GFEM and LFEM meshes, which are incompatible at the interface.
Once the displacements and rotations are computed at the interface nodes located on the middle plane of the LFEM, a strategy is needed to compute the BCs in all the nodes at the interface level. As known, the commercial software gives translational displacements (u_x, u_y, u_z) and rotations (θ_x, θ_y, θ_z) at the interface nodes in the case of beam and plate models. On the other hand, the use of Lagrange polynomials in CUF results solely in pure displacement degrees of freedom (DOFs) at each node. Therefore, a strategy must be provided to transform rotational DOFs of the GFEM in pure displacements for CUF LFEM.
This issue can be resolved via two approaches based on the type of elements of the GFEM. Reissner - Mindlin displacement field is used when the GFEM is made of 2D shell elements, in order to compute the translational displacements for each node at the interface of the LFEM. The Reissner - Mindlin displacement field reads:

$$\begin{aligned} u(x,y,z) &= u_0(x,y) + z\theta_y(x,y), \\ v(x,y,z) &= v_0(x,y) - z\theta_x(x,y), \\ w(x,y,z) &= w_0(x,y). \end{aligned} \tag{3.16}$$

When the GFEM is made of 1D beam elements, Timoshenko displacement field is used, i.e.

$$\begin{aligned} u(x,y,z) &= u_0(y), \\ v(x,y,z) &= v_0(y) + x\theta_z(y) - z\theta_x(y), \\ w(x,y,z) &= w_0(y). \end{aligned} \tag{3.17}$$

Where u_0, v_0, w_0 are the displacements and θ_x, θ_y, θ_z are the rotations of the nodes of the GFEM located at the interface. In both cases, the rotations are used to compute displacements in all the cross-section nodes at the interface level and the resulting displacements constitute the BCs for the LFEM.

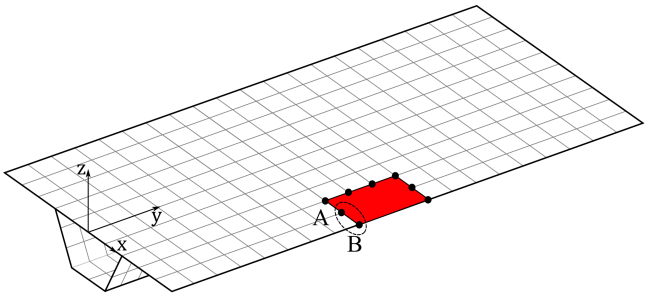

(a) Global and local regions

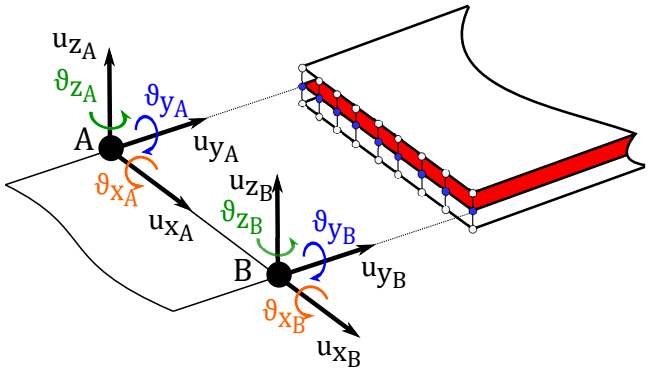

(b) Global to local

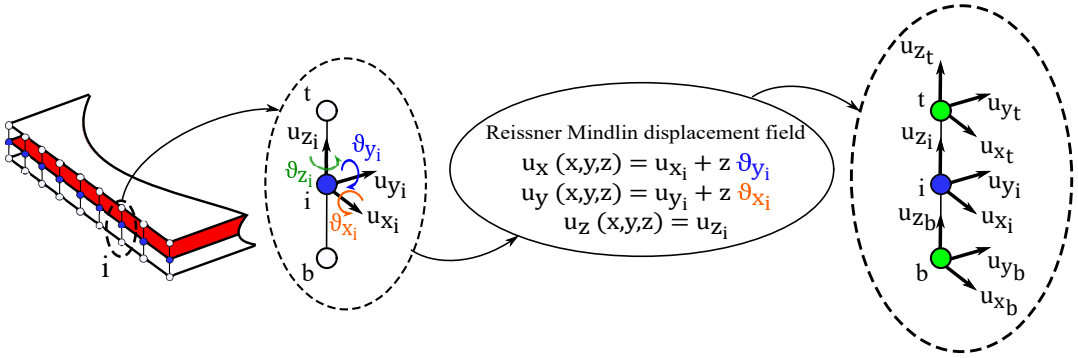

(c) Kinematics from global to local

Figure 3.7: Application of geometrical BCs.

For instance, in Fig. 3.7(c), the displacements and rotations computed at the node 'i' give the translational displacement at the nodes 't' and 'b' through the use of the Reissner - Midlin displacement field. In this way, it is possible to obtain from the displacements and rotations in the middle plane the translational displacements in all the nodes belonging to the interface.

It should be noted that the application of displacements as BCs only concerns the nodes at the interface between the GFEM and the ZOI. All other mechanical (nodal forces, distributed BCs imposed in the GFEM within the zone of interest must be transferred to the LFEM to obtain a correct evaluation of the stress state.

3.3.2 Coupling effects

As shown in the work of Mao *et al.* [108], the application of the BCs in terms of imposed displacements and rotations on the boundary of the LFEM introduces detrimental effects in the accuracy of the solution of the local static problem.
There are several strategies available to reduce these effects. In this work the following techniques are used:

- Once the critical local region is identified, a transition zone surrounding the actual ZOI is considered, as shown in Fig. 3.8. The displacements and rotations are applied on the nodes located at the edge of this zone following the strategy described in the previous section.

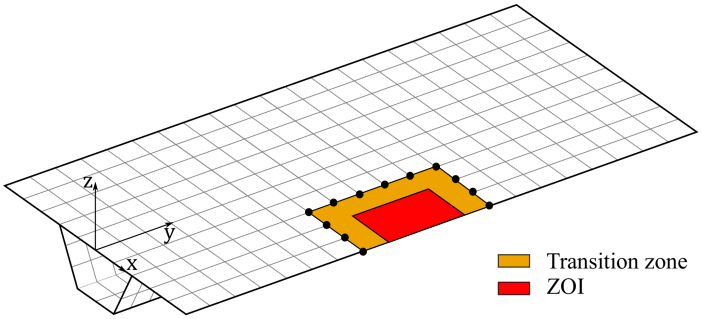

Figure 3.8: ZOI with the transition zone.

- A local refinement of the mesh is adopted to confine the detrimental effects of the BCs application into the interface zone. This strategy consists of a non-uniform mesh in which the structural nodes and the sub-domain expansion points along x-axis are distributed with the square root of the well-know *Chebyshev* node formula. For instance, the sub-domain expansion points along x-axis are computed as:

$$x_k = \sqrt{\cos(\frac{2k-1}{2n}\pi)}, \qquad k = 1, ..., n_x. \tag{3.18}$$

  Where n_x is a positive integer computed from the number of sub-domains $N_{x_{exp}}$ used for the cross-section of the LFEM along the x-axis, $n_x = 2 \cdot N_{x_{exp}} - (N_{x_{exp}} - 1)$. Using the above formula, the mesh of the LFEM is refined in the proximity of the BCs. In this way, it is possible to limit the detrimental effects of the BCs only in this refined zone. Instead, the sub-domain expansion points along z-axis are equally spaced. Figure 3.9(a) shows an example of the cross-section for a LFEM wherein the nodes distribution is done according to the Eq. (3.18), while in Fig. 3.9(b) the corresponding LFEM in the CUF framework is presented. In both images, it is possible to remark the refinement in the proximity of the boundaries of the model to confine the detrimental effects of the BCs application.

3.4 Numerical Examples

This section consists of two parts. The first part is dedicated to the validation of the global-local modelling strategy in the CUF framework. Several examples of metal and

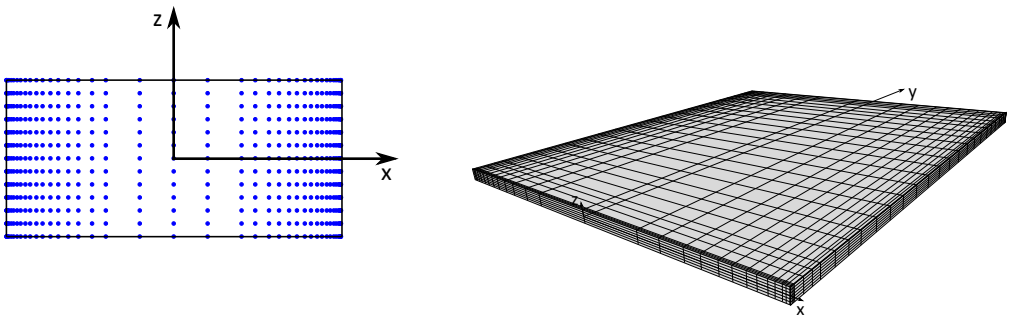

(a) Local cross-section refinement (b) Local plate region in *CUF* framework

Figure 3.9: Mesh refinements to decrease the detrimental effect of application of BCs

composite structures have been analysed to show the effectiveness of the proposed method. Instead, the second part is dedicated to the study of the complex phenomenon of free-edge in composite structures. The global-local modelling approach is initially tested on benchmarks taken from the literature and then used in the study of two special cases.

3.4.1 Preliminary numerical examples

Cantilever beam with a point load at the free edge

The first test case deals with a very simple model of a cantilever beam subjected to a concentrated force applied at $y = L$. The goal is to show the effectiveness of the proposed global-local modelling strategy in describing the 3D stress field with a reduced computational cost compared to FE models made of solid elements available in commercial codes. The structure is made of isotropic material with Young's modulus $E = 75$ GPa, Poisson ratio, $\nu = 0.33$ and density, $\rho = 2700$ kg/m^3, has a length L equal to 90.0 mm and has a rectangular cross-section with the following characteristic dimensions: $b = 1.0$ mm and $h = 10.0$ mm. The geometrical features of the structure is illustrated in Fig. 3.10.

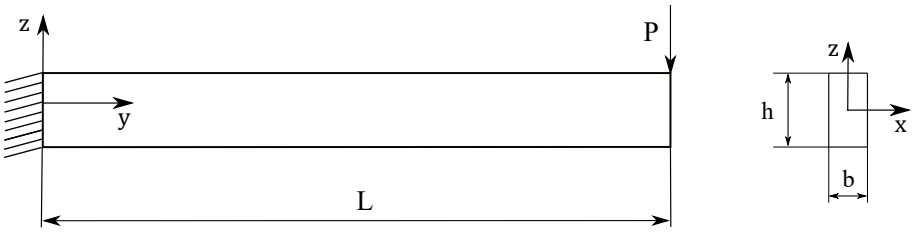

Figure 3.10: Geometrical features of the cantilever beam

A point load P along z-axis is applied at [0, L, 0] and its magnitude is equal to -1 N.

The ZOI is located between points A = [0, 30, 0] mm and B = [0, 60, 0] mm in the GFEM reference system and a finite element analysis is carried out for the calculation of displacements and rotations at such points on the borders of the local region. The static analysis is performed on a GFEM realized with the commercial software *MSc Nastran* and is constituted of 30 beam elements.

Fig. 3.11 shows GFEM, the ZOI where displacements (u_A, u_B) and rotations (θ_A, θ_B) resulting from the static analysis conducted on the GFEM are applied on its bound-

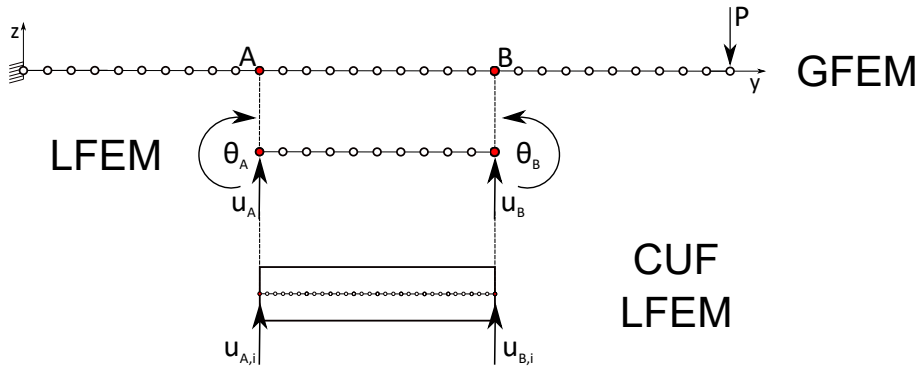

Figure 3.11: GFEM and LFEM for the cantilever beam

ary. Conversely the displacements u_{A_i} and u_{B_i} are the generic translational cross-section displacements at node 'i' of the LFEM in the CUF framework. These latter ones are calculated using Timoshenko's displacement field exploiting the vertical displacements (u_A, u_B) and rotations (θ_A, θ_B) resulting from the static analysis on the GFEM.

(a) 3 x 3 L9 (b) 1 x 5 L16

Figure 3.12: Sub-domain distributions over the cross-section of the local CUF beam model

Two different CUF LFEMs have been used: 3x3 L9 and 1x5 L16, where 3x3 L9 means that three sub-domains L9 are used along the x-axis and three along the z-axis, whilst in the second LFEM one L16 sub-domain along x and five sub-domains L16 along z. For both LFEMs, 10 B4 elements are used for the structural mesh along y-axis. The distribution of sub-domains in the cross-section of the two models is illustrated in Fig. 3.12.
Fig. 3.13 shows the distribution of the shear σ_{yz} along the y-axis at $x = 0, z = h/2$ comparing: a Timoshenko beam model, a 3D *MSc-Nastran* model and the two LFEMs described above.
Table 3.2 and Fig. 3.14 show the comparison between the 3D model and the proposed

	σ_{yy} $[MPa]$	σ_{yz} $[MPa]$	DOFs
ABAQUS 3D	2.571	−0.148	14209
NASTRAN 1D / CUF - 3x3 L9	2.721	−0.149	546 / 4557
NASTRAN 1D / CUF - 1x5 L16	2.717	−0.153	546 / 5952

Table 3.2: σ_{yy} and σ_{yz} for the cantilever beam with a point load

modelling strategy in terms of axial stress σ_{yy} and shear stress σ_{yz}.
The distributions of Fig. 3.14 are computed at $x = 0$, $y_{global} = 45.0$ $[mm]$ and the stress

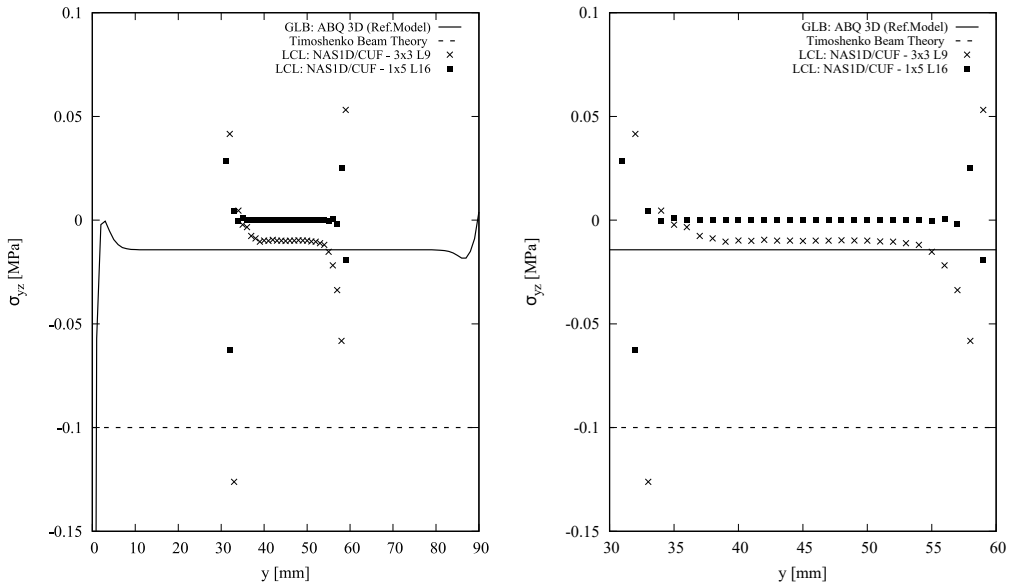

(a) σ_{yz} along the y axis in the global reference (b) σ_{yz} along the y axis in the local reference

Figure 3.13: Shear σ_{yz} distribution along the y axis at the top of cross-section.

values, which are reported in Table 3.2, are at the z coordinate that gives the maximum value of these stress.
The analysis of these preliminary results allows inferring the following remarks:

- The global-local modelling strategy allows correctly describing 3D stress field with low computational effort. In fact, it is known from theory of elasticity that the shear stress σ_{yz} has to be null at the top and the bottom of the cross-section for the equilibrium but this result cannot be obtained with a 1D model and not even with a full 3D model in which the σ_{yz} is computed but it is not zero. With CUF higher-order beam model, it is possible to obtain nearest null shear σ_{yz} stress at the top and the bottom of the cross-section.

- The global-local modelling approach, after an initial oscillation that is due to the BCs application, can detect a nearest null shear stress σ_{yz}. It is important to isolate a suitable region for local analysis, since the application of BCs can affect the accuracy of results. It is recommended to consider a larger area for the local analysis by including a transition zone around the ZOI in order to avoid the detrimental effects of BCs application.

- Table 3.2 compares the axial and shear stresses obtained via the 3D FE model composed of solid elements and global-local analyses based on CUF beam elements. All the results provided by the global-local analysis are in very good agreement with those resulting from the Abaqus 3D model, which constitutes a numerical reference solution. The significant achievement is the reduction of the computational cost and the possibility to detect the shear stress correctly with a higher-order beam model.

- Figure 3.14 shows the stress distribution through the thickness at $y_{global} = 45.0\ mm$. There are no remarkable differences for the axial stress σ_{yy}, however in the case of shear stress σ_{yz}, it can be noticed that only the LFEM with 1x5 L16 subdomains can

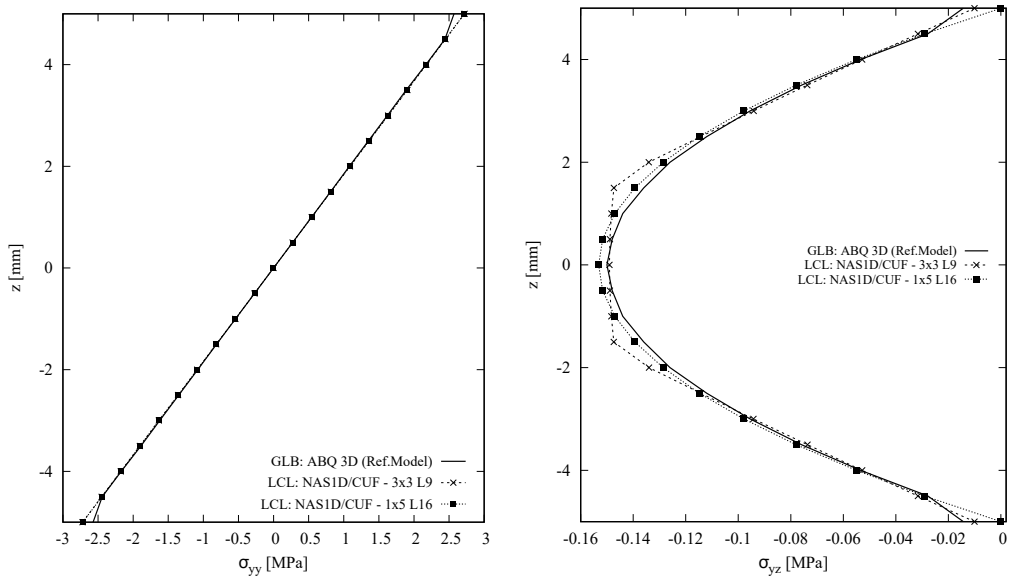

(a) Axial stress σ_{yy} (b) Shear stress σ_{yz}

Figure 3.14: Axial σ_{yy} and shear σ_{yz} distribution along the z axis at $x_{global} = 0$ $[mm]$, $y_{global} = 45.0$ $[mm]$ for the cantilever beam.

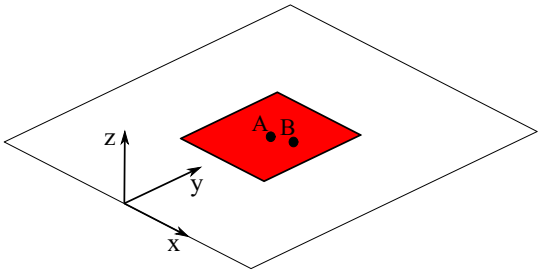

Figure 3.15: Global and local regions of the isotropic plate under bending.

detect a close to zero stress at the top and bottom of the cross-section, as predicted by the theory.

Isotropic plate under bending

An isotropic square plate is considered in this example. The plate is characterised by a width $b = 1.0$ [m] and a thickness $t = 0.01$ [m]. An isotropic material is used for the structure with $E = 75$ GPa, Poisson's ratio, $\nu = 0.33$ and density, $\rho = 2700$ kg/m^3. The plate is clamped on each side and a pressure $P = 1$ Pa is applied at the top surface of the plate.
Fig. 3.15 shows the GFEM and the LFEM of the plate and highlights points A and B wherein the in-plane and out-plane stresses are evaluated, respectively. The global analysis is performed in *MSC-Nastran* and consists of 60 x 60 plate elements (DOFs = 22326). The boundaries of the ZOI are: $-0.167 \leq x \leq 0.167$ m and $0.300 \leq y \leq 0.700$ m; point A is located in the middle of the plate ($x_A = 0.00$ m and $y_A = 0.500$ m) and point B is located at $x_B = 0.050$ m and $y_B = 0.550$ m.

A C3D8 ABAQUS solid model is build as a reference solution for the in-plane and out-plane stresses and it consists of 100 x 100 in-plane divisions and 10 out-of-plane divisions (DOFs = 855393). The LFEM consists of 20 B4 structural elements and 10 x 9 L9 sub-domains across the cross-section of the beam model (DOFs = 107787). In Fig. 3.16 the structural mesh of the beam axis and the distribution of the L9 over the cross-section are presented. It is noteworthy that the distributions of the structural nodes of the beam axis and the points of the L9 sub-domains of the cross-section follow the square root of *Chebyshev* node formula, see Eq.(3.18). In Fig. 3.16(b) the grey rectangles represent the L9 sub-domains but the points of each sub-domain are not reported. Similarly, in Fig. 3.16(a), the 20 B4 structural elements are shown but only the shared nodes between the elements are represented.

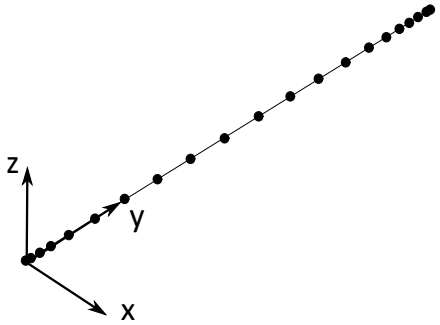

(a) Structural mesh along the beam axis - 20 B4

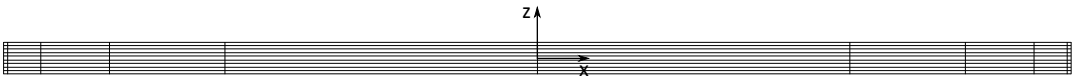

(b) Sub-domain distribution over the cross-section

Figure 3.16: Structural mesh along the beam axis and sub-domain distribution over the cross-section of the local 1D *CUF* model.

This benchmark is used to show that the global-local analysis in the CUF framework can detect the in-plane stresses in accordance with the global 2D model in *MSC-Nastran* and it can also describe of the out-plane stress that cannot be obtained from the GFEM.

Fig. 3.17 shows the displacement field magnitude in the GFEM and in the CUF LFEM, while the axial stress σ_{yy} distribution through the thickness at the point A of the plate is presented in Fig. 3.18.
The shear stresses σ_{xy} and σ_{yz} are computed at the point B and they are shown in Fig. 3.19.
From the obtained results, the following considerations arise:

- The benchmark represents a typical plate problem, where the characteristic length of the plate b is much larger than the thickness t. This structure can be easily studied with the FE method using plate elements and, in the case of stress analysis, the in-plane stresses can be detected with a reasonable level of accuracy. Due to underlying kinematic assumptions, plate elements based on the classical theories such as Kirchoff or Reissner-Mindlin are unable to detect out-of-plane stresses. A 3D GFEM is set but, for this particular case, the computational cost can be very

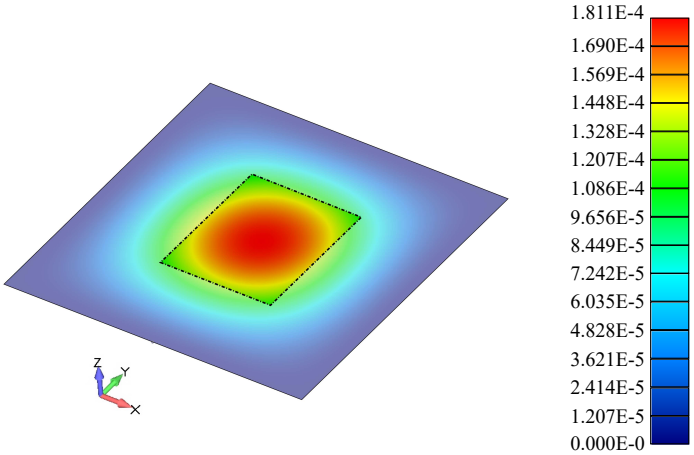

(a) Displacement magnitude in the GFEM

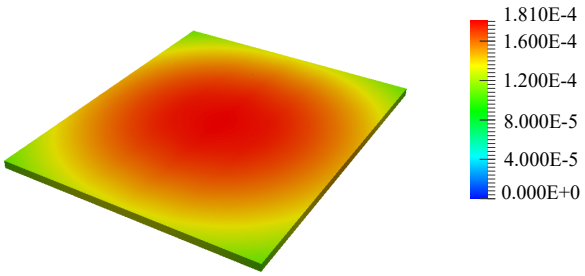

(b) Displacement magnitude in the CUF LFEM

Figure 3.17: Comparison between the GFEM and the CUF LFEM in terms of displacement magnitude in mm.

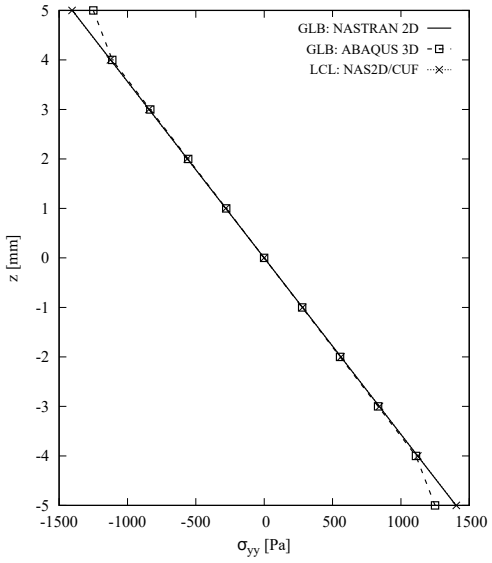

Figure 3.18: Axial stress σ_{yy} along the z-axis at the central point of the Plate, A.

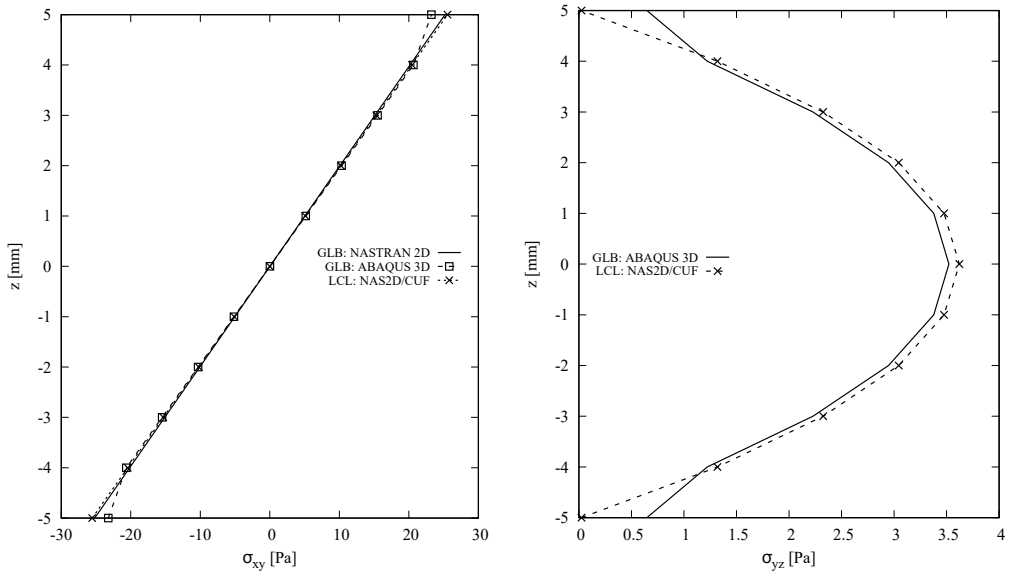

(a) Shear stress σ_{xy} (b) Shear stress σ_{yz}

Figure 3.19: Shear stresses σ_{xy} and σ_{yz} along the z-axis for the local region of the isotropic plate. The stresses are computed at point B.

high so for this problem, a global-local approach can be useful to detect the 3D stress field in the most critical subregions of the structure.

- The global-local analysis detects correctly the results given by the global static analysis of the 2D model with the commercial software and provides the distribution of the out-plane stresses too. Figure 3.19(b) shows that the accuracy level of the CUF LFEM is higher than the solid GFEM in the detection of the shear stress σ_{yz}; in fact, it correctly predicts the null value of σ_{yz} at the top and bottom of the cross-section.

- The computational costs required by the proposed global-local modelling approach are strongly reduced when compared to the FE model made of solid elements: the overall number of DOFs required by the global-local analysis is one seventh of those required by the 3D FE model built in the Abaqus environment.

Notched plate under uni-axial tension

This example is an application of the current global-local modelling approach in the refined analysis of specific regions within a structure, where stress concentration is expected to occur. The structure is a plate of length $L = 150$ mm and width $W = 36$ mm with a central through hole of radius $R = 3$ mm, clamped at one end and subjected to a uniform displacement of $u_x = 0.025$ mm at the other end. A schematic representation of the structure, along with the applied BCs is given in Fig. 3.20.
In this example, a 3D ABAQUS coarse model is used as GFEM, whose displacements are then used to drive the CUF LFEM. The region around the hole, where the maximum stresses are expected to occur, is considered as a ZOI and is shown in Fig. 3.21.
A refined 3D analysis of the entire global structure has also been performed in ABAQUS, which constitutes the numerical reference solution. The mesh details of the various numerical models are listed in Table 3.3. The results of the various analyses are presented

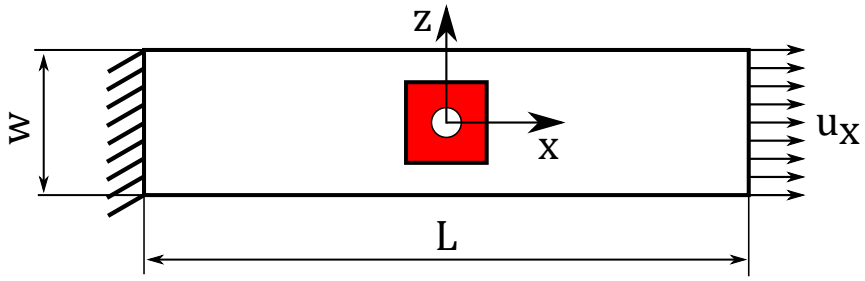

Figure 3.20: Schematic representation of the notched specimen along with the applied boundary conditions.

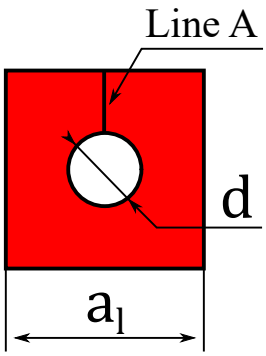

Figure 3.21: The ZOI considered for a refined analysis in CUF.

hereinafter. The axial stress σ_{xx} along the line joining the points [x = 0.0, y = 1.25, z = 3.0] and [x = 0.0, y = 1.25, z = 10.0], i.e. the line A as shown in Fig. 3.21, has been plotted in Fig. 3.22.

Models	Mesh Type	DOFs
GLB: ABAQUS 3D (Ref.)	42120 C3D8	155898
LCL:ABQ3D/CUF	510 C3D8/1 B4 - 112 L9	2709/5760

Table 3.3: Mesh data for the numerical models used in the analysis of the notched specimen

The following observations can be made:

1. A refined solution of the ZOI can be found via the global-local analysis, which requires about 18 times fewer DOFs with respect to a full 3D finite element analysis.

2. From Fig. 3.22, it can be seen that accurate stresses can be obtained from the local CUF analysis without the need for extensive mesh refinement. This is due to the use of advanced structural theories within the CUF model.

3. Fig. 3.23 shows the axial stress σ_{xx} in the plane x-z comparing the results from the global ABAQUS 3D models and those from the global-local analysis and confirms

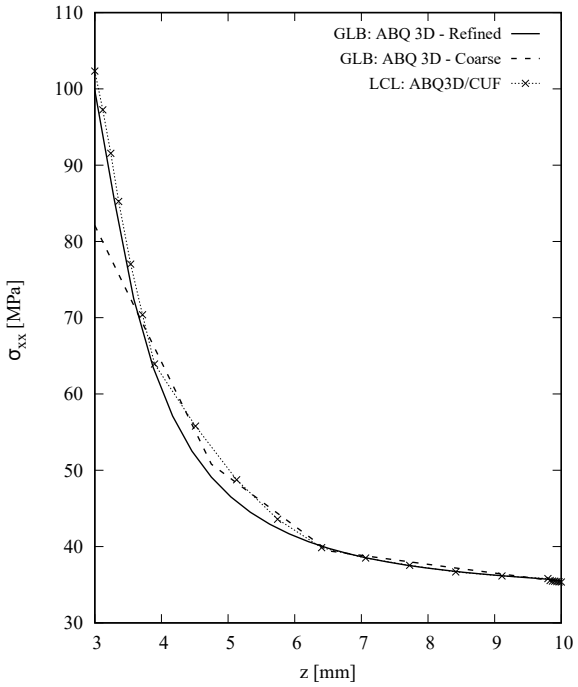

Figure 3.22: Axial stress σ_{xx} along the z axis.

that this last can detect complex stress fields with a comparable accuracy to the refined 3D models. The plot of Fig. 3.23(b) is realised through an interface ABAQUS - CUF that permits to show the results of CUF local analysis using ABAQUS visualization tools.

Cantilever composite beam under bending

In this example, a composite beam with 3 plies is considered. The considered beam is clamped at one end and free at the other end, as described in [139].
The cross-section of the structure is presented in Fig. 3.24 and the structure is loaded by a point load along the z-direction at the centre of the free end and its magnitude is $-1 \cdot 10^{-3}\ N$.

The geometrical parameters of the structure are the length $L = 2.0\ m$ and the cross-section width $b = 0.1\ m$. The total thickness of the cross-section is $t = 0.003\ m$, the ply thickness is $t_{ply} = 0.001\ m$ and stacking sequence of the laminate is $[0°/90°/0°]$. An orthotropic material is considered with the following material properties: $E_{11} = 40\ GPa$, $E_{22} = E_{33} = 4.0\ GPa$, $\nu_{12} = \nu_{13} = \nu_{23} = 0.25$, $G_{12} = G_{13} = G_{23} = 1.0\ GPa$. The GFEM is built in *MSC-Nastran* with a mesh of 10 x 200 plate elements.
The ZOI is a square region and constitutes a very small region within the global structure. It is located at the centre of the model and its geometrical parameters are $L_{local} = 10.0\ mm$, $b_{local} = 10.0\ mm$ $h_{local} = t = 3.0\ mm$. The GFEM with the highlighted ZOI is illustrated in Fig. 3.25.
In the CUF LFEM 20 B4 structural beam elements are used along the y-axis direction and two different types of LE sub-domain distributions are adopted. The first one consists

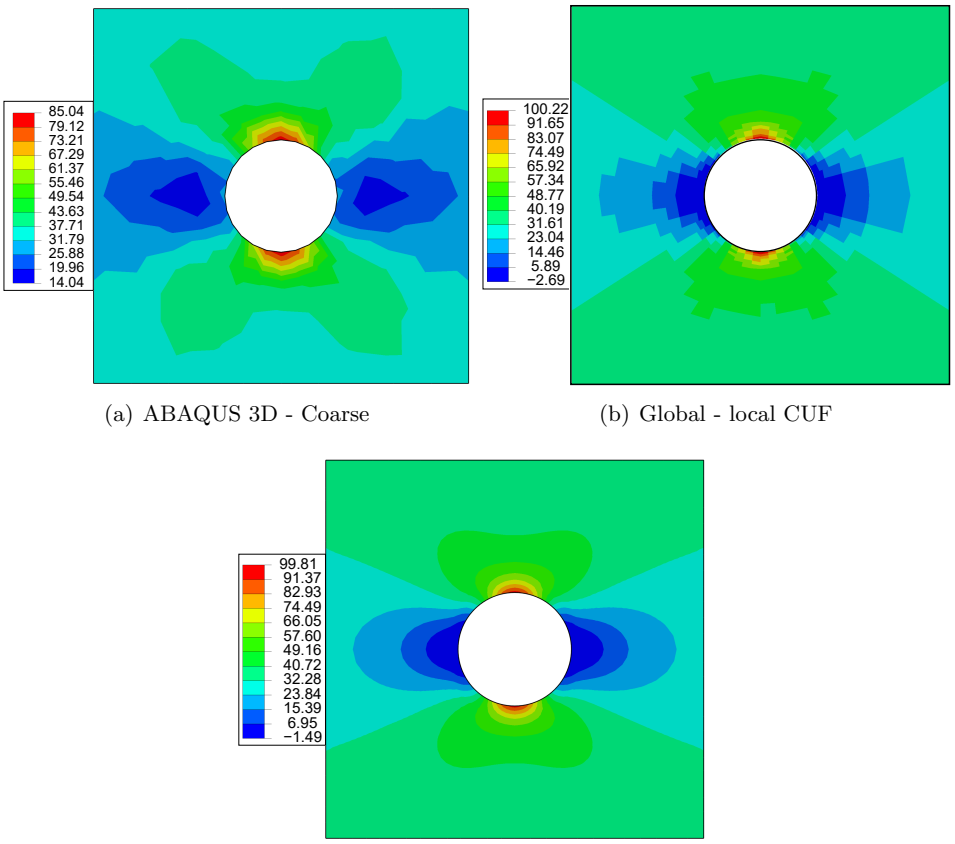

(a) ABAQUS 3D - Coarse

(b) Global - local CUF

(c) ABAQUS 3D - Refined

Figure 3.23: Axial stress σ_{xx} $[MPa]$ in the plane x-z of the notched plate.

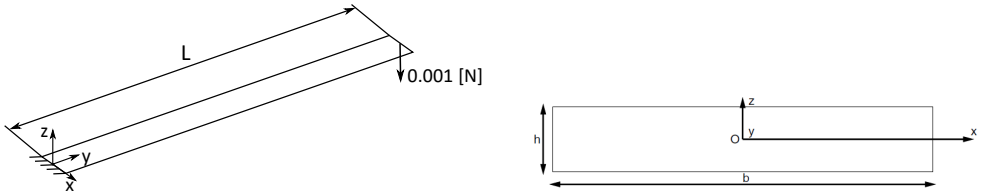

(a) Plate model

(b) Rectangular cross-section

Figure 3.24: Beam model and the geometrical parameters of its cross section.

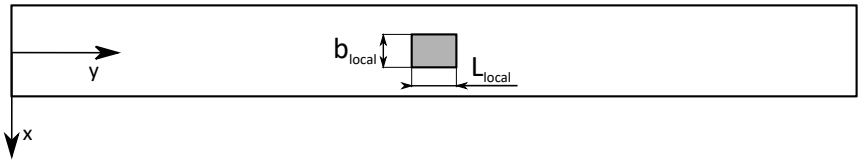

Figure 3.25: GFEM and the ZOI for the cantilever composite beam.

of 5x9 L9 sub-domains (5 along x and 9 along z) while the second one consists of 5x9 L16 sub-domains (5 along x and 9 along z) with 3 sub-domains for each layer of the structure.

The results of the static analysis are evaluated at the centre of the local region that is coincident with the global one.
In Fig. 3.26, the axial stress σ_{yy} and shear stress σ_{yz} distribution through the thickness are presented. The plot compares the results of the global analysis in *MSC-Nastran* with those of the global-local analysis.

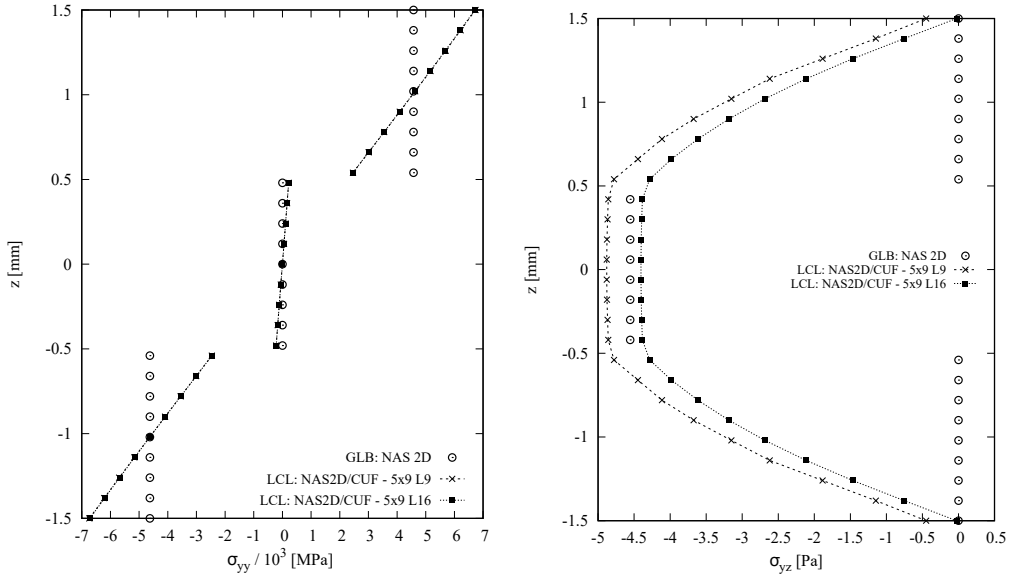

(a) Axial stress σ_{yy}

(b) Shear stress σ_{yz}

Figure 3.26: Axial stress σ_{yy} and Shear stress σ_{yz} along the z-axis for the cantilever composite beam.

The following considerations can be inferred from the graphs reported in Fig. 3.26:

- For this benchmark, the commercial code always gives constant values of in-plane and out-plane stresses in each layer of the laminate. With the global-local modelling approach, it is possible to detect the real trend of all the stresses.
- In Fig. 3.26(a), it can be noticed that both the CUF LFEMs catch the linear behaviour of the axial stress through the thickness of each layer and the results of the LFEMs coincide with those of the global one only in the middle of each layer. As known, the commercial code gives just the average stress value of each layer.
- In Fig. 3.26(b), it can be noticed that both LFEMs capture the quadratic behaviour of the shear stress. In particular, the LFEM with 5x9 L16 sub-domains is able to predict the null value of the σ_{yz} at the top and bottom of the cross-section

3.4.2 Free edge benchmarks

The numerical results presented here below are focused on the study of the free-edge phenomenon in composite structures. This phenomenon is characterised by extremely high peaks of interlaminar stress and occurs in laminates at the interface between different layers in the proximity of discontinuities of the structure. e.g. free edges, holes, etc. It has been proven that this phenomenon can be a crucial factor in the damage onset in

composite materials, see [140]. The usual methods based on FEs involve the use of ad-hoc refinements in the vicinity of the free-edge for an accurate determination of interlaminar stresses, see [141–143] for further details. The use of refined 3D FE models can provide accurate solutions but the computational cost of these models is huge due to the necessity to keep a satisfactory FE aspect-ratio along the three directions. The effectiveness of CUF higher-order beam models in the study of free-edge stress fields in multilayer composites has already been demonstrated by de Miguel et al. [144].
The global-local approach developed in this thesis succeeds in studying the stress field in the proximity of the free-edge with a CUF LFEM using the information of GFEM made of 1D or 2D classical elements.

Four-ply composite plate under tensile stress

The first benchmark on the study of free-edge is taken from [145], where several specimens in G947/M18 carbon-epoxy were tested in delamination tensile and compressive tests. In this study, the four-ply composite specimen $[10°/-10°]_s$ is selected and the purpose is to correctly describe the interlaminar shear stress σ_{yz} in the proximity of the free edge. The mechanical properties of the considered material are listen in Table 3.4.

E_{11} [GPa]	E_{22} [GPa]	E_{33} [GPa]	G_{12} [GPa]	G_{13} [GPa]	G_{23} [GPa]	ν_{12}	ν_{13}	ν_{23}
97.6	8.0	8.0	3.1	3.1	2.7	0.37	0.37	0.50

Table 3.4: Mechanical properties of the G947/M18 material, [145].

The global structure has a length L equal to 200.0 mm and has a width b equal to 20.0 mm. The thickness of the plate is $h = 0.76$ mm.
The structure is fixed on one side and subjected to a displacement δ_y along y axis on the opposite side, in such a way that the resulting longitudinal strain is $\varepsilon_{yy} = 0.001$. The geometrical features and the BCs of the structure are illustrated in Fig. 3.27.

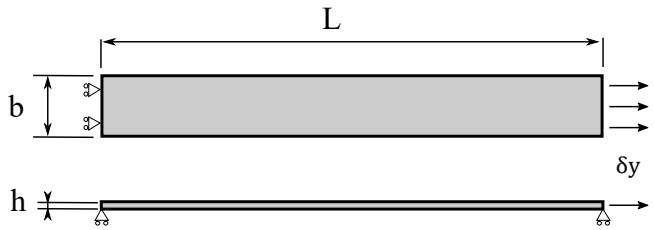

Figure 3.27: Four-ply composite plate subject to uni-axial longitudinal strain $\epsilon_{yy} = 0.001$.

The GFEM is built in *MSc-Nastran* with a mesh of 10 x 200 plate elements.
The ZOI is a rectangular region located at the centre of the model and its geometrical parameters are $L_{local} = 10.0$ mm, $b_{local} = 10.0$ mm, see Fig. 3.28.

The shear stress distribution σ_{yz} is presented in Fig. 3.29. The figure compares the distribution of the σ_{yz} along the x-coordinate at the interface between dissimilar layers (Fig. 3.29(a)) and z-coordinate (Fig. 3.29(b)) obtained through the proposed global-local modelling approach with those given by Lagunegrand *et al.* [145] and Martin *et al.* [142] whenever possible. In this case, the LFEM consists on 15 L9 sub-domains along the x-axis, 9 L9 sub-domains for each layer, and 6 B4 elements. The cross-section mesh is refined

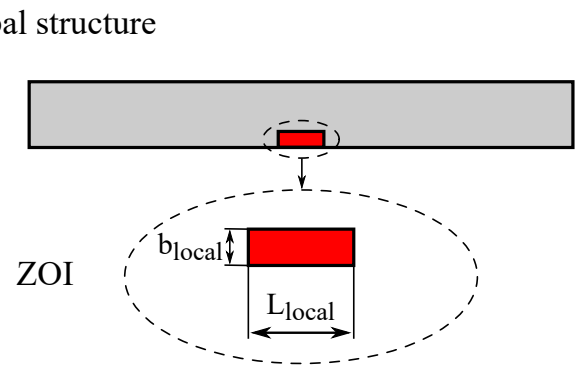

Figure 3.28: The ZOI where the shear stress σ_{yz} is evaluated.

along x using the square root of the Chebyshev node distribution (which is also used to distribute the nodes along the beam axis).

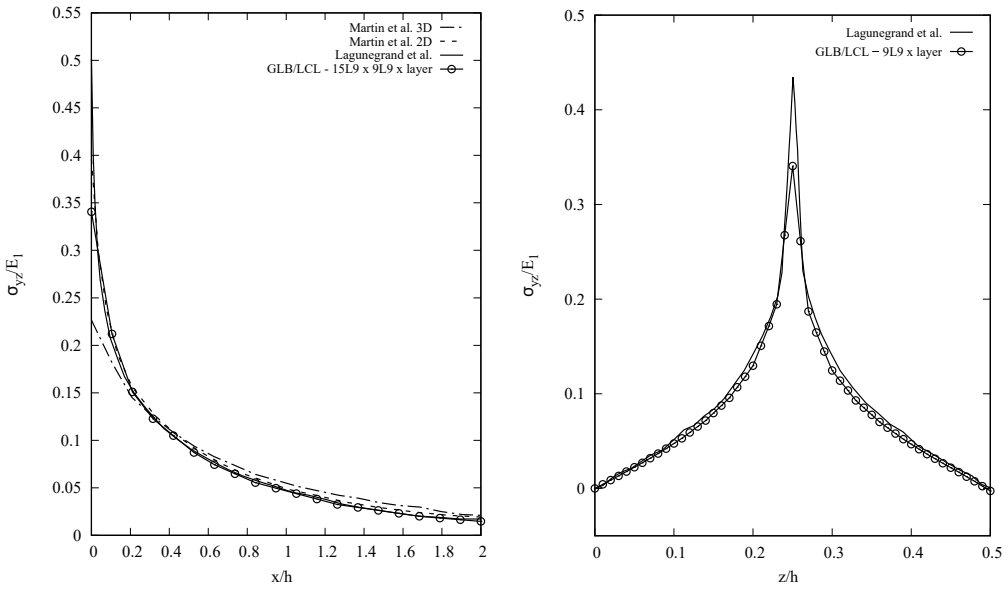

(a) Shear stress σ_{yz} at $10°/-10°$ interface versus x

(b) Shear stress σ_{yz} at the free-edge versus z

Figure 3.29: Interlaminar shear stress σ_{yz} distributions.

Fig. 3.30 shows the cross section mesh influence in the detection of the σ_{yz} in the free edge vicinity. In this case the LFEM consists of 15 L9 sub-domains along the x-axis and six B4 elements along the beam axis. Moreover, but a sub-domains convergence study along the z-axis is done in order to find the best compromise between accuracy of results and reduced computational effort.

The global-local analysis of structure has highlighted several important aspects:

- The proposed approach allows for correctly describing the shear stress σ_{yz} in the free edge vicinity. In Fig. 3.28 the distribution of σ_{yz} is in good agreement with the results available in the literature but with the advantage of not requiring any ad-hoc formulation for the model.

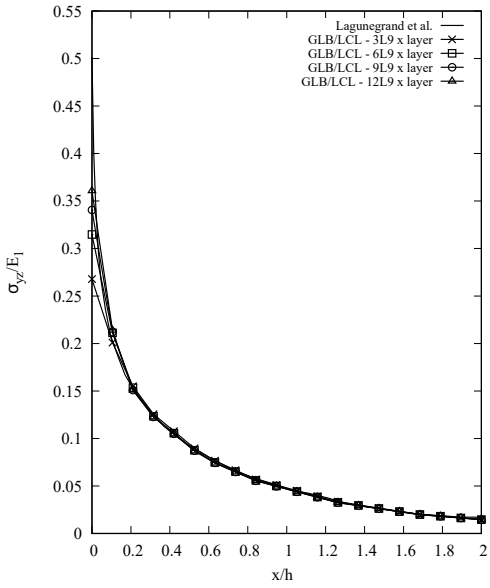

Figure 3.30: Sub-domain convergence study along the z-axis at the free-edge.

- The sensitivity of the results to the number of sub-domains along z-axis is illustrated in Fig. 3.30. As expected, a model with more sub-domains per layer is closer to the experimental results given by Lagunegrand *et al.* [145]. Of course, the greater the number of sub-domains the higher the computational costs.

Ten-ply composite plate under tensile stress

For this benchmark, the specimen taken from the work by Lorriot *et al.* [146] is considered. The specimen geometry is reported in Fig.3.31. The material used for the structure is a carbon/epoxy T800/914 ply and its mechanical properties are reported in Table 3.5. The multilayer plate is characterised by the following stack: $[15^\circ_2/90^\circ/-15^\circ_2]_s$.

E_{11} [GPa]	E_{22} [GPa]	E_{33} [GPa]	G_{12} [GPa]	G_{13} [GPa]	G_{23} [GPa]	ν_{12}	ν_{13}	ν_{23}
159.0	8.4	8.4	4.1	4.1	4.1	0.33	0.33	0.50

Table 3.5: Elastic properties of the carbon/epoxy T800/914 ply, [146].

The geometrical parameters of the plate are: $L = 300.0$ mm (length), $b = 200.0$ mm (width) and $h = 1.25$ mm (thickness).
The structure is fixed on one face and subjected to a traction load $P = 1.0\ MPa$ on the opposite face. The ZOI is a square region located in the middle of the structure and whose side length is $a_{local} = 10.0$ mm. The geometrical features, the BCs of the GFEM and the LFEM are shown in Fig. 3.31.

The GFEM is made of of 40 x 60 linear plate elements and it is built within *MSC-Nastran*. Instead, the LFEM is composed of 15 L9 sub-domains along the x-axis, 6 L9 sub-domains for each layer, and 6 B4 elements.

Fig. 3.32 shows the shear stress distribution σ_{yz} resulted from the global-local analysis. Fig. 3.32(a) depicts the shear stress σ_{yz} at $-15^\circ/90^\circ$ interface versus x in the proximity

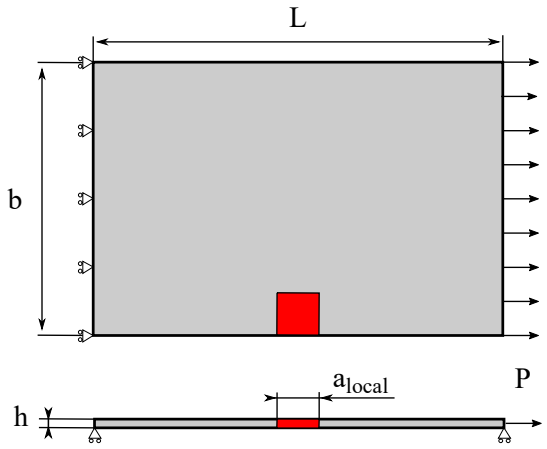

Figure 3.31: Ten-ply composite plate with uni-axial pressure traction $P = 1.0\ MPa$.

of the free-edge, while Fig. 3.32(b) gives the shear stress pattern along z-axis. These distributions are compared with those given by Lorriot *et al.* [146].

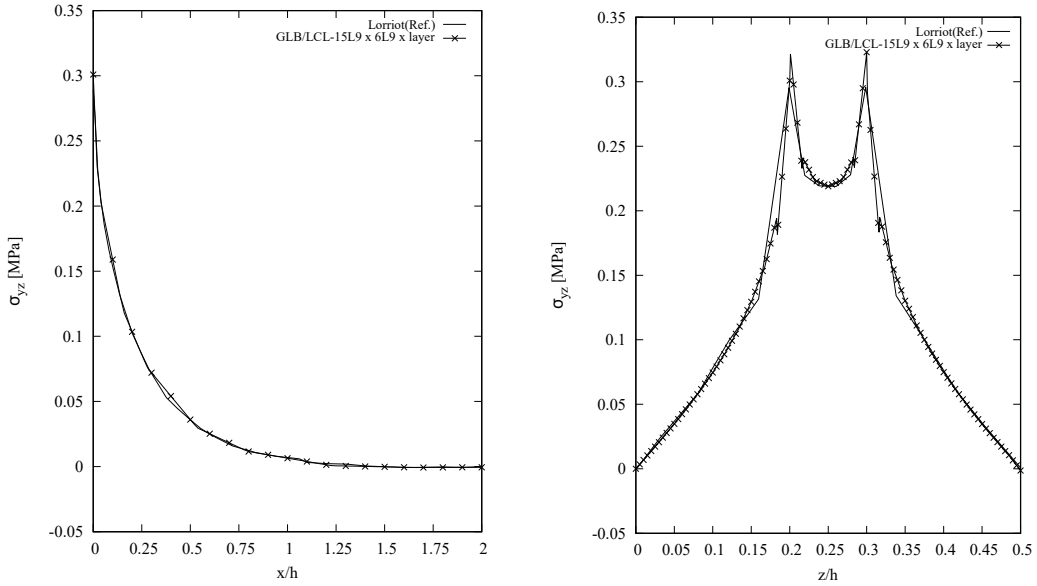

(a) Shear stress σ_{yz} at $-15^\circ/90^\circ$ interface versus x

(b) Shear stress σ_{yz} at the free-edge versus z

Figure 3.32: Shear stress σ_{yz} in the free edge for the $T800/914$ - $[15^\circ_2/90^\circ/-15^\circ_2]_s$ plate.

Fig. 3.32(a) reports the shear stress field in the CUF LFEM. In this figure, it is particularly important to observe the shear stress peaks occurring at the interface between different layers. Fig. 3.33 plots the σ_{yz} at the free-edge of the ZOI.

The results presented in Fig. 3.32 show that the global-local approach is able to correctly identify the stress field in the proximity of the free edge. Also in this case, results are in agreement with the experimental ones provided in [146]. It is noteworthy that the global-local analysis allows obtaining a correct description of the 3D stress field by starting from the BCs extracted from a low-fidelity GFEM and applied on the boundary of the

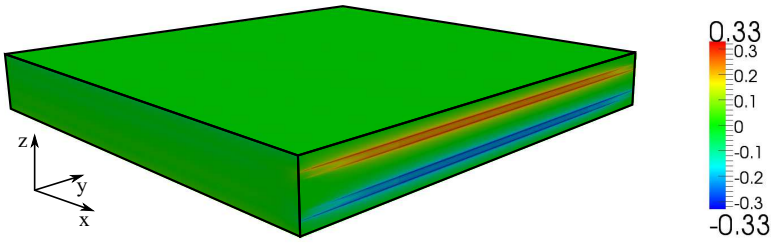

Figure 3.33: Shear stress σ_{yz} at the free-edge of the ZOI.

CUF LFEM.

Peaks of interlaminar stresses at the interface of different layers are responsible for the damage onset. These areas are of particular interest to prevent delamination of the layers and must be studied with special attention. Particularly, these peaks may have different intensity depending on the difference between the orientation angles of two consecutive plies. To this end, it is reasonable to create a model identical to the one previously analyzed but considering a different stack sequence, i.e. $[0°/45°/0_2°/90°]_s$. By keeping the same geometry, material, and BCs, the shear σ_{yz} and peel σ_{zz} inter-laminar stresses of the two models are compared in Fig. 3.34. From this figure, it can be observed that although

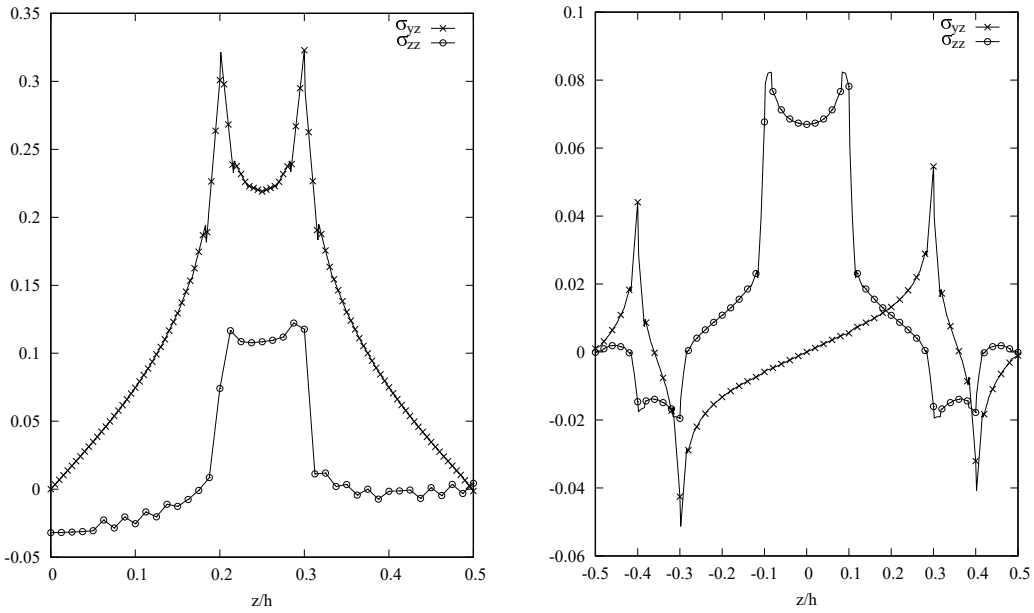

(a) Inter-laminar stress distributions through the thickness of the $[15_2°/90°/-15_2°]_s$ plate

(b) Inter-laminar stress distributions through the thickness of the $[0°/45°/0_2°/90°]_s$ plate

Figure 3.34: Inter-laminar stresses in the free edge for the $[15_2°/90°/-15_2°]_s$ and $[0°/45°/0_2°/90°]_s$ plates.

the structures have the same BCs, in one prevails the shear stress (Fig. 3.34(a)) and in the other the peal stress (Fig. 3.34(b)). The trend of inter-laminar stress is completely different in the two cases and the same is true for the presence of peaks.

C-shape stringer and failure index analysis

The aim of this last benchmark is to show that the proposed global-local modelling strategy based on CUF can be easily extended to general structures overcoming the limitations that can be found in the solutions available in the literature. Here, a composite stringer with a C-shape cross-section is considered as a benchmark problem. The geometry is shown in Fig. 3.35: the length of the stringer is $L = 2.0$ m, the width is $b = 0.05$ m and the height is $h = 0.1$ m. The thickness of the stringer walls is $t = 2.54$ mm. The stringer is made of IM7/8552 ply, whose elastic constants are reported in Tab 3.6. The considered stack sequence is $[0°/90°/45°/-45°]$.

E_{11} [GPa]	E_{22} [GPa]	E_{33} [GPa]	G_{12} [GPa]	G_{13} [GPa]	G_{23} [GPa]	ν_{12}	ν_{13}	ν_{23}
165.0	9.0	9.0	5.6	5.6	2.8	0.34	0.34	0.50

Table 3.6: Elastic properties of the IM7/8552 ply.

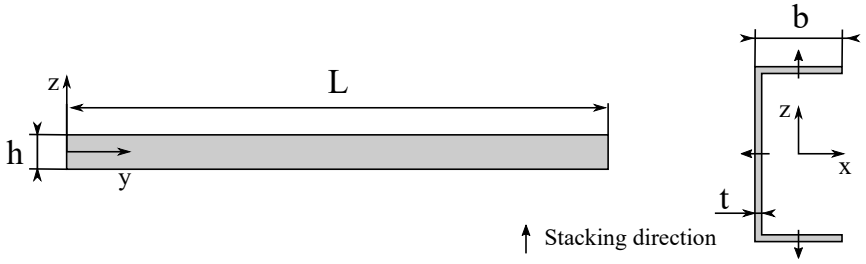

Figure 3.35: C-shape stringer geometry

The stringer is clamped at one end and loaded by three different load sets: tensile load $T = 1000$ [N], bending moment $M_x = 100$ [Nm] and a torsion moment $M = 100$ [Nm]. Each load is applied at the section centre of gravity (CG) of the free end cross-section making the use of a Multi Point Constraint (MPC) element, as illustrated in Fig. 3.36. Different critical ZOIs can be selected in the C-shape stringer, as shown in Fig. 3.37. Each

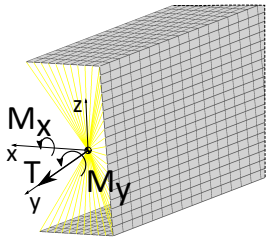

Figure 3.36: Applied loads and MPC elements at the free end of the stringer.

ZOI has the same length $L_l = 0.04$ $[m]$ and width $b_l = 0.04$ $[m]$ and the stresses σ_{zz} and σ_{yz} are evaluated at point P, that is always positioned on the free edge at $L_l/2$.

The GFEM is built in *MSc-Nastran* and consist of 7800 linear plate elements.
Figs. 3.38, 3.39, 3.40 show the transverse σ_{zz} stress and shear σ_{yz} stress distributions through the thickness of the structure. These distributions are calculated in the local regions of the GFEM in Fig. 3.37 and are calculated for each load condition of the structure.

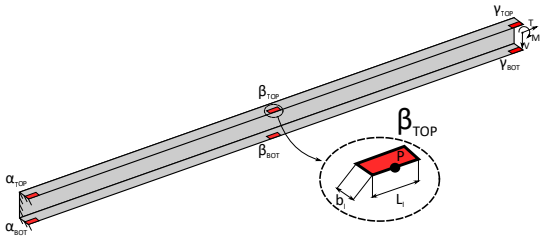

Figure 3.37: ZOIs for the C-shape stringer.

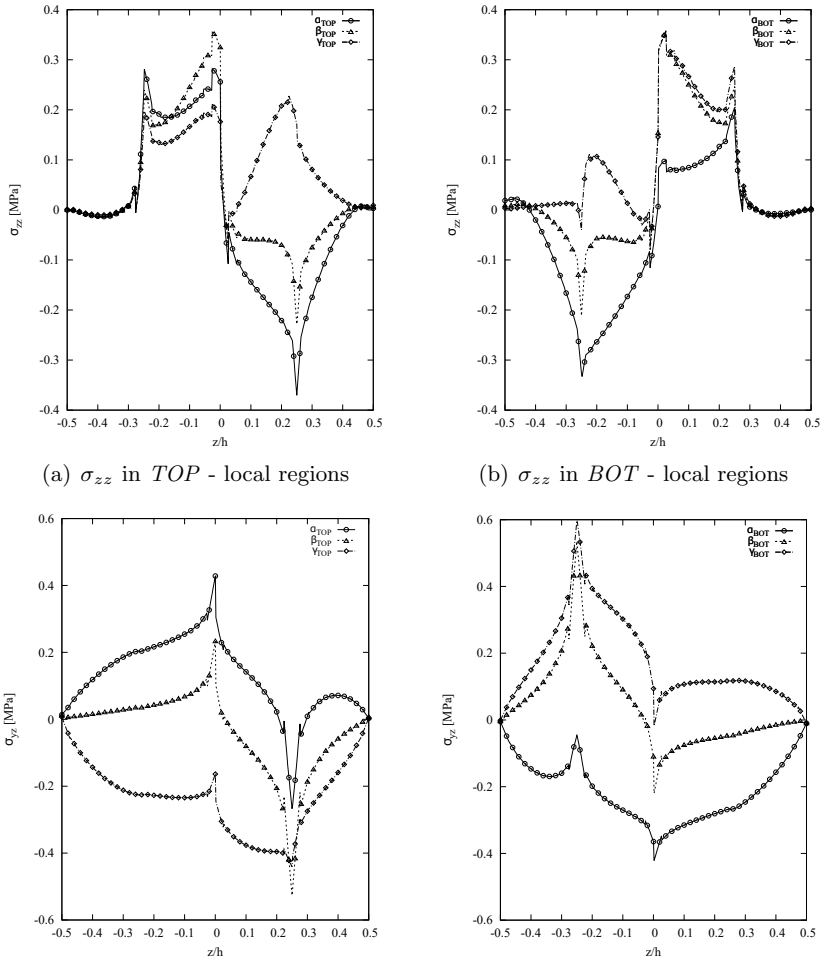

(a) σ_{zz} in *TOP* - local regions

(b) σ_{zz} in *BOT* - local regions

(c) σ_{yz} in *TOP* - local regions

(d) σ_{yz} in *BOT* - local regions

Figure 3.38: Transversal stress σ_{zz} and shear stress σ_{yz} distributions of the ZOIs in tensile load case.

From these results, one can infer that the global-local modelling strategy based on CUF is able to catch the free-edge effects in the three different load conditions. This assessment also confirms that the approach is completely general and it is applicable to complex geometries.

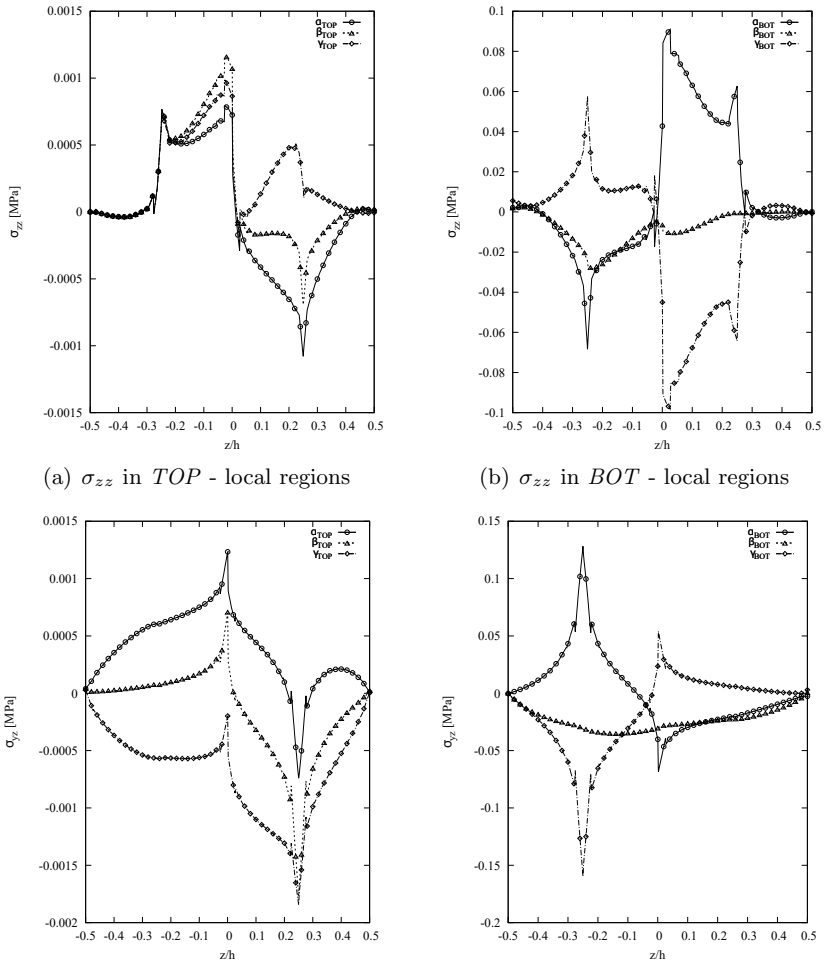

(a) σ_{zz} in TOP - local regions

(b) σ_{zz} in BOT - local regions

(c) σ_{yz} in TOP - local regions

(d) σ_{yz} in BOT - local regions

Figure 3.39: Transversal stress σ_{zz} and shear stress σ_{yz} distributions of the ZOIs in bending load case.

3.5 Conclusions

Global-local approaches are needed when a complex structure requires a detailed stress analysis in critical regions. In this Chapter, a two-step methodology has been developed for global-local stress analysis in the CUF framework which has proven to be very efficient in evaluating complex stress and stain states in composite structures. In the first step, a preliminary static analysis on the classical FE models made of 1D/2D elements by using commercial software is done for identifying the ZOIs and obtaining all the necessary information (geometrical parameters, material, stack sequence, and BCs) for the pre-processing phase of the LFEMs. The second step is dedicated to the static analysis of the LFEM formulated in the CUF framework by using geometrical BCs resulting from the GFEM and applied to the boundary of the transition zone surrounding the ZOI. Two classes of numerical meaningful benchmarks have been proposed to assess the validity of the methodology. The first family of benchmarks has shown that the proposed global-local modelling approach is able to compute accurate 3D stress fields within the ZOIs by significantly reducing the computational burden with respect to detailed LFEMs made of

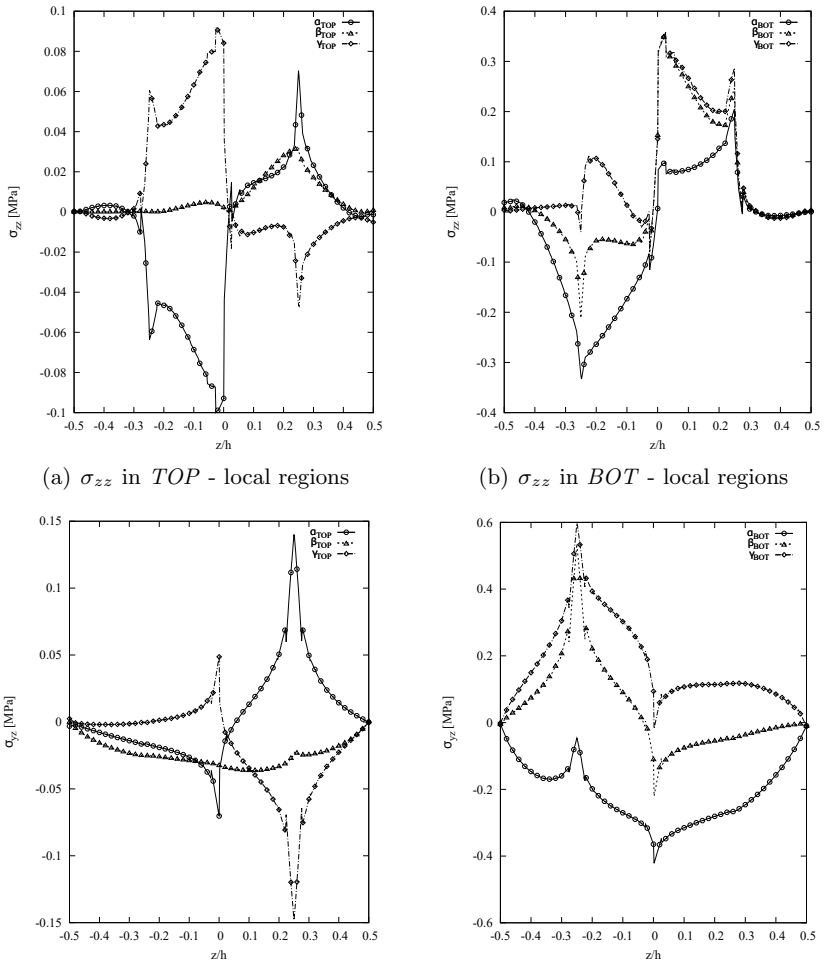

(a) σ_{zz} in TOP - local regions

(b) σ_{zz} in BOT - local regions

(c) σ_{yz} in TOP - local regions

(d) σ_{yz} in BOT - local regions

Figure 3.40: Transversal stress σ_{zz} and shear stress σ_{yz} distributions of the ZOIs in torsion load case.

3D solid elements. The second class of benchmarks was devoted to the study of the free-edge phenomenon in composite structures. In this case, as well, the global-local approach has proven to be effective in the description of the inter-laminar stresses, which are often the cause of the failure onset in composites.

Chapter 4

Polar Method and Composite Laminate Mechanics

4.1 Introduction

This Chapter is devoted to the presentation of the polar method introduced by Verchery in 1979 [147], which is used in this thesis to describe the stiffness and the strength tensors of uncoupled, homogeneous and orthotropic laminates in the framework of the multi-scale optimisation strategy presented in Chapters 5, 6 and 7.
The Chapter is organised as follows: Section 4.2 and 4.3 show the fundamentals of the polar method for plane elasticity and the application to the framework of the FSDT, respectively. The polar description of laminate strength tensors are described in Section 4.4, while the elastic and geometrical bounds for the PPs are discussed in Section 4.5. Finally, a general class of solutions, which will be used in the following chapters of this work for the optimal design of the laminate lay-up, i.e. the quasi-trivial (QT) stacking sequences (SSs), is presented in Section 4.6. The concluding remarks of Section 4.7 end the chapter.

4.2 Fundamentals of the polar method

The polar method is a powerful mathematical technique that allows expressing any n-order plane tensor through a set of tensor invariants [50].
Consider a local frame $\Gamma = \{\mathrm{O},\ x_1,\ x_2,\ x_3\}$: the polar representations of symmetric second-order tensors and elasticity-like fourth-order tensors (i.e. tensors having both minor and major symmetries) are provided here below.

- **Second-order symmetric tensor**
  The components of a second-order symmetric tensor Z_{ij}, $(i,j = 1,2)$ in the local reference frame are expressed as follows:

$$Z_{11} = T + R\cos 2\Phi, \quad Z_{12} = R\sin 2\Phi, \quad Z_{22} = T - R\cos 2\Phi, \tag{4.1}$$

  where T is the isotropic modulus, R the deviatoric one and Φ the polar angle. In Eq. (4.1), the three independent Cartesian components of a second-order plane symmetric tensor are expressed in terms of three PPs: among them, only two are tensor invariants, i.e. T and R, while the last one, namely the polar angle, is needed to set the reference frame. The converse relations are:

$$T = \frac{Z_{11} + Z_{22}}{2}, \quad R\mathrm{e}^{\mathrm{i}2\Phi} = \frac{Z_{11} - Z_{22}}{2} + \mathrm{i}Z_{12}, \tag{4.2}$$

where $\mathrm{i} = \sqrt{-1}$ is the imaginary unit.

As reported in [50], the only possible symmetry is the isotropy for a second-order plane tensor. This condition can be obtained when the deviatoric modulus of the tensor is null, i.e. $R = 0$. Moreover, using the polar formalism, it is possible to easily express the components of the second-order tensor in a very straightforward manner in the frame Γ^I (turned counter-clock wise by an angle θ around the x_3 axis) as follows:

$$Z_{xx} = T + R\cos 2(\Phi - \theta), \quad Z_{xy} = R\sin 2(\Phi - \theta), \quad Z_{22} = T - R\cos 2(\Phi - \theta). \tag{4.3}$$

Eq. (4.3) shows that, within the polar formalism, the change of frame can be easily obtained by subtracting the angle θ from the polar angle Φ.

- **Fourth-order symmetric tensor** Consider a fourth-order elasticity-like plane tensor L_{ijkl}, $(i, j, k, l = 1, 2)$ (expressed within the local frame). Its polar representation reads:

$$\begin{array}{lcccccccccc}
L_{1111} &=& & T_0 &+& 2T_1 &+& R_0\cos 4\Phi_0 &+& 4R_1\cos 2\Phi_1 & , \\
L_{1122} &=& - & T_0 &+& 2T_1 &-& R_0\cos 4\Phi_0 & & & , \\
L_{1112} &=& & & & & & R_0\sin 4\Phi_0 &+& 2R_1\sin 2\Phi_1 & , \\
L_{2222} &=& & T_0 &+& 2T_1 &+& R_0\cos 4\Phi_0 &-& 4R_1\cos 2\Phi_1 & , \\
L_{2212} &=& & & & & - & R_0\sin 4\Phi_0 &+& 2R_1\sin 2\Phi_1 & , \\
L_{1212} &=& & T_0 & & & - & R_0\cos 4\Phi_0 & & & .
\end{array} \tag{4.4}$$

As it clearly appears from Eq. (4.4), the six independent Cartesian components of L_{ijkl} are expressed in terms of six PPs: T_0 and T_1 are the isotropic moduli, R_0 and R_1 are the anisotropic ones, while Φ_0 and Φ_1 are the polar angles. Only five quantities are tensor invariants, namely the polar moduli T_0, T_1, R_0, R_1 together with the angular difference $\Phi_0 - \Phi_1$. One of the two polar angles, Φ_0 or Φ_1, can be arbitrarily chosen to set the reference frame. The converse relations are:

$$\begin{array}{rcll}
8T_0 &=& L_{1111} - 2L_{1122} + 4L_{1212} + L_{2222} & , \\
8T_1 &=& L_{1111} + 2L_{1122} + L_{2222} & , \\
8R_0\mathrm{e}^{\mathrm{i}4\Phi_0} &=& L_{1111} - 2L_{1122} - 4L_{1212} + L_{2222} + 4\mathrm{i}(L_{1112} - L_{2212}) & , \\
8R_1 e^{\mathrm{i}2\Phi_1} &=& L_{1111} - L_{2222} + 2\mathrm{i}(L_{1112} - L_{2212}) & .
\end{array} \tag{4.5}$$

Thanks to the polar formalism it is very easy to express the Cartesian components of the fourth-order tensor in the frame Γ^I, in fact it suffices to subtract the angle θ from the polar angles Φ_0 and Φ_1 as follows:

$$\begin{array}{lcccccccccc}
L_{xxxx} &=& & T_0 &+& 2T_1 &+& R_0\cos 4(\Phi_0 - \theta) &+& 4R_1\cos 2(\Phi_1 - \theta) & , \\
L_{xxyy} &=& - & T_0 &+& 2T_1 &-& R_0\cos 4(\Phi_0 - \theta) & & & , \\
L_{xxxy} &=& & & & & & R_0\sin 4(\Phi_0 - \theta) &+& 2R_1\sin 2(\Phi_1 - \theta) & , \\
L_{yyyy} &=& & T_0 &+& 2T_1 &+& R_0\cos 4(\Phi_0 - \theta) &-& 4R_1\cos 2(\Phi_1 - \theta) & , \\
L_{yyxy} &=& & & & & - & R_0\sin 4(\Phi_0 - \theta) &+& 2R_1\sin 2(\Phi_1 - \theta) & , \\
L_{xyxy} &=& & T_0 & & & - & R_0\cos 4(\Phi_0 - \theta) & & & .
\end{array} \tag{4.6}$$

In the case of a fourth-order elasticity-like tensor, the real plus-value of the polar method is really significant: the polar invariants are directly linked to the (elastic) symmetries of the tensor, thus having an immediate physical meaning. Indeed, the

polar formalism offers an algebraic characterisation of the elastic symmetries, which can be seen as an alternative to the classical geometrical approach to the problem of finding the elastic symmetries of a material. In particular, it can be proved that, for a fourth-order elasticity-like plane tensor, four different types of elastic symmetries exist [51]. They are briefly recalled in the following.

- *Ordinary orthotropy*: this symmetry corresponds to the algebraic condition

$$\Phi_0 - \Phi_1 = K\frac{\pi}{4}, \quad K = 0, 1\ . \tag{4.7}$$

  Indeed, for the same set of tensor invariants, i.e. T_0, T_1, R_0, R_1, two different shapes of orthotropy exist, depending on the value of K. Vannucci [51] proved that they correspond to the so-called low ($K = 0$) and high ($K = 1$) shear modulus orthotropic materials. However, this classification is rather limiting since the difference between these two classes of orhtotropy concerns, more generally, the global mechanical response of the material, see [51, 54].
- R_0 - *Orthotropy*: the algebraic condition to attain this "special" orthotropy is

$$R_0 = 0. \tag{4.8}$$

  In this case, the Cartesian components of the fourth-order tensor L_{ijkl} change (as a result of a frame rotation) as those of a second-order tensor, see Eqs. (4.1), 4.4).
- *Square symmetry*: it can be obtained by imposing the following condition

$$R_1 = 0. \tag{4.9}$$

  This symmetry represents the 2D case of the well-known 3D cubic syngony.
- *Isotropy*: the fourth-order elasticity-like tensor is isotropic when its anisotropic moduli are null, i.e. when the following condition is satisfied

$$R_0 = R_1 = 0. \tag{4.10}$$

4.2.1 Thermodynamic existence conditions

Let W be the stored-energy density function for an anisotropic linear hyperelastic material. This energy density, under the hypothesis of plane elasticity is written as:

$$W := \frac{1}{2}\boldsymbol{\sigma}\boldsymbol{\varepsilon} = Tt + Rr\ \cos 2(\Phi - \phi), \tag{4.11}$$

where T, R, Φ are the PPs of the Cauchy's stress tensor $\boldsymbol{\sigma}$ and t, r, ϕ the counterparts for the linearised strain vector $\boldsymbol{\varepsilon}$. Using the constitutive equation for the material $\boldsymbol{\sigma} = \mathbb{C}\boldsymbol{\varepsilon}$ and considering that $\mathbb{C}$ is a fourth-order elasticity-like plane tensor of PPs T_0, T_1, R_0, R_1, Φ_0, Φ_1, Eq. (4.11) reads:

$$W = 4T_1t^2 + 8R_1rt\cos 2(\Phi 11 - \phi) + 2r^2[T_0 + R_0\cos 4(\Phi_0 - \phi)], \tag{4.12}$$

which can be arranged in a quadratic form of r and t as follows:

$$W = \begin{Bmatrix} r & t \end{Bmatrix} \begin{bmatrix} 2[T_0 + R_0\cos 4(\Phi_0 - \phi)] & 4R_1\cos 2(\Phi_1 - \phi) \\ 4R_1\cos 2(\Phi_1 - \phi) & 4T_1 \end{bmatrix} \begin{Bmatrix} r \\ t \end{Bmatrix}. \tag{4.13}$$

Inasmuch as W has to be positive-definite, the following conditions hold:

$$\begin{cases} T_0 + R_0 \cos 4(\Phi_0 - \phi) > 0, \\ T_1[T_0 + R_0 \cos 4(\Phi_0 - \phi)] > 2R_1^2 \cos^2 2(\Phi_1 - \phi). \end{cases} \tag{4.14}$$

Since all of the leading principal minors of the matrix appearing in Eq. (4.13) must have positive determinant, the study of Eq. (4.14) provides the following elastic bounds:

$$\begin{cases} T_0, T_1, R_0, R_1 > 0, \\ T_0 > R_0, \\ T_1(T_0^2 - R_0^2) > 2R_1^2[T_0 - R_0 \cos 4(\Phi_0 - \Phi_1)]. \end{cases} \tag{4.15}$$

4.3 The polar analysis of the first-order shear deformation theory

The FSDT framework [133] is used to describe the mechanical behaviour of the laminate in this Thesis. For the sake of simplicity, all the equations governing the laminate mechanical response are formulated in the context of the Voigt's (or matrix) notation. The passage from tensor notation to Voigt's notation can be easily expressed by the following two-way relationships among indexes (for both local and global frames):

$$\begin{array}{rcl} \{11,\ 22,\ 33,\ 44,\ 55,\ 66\} & \Leftrightarrow & \{1,\ 2,\ 3,\ 4,\ 5,\ 6\} \quad , \\ \{xx,\ yy,\ zz,\ zy,\ zx,\ yx\} & \Leftrightarrow & \{x,\ y,\ z,\ q,\ r,\ s\} \quad , \end{array} \tag{4.16}$$

Consider a multilayer plate composed of n identical layers (i.e. layers having same material properties and thickness), ϕ_k the orientation angle of the $k-th$ ply ($k = 1 \ \ldots \ n$): t_{ply} is the thickness of the elementary lamina and $h = n\ t_{\text{ply}}$ the overall thickness of the plate, as illustrated in Fig. 4.1.

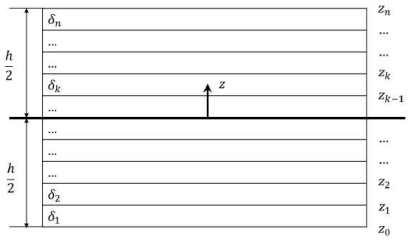

Figure 4.1: Definition of the geometrical parameters of the laminate.

In the framework of the FSDT [133] the constitutive law of the laminate (expressed within its global frame $\Gamma = \{O; x, y, z\}$) can be stated as:

$$\mathbf{r} = \mathbf{K}_{\text{lam}} \boldsymbol{\varepsilon}, \tag{4.17}$$

where $\mathbf{r}$ and $\boldsymbol{\varepsilon}$ are the vectors of the generalised forces per unit length and strains of the laminate middle plane, respectively, whilst $\mathbf{K}_{\text{lam}}$ is the laminate stiffness matrix (Voigt's

notation). In this framework, the analytical form of these arrays is:

$$\mathbf{r} = \begin{Bmatrix} \mathbf{n} \\ \mathbf{m} \\ \mathbf{q} \end{Bmatrix}, \quad \mathbf{K}_{\text{lam}} = \begin{bmatrix} \mathbf{A} & \mathbf{B} & \mathbf{0} \\ & \mathbf{D} & \mathbf{0} \\ \text{sym} & & \mathbf{H} \end{bmatrix}, \quad \boldsymbol{\varepsilon} = \begin{Bmatrix} \boldsymbol{\varepsilon_0} \\ \boldsymbol{\chi_0} \\ \boldsymbol{\gamma_0} \end{Bmatrix}. \tag{4.18}$$

In Eq. (4.18), $\mathbf{A}$, $\mathbf{B}$ and $\mathbf{D}$ are the membrane, membrane/bending coupling and bending stiffness matrices of the laminate, while $\mathbf{H}$ is the out-of-plane shear stiffness matrix. $\mathbf{n}$, $\mathbf{m}$ and $\mathbf{q}$ are the vectors of membrane forces, bending moments and shear forces per unit length, respectively, whilst $\boldsymbol{\varepsilon_0}$, $\boldsymbol{\chi_0}$ and $\boldsymbol{\gamma_0}$ are the vectors of in-plane strains, curvatures and out-of-plane shear strains of the laminate middle plane, respectively, [133]. The expressions of matrices $\mathbf{A}$, $\mathbf{B}$ and $\mathbf{D}$ are:

$$\begin{aligned} \mathbf{A} &= \tfrac{h}{n} \textstyle\sum_{k=1}^{n} \mathbf{Q}(\delta_k), \\ \mathbf{B} &= \tfrac{1}{2} \left(\tfrac{h}{n}\right)^2 \textstyle\sum_{k=1}^{n} b_k \mathbf{Q}(\delta_k) \\ \mathbf{D} &= \tfrac{1}{12} \left(\tfrac{h}{n}\right)^3 \textstyle\sum_{k=1}^{n} d_k \mathbf{Q}(\delta_k), \end{aligned} \tag{4.19}$$

with

$$\begin{aligned} b_k &= 2k - n - 1, \qquad \textstyle\sum_{k=1}^{n} b_k = 0, \\ d_k &= 12k(k - n - 1) + 4 + 3n(n + 2), \qquad \textstyle\sum_{k=1}^{n} d_k = n^3. \end{aligned} \tag{4.20}$$

It can be noticed that, in Eq. (4.19), $\mathbf{Q}(\delta_k)$ is the in-plane reduced stiffness matrix of the k-th ply. Moreover, in the literature one can find different expressions for the out-of-plane shear stiffness matrix of the laminate $\mathbf{H}$. In the following only two representations are considered, namely:

$$\begin{cases} \tfrac{h}{n} \textstyle\sum_{k=1}^{n} \tilde{\mathbf{Q}}(\delta_k), & \text{(basic)}, \\ \tfrac{5h}{12n^3} \textstyle\sum_{k=1}^{n} \left(3n^2 - d_k\right) \tilde{\mathbf{Q}}(\delta_k), & \text{(modified)}. \end{cases} \tag{4.21}$$

In Eq. (4.21) $\tilde{\mathbf{Q}}(\delta_k)$ is the out-of-plane shear stiffness matrix of the elementary ply. The first form of the matrix $\mathbf{H}$ is the basic one, wherein the shear stresses are constant through the thickness of each lamina. However, as widely discussed in [133], this approximation is not accurate at least for three reasons: a) a constant out-of-plane shear stress field does not satisfy the local equilibrium equations of each lamina, b) the shear stresses are discontinuous at the layers interfaces and c) the out-of-plane shear stresses must be null on both top and bottom surfaces of the plate if no tangential forces are applied. To these purposes several modifications of the expression of $\mathbf{H}$ have been proposed by many researchers in order to take into account for the previous aspects, see [133]. In particular, the second form of matrix $\mathbf{H}$ shown in Eq. (4.21) takes into account for the parabolic variation of the shear stresses through the thickness of each lamina (which satisfies the local equilibrium). Moreover, when using such a formulation, shear stresses vanish on both top and bottom faces of the plate. However, this modified form of $\mathbf{H}$ does not take into account for the continuity of the shear stresses at the interfaces of the plies. For a deeper insight on such aspects the reader is addressed to [133]. It is noteworthy that, when passing from the lamina material frame Γ to the laminate global frame Γ^I, the terms of the matrix $\mathbf{Q}(\delta_k)$ behave like those of a fourth-rank elasticity-like tensor, see [5, 51]. On the other hand, the components of $\tilde{\mathbf{Q}}(\delta_k)$ behave like those of a second-rank symmetric tensor with the local frame turned clockwise by an angle δ_k around the x_3 axis. Therefore

$\mathbf{Q}(\delta_k)$ and $\tilde{\mathbf{Q}}(\delta_k)$ can be expressed (within the laminate global frame) by means of the polar formalism as follows:

$$\begin{array}{rcrcrcrcrcl}
\mathrm{Q_{xx}}\,(\delta_k) &=& & T_0 &+& 2T_1 &+& R_0\cos 4(\Phi_0-\delta_k) &+& 4R_1\cos 2(\Phi_1-\delta_k) &,\\
\mathrm{Q_{xy}}\,(\delta_k) &=& - & T_0 &+& 2T_1 &-& R_0\cos 4(\Phi_0-\delta_k) & & &,\\
\mathrm{Q_{xs}}\,(\delta_k) &=& & & & & & R_0\sin 4(\Phi_0-\delta_k) &+& 2R_1\sin 2(\Phi_1-\delta_k) &,\\
\mathrm{Q_{yy}}\,(\delta_k) &=& & T_0 &+& 2T_1 &+& R_0\cos 4(\Phi_0-\delta_k) &-& 4R_1\cos 2(\Phi_1-\delta_k) &,\\
\mathrm{Q_{ys}}\,(\delta_k) &=& & & & & - & R_0\sin 4(\Phi_0-\delta_k) &+& 2R_1\sin 2(\Phi_1-\delta_k) &,\\
\mathrm{Q_{ss}}\,(\delta_k) &=& & T_0 & & & - & R_0\cos 4(\Phi_0-\delta_k) & & &.
\end{array} \tag{4.22}$$

and

$$\mathrm{Q_{qq}}\,(\delta_k) = T+R\cos 2(\Phi-\delta_k);\quad \mathrm{Q_{qr}}\,(\delta_k) = R\sin 2(\Phi-\delta_k);\quad \mathrm{Q_{rr}}\,(\delta_k) = T-R\cos 2(\Phi-\delta_k) \tag{4.23}$$

In the above equations the material frame of the k-th lamina (and not the global one) is turned counter-clock wise by an angle δ_k around the x_3 axis. In Eqs. (4.22, 4.23) T_0, T_1, R_0, R_1, Φ_0 and Φ_1 are the PPs of the in-plane reduced stiffness matrix of the lamina, while T, R, and Φ are those of the reduced out-of-plane stiffness matrix: all of these parameters solely depend upon the ply material properties (e.g. if the ply is orthotropic the polar parameters of $\mathbf{Q}(\delta_k)$ depend upon E_1, E_2, G_{12} and ν_{12}, while those of $\tilde{\mathbf{Q}}(\delta_k)$ depend upon G_{23} and G_{13}). In order to better analyse and understand the mechanical response of the laminate, it is useful to homogenise the units of the matrices $\mathbf{A}$, $\mathbf{B}$, $\mathbf{D}$ and $\mathbf{H}$ to those of the ply reduced stiffness matrices as follows:

$$\mathbf{A}^* = \frac{1}{h}\mathbf{A},\ \mathbf{B}^* = \frac{2}{h^2}\mathbf{B},\ \mathbf{D}^* = \frac{12}{h^3}\mathbf{D},\ \mathbf{H}^* = \begin{cases} \frac{1}{h}\mathbf{H} & \text{(basic)},\\ \frac{12}{5h}\mathbf{H} & \text{(modified)}. \end{cases} \tag{4.24}$$

In the framework of the polar formalism it is possible to express also matrices $\mathbf{A}^*$, $\mathbf{B}^*$, $\mathbf{D}^*$ and $\mathbf{H}^*$ in terms of their PPs. In particular, the homogenised membrane, membrane/bending coupling and bending stiffness matrices behave like a fourth-order elasticity-like tensor while the homogenised shear matrix behaves like a second-order symmetric tensor. Moreover, the PPs of these matrices can be expressed as functions of the PPs of the lamina reduced stiffness matrices and of the geometrical properties of the stack (i.e. layer orientation and position). The polar representation of $\mathbf{A}^*$, $\mathbf{B}^*$, $\mathbf{D}^*$ and $\mathbf{H}^*$ is:

$$\begin{array}{ll} T_0^{A^*} = T_0, & T_1^{A^*} = T_1,\\ R_0^{A^*}\mathrm{e}^{\mathrm{i}4\Phi_0^{A^*}} = \frac{1}{n}R_0\mathrm{e}^{\mathrm{i}4\Phi_0}\sum_{k=1}^{n}\mathrm{e}^{\mathrm{i}4\delta_k}, & R_1^{A^*}\mathrm{e}^{\mathrm{i}2\Phi_1^{A^*}} = \frac{1}{n}R_0\mathrm{e}^{\mathrm{i}2\Phi_1}\sum_{k=1}^{n}\mathrm{e}^{\mathrm{i}2\delta_k}, \end{array} \tag{4.25}$$

$$\begin{array}{ll} T_0^{B^*} = 0, & T_1^{B^*} = 0,\\ R_0^{B^*}\mathrm{e}^{\mathrm{i}4\Phi_0^{B^*}} = \frac{1}{n}R_0\mathrm{e}^{\mathrm{i}4\Phi_0}\sum_{k=1}^{n}\mathrm{e}^{\mathrm{i}4\delta_k}, & R_1^{B^*}\mathrm{e}^{\mathrm{i}2\Phi_1^{B^*}} = \frac{1}{n}R_0\mathrm{e}^{\mathrm{i}2\Phi_1}\sum_{k=1}^{n}\mathrm{e}^{\mathrm{i}2\delta_k}, \end{array} \tag{4.26}$$

$$\begin{array}{ll} T_0^{D^*} = T_0, & T_1^{D^*} = T_1,\\ R_0^{D^*}\mathrm{e}^{\mathrm{i}4\Phi_0^{D^*}} = \frac{1}{n}R_0\mathrm{e}^{\mathrm{i}4\Phi_0}\sum_{k=1}^{n}\mathrm{e}^{\mathrm{i}4\delta_k}, & R_1^{D^*}\mathrm{e}^{\mathrm{i}2\Phi_1^{D^*}} = \frac{1}{n}R_0\mathrm{e}^{\mathrm{i}2\Phi_1}\sum_{k=1}^{n}\mathrm{e}^{\mathrm{i}2\delta_k}, \end{array} \tag{4.27}$$

while that of matrix $[\mathrm{H}^*]$ (see [5]) can be stated as:

$$T^{H^*} = \begin{cases} T & \text{(basic)},\\ 2T & \text{(modified)}, \end{cases} \quad R^{H^*}\mathrm{e}^{\mathrm{i}2\Phi^{H^*}} = \begin{cases} \frac{1}{n}R\mathrm{i}^{\mathrm{i}2\Phi}\sum_{k=1}^{n}\mathrm{e}^{-\mathrm{i}2\delta_k} & \text{(basic)},\\ \frac{1}{n^3}R\mathrm{e}^{\mathrm{i}2\Phi}\sum_{k=1}^{n}(3n^2-d_k)\mathrm{e}^{-\mathrm{i}2\delta_k} & \text{(modified)}. \end{cases} \tag{4.28}$$

From Eqs. (4.25-4.28) it seems that, at the macro-scale, the laminate behaviour is governed by a set of 21 PPs: six for each one of the matrices $\mathbf{A}^*$, $\mathbf{B}^*$ and $\mathbf{D}^*$ and three for the shear stiffness matrix. In this set, the isotropic moduli of $\mathbf{B}^*$ are null, whilst those of $\mathbf{A}^*$, $\mathbf{D}^*$ and $\mathbf{H}^*$ are identical (or proportional) to the isotropic moduli of the layer reduced stiffness matrices. The only PPs which depend upon the geometrical properties of the stack (i.e. orientation angles and positions of the plies) are the anisotropic moduli and polar angles of $\mathbf{A}^*$, $\mathbf{B}^*$ and $\mathbf{D}^*$ together with the deviatoric modulus and polar angle of $\mathbf{H}^*$ for an overall number of 14 PPs to be designed in order to achieve the desired mechanical response for the laminate at the macroscopic-scale. However, as detailed in [5, 57], the deviatoric modulus and the polar angle of matrix $\mathbf{H}^*$ can be expressed (depending on the considered formulation for $\mathbf{H}^*$) as a linear combination of the anisotropic polar modulus R_1 and the related polar angle Φ_1 of matrices $\mathbf{A}^*$ and $\mathbf{D}^*$ as follows:

$$R^{H^*}\mathrm{e}^{\mathrm{i}2\Phi^{H^*}} = \begin{cases} R_1^{A^*}\mathrm{e}^{\mathrm{i}2\left(\Phi+\Phi_1-\Phi_1^{A^*}\right)} & \text{(basic)}, \\ \dfrac{R}{R_1}\mathrm{e}^{\mathrm{i}2(\Phi+\Phi_1)}\left(3R_1^{A^*}\mathrm{e}^{-\mathrm{i}2\Phi_1^{A^*}} - R_1^{D^*}\mathrm{e}^{-\mathrm{i}2\Phi_1^{D^*}}\right) & \text{(modified)}. \end{cases} \tag{4.29}$$

Eq. (4.29) means that (when the material of the elementary ply is set *a priori*) the overall mechanical response of the laminate depends only on the anisotropic polar moduli and the related polar angles of matrices $\mathbf{A}^*$ and $\mathbf{D}^*$, even in the framework of the FSDT. In particular the number of PPs to be designed remains unchanged when passing from the CLT to the FSDT: the designer can act (through a variation of the geometric parameters such as layers orientations and positions) only on the anisotropic polar moduli and the polar angles of the membrane, membrane/bending coupling and bending stiffness matrices, the deviatoric modulus and the polar angle of the shear stiffness matrix being directly related to them. Moreover, as it clearly appears from the first expression of Eq. (4.29), when using the basic definition of the laminate shear stiffness matrix, the ratio between the deviatoric part of the matrix $\mathbf{H}^*$, i.e. $R^{H^*}\mathrm{e}^{\mathrm{i}2\Phi^{H^*}}$, and the anisotropic term $R_1^{A^*}\mathrm{e}^{-\mathrm{i}2\Phi_1^{A^*}}$ of matrix $\mathbf{A}^*$ is constant once the material of the constitutive layer is chosen: such a ratio does not depend upon the layers orientations and positions, rather it depends only on the material properties of the constitutive layer (i.e. the polar parameters R_1, Φ_1, R, Φ).
As a conclusive remark of this section, it is noteworthy that since in almost all of the real-life engineering applications the designers look for an uncoupled laminate (i.e. $\mathbf{B}^*=0$), the total number of laminate parameters reduces from 12 to eight. Mechanically, when $\mathbf{B}^*=0$ the in-plane forces do not produce curvatures and, equivalently, bending moments do not deform the laminate middle plane. In addition, by means of the polar formalism it is possible to further reduce the total number of PPs to be conceived. In fact, considering quasi-homogeneous laminates [5, 50], i.e. laminates which satisfy the following conditions:

$$\mathbf{B}^* = 0, \quad \mathbf{C}^* = \mathbf{A}^* - \mathbf{D}^* = 0, \tag{4.30}$$

The total number of laminate PPs reduces from eight to four. The only quantities to be conceived are the anisotropic polar moduli and the related polar angles of the laminate membrane stiffness matrix (or the bending one since they are identical), namely $R_0^{A^*}$, $R_1^{A^*}$, $\Phi_0^{A^*}$, $\Phi_1^{A^*}$ and this result holds even when stating the laminate design problem in the framework of the FSDT.

4.4 Polar description of the laminate strength

The laminate strength properties can be described through the polar method. As reported in [60], the laminate stress-based failure criteria can be expressed in a compact matrix notation as:

$$\mathrm{FI}_\tau = \sigma^T \mathbf{F}_\tau \sigma + \sigma^T \mathbf{f}_\tau \leqslant 1, \tag{4.31}$$

where τ is an index denoting the failure criterion (i.e. Tsai-Hill, Hofmann, Tsai-Wu).

The failure index averaged over the thickness of the laminate $\mathrm{FI}_{\mathrm{lam}}$ can be derived as reported in [54, 60]. This one can be written as follow under the hypotheses of multilayer plates made of identical plies in the FSDT framework:

$$\mathrm{FI}_{\mathrm{lam}} = \frac{1}{h}\left(\boldsymbol{\varepsilon}^{\mathrm{T}} \begin{bmatrix} \mathbf{G}_A & \mathbf{G}_B & \mathbf{0} \\ & \mathbf{G}_D & \mathbf{0} \\ \mathrm{sym} & & \mathbf{G}_H \end{bmatrix} \boldsymbol{\varepsilon} + \boldsymbol{\varepsilon}^{\mathrm{T}} \begin{Bmatrix} \mathbf{g}_{\mathrm{A}} \\ \mathbf{g}_{\mathrm{D}} \\ \mathbf{0} \end{Bmatrix}\right) \leqslant 1. \tag{4.32}$$

In Eq. (4.32), $\mathbf{G}_A$ is the laminate membrane strength tensor, $\mathbf{G}_B$ the membrane/bending coupling strength tensor, $\mathbf{G}_D$ the bending strength tensor, $\mathbf{G}_H$ the shear strength tensor, whilst $\mathbf{g}_A$ and $\mathbf{g}_D$ are the membrane and bending strength vectors related to the linear part of the failure criterion. Eq. (4.32) represents the failure criterion for a multilayer plate modelled as equivalent single layer. The reader is addressed to [60] for further details about this topic.

The $\mathbf{G}_A$, $\mathbf{G}_B$, $\mathbf{G}_D$ behave like fourth-order elasticity-like tensors, $\mathbf{G}_H$ behaves like a second-order symmetric tensor turned clockwise (although the true rotation of the lamina reference system is counter-clockwise) and vectors $\mathbf{g}_A$ and $\mathbf{g}_D$ behave like a second-order symmetric tensors.
As for the laminate stiffness tensors, it is useful to introduce the dimensionless strength matrices:

$$\begin{array}{llll} \mathbf{G}_A^* \coloneqq \frac{1}{h}\,\mathbf{G}_A, & \mathbf{G}_B^* \coloneqq \frac{2}{h^2}\,\mathbf{G}_B, & \mathbf{G}_D^* \coloneqq \frac{12}{h^3}\,\mathbf{G}_D, & \mathbf{G}_H^* \coloneqq \frac{1}{h}\,\mathbf{G}_H, \\ \mathbf{g}_A^* \coloneqq \frac{1}{h}\,\mathbf{G}_A, & \mathbf{g}_D^* \coloneqq \frac{2}{h^2}\,\mathbf{g}_A. & & \end{array} \tag{4.33}$$

Consider a single lamina: let $\{\Gamma_0, \Gamma_1, \Lambda_0, \Lambda_1, \Omega_0, \Omega_1\}$ be the PPs of the in-plane reduced strength matrix, $\{\Gamma, \Lambda, \Omega\}$ be the PPs of the out-of-plane strength tensor, $\{\gamma, \lambda, \theta\}$ be the PPs of the in-plane strength vector. As done for the expressions of the stiffness matrices introduced in Section 4.3, the following expressions hold:

- tensor $\mathbf{G}_A^*$

$$\begin{array}{cc} \Gamma_0^{G_A^*} = \Gamma_0, & \Gamma_1^{G_A^*} = \Gamma_1, \\ \Lambda_0^{G_A^*} \mathrm{e}^{\mathrm{i}4\Omega_0^{G_A^*}} = \frac{\Lambda_0 \mathrm{e}^{\mathrm{i}4\Omega_0}}{N} \sum_{k=1}^N \mathrm{e}^{\mathrm{i}4\theta_k}, & \Lambda_1^{G_A^*} \mathrm{e}^{\mathrm{i}2\Omega_1^{G_A^*}} = \frac{\Lambda_1 \mathrm{e}^{\mathrm{i}2\Omega_1}}{N} \sum_{k=1}^N \mathrm{e}^{\mathrm{i}2\theta_k}; \end{array} \tag{4.34}$$

- tensor $\mathbf{G}_B^*$

$$\begin{array}{cc} \Gamma_0^{G_B^*} = 0, & \Gamma_1^{G_B^*} = 0, \\ \Lambda_0^{G_B^*} \mathrm{e}^{\mathrm{i}4\Omega_0^{G_B^*}} = \frac{\Lambda_0 \mathrm{e}^{\mathrm{i}4\Omega_0}}{N^2} \sum_{k=1}^N b_k \mathrm{e}^{\mathrm{i}4\theta_k}, & \Lambda_1^{G_B^*} \mathrm{e}^{\mathrm{i}2\Omega_1^{G_B^*}} = \frac{\Lambda_1 \mathrm{e}^{\mathrm{i}2\Omega_1}}{N^2} \sum_{k=1}^N b_k \mathrm{e}^{\mathrm{i}2\theta_k}; \end{array} \tag{4.35}$$

- tensor $\mathbf{G}_D^*$

$$\begin{array}{cc} \Gamma_0^{G_D^*} = \Gamma_0, & \Gamma_1^{G_D^*} = \Gamma_1, \\ \Lambda_0^{G_D^*} \mathrm{e}^{\mathrm{i}4\Omega_0^{G_D^*}} = \frac{\Lambda_0 \mathrm{e}^{\mathrm{i}4\Omega_0}}{N^3} \sum_{k=1}^N d_k \mathrm{e}^{\mathrm{i}4\theta_k}, & \Lambda_1^{G_D^*} \mathrm{e}^{\mathrm{i}2\Omega_1^{G_D^*}} = \frac{\Lambda_1 \mathrm{e}^{\mathrm{i}2\Omega_1}}{N^3} \sum_{k=1}^N d_k \mathrm{e}^{\mathrm{i}2\theta_k}; \end{array} \tag{4.36}$$

- tensor $\mathbf{G}_H^*$

$$\begin{aligned} \Gamma_1^{G_H^*} &= \Gamma, \\ \Lambda^{G_H^*} \mathrm{e}^{\mathrm{i}2\Omega^{G_H^*}} &= \frac{\Lambda \mathrm{e}^{\mathrm{i}2\Omega}}{N} \sum_{k=1}^{N} \mathrm{e}^{-\mathrm{i}2\theta_k}; \end{aligned} \tag{4.37}$$

- tensor $\mathbf{g}_A^*$

$$\begin{aligned} \gamma_1^{g_A^*} &= \gamma, \\ \lambda^{g_A^*} \mathrm{e}^{\mathrm{i}2\omega^{g_A^*}} &= \frac{\lambda \mathrm{e}^{\mathrm{i}2\omega}}{N} \sum_{k=1}^{N} \mathrm{e}^{\mathrm{i}2\theta_k}; \end{aligned} \tag{4.38}$$

- tensor $\mathbf{g}_D^*$

$$\begin{aligned} \gamma_1^{g_D^*} &= 0, \\ \lambda^{g_D^*} \mathrm{e}^{\mathrm{i}2\omega^{g_D^*}} &= \frac{\lambda \mathrm{e}^{\mathrm{i}2\omega}}{N^2} \sum_{k=1}^{N} b_k \mathrm{e}^{\mathrm{i}2\theta_k}. \end{aligned} \tag{4.39}$$

As discussed in [95], the equations related to arrays $\mathbf{G}_H^*$, $\mathbf{g}_A^*$ and $\mathbf{g}_D^*$ can be simplified. In fact their deviatoric part can be expressed in terms of the in-plane strength PPs as follows:

$$\begin{aligned} \Lambda^{G_H^*} \mathrm{e}^{\mathrm{i}2\Omega^{G_H^*}} &= \Lambda_1^{G_A^*} \frac{\Lambda}{\Lambda_1} \mathrm{e}^{\mathrm{i}2(\Omega - \Omega_1 - \Omega^{G_A^*})}, \\ \lambda^{g_A^*} \mathrm{e}^{\mathrm{i}2\omega^{g_A^*}} &= \Lambda_1^{G_A^*} \frac{\lambda}{\Lambda_1} \mathrm{e}^{\mathrm{i}2(\Omega^{G_A^*} + \omega - \Omega_1)}, \\ \lambda^{g_D^*} \mathrm{e}^{\mathrm{i}2\omega^{g_D^*}} &= \Lambda_1^{G_B^*} \frac{\lambda}{\Lambda_1} \mathrm{e}^{\mathrm{i}2(\Omega^{G_B^*} + \omega - \Omega_1)}. \end{aligned} \tag{4.40}$$

Moreover, the relation between stiffness and strength PPs is expressed by the following equations (see [60]):

$$\begin{aligned} \Omega_0^{G_A^*} \mathrm{e}^{\mathrm{i}4\Omega_0^{G_A^*}} &= R_0^{A^*} \frac{\Lambda_0}{R_0} \mathrm{e}^{\mathrm{i}4(\Phi_0^{A^*} + \Omega_0 - \Phi_0)}, \\ \Omega_1^{G_A^*} \mathrm{e}^{\mathrm{i}2\Omega_1^{G_A^*}} &= R_1^{A^*} \frac{\Lambda_1}{R_1} \mathrm{e}^{\mathrm{i}2(\Phi_1^{A^*} + \Omega_1 - \Phi_1)}, \\ \Omega_0^{G_B^*} \mathrm{e}^{\mathrm{i}4\Omega_0^{G_B^*}} &= R_0^{B^*} \frac{\Lambda_0}{R_0} \mathrm{e}^{\mathrm{i}4(\Phi_0^{B^*} + \Omega_0 - \Phi_0)}, \\ \Omega_1^{G_B^*} \mathrm{e}^{\mathrm{i}2\Omega_0^{G_B^*}} &= R_1^{B^*} \frac{\Lambda_1}{R_1} \mathrm{e}^{\mathrm{i}2(\Phi_1^{B^*} + \Omega_1 - \Phi_1)}, \\ \Omega_0^{G_D^*} \mathrm{e}^{\mathrm{i}4\Omega_0^{G_D^*}} &= R_0^{D^*} \frac{\Lambda_0}{R_0} \mathrm{e}^{\mathrm{i}4(\Phi_0^{D^*} + \Omega_0 - \Phi_0)}, \\ \Omega_1^{G_D^*} \mathrm{e}^{\mathrm{i}2\Omega_0^{G_D^*}} &= R_1^{D^*} \frac{\Lambda_1}{R_1} \mathrm{e}^{\mathrm{i}2(\Phi_1^{D^*} + \Omega_1 - \Phi_1)}. \end{aligned} \tag{4.41}$$

This result implies that (when the material of the elementary ply is chosen a priori) the overall mechanical response of the laminate, in terms of both stiffness and strength, depends only on the anisotropic polar moduli and the polar angles of the matrices $\mathbf{A}^*$, $\mathbf{B}^*$, $\mathbf{D}^*$, or equivalently to those of matrices $\mathbf{G}_A^*$, $\mathbf{G}_B^*$ $\mathbf{G}_D^*$. This important result highlights that, at the macroscopic level, the stiffness and the strength of the laminate are strictly linked.

4.5 Geometrical bounds

The set of inequalities reported in Eq. (4.15) can be applied to each one of the matrices $\mathbf{A}^*$ and $\mathbf{D}^*$ because they are positive-definite. Such conditions define an elastic domain containing all the admissible values of the PPs for the membrane and bending stiffness matrices. These cannot be applied to tensor $\mathbf{B}^*$ because it is non positive-definite. As shown in [52], more restrictive conditions than the elastic ones exist when a laminate with identical layers and with different orientation angles is considered. These conditions are named '*geometrical bounds*', and they depend on the geometry of the stack, i.e. the combination of the orientation angles and positions within the stack. The geometrical bounds for a generic uncoupled and anisotropic laminate are:

$$\begin{cases} 0 \leqslant \frac{R_0^T}{R_0} \leqslant 1, \\ 0 \leqslant \frac{R_1^T}{R_1} \leqslant 1, \\ 2\left(\frac{R_1^T}{R_1}\right)^2 \leqslant \frac{\left(\frac{R_0^T}{R_0}\right)^2}{1-(-1)^K \frac{R_0^T}{R_0}\cos 4(\Phi_0^T - \Phi_1^T)}, \\ T = A^*,\ D^*. \end{cases} \tag{4.42}$$

The domain defined by the geometrical bounds is always smaller than the elastic one as demonstrated in [52]. This result means that this domain can never cover the whole range covered by a single elementary layer. Finally, the complete set of constraints for the case of uncoupled, fully-orthotropic laminates is reported below:

$$\begin{cases} 1 \leqslant \frac{R_0^T}{R_0} \leqslant 1, \\ 0 \leqslant \frac{R_1^T}{R_1} \leqslant 1, \\ 2\left(\frac{R_1^T}{R_1}\right)^2 - 1 - (-1)^{K_T - K}\frac{R_0^T}{R_0} \leqslant 0, \\ T = A^*,\ D^*. \end{cases} \tag{4.43}$$

4.6 Quasi-trivial Stacking Sequences

QT SSs play an important role in the multi-scale optimisation strategy presented in Chapters 5 - 7 and they are briefly introduced here. Mathematically speaking, a SS made of n layers can be defined as the ordered set:

$$\mathrm{SS} \coloneqq \{\theta_k : 1 \leqslant k \leqslant n\} \tag{4.44}$$

where θ_k is the orientation angle of the $k-th$ ply (plies are ordered from the bottom surface to the top one of the laminate).
Consider the properties of homogeneity, (i.e. $\mathbf{C}^* = \mathbf{0}$), and uncoupling, (i.e. $\mathbf{B}^* = \mathbf{0}$), introduced in Sec 4.3. The homogeneity property allows integrating in a straightforward way the design of the bending matrix $\mathbf{D}^*$, which is quite difficult because its behaviour depends not only on the plies orientation angles, but also on their position within the SS. Conversely, since coefficients $\{b_k\}$ have an antisymmetric distribution with respect to the laminate middle plane, a simple way to obtain $\mathbf{B}^* = \mathbf{0}$ consists of using a symmetric SSs, as commonly done in several works [148–150]. The existence of uncoupled anti-symmetric stacks was shown in [151], while in [49], the existence of asymmetric uncoupled SSs was shown. In [152], a special class of uncoupled and possibly homogeneous laminates was found; the solutions belonging to this class are called QT and represent a class of arithmetically exact solutions. Furthermore, authors showed that the number of independent QT solutions is much larger than the number of symmetric SSs. QT stacks are characterised by an interesting and very useful property: membrane/bending uncoupling and/or homogeneity requirements can be exactly met regardless of the value of the orientation angles, see [37]. In particular, these requirements can be fulfilled by acting only on the position of the layers into the stack, see [37, 152]. QT SSs have been efficiently used in many practical problems [4, 6, 38, 95, 153]. In particular, QT sequences represent an equivalence class for all possible orientations that each group of plies can assume. As an example, $\{90°,\ -16°,\ 90°,\ 90°,\ -16°,\ 90°\}$ and $\{1°,\ 46°,\ 1°,\ 1°,\ 46°,\ 1°\}$ are elements

of the same equivalence class [{1, 2, 1, 1, 2, 1}], where 1 and 2 are just labels identifying two possibly distinct orientations. Of course, the choice of the orientations depends upon the desired elastic behaviour of the laminate. To explain clearly the concept of QT SSs, consider a laminate with n plies and $m \leqslant n$ different orientations and define

$$G_j \coloneqq \{k : \theta_k = \theta_j\}\,, \tag{4.45}$$

the set of indices within the SS sharing the same orientation θ_j . Conditions for uncoupling and homogeneity can be than split as multiple sums over the different sets $G_j, j = 1, ..., m$ [37]. Therefore, the uncoupling condition reads:

$$\sum_{k=1}^{n} b_k \mathrm{e}^{\mathrm{i}\beta\theta_k} = \sum_{j=1}^{m} \mathrm{e}^{\mathrm{i}\beta\theta_j} \sum_{k\in G_j} b_k = 0, \qquad \beta = 2, 4, \tag{4.46}$$

while the homogeneity requirement can be expressed as:

$$\sum_{k=1}^{n} c_k \mathrm{e}^{\mathrm{i}\beta\theta_k} = \sum_{j=1}^{m} \mathrm{e}^{\mathrm{i}\beta\theta_j} \sum_{k\in G_j} c_k = 0, \qquad \beta = 2, 4. \tag{4.47}$$

This result leads to the definition of saturated group which is a group of plies oriented at θ_j (for some j) satisfying the following conditions:

$$\sum_{k\in G_j} b_k = 0, \qquad \sum_{k\in G_j} c_k = 0. \tag{4.48}$$

Consequently, a SS is said QT if it is entirely composed of saturated groups. If not specified, the quasi-triviality has to be intended with respect to coefficients $\{b_k\}$ and $\{c_k\}$. In this case, the SS is said QT quasi-homogeneous (QH).

4.7 Conclusions

In this Chapter, the fundamentals of the Polar Method have been introduced. The Polar method is an elegant representation and a powerful tool that can be used both to describe the anisotropic behaviour of multilayer plates and for design purposes. In this thesis, the Polar method is used to describe both the stiffness and the strength matrices and vectors of QH orthotropic laminates in the FSDT framework.

Chapter 5

Multi-scale design of constant stiffness composites

5.1 Introduction

This Chapter focuses on the design/optimisation problem of CSCs. The discussion is here limited to CSCs reinforced through unidirectional fibres, i.e. those composites showing a strong anisotropic behaviour at the macroscopic scale, which can be described through a given set of pertinent mechanical properties. To illustrate the difficulty of properly design/optimise at each relevant scale a composite structure, a simplified benchmark problem (representative of a real-world engineering application) is considered in this Chapter: the least-weight design of a composite stiffened panel subject to requirements of different nature (geometrical, mechanical, technological, etc.). To face this problem, the MS2LOS developed by Montemurro and his co-workers, see [3–8] is used. This approach aims at optimising simultaneously both geometrical and mechanical parameters for skin and stiffeners at each characteristic scale. The MS2LOS relies, on the one hand, on the utilisation of the PPs, already introduced in Chapter. 4, in the framework of equivalent single layer theories for describing the macroscopic behaviour of each laminate composing the panel and, on the other hand, on a special genetic algorithm in order to perform the solution search for the considered problem. In this background, at the first level of the MS2LOS the goal is to find the optimum value of geometric and mechanical design variables of the panel minimising its mass and meeting the set of imposed constraints. The second-level problem focuses on the laminate mesoscopic scale (i.e. the ply-level) and aims at finding at least one optimum stack (for each laminate composing the panel) meeting the geometrical and material parameters provided by the first-level problem. The quality of the optimum configurations is investigated, a posteriori, through a refined finite element model of the stiffened panel making use of elements with different kinematics and accuracy in the CUF framework presented in Chapter 3. This Chapter is organised as follows: the MS2LOS is described in Section 5.2, whilst the design problem is presented in Section 5.3. The mathematical formulation of the first-level problem is detailed in Section 5.4, while the problem of determining suitable laminates is formulated in Section 5.5. The description of the FE models are given in Section 5.6, while the numerical results of the optimisation procedure are shown in Section 5.7. Finally, Section 5.8 ends the chapter with some concluding remarks.

Publication related to this chapter: The methodology and the results presented in this Chapter have been published in [6].

5.2 The multi-scale two level optimisation strategy

The MS2LOS is briefly recalled here. This approach is based on the utilisation of the polar formalism and on the use of the ERASMUS code [5] coupled with ANSYS® software. The aim is to propose a general formulation of the design problem without introducing simplifying hypotheses and by considering, as design variables, the full set of geometric and mechanical parameters defining the behaviour of the composite at each characteristic scale.
In the framework of the MS2LOS, the optimisation problem of a composite structure can be split in two distinct (but related) optimisation problems.

- *First-level problem* - FLP. This phase consists of the optimisation of the stiffness/strength properties of the laminates constituting the structure and their geometrical parameters, as well. At this level (macroscopic scale), each laminate is modelled as an equivalent homogeneous anisotropic plate whose behaviour is described in terms of the laminate characteristic stiffness matrices expressed through the polar formalism in the framework of the FSDT, as discussed in Section 4.3. During this phase, requirements of different nature can be considered: mass, buckling load, stiffness, laminate strength, technological and manufacturing constraints, etc. These requirements are opportunely formulated as optimisation constraints of the problem.
- *Second-level problem* - SLP. SLP is formulated at the laminate mesoscopic scale (ply-level). The goal is the determination of a suitable lay-up for each laminate composing the structure meeting the optimum combination of geometrical parameters and PPs provided by the FLP. The design variables of this level are the layers orientation angles. The SLP is formulated always in the most general case and no restrictions are imposed on the laminate SS to achieve the optimum value of the design variables resulting from the FLP.

5.3 Problem description

The MS2LOS is applied to the repetitive unit (RU) of a composite stiffened panel used in aerospace structures. The RU is composed by the union of a skin and a "omega" shaped stringer (or stiffener) as illustrated in Fig. 5.1.

The overall sizes of the RU are set *a priori*: $a = 150$ mm is the width of the RU, while $b = 600$ mm is its length, which also represents the distance between two consecutive ribs. The stiffeners are equispaced over the panel with a step length equal to a. Both skin and stiffener are made of carbon-epoxy unidirectional orthotropic laminate, whose properties are listed in Table 5.1 (taken from [56–58]).

The main hypotheses about the macroscopic mechanical response of the RU focus on the laminates behaviour and geometry (for both skin and stringer).

- Each laminate is made of identical plies (i.e. same thickness t_{ply} and material).
- The material of the constitutive layer has a linear elastic behaviour.
- Each laminate is quasi-homogeneous and fully orthotropic [4, 58, 94].
- At the macroscopic scale the elastic response of each laminate is described in the theoretical framework of the FSDT and the stiffness matrices of the plate are expressed in terms of the laminate PPs [56–58].

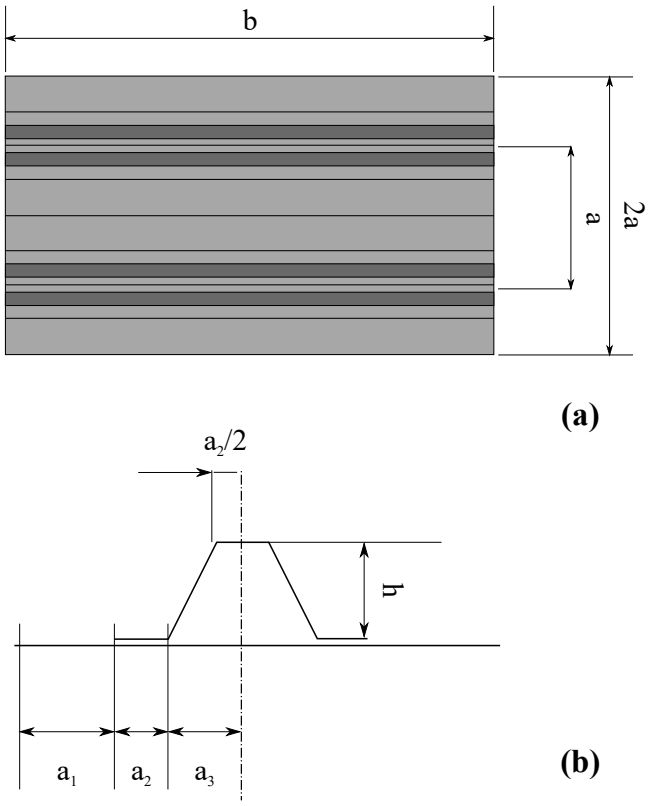

Figure 5.1: (a) Geometry and overall size of the stiffened panel (only two repetitive units for sake of simplicity) and (b) geometric parameters of the repetitive unit.

Technical constants		Polar parameters of $\mathbf{Q}$ [a]		Polar parameters of $\tilde{\mathbf{Q}}$ [b]	
E_1 [MPa]	161000.0	T_0 [MPa]	23793.3868	T [MPa]	5095.4545
E_2 [MPa]	9000.0	T_1 [MPa]	21917.8249	R [MPa]	1004.5454
G_{12} [MPa]	6100.0	R_0 [MPa]	17693.3868	Φ [deg]	90.0
ν_{12}	0.26	R_1 [MPa]	19072.0711		
ν_{23}	0.10	Φ_0 [deg]	0.0		
		Φ_1 [deg]	0.0		
Density and thickness					
ρ [Kg/mm^3]	1.58×10^{-6}				
t_{ply} [mm]	0.125				

[a] In-plane reduced stiffness matrix of the ply.
[b] Out-of-plane shear stiffness matrix of the ply.

Table 5.1: Material properties of the carbon-epoxy ply taken from [56–58].

- No delamination occurs at the interface of the plies (perfect bonding condition).
- No delamination occurs at the interface between stringer bottom flange and skin.

No simplifying hypotheses are made on the geometric and mechanical parameters of the RU (e.g. on the nature of the laminates SSs). The key-point of the MS2LOS is to avoid the use of *a priori* assumptions that extremely shrink the solution space (e.g. the utilisation

of symmetric, balanced stacks to attain membrane/bending uncoupling and membrane orthotropy, respectively) to search the real global optimum for a given problem.

5.4 First-level problem formulation

In this phase, the overall features of the structure at the macroscopic scale have to be optimised. The mass minimisation of the stiffened panel RU will be performed by satisfying the set of optimisation constraints listed below:

1. A constraint on the first buckling load of the RU;
2. Geometric and technological constraints related to the geometrical parameters of the RU;
3. Feasibility constraints on the laminate PPs of both skin and stringer.

These aspects are detailed in the following subsections.

5.4.1 Geometrical design variables

The design variables for the problem at hand are of two types: *geometrical* and *mechanical*. Not all the geometrical parameters are included among the design variables. The overall sizes a and b of the RU are fixed, whilst other geometric parameters can be expressed in terms of the geometric design variables. These last are:

- The laminate thickness for both skin and stringer, i.e. t_S and t_B, respectively;
- The width a_2 of the stringer bottom flange;
- The stringer height h;
- The size a_3.

The size a_1 is computed as:

$$a_1 = \frac{a}{2} - a_2 - a_3 \ , \tag{5.1}$$

while the angle of the inclined wall of the stiffener is

$$\theta = \operatorname{atan}\left(\frac{h}{a_3 - \frac{a_2}{2}}\right) \ . \tag{5.2}$$

The previous design variables must satisfy a set of technological and geometrical requirements. Firstly, the overall thickness of the laminates composing the RU is a *discrete variable*, the discretisation step being equal to the thickness of the elementary layer, i.e. t_{ply} (see Table 5.1):

$$t_\alpha = n_\alpha t_{\text{ply}} \ , \quad \alpha = S, B \ , \tag{5.3}$$

where n_S and n_B are the number of layers for skin and stiffener, respectively. According to the hypotheses on the macroscopic behaviour of the laminate made in Section 5.3, it should be noticed that the thickness of the constitutive lamina of both of skin/stringer laminates is constant. Consequently, by optimising the total thickness of the skin and the stringer during the FLP, one can immediately infer the optimised number of layers for the

skin and stringer to be used during the SLP. Secondly, parameters a_i, $(i = 1, 2, 3)$ have to meet the following conditions:

$$a_1 > 0 \ , \quad a_3 \geq \frac{a_2}{2}. \tag{5.4}$$

The first inequality is used to avoid contact between two consecutive stringers, while the second one is imposed to keep θ non-negative. In the framework of the FLP, it is useful to introduce dimensionless geometric design variables, as follows:

$$c_1 \coloneqq 2\frac{a_2}{a}, \ c_2 \coloneqq 2\frac{a_3}{a_2}, \ c_3 \coloneqq \frac{h}{a_2}. \tag{5.5}$$

The vector of geometrical design variables is defined as:

$$\boldsymbol{\xi}_g^{\mathrm{T}} = \{n_S, n_B, c_1, c_2, c_3\} \ . \tag{5.6}$$

Therefore, inequalities of Eq. (5.4) can be reformulated in terms of dimensionless geometric design variables as:

$$\begin{aligned} g_1\left(\boldsymbol{\xi}_g\right) &= 2c_1 + c_1c_2 - 2 < 0, \\ g_2\left(\boldsymbol{\xi}_g\right) &= 1 - c_2 \leq 0. \end{aligned} \tag{5.7}$$

5.4.2 Mechanical design variables

Consider the laminate normalised stiffness matrices of Eq. (4.24). As discussed in Sections 4.2 and 4.3, in the framework of the polar formalism it is possible to express the Cartesian components of these matrices in terms of their elastic invariants. As shown in Section 4.3, in the FSDT framework [56, 57], for a fully orthotropic, quasi-homogeneous laminate (i.e. a laminate having the same orthotropic behaviour in terms of normalised membrane and bending stiffness matrices and whose membrane/bending coupling stiffness matrix is null) the overall number of independent PPs describing its mechanical response reduces to only three, i.e. the anisotropic moduli $R_{0K}^{A^*} \coloneqq (-1)^{K^{A^*}} R_0^{A^*}$ and $R_1^{A^*}$ and the polar angle $\Phi_1^{A^*}$ (this last representing the orientation of the main orthotropy axis) of matrix $\mathbf{A}^*$. In addition, in the formulation of the FLP, the conditions of Eq. (4.43) must be respected. These constraints ensure that the optimum values of the polar parameters resulting from the first step correspond to a feasible laminate that will be designed during the second step of the MS2LOS. Since the laminate is quasi-homogeneous, the constraints of Eq. (4.43) can be written only for matrix $\mathbf{A}^*$ and they are rearranged as following:

$$\begin{cases} -R_0 \leq R_{0K}^{A^*} \leq R_0 \ , \\ 0 \leq R_1^{A^*} \leq R_1 \ , \\ 2\left(\dfrac{R_1^{A^*}}{R_1}\right)^2 - 1 - \dfrac{R_{0K}^{A^*}}{R_0} \leq 0 \ . \end{cases} \tag{5.8}$$

In Eq. (5.8), R_0 and R_1 are the anisotropic moduli of the ply reduced stiffness matrix [56]. As in the case of geometric design variables, it is very useful to introduce the following dimensionless PPs:

$$\rho_0 = \frac{R_{0K}^{A^*}}{R_0}, \ \rho_1 = \frac{R_1^{A^*}}{R_1} \ . \tag{5.9}$$

Therefore, Eq. (5.8) reads:

$$\begin{cases} -1 \leq \rho_0 \leq 1 \ , \\ 0 \leq \rho_1 \leq 1 \ , \\ 2\left(\rho_1\right)^2 - 1 - \rho_0 \leq 0 \ . \end{cases} \tag{5.10}$$

The mechanical design variables must be considered for each laminate constituting the panel RU, i.e. for both skin and stiffener laminates ($\rho_{0\alpha}$ and $\rho_{1\alpha}$ with $\alpha = S, B$). Moreover, the main orthotropy direction of the generic laminate can be set equal to zero, i.e. $\Phi_1^{A^*} = 0$ for skin and stringer, which means that the main orthotropy axis is aligned with the direction of the applied load. Therefore, the dimensionless mechanical parameters defined above can be grouped into the vector of mechanical design variables:

$$\boldsymbol{\xi}_m^{\mathrm{T}} = \{\rho_{0S}, \rho_{1S}, \rho_{0B}, \rho_{1B}\} \ . \tag{5.11}$$

First and second constraints of Eq. (5.10) can be taken into account as admissible intervals for the relevant optimisation variables, i.e. on ρ_0 and ρ_1. Hence, the resulting feasibility constraints on the skin and stringer dimensionless PPs become:

$$\begin{aligned} g_3(\boldsymbol{\xi}_m) &= 2\left(\rho_{1S}\right)^2 - 1 - \rho_{0S} \leq 0 \ , \\ g_4(\boldsymbol{\xi}_m) &= 2\left(\rho_{1B}\right)^2 - 1 - \rho_{0B} \leq 0 \ . \end{aligned} \tag{5.12}$$

For a wide discussion upon the laminate feasibility and geometrical bounds as well as on the importance of the quasi-homogeneity assumption the reader is addressed to [52].

5.4.3 Mathematical statement of the problem

The aim of the FLP is the minimisation of the mass of the RU of the stiffened panel by satisfying, simultaneously, constraints of different nature. Geometrical and mechanical design variables can be collected into the following vector:

$$\boldsymbol{\xi}^T = \{\boldsymbol{\xi}_{\boldsymbol{g}}^T, \boldsymbol{\xi}_{\boldsymbol{m}}^T\} \ . \tag{5.13}$$

In this context, the FLP can be formulated as a classical CNLPP:

$$\begin{aligned} &\min_{\boldsymbol{\xi}} \ \frac{M\left(\boldsymbol{\xi}\right)}{M_{\mathrm{ref}}}, \\ &\text{subject to:} \\ &\begin{cases} 1.05 - \dfrac{\lambda\left(\boldsymbol{\xi}\right)}{\lambda_{\mathrm{ref}}} \leq 0 \ , \\ g_i(\boldsymbol{\xi}) \leq 0 \ , \text{ with } i = 1, \cdots, 4 \ . \end{cases} \end{aligned} \tag{5.14}$$

The design space of the FLP, together with the type of each design variable, is detailed in Table 5.2. In Eq. (5.14), M is the overall mass of the RU, λ is the first buckling load of the stiffened panel, while M_{ref} and λ_{ref} are the counterparts for a *reference solution*, which is subject to the same BCs as those applied on the RU of the panel that will be optimised. The properties of the reference configuration of the RU are reported in Table 5.3.

5.4.4 Numerical strategy

Problem (5.14) is a non-convex CNLPP. This is due to the nature of the buckling function, which is non-convex, and to the non-linear feasibility constraints on the laminate PPs. The total number of design variables is nine while that of optimisation constraints is five (see Eq. (5.14)). Furthermore, the nature of design variables is different (see Table 5.2): integer (n_S and n_B), discrete (c_1, c_2, c_3) and continuous (ρ_{0S}, ρ_{1S}, ρ_{0B}, ρ_{1B}) variables are involved in the definition of this CNLPP.

Design variable	Type	Lower bound	Upper bound	Discretisation step
ρ_{0S}	continuous	-1.0	1.0	-
ρ_{1S}	continuous	0	1.0	-
ρ_{0B}	continuous	-1.0	1.0	-
ρ_{1B}	continuous	0	1.0	-
c_1	discrete	0.01	0.45	0.001
c_2	discrete	1.00	3.00	0.01
c_3	discrete	1.00	3.00	0.01
n_S	integer	20	32	1
n_B	integer	20	32	1

Table 5.2: Design space of the first-level problem.

For the resolution of problem (5.14) the GA ERASMUS [5, 154, 155] coupled with the FE model of the panel RU (for assessing the first buckling load of the structure) has been utilised as optimisation tool to carry out the solution search, see Fig. 5.2. The GA ERASMUS has been already successfully applied to solve different kinds of real-world engineering problems, see for example [7, 8, 39, 55, 63–67, 121, 122, 156, 156–164]. As shown in Fig. 5.2, for each individual at each generation, the numerical tool performs a FE analysis for calculating the first buckling load (eigenvalue problem) of the stiffened panel as well as its weight. The inputs of the FE model of the RU (implemented in ANSYS® APDL environment) are both geometrical and mechanical parameters (generated by ERASMUS). The GA elaborates the results provided by the FE model in order to execute the genetic operations. These operations are repeated until the GA meets the user-defined convergence criterion.

The generic individual of the GA ERASMUS represents a potential solution for the problem at hand. The genotype of the individual for problem (5.14) is characterised by only one chromosome composed of nine genes, each one coding a component of the vector of design variables, see Eq. (5.13).

5.5 Second-level problem formulation

The second-level problem is devoted to the lay-up design of the both skin and stringer laminates. The goal is to determine at least one SS satisfying the optimum values of both geometric and PPs resulting from the first level of the strategy and having the elastic symmetries imposed to the laminate within the formulation of the FLP, i.e. quasi-homogeneity and orthotropy. In the framework of the FSDT, this problem can be stated in the form of an unconstrained minimisation problem [56, 57]:

$$\min_{\boldsymbol{\delta}} \quad I\left(f_i\left(\boldsymbol{\delta}\right)\right), \tag{5.15}$$

with

$$I\left(f_i\left(\boldsymbol{\delta}\right)\right) = \sum_{i=1}^{6} f_i\left(\boldsymbol{\delta}\right) \ . \tag{5.16}$$

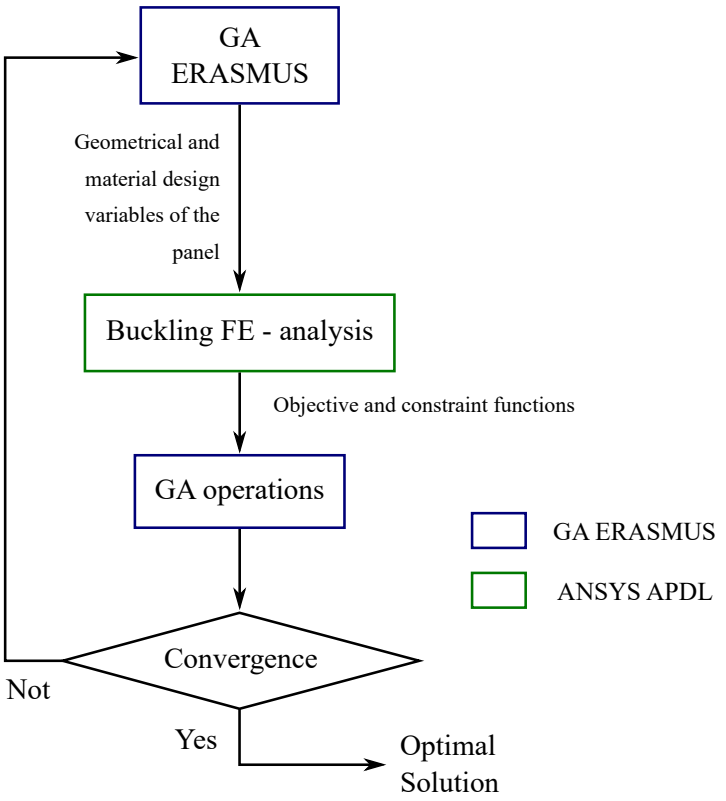

Figure 5.2: Logical flow of the numerical procedure for the solution search of the first-level problem.

where $\boldsymbol{\delta} \in \mathbb{R}^n$ is the vector of the layer orientations, i.e. the design variables of this phase, while $f_i(\boldsymbol{\delta})$ are quadratic functions in the space of PPs, each one representing a requirement to be satisfied, such as orthotropy, uncoupling, etc. For the problem at hand the partial objective functions read:

$$f_1(\boldsymbol{\delta}) = \left(\frac{|\Phi_0^{A^*}(\boldsymbol{\delta}) - \Phi_1^{A^*}(\boldsymbol{\delta})|}{\pi/4} - K^{A^*(opt)} \right)^2 , \quad f_2(\boldsymbol{\delta}) = \left(\frac{R_0^{A^*}(\boldsymbol{\delta}) - R_0^{A^*(opt)}}{R_0} \right)^2 ,$$
$$f_3(\boldsymbol{\delta}) = \left(\frac{R_1^{A^*}(\boldsymbol{\delta}) - R_1^{A^*(opt)}}{R_1} \right)^2 , \quad f_4(\boldsymbol{\delta}) = \left(\frac{|\Phi_1^{A^*}(\boldsymbol{\delta}) - \Phi_1^{A^*(opt)}|}{\pi/4} \right)^2 , \quad f_5(\boldsymbol{\delta}) = \left(\frac{||\mathbf{C}(\boldsymbol{\delta})||}{||\mathbf{Q}||} \right)^2 ,$$
$$f_6(\boldsymbol{\delta}) = \left(\frac{||\mathbf{B}^*(\boldsymbol{\delta})||}{||\mathbf{Q}||} \right)^2 , \tag{5.17}$$

where $f_1(\boldsymbol{\delta})$ represents the elastic requirement on the orthotropy of the laminate having the prescribed shape (imposed by the value of K^{A^*} provided by the FLP), $f_2(\boldsymbol{\delta})$, $f_3(\boldsymbol{\delta})$ and $f_4(\boldsymbol{\delta})$ are the requirements related to the prescribed values of the optimal PPs resulting from the FLP, while $f_5(\boldsymbol{\delta})$ and $f_6(\boldsymbol{\delta})$ are linked to the quasi-homogeneity condition.

$I(f_i(\boldsymbol{\delta}))$ is a positive semi-definite convex function in the space of the laminate PPs, since it is defined as a sum of convex functions, see Eqs. (5.16)-(5.17). Nevertheless, such a function is highly non-convex in the space of plies orientations because the laminate PPs depend upon circular functions of the layers orientation angles. Moreover, the absolute minima of $I(f_i(\boldsymbol{\delta}))$ are known *a priori* since they are the zeroes of this function. For more

details about the nature of the SLP see [56, 57]. It is noteworthy that problem (5.15) must be solved two times, i.e. for each laminate composing the skin and the stiffener. In order to simplify the problem of retrieving an optimum stack, the search space for problem (5.15) has been restricted to the class of QT SSs, already discussed in Chapter 4. In this background, the functions $f_5(\boldsymbol{\delta})$ and $f_6(\boldsymbol{\delta})$ in Eq. (5.17) are identically null for QT stacks. Suppose now to fix both the number of plies and that saturated groups, namely n and n_g. As discussed in [36], the problem of determining QT stacks for a given couple of n and n_g can give rise to a huge number of solutions: the number of QT stacks rapidly increases along with n. To this purpose a database of QT stacks has been built for different combinations of n and n_g [37].

For the problem at hand, and for each considered case (i.e. skin and stringer laminates), the optimum number of plies $n_\alpha, (\alpha = S, B)$ constitutes a result of the FLP, while the number of saturated groups n_g has been fixed *a priori*. Let be n_{sol} the number of QT stacks for a particular combination of n_α and n_g. Each solution collected within the database is uniquely defined by means of an identifier ID_{sol} (i.e. an integer) that varies in the range $[1, n_{sol}]$. Therefore, ID_{sol} represents a further design variable along with the n_g orientation angles of the different saturated groups, i.e. $\boldsymbol{\theta} \in \mathbb{R}^{n_g}$. The design variables can be thus collected into the following vector,

$$\boldsymbol{\eta}^T = \left\{\mathrm{ID}_{sol}, \theta_1, ..., \theta_{n_g}\right\}, \tag{5.18}$$

and problem (5.15) can be reformulated as

$$\min_{\boldsymbol{\eta}} \sum_{i=1}^{4} f_i(\boldsymbol{\eta}) \ , \tag{5.19}$$

$f_5(\boldsymbol{\eta})$ and $f_6(\boldsymbol{\eta})$ being identically null. In this background, the solution search for problem (5.19) is performed by means of the GA ERASMUS. In the case of QT stacks the structure of the individual genotype is simple because it is composed of a single chromosome with $n_g + 1$ genes: the first one codes the variable ID_{sol} whilst the remaining genes code the orientation angles of every saturated group which are discrete variables in the range [-89°, 90°] with a step length equal to 1°.

5.6 Finite element models of the stiffened panel

In this section two FE models of the stiffened panel RU are presented: the first one is used in the framework of the FLP of the MS2LOS approach while the second one is only for verification purposes and is realised in the framework of CUF .

5.6.1 The finite element model for the optimisation procedure

The FE model of the panel RU used at the first-level of the MS2L strategy is built using the FE commercial code ANSYS® APDL. This model has the purpose to compute the first-buckling factor constraint by solving an eigenvalue buckling analysis for each individual, i.e. for each point in the design space, at the current generation. In so doing, the FE model is properly parametrised; in fact, it takes into account a variable geometry, material and mesh. An *ad-hoc* input file for the FE code is created for each individual that is interfaced with the GA-ERASMUS.

The FE model of the RU is illustrated in Fig. 5.3. The model has been built by using a combination of eight-nodes shell elements (ANSYS SHELL281 elements) and non-linear

multi-point constraints elements (ANSYS MPC184 elements) both with six Degrees Of Freedom (DOFs) per node.

As far as concerns SHELL281 elements, their mechanical behaviour is described by defining directly the homogenised stiffness matrices $\mathbf{A}^*$, $\mathbf{B}^*$, $\mathbf{D}^*$ and $\mathbf{H}^*$ (in this example the basic form of Eq. (4.21) has been used for matrix $\mathbf{H}^*$).

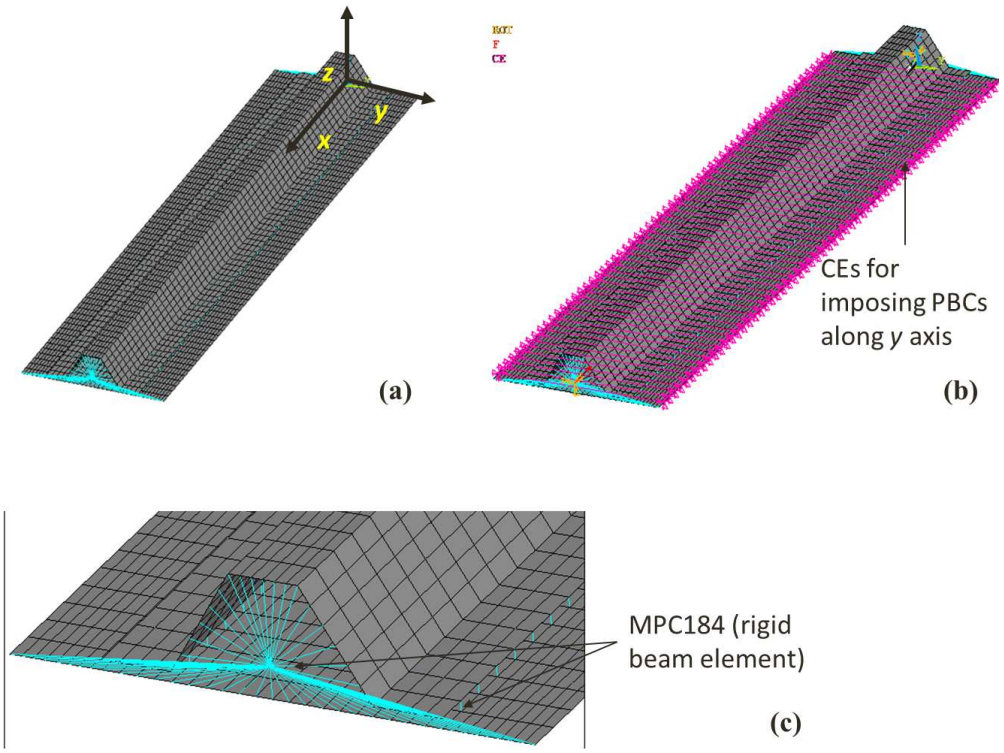

Figure 5.3: (a) FE model of the repetitive unit and related reference frame, (b) details of CEs for PBCs along y-axis and (c) details of MPC184 elements.

The compatibility of the displacement field between skin and stringer is achieved through ANSYS MPC184 elements whose formulation is based upon a classical multi-point constraint element scheme [165]. MPC184 elements are defined between each couple of nodes belonging to contiguous shell elements as depicted in Fig. 5.3. In particular, MPC184 elements are defined between nodes of the middle plane of the skin (master nodes) and those of the middle plane of the bottom flanges of the stringer (slave nodes).

Furthermore, MPC184 elements have been used to rigidify the end transverse sections of the RU, in order to simulate the presence of ribs (these last having an in-plane stiffness one/two order of magnitude higher than the flexural stiffness of the RU). In particular, two *pilot nodes* A$=\{0,0,\hat{z}\}$ and B$=\{b,0,\hat{z}\}$ have been defined according to the RU global frame depicted in Fig. (5.3 ($\hat{z}$ is the z component of the barycentre of lines belonging to a given transverse section). Then, nodes A and B have been connected (through MPC184 elements) to those located on lines of the corresponding transverse section, i.e., lines belonging to the planes $x=0$ and $x=b$, respectively (see Fig. (5.3). The BCS for nodes A and B are

$$\begin{aligned} &\text{node A:} \qquad u_i = 0,\ \beta_i = 0; \\ &\text{node B:} \qquad F_x = 1\text{N},\ u_y = u_z = 0,\ \beta_i = 0, \\ &(i = x, y, z). \end{aligned} \tag{5.20}$$

In Eq. (5.20) u_i and β_i are nodal displacements and rotations, respectively, whilst F_x is the x component of the nodal force.

It is noteworthy that in problem (5.14) the first-buckling load of the stiffened panel is assessed by considering pertinent BCs on its RU. This fact implicitly implies the hypothesis of a panel having an "infinite" length along y-axis, according to the frame depicted in Fig. (5.3. To take into account for this aspect, periodic boundary conditions (PBCs) must be considered:

$$\begin{aligned} &u_i\left(x, -\frac{a}{2}, 0\right) - u_i\left(x, \frac{a}{2}, 0\right) = 0,\ \forall x \in]0, b[\,, \\ &\beta_i\left(x, -\frac{a}{2}, 0\right) - \beta_i\left(x, \frac{a}{2}, 0\right) = 0,\ \forall x \in]0, b[\,, \\ &(i = x, y, z). \end{aligned} \tag{5.21}$$

PBCs of Eq. (5.21) must be defined for each couple of nodes belonging to the skin lateral edges (i.e. lines located at $y = \pm a/2$) except those placed on the lines at $x = 0$ and $x = b$, these last being already connected to the pilot nodes A and B, respectively. PBCs are defined through ANSYS constraint equations (CEs) [165] between homologous nodes of the skin lateral edges

Finally, before starting the optimisation process, a sensitivity study (not reported here for the sake of brevity) on the proposed FE model with respect to the mesh size has been conducted: it was observed that a mesh having 56959 DOFs is sufficient to properly evaluate the first buckling load of the stiffened panel.

5.6.2 The enhanced finite element model for the verification phase

A higher-order model is realised for the verification of the results given by ERASMUS / ANSYS. This model makes use of refined beam elements in the CUF framework, as already discussed in Section 3.2. The primary purpose of the higher-order beam model is to verify the effectiveness of the optimised solutions in terms of buckling loads with respect to the reference solution. In this phase, the CUF model is not interfaced with the MS2LOS, and it does not influence the optimisation of the panel RU. CUF analyses are done a posteriori when the stacks of the tested skin/stiffener configurations are available. The integration of the CUF framework within the MS2LOS is the object of Chapter 7 where the CUF will play an essential role in the optimisation of a simplified wing-box structure. The linearised buckling formulation in terms of CUF is based on the computation of the tangent stiffness matrix $\mathbf{K_T}$.

The FN of matrix ${\mathbf{K_T}}^{ij\tau s}$ is derived from the linearisation of the equilibrium equations that are obtained with the Newton-Raphson method, also known as *Tangent Method*, see [166]. Assuming a conservative load case, the linearisation of the tangent stiffness matrix is obtained from the linearisation of the virtual variation of the non-linear internal energy $\delta(\delta L_{int})$. Consider the stress stress vector $\boldsymbol{\sigma}$ and the strain vector $\boldsymbol{\varepsilon}$, the $\delta(\delta L_{int})$ reads:

$$\delta(\delta L_{int}) =< \delta(\delta\boldsymbol{\varepsilon}^{\mathrm{T}})\boldsymbol{\sigma} > \approx < \delta\boldsymbol{\varepsilon}^{\mathrm{T}}\boldsymbol{\sigma} > + < \delta(\delta\boldsymbol{\varepsilon}^{\mathrm{T}})\boldsymbol{\sigma} >, \tag{5.22}$$

where $< (\cdot) >= \int_V (\cdot)\, dV$. Under the hypothesis of small deformations, $V = \Omega \times L$ is the initial volume of the beam structure. In Eq. (5.22), $\boldsymbol{\varepsilon}$ contains the *Green-Lagrange* non linear strains which are characterised by the quadratic derivatives of displacements. This strain vector can be written highlighting the linear and non linear contributions as follow:

$$\boldsymbol{\varepsilon} = \boldsymbol{\varepsilon}_l + \boldsymbol{\varepsilon}_{nl} \Longrightarrow \boldsymbol{\varepsilon} = (\mathbf{b}_l + \mathbf{b}_{nl})\mathbf{u}, \tag{5.23}$$

with $\boldsymbol{\varepsilon} = \{\varepsilon_x, \varepsilon_y, \varepsilon_z, \varepsilon_r, \varepsilon_q, \varepsilon_s\}^{\mathrm{T}}$ and $\mathbf{u} = \{u_x, u_y, u_z\}^{\mathrm{T}}$. The terms $\mathbf{b}_l$ and $\mathbf{b}_{nl}$ are linear and non linear differential matrix operators respectively which stand as:

$$\mathbf{b}_l = \begin{Bmatrix} \frac{\partial(\cdot)}{\partial x} & 0 & 0 \\ 0 & \frac{\partial(\cdot)}{\partial y} & 0 \\ 0 & 0 & \frac{\partial(\cdot)}{\partial z} \\ \frac{\partial(\cdot)}{\partial z} & 0 & \frac{\partial(\cdot)}{\partial x} \\ 0 & \frac{\partial(\cdot)}{\partial z} & \frac{\partial(\cdot)}{\partial y} \\ \frac{\partial(\cdot)}{\partial y} & \frac{\partial(\cdot)}{\partial x} & 0 \end{Bmatrix},$$

$$\mathbf{b}_{nl} = \begin{Bmatrix} \frac{1}{2}\left(\frac{\partial(\cdot)}{\partial x}\right)^2 & \frac{1}{2}\left(\frac{\partial(\cdot)}{\partial x}\right)^2 & \frac{1}{2}\left(\frac{\partial(\cdot)}{\partial x}\right)^2 \\ \frac{1}{2}\left(\frac{\partial(\cdot)}{\partial y}\right)^2 & \frac{1}{2}\left(\frac{\partial(\cdot)}{\partial y}\right)^2 & \frac{1}{2}\left(\frac{\partial(\cdot)}{\partial y}\right)^2 \\ \frac{1}{2}\left(\frac{\partial(\cdot)}{\partial z}\right)^2 & \frac{1}{2}\left(\frac{\partial(\cdot)}{\partial z}\right)^2 & \frac{1}{2}\left(\frac{\partial(\cdot)}{\partial z}\right)^2 \\ \frac{\partial(\cdot)}{\partial x}\frac{\partial(\cdot)}{\partial z} & \frac{\partial(\cdot)}{\partial x}\frac{\partial(\cdot)}{\partial z} & \frac{\partial(\cdot)}{\partial x}\frac{\partial(\cdot)}{\partial z} \\ \frac{\partial(\cdot)}{\partial y}\frac{\partial(\cdot)}{\partial z} & \frac{\partial(\cdot)}{\partial y}\frac{\partial(\cdot)}{\partial z} & \frac{\partial(\cdot)}{\partial y}\frac{\partial(\cdot)}{\partial z} \\ \frac{\partial(\cdot)}{\partial x}\frac{\partial(\cdot)}{\partial y} & \frac{\partial(\cdot)}{\partial x}\frac{\partial(\cdot)}{\partial y} & \frac{\partial(\cdot)}{\partial x}\frac{\partial(\cdot)}{\partial y} \end{Bmatrix}.$$

The approximation in the Eq. (5.22) comes from the consideration that the stress field is linear. The first term of the Eq. (5.22) can be written as:

$$< \delta\boldsymbol{\epsilon}^T \boldsymbol{\sigma} >= \delta\mathbf{u}_{\tau i}^T \mathbf{K}^{ij\tau s} \mathbf{u}_{sj} \tag{5.24}$$

where the $\mathbf{K}^{ij\tau s}$ is the FN of the stiffness matrix already discussed in the Section 3.2.1. The second term of the Eq. (5.22) $< \delta(\delta\boldsymbol{\epsilon}^T)\boldsymbol{\sigma} >$ needs the linearisation of the non-linear geometrical relations. According to Crisfield [167] and using Eq. (5.23) the term $\delta(\delta\epsilon)$

reads:

$$\delta(\delta\boldsymbol{\epsilon}) = \left\{ \begin{array}{c} (\delta u_{x_{,x}})_v \delta u_{x_{,x}} + (\delta u_{y_{,x}})_v \delta u_{y_{,x}} + (\delta u_{z_{,x}})_v \delta u_{z_{,x}} \\ \\ (\delta u_{x_{,y}})_v \delta u_{x_{,y}} + (\delta u_{y_{,y}})_v \delta u_{y_{,y}} + (\delta u_{z_{,y}})_v \delta u_{z_{,y}} \\ \\ (\delta u_{x_{,z}})_v \delta u_{x_{,z}} + (\delta u_{y_{,z}})_v \delta u_{y_{,z}} + (\delta u_{z_{,z}})_v \delta u_{z_{,z}} \\ \\ [(\delta u_{x_{,x}})_v \delta u_{x_{,z}} + \delta u_{x_{,x}} (\delta u_{y_{,z}})_v] + [(\delta u_{y_{,x}})_v \delta u_{y_{,z}} + \delta u_{y_{,x}} (\delta u_{y_{,z}})_v] + \\ + [(\delta u_{z_{,x}})_v \delta u_{z_{,z}} + \delta u_{z_{,x}} (\delta u_{z_{,z}})_v] \\ \\ [(\delta u_{x_{,y}})_v \delta u_{x_{,z}} + \delta u_{x_{,y}} (\delta u_{x_{,z}})_v] + [(\delta u_{y_{,y}})_v \delta u_{y_{,z}} + \delta u_{y_{,y}} (\delta u_{y_{,z}})_v] + \\ + [(\delta u_{z_{,y}})_v \delta u_{z_{,z}} + \delta u_{z_{,y}} (\delta u_{z_{,z}})_v] \\ \\ [(\delta u_{x_{,x}})_v \delta u_{x_{,y}} + \delta u_{x_{,x}} (\delta u_{x_{,y}})_v] + [(\delta u_{y_{,x}})_v \delta u_{y_{,y}} + \delta u_{y_{,x}} (\delta u_{y_{,y}})_v] + \\ + [(\delta u_{z_{,x}})_v \delta u_{z_{,y}} + \delta u_{z_{,x}} (\delta u_{z_{,y}})_v] \end{array} \right\},$$

where the subscript 'v' denotes the variations.
Using CUF and the FE approximation, the linearised variable δu and the variations $(\delta u)_v$ can be written as:

$$\begin{aligned} \delta\mathbf{u} &= F_s \mathbf{N}_j \delta\mathbf{u}_{sj}, \\ (\delta\mathbf{u})_v &= F_\tau \mathbf{N}_i \delta\mathbf{u}_{\tau i}, \end{aligned} \tag{5.25}$$

and, in this way, it is easy to verify that $\delta(\delta\boldsymbol{\epsilon})$ reads:

$$\delta(\delta\boldsymbol{\epsilon}) = \mathbf{B}^*_{nl} \left\{ \begin{array}{c} \delta u_{x_{\tau i}} \delta u_{x_{sj}} \\ \delta u_{y_{\tau i}} \delta u_{y_{sj}} \\ \delta u_{z_{\tau i}} \delta u_{z_{sj}} \end{array} \right\}, \tag{5.26}$$

or

$$\delta(\delta\boldsymbol{\epsilon}^T) = \left\{ \begin{array}{c} \delta u_{x_{\tau i}} \delta u_{x_{sj}} \\ \delta u_{y_{\tau i}} \delta u_{y_{sj}} \\ \delta u_{z_{\tau i}} \delta u_{z_{sj}} \end{array} \right\}^T (\mathbf{B}^*_{nl})^T, \tag{5.27}$$

where:

$$\mathbf{B}^*_{nl} = \begin{bmatrix} F_{\tau,x} F_{s,x} N_i N_j & F_{\tau,x} F_{s,x} N_i N_j & F_{\tau,x} F_{s,x} N_i N_j \\ F_\tau F_s N_{i,y} N_{j,y} & F_\tau F_s N_{i,y} N_{j,y} & F_\tau F_s N_{i,y} N_{j,y} \\ F_{\tau,z} F_{s,z} N_i N_j & F_{\tau,z} F_{s,z} N_i N_j & F_{\tau,z} F_{s,z} N_i N_j \\ F_{\tau,x} F_{s,z} N_i N_j + F_{\tau,z} F_{s,x} N_i N_j & F_{\tau,x} F_{s,z} N_i N_j + F_{\tau,z} F_{s,x} N_i N_j & F_{\tau,x} F_{s,z} N_i N_j + F_{\tau,z} F_{s,x} N_i N_j \\ F_{\tau,z} F_s N_i N_{j,y} + F_\tau F_{s,x} N_{i,y} N_j & F_{\tau,z} F_s N_i N_{j,y} + F_\tau F_{s,x} N_{i,y} N_j & F_{\tau,z} F_s N_i N_{j,y} + F_\tau F_{s,x} N_{i,y} N_j \\ F_{\tau,x} F_s N_i N_{j,y} + F_\tau F_{s,x} N_{i,y} N_j & F_{\tau,x} F_s N_i N_{j,y} + F_\tau F_{s,x} N_{i,y} N_j & F_{\tau,x} F_s N_i N_{j,y} + F_\tau F_{s,x} N_{i,y} N_j \end{bmatrix}.$$

Therefore, the term $< \delta(\delta\boldsymbol{\epsilon}^T)\boldsymbol{\sigma} >$ can be written as:

$$\begin{aligned} < \delta(\delta\boldsymbol{\epsilon}^T)\boldsymbol{\sigma} > =< \left\{ \begin{array}{c} \delta u_{x_{\tau i}} \delta u_{x_{sj}} \\ \delta u_{y_{\tau i}} \delta u_{y_{sj}} \\ \delta u_{z_{\tau i}} \delta u_{z_{sj}} \end{array} \right\}^T > (\mathbf{B}^*_{nl})^T \sigma = \delta\mathbf{u}^T_{\tau i} < \mathrm{diag}((\mathbf{B}^*_{nl})^T \sigma) > \delta\mathbf{u}_{sj} = \\ = \delta\mathbf{u}^T_{\tau i} (\mathbf{K}^{ij\tau s}_{\sigma_l} + \mathbf{K}^{ij\tau s}_{\sigma_{nl}}) \delta\mathbf{u}_{sj} = \delta\mathbf{u}^T_{\tau i} \mathbf{K}^{ij\tau s}_{\sigma} \delta\mathbf{u}_{sj} \end{aligned} \tag{5.28}$$

where the matrix $\mathbf{K}^{ij\tau s}_{\sigma}$ is the FN of the often called "Geometric Stiffness Matrix". Eq. (5.22) is now written to highlight the contributions of the $\mathbf{K}^{ij\tau s}$ and $\mathbf{K}^{ij\tau s}_{\sigma}$. The tangent stiffness FN is the summation of the previous FN contributions, i.e.

$$\delta(\delta L_{int}) =< \delta(\delta\boldsymbol{\epsilon}^T \boldsymbol{\sigma}) >= \delta\mathbf{u}^T_{\tau i} (\mathbf{K}^{ij\tau s}_0 + \mathbf{K}^{ij\tau s}_{\sigma}) \delta\mathbf{u}_{sj} = \delta\mathbf{u}^T_{\tau i} \mathbf{K}^{ij\tau s}_T \delta\mathbf{u}_{sj}. \tag{5.29}$$

To solve the linear buckling problem, the linear part of the FN of the geometrical stiffness matrix is considered. In other words, the non linear strains are not taken into account in the calculation of $K_\sigma^{ij\tau s}$

$$\mathbf{K}_\sigma^{ij\tau s} \approx \mathbf{K}_{\sigma_l}^{ij\tau s} \tag{5.30}$$

$\mathbf{K}_\sigma^{ij\tau s}$ is a diagonal matrix and its expression is given in the following for the sake of completeness:

$$\begin{aligned}\mathbf{K}_\sigma^{ij\tau s} = \Big(&< \sigma_{xx}^0 F_{\tau,x} F_{s,x} N_i N_j > + < \sigma_{zz}^0 F_{\tau,z} F_{s,z} N_i N_j > + < \sigma_{xy}^0 F_{\tau,x} F_s N_i N_{j,y} > + \\ &+ < \sigma_{xy}^0 F_\tau F_{s,x} N_{i,y} N_j > + < \sigma_{xz}^0 F_{\tau,x} F_{s,z} N_i N_j > + < \sigma_{xz}^0 F_{\tau,z} F_{s,x} N_i N_j > + \\ &+ < \sigma_{yz}^0 F_{\tau,z} F_s N_i N_{j,y} > + < \sigma_{yz}^0 F_\tau F_{s,z} N_{i,y} N_j > \Big) \mathbf{I},\end{aligned} \tag{5.31}$$

where $\mathbf{I}$ is the 3×3 identity matrix and $\boldsymbol{\sigma}^0$ is the initial stress state.
As for the elemental linear stiffness matrix and given the cross-sectional functions F_τ and the 1D shape functions N_i, the FN of the geometric stiffness matrix can be expanded in an automatic way by employing CUF to give the elemental matrix for any desired beam theory. Finally, once the global matrices are assembled in the classical way of FEM, the buckling problem can be solved.
The buckling problem is an eigenvalue problem and the resolution of this problem consists in finding the eigenvalues of the following equation:

$$|\mathbf{K} + \lambda_k \mathbf{K}_\sigma| = 0. \tag{5.32}$$

The $k-th$ critical load vector $\mathbf{F}_{cr_k}$ is obtained as the product of λ_k and the initial load vector $\mathbf{F}$:

$$\mathbf{F}_{cr_k} = \lambda_k \mathbf{F}. \tag{5.33}$$

The most important advantage of using higher-order beam models in the framework of CUF is that the computation of $\mathbf{K}_\sigma$ is made by using the whole initial stress field of the structure without simplified hypothesis. Consequently, the estimation of the critical loads is more accurate then that obtained by commercial FE codes wherein standard laminate theories, like CLT, FSDT, etc., are used.

5.7 Numerical results

Before starting the multi-scale optimisation process a reference structure must be defined in order to establish reference values for the RU mass and for the first buckling load of the stiffened panel: both material and geometrical properties of the reference solution are reported in Tables 5.1 and 5.3, respectively.

The reference solution is subject to the same set of BCs, i.e. Eqs. (5.20) and (5.21), as those applied on the RU of the panel that will be optimised. One can notice that the reference structure has a laminated skin composed of a symmetric, balanced SS made of 28 layers (therefore the resulting laminate is uncoupled and orthotropic in membrane, but not in bending), whilst the stringer laminate is made of 32 plies with a symmetric quasi-isotropic stack (the laminate is uncoupled and the membrane stiffness matrix is isotropic, but the bending one is totally anisotropic). This reference solution corresponds to a classical configuration used in the aeronautical field: its mass and its stiffness properties (in

a [mm]	150.00	
b [mm]	600.00	
a_2 [mm]	15.00	
a_3 [mm]	21.50	
h [mm]	30.00	
M_{ref} [Kg]	0.92	
λ_{ref}[N]	451107.00	
Stacking sequence	Part	N. of plies
$[(45/-45/90_2)_2/(45/-45)_3]_s$	skin (S)	28
$[45_2/0_2/-45_2/90_4/-45_2/0_2/45_2]_s$	stringer (B)	32

Table 5.3: Reference solution for the stiffened panel design problem.

terms of buckling load) still represent a "good" compromise between weight and stiffness requirements.

Regarding the setting of the genetic parameters for the GA ERASMUS utilised to perform the solution search for both first and second-level problems they are listed in Table 5.4. Moreover, concerning the constraint-handling technique for the FLP the Au-

Genetic parameters		
	1^{st} level problem	2^{nd} level problem
N. of populations	1	1
N. of individuals	200	500
N. of generations	150	500
Crossover probability	0.85	0.85
Mutation probability	0.005	0.002
Selection operator	roulette-wheel	roulette-wheel
Elitism operator	active	active

Table 5.4: Genetic parameters of the GA ERASMUS for first and second-level problems.

tomatic Dynamic Penalisation (ADP) method has been considered, see [154]. For more details on the numerical techniques developed within the new version of ERASMUS and the meaning of the values of the different parameters tuning the algorithm the reader is addressed to [5].

5.7.1 Optimum configurations of the panel

The optimum values of both geometric and mechanical design variables (dimensionless variables) resulting from the FLP are listed in Table 5.5.

When comparing the optimum solution of the FLP with the reference configuration, one can notice the number of plies reduces from 28 to 20 for the skin laminate and from 32 to 28 for the stringer one. Moreover, both laminates are quasi-homogeneous and fully orthotropic (both membrane and bending stiffness matrices) with an ordinary orthotropy shape (parameter $K^{A^*} = 0$ because the anisotropic polar modulus R_{0K}^{A*} is positive for both cases, see [58]). However, the skin laminate gets a lower value of the modulus R_1^{A*} (an order of magnitude lower than the corresponding value of R_{0K}^{A*}) which means that this solutions tends to exhibit a *square symmetric* behaviour (for both membrane and bending

Geometric parameters				
a_2 [mm]	a_3 [mm]	h [mm]	n_S	n_B
21.300	29.607	31.950	20	28
Polar parameters				
			R_{0K}^{A*} [MPa]	R_1^{A*} [MPa]
Skin (S)			3511.00	242.36
Stringer (B)			9391.51	12080.84

Table 5.5: Numerical results of the first-level problem.

stiffness matrices), as illustrated in the polar diagrams of Fig. (5.4). For a deeper insight on these aspects the interested reader is addressed to [56, 58].

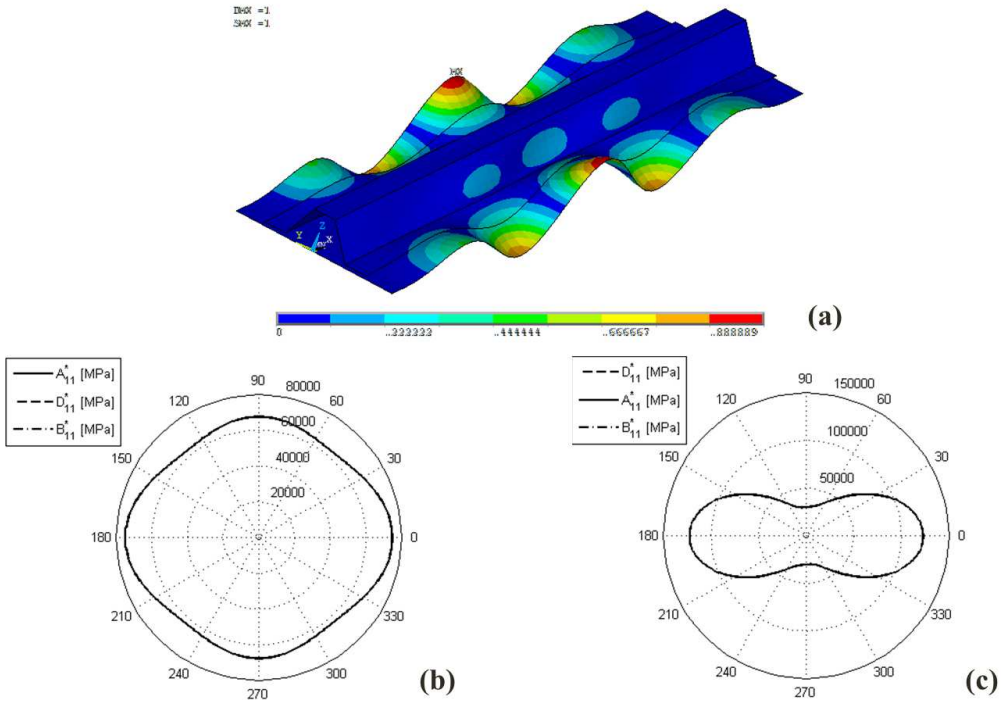

Figure 5.4: Numerical properties of the optimum panel S1-B1. (a) Deformed shape of the first buckling mode (normalized displacement) and polar diagram of the first component of the homogenized laminate in-plane stiffness matrices [MPa] for (b) skin and (c) stringer.

Table 5.6 reports the first two best stacking sequences, for both skin and stringer, which represents just as many solutions for problem (5.19).

As stated in Subsection 5.5 the SLP is solved in the space of QT stacks. In this background, after fixing the number of plies n and the number of saturated groups n_g the design variables are the identifier of the QT solution (to be searched within a database) as well as the orientation angle of each saturated group, see Eq. (5.18). Because problem (5.19) is highly non-convex in the space of the orientation angles of saturated groups, it is possible to find several solutions (theoretically an infinite number) meeting the optimum

ID	Best stacking sequence	N. of plies
	Skin (S)	
S1	$[-63/0/63/0/63/-63/0/0/63/-63/63/-63/0/0/63/-63/0/-63/0/63]$	20
S2	$[43/90/0/0/-43/90/-43/90/0/-43/43/90/0/43/0/43/90/90/0/-43]$	20
	Stringer (B)	
B1	$[1/61/1/1/1/-51/1/1/-51/1/1/1/61/1/1/-51/1/1/1/61/1/1/61/1/1/1/-51/1]$	28
B2	$[0/59/-1/-54/2/0/2/2/2/0/-54/-1/59/2/0/0/-54/-1/0/59/0/2/59/2/-1/-54/2/0]$	28

Table 5.6: Numerical results of the second-level problem (first two optimum stacks for both skin and stringer).

value of the laminate PPs provided by the FLP.

For the problem at hand, the number of plies for both skin and stringer laminates, (n_S and n_B, respectively) is a direct result of the FLP, while the number of saturated groups has been set equal to

- three for stacks S1 and B1,
- four for stack S2,
- five for stack B2.

As it can be easily inferred from the results listed in Table 5.7, by combining the previous stacks it is possible to get four different optimum configurations of the stiffened panel.

	Panel configurations			
	S1-B1	S1-B2	S2-B1	S2-B2
M [Kg]	0.814 (-11.5%)			
λ [N]	495503.23 (10%)	495386.87 (10%)	499138.30 (11%)	499027.68 (11%)

Table 5.7: Properties of the optimum solution (in terms of mass and buckling load) for different skin-stringer configurations; for each property the percentage difference between the optimum configuration and the reference one is indicated in parentheses.

Indeed, these optimum panels really represent equivalent solutions. Since they share the same macroscopic geometrical parameters they have the same mass, i.e. $M = 0.814$ Kg which represents a significant reduction (-11.5%) when compared to the reference configuration. Furthermore, these optimal configurations differ only in terms of the optimum stack composing skin and stiffener laminates but they show almost the same buckling response: the percentage increment of the first buckling load (with respect to the reference value λ_{ref}) ranges from 10% to 11%, see Table 5.7.

Therefore, each optimum configuration is simultaneously lighter and stiffer than the reference one and this result has been achieved only by abandoning the usual engineering rules and hypotheses related to the nature of the SS of the laminates composing the panel.

Fig. 5.4 shows the deformed shape related to the first buckling mode as well as the first component of the normalised stiffness matrices of the laminate, i.e. $\mathbf{A}^*$, $\mathbf{B}^*$ and $\mathbf{D}^*$ for both skin and stringer for the configuration S1-B1: the solid line refers to the membrane stiffness matrix, the dashed one to the bending stiffness matrix, while the dash-dotted

one is linked to the membrane/bending coupling stiffness matrix. It can be noticed that the laminate is uncoupled as the dash-dotted curve disappears, homogeneous as the solid and dashed curves are coincident and orthotropic because there are two orthogonal axes of symmetry in the plane. In addition, for both laminates the main orthotropy axis is oriented at $\Phi_1^{A^*} = 0°$ according to the hypothesis of the FLP. The same considerations can be repeated also for the rest of the optimum solutions.

5.7.2 Verification of the optimum configurations

A one-dimensional, high-order model based on CUF is used for validating the reference and optimised RU analyses. The present CUF model employs a LW refined kinematics for the accurate description of the pre-stress state of the RU subjected to compression and, thus, for enhanced evaluation of buckling loads. The CUF-LW models of the reference and optimised RU panels have 372588 and 333792 DOFs, respectively. As in the case of the ANSYS model, PBCs are imposed by using the direct penalty approach. However, it is important to underline that, because the employed LW CUF models have only pure translational displacements as unknowns, only the first line of Eq. (5.21) is enforced.

The Table 5.8 shows the first critical buckling load for the optimised configurations given by CUF high order beam models and the comparison with those resulting from ANSYS model.

Panel configurations					
λ	REF	S1-B1	S1-B2	S2-B1	S2-B2
CUF [N]	390870	450323	450430	451843	452615
ANSYS [N]	445074 (14%)	483951 (7.5%)	483838 (7.4%)	487493 (7.9%)	487386 (7.7%)

Table 5.8: Comparison of the first buckling load between ANSYS FE model and high-order beam CUF model for both reference and optimum solutions; the percentage difference between ANSYS and CUF models is indicated in parentheses.

Fig. 5.5 shows the deformed shape for the first buckling mode related to the optimised configuration S1-B1, whereas Fig. 5.7 and Fig. 5.8 present the distributions of axial σ_{xx}, shear σ_{xz} and the transversal σ_{zz} stresses for skin and stringer, respectively. These stresses are computed in the zones A-A' and B-B' of Fig. 5.6 at the critical buckling load.
It should be underlined that the adopted ANSYS model provides a good distribution of axial stresses. In contrast, and according to CUF reference solutions, the ANSYS FE model is not able to properly describe shear and transverse normal stresses and this would directly affect the accuracy of the first buckling load assessment. The differences between the results of the ANSYS FE model and the refined CUF solution for the optimum panels range from 7.4% to 7.9%, while for the reference configuration the percentage difference is significant (up to 14%). This higher discrepancy is probably related to the anisotropic bending behaviour of the reference solution. These differences are reasonable and are related to the 3D stress distributions within each constitutive layer and the different order of accuracy characterising the CUF LW beam model. Of course, this stress field strongly affects the geometrical stiffness matrix and cannot be acquired by ANSYS shell elements which are based on the FSDT hypotheses. It is noteworthy that, according to CUF numerical results, the gain in terms of stiffness is even higher than that foreseen by ANSYS,

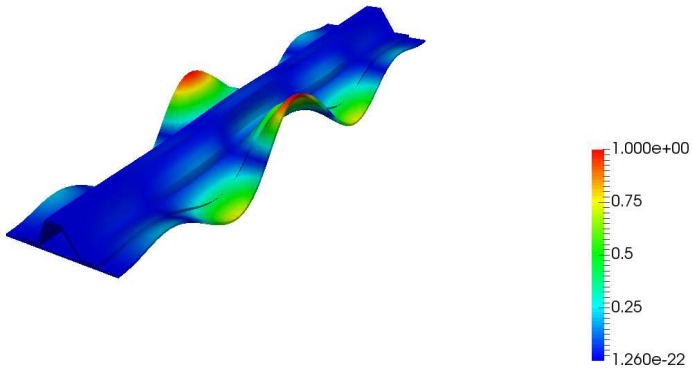

Figure 5.5: Deformed shape of the first buckling mode (normalized displacement) of the optimum panel S1-B1 for the higher order CUF model.

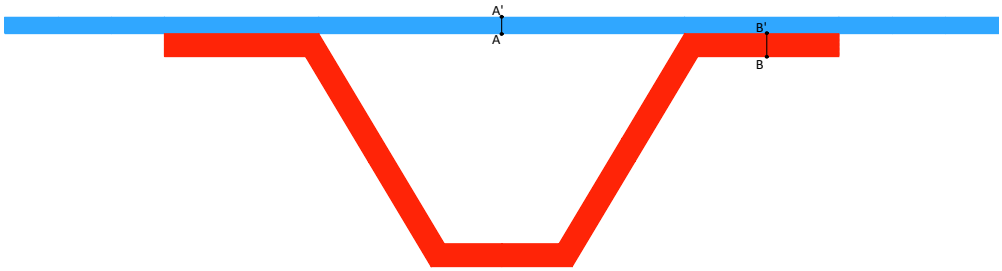

Figure 5.6: Beam cross-section.

ranging from 15.2% for solution B1-S1 to 15.8% for solution B2-S2, as can be deduced from Table 5.8.

5.8 Conclusions

The design strategy presented in this Chapter is a numerical optimisation procedure characterised by several features that make it an innovative, effective and general method for the multi-scale design of composite structures. In the present work this strategy has been applied to the multi-scale optimisation of the repetitive unit of a composite stiffened panel. On the one hand, the design process is not submitted to restrictions: any parameter characterising the structure (at each relevant scale) is an optimisation variable. This allows searching for a true global minimum without making simplifying hypotheses on the nature of the laminate SS. On the other hand, the multi-scale design problem has been split into two optimisation sub-problems which are solved subsequently within the same numerical procedure. The FLP focuses on the macroscopic scale of the panel: each laminate composing the structure is considered as an equivalent homogeneous anisotropic plate (for both skin and stringer) and its macroscopic mechanical response is described

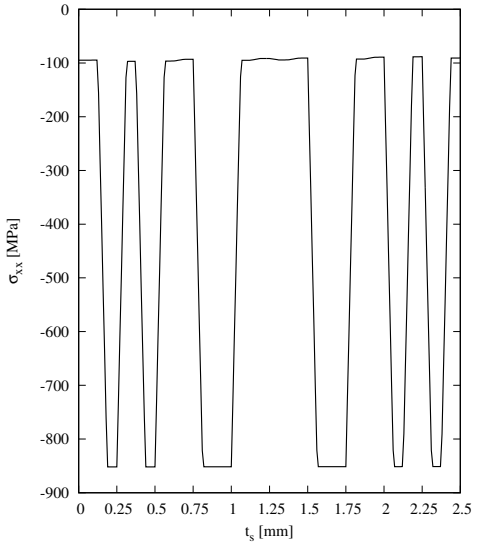

(a) Skin (A-A'). σ_{xx}

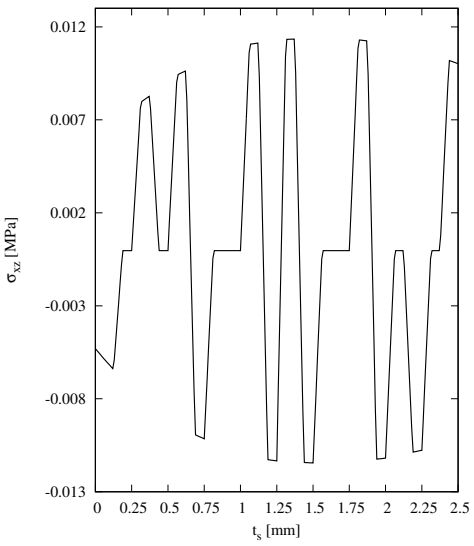

(b) Skin (A-A'). σ_{xz}

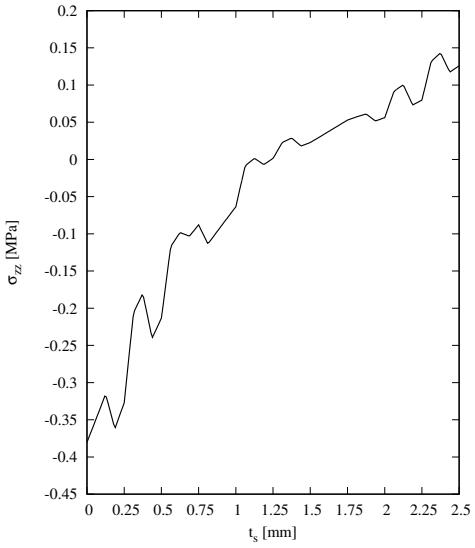

(c) Skin (A-A'). σ_{zz}

Figure 5.7: Stress distributions through the skin thickness. A-A'

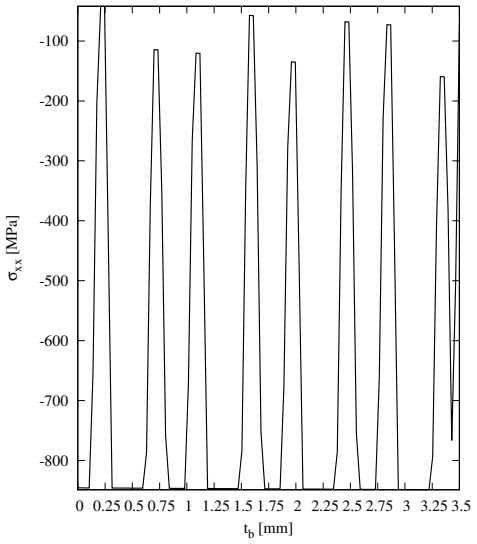

(a) Stringer (B-B'). σ_{xx}

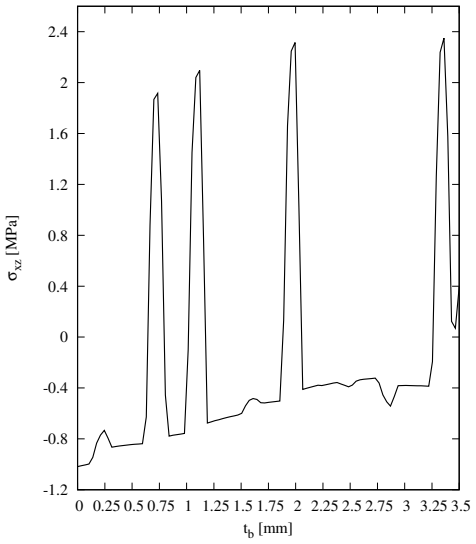

(b) Stringer (B-B'). σ_{xz}

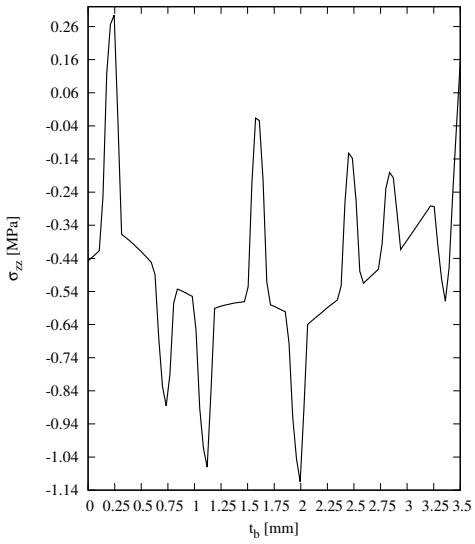

(c) Stringer (B-B'). σ_{zz}

Figure 5.8: Stress distributions through the stringer thickness. B-B'

in terms of PPs. Furthermore, also geometric design variables describing the topology of both skin and stiffener are involved at this level. At this stage, the mechanical properties of the multilayer plates are represented by means of the polar formalism. The SLP of the procedure is devoted to the laminate mesoscopic scale: the goal is to find at least one optimum stack (for both stringer and skin) meeting, on the one hand, the elastic requirements imposed to the laminate (quasi-homogeneity and orthotropy) during the FLP and, on the other hand, the optimum value of the laminate PPs resulting from the first step. The utilisation of an evolutionary strategy, together with the fact that the problem is stated in the most general sense, allows finding some non-conventional configurations more efficient than the standard ones. In fact, the considered numerical example proves that, when standard rules for tailoring laminate stacks are abandoned and all the parameters characterising the structure are included within the design process, a significant weight saving can be obtained: up to 11.5% with respect to the reference structure with enhanced mechanical properties in terms of first buckling load (the percentage increment ranges from 9% to 9.5% depending on the considered optimum solution). In a second time, both reference and optimum configurations of the stiffened panel have been analysed by means of a high-order layer-wise FE model developed in the framework of CUF. This analysis reveals that the buckling load provided by the ANSYS FE model (which is built by using shell elements based on FSDT) is overestimated and that the percentage difference ranges from $7.4 \div 7.9\%$ for optimum solutions to 14% for the reference configuration. This discrepancy is related to the calculation of the 3D stress field in each layer, which strongly affects the geometric stiffness matrix used to evaluate the first buckling load of the panel. Nevertheless, despite these discrepancies, classical shell elements based on FSDT can be reliably employed in the framework of the MS2LOS because they allow finding true optimum solutions without using expensive models, in terms of both number of DOFs and computational cost. Moreover, according to CUF results, the optimum configurations are really efficient when compared to the reference one: the weight saving is always the same, but the gain in terms of stiffness is even higher than that foreseen by ANSYS, ranging from 15.2% to 15.8% depending on the optimum solution. These results unquestionably prove the effectiveness and the robustness of the optimisation approach proposed in this Chapter and provide confidence for further research in this direction. In Chapter 7 the integration of high-order models based on CUF within the MS2LOS will be presented to increase the accuracy of the methodology when an accurate assessment of the complex 3D stress field is of paramount importance for the problem at hand.

Chapter 6

Multi-scale design of variable stiffness composites

6.1 Introduction

The main purpose of this Chapter is to apply the MS2LOS to the maximisation of the first buckling load of a VAT composite subject to feasibility constraints. The MS2LOS has been already extended to the VAT composite, and its effectiveness was proved in [78, 94, 95, 98, 168].
This Chapter focuses on the FLP of the MS2LOS, that aims at determining, at the macroscopic scale, the optimum distribution of the VAT laminate PPs to satisfy the requirements of the problem at hand. At the macroscopic scale, the VAT laminate is modelled as an equivalent homogeneous anisotropic plate whose mechanical behaviour is described in terms of PPs (which vary locally over the structure). The FSDT is always used to take into account for the influence of the transverse shear stiffness on the overall mechanical response of the VAT composite in the FE model, and B-spline surfaces are employed to represent the point-wise variation of the PPs fields.
The main contribution of the Chapter consists in the derivation of the expression of the gradient of each physical response in terms of the design variables involved in the definition of the B-spline surfaces representing the PPs distributions over the structure. In particular, the derivation of the analytical form of the gradient of the first buckling factor is anything but trivial and exploits two main properties of B-spline blending functions: the strong convex-hull property and the local support property. Thanks to the B-spline surfaces formalism, the optimised solutions are no longer related to the mesh of the FE model. Rather they are fully CAD-compatible and can be directly passed to the G-Code behind AFP and additive manufacturing processes for manufacturing purposes. The effectiveness of the developed approach is proven on two meaningful benchmarks taken from the literature.
The Chapter is organised as follows: the overview of the design problem and a brief reminder on the MS2LOS in the case of VAT composites are reported in Section 6.2. The fundamentals of the B-spline framework are reported in Section 6.3, while the mathematical formulation of the first-level problem is presented in Section 6.5. The FE model of the VAT laminate plate, for both benchmarks, is described in Section 6.6, while the numerical results are presented and discussed in Section 6.7. Finally, Section 6.8 is devoted to concluding remarks and prospects.

Publication related to this chapter: The methodology and the results presented in this Chapter have been published in [169].

6.2 The multi-scale two level optimisation strategy for variable angle tow laminates

In the context of the MS2LOS [78, 94], extended to VAT composites, the optimum design of the VAT laminate is always articulated in two sub-problems stated at different scales, as for the CSC.
The FLP aims at determining the optimum distribution of the VAT laminate mechanical design variables satisfying the requirements of the design problem. At this level, the optimisation is performed at the macroscopic scale of the VAT plate, which is modelled as an equivalent homogeneous anisotropic continuum. The laminate PPs [56–58] are the design variables of the optimisation problem, which describe the mechanical behaviour of the VAT plate and, in this case, vary point-wise over the structure. The point-wise variation is got by means of the B-spline surfaces framework.
The SLP is devoted to the determination of a suitable lay-up which satisfies the optimum distribution of PPs resulting from the FLP.
In the Chapter, only the FLP of the MS2LOS is faced and the related mathematical framework, presented in [78], is extended to eigenvalue buckling problems. Inasmuch as the SLP formulation is not affected by the modifications introduced in the FLP (and the main steps of the related resolution strategy remain unchanged), this part will not be detailed in the following Sections. For more details on the SLP formulation and on the related mathematical background, the reader is addressed to [4, 170].

6.3 Fundamentals of B-spline surfaces

The fundamentals of B-spline surfaces, widely discussed in [171], are here briefly recalled for the sake of clarity.
The parametric equation of a B-spline surface reads:

$$\mathbf{S}(u_1, u_2) \coloneqq \sum_{i_1=0}^{n_1} \sum_{i_2=0}^{n_2} N_{i_1,p_1}(u_1) N_{i_2,p_2}(u_2) \mathbf{P}_{i_1,i_2}, \tag{6.1}$$

where $\mathbf{S}(u_1, u_2) \in \mathbb{R}^3$ is a bivariate vector-valued piecewise rational function, (u_1, u_2) are scalar dimensionless parameters, both defined in the interval $[0, 1]$, while p_1 and p_2 are the degrees of the B-spline blending functions along u_1 and u_2 directions, respectively; $\mathbf{P}_{i_1,i_2} = \{X^{(1)}_{i_1,i_2}, X^{(2)}_{i_1,i_2}, X^{(3)}_{i_1,i_2}\}$ are the Cartesian coordinates of the generic control point (CP), with $i_1 = 0, ..., n_1$, $i_2 = 0, ..., n_2$ and $\mathbf{X}^{(j)} \in \mathbb{R}^{(n_1+1)\times(n_2+1)}$, $j = 1, 2, 3$. The set of $(n_1 + 1) \times (n_2 + 1)$ CPs constitutes the so-called *control net*. $N_{i_1,p_1}(u_1)$ and $N_{i_2,p_2}(u_2)$ are the B-spline blending functions defined by means of the Bernstein's polynomials. The generic blending function $N_{i_j,p_j}(u_j)$, with $j = 1, 2$, can be obtained in a recursive way as follows:

$$N_{i_j,0}(u_j) \coloneqq \begin{cases} 1 \text{ if } v^{(j)}_{i_j} \leq u_j < v^{(j)}_{i_j+1}, \\ 0 \text{ otherwise}, \end{cases} \tag{6.2}$$

$$N_{i_j,q}(u_j) = \frac{u_j - v^{(j)}_{i_j}}{v^{(j)}_{i_j+q} - v^{(j)}_{i_j}} N_{i_j,q-1}(u_j) + \frac{v^{(j)}_{i_j+q+1} - u_j}{v^{(j)}_{i_j+q+1} - v^{(j)}_{i_j+1}} N_{i_j+1,q-1}(u_j), \quad q = 1, ..., p_j, \tag{6.3}$$

where $v_{i_j}^{(j)}$ is the i_j-th component of the generic non-periodic non-uniform *knot vector*:

$$\mathbf{v}^{(j)} = \{\underbrace{0,\dots,0}_{p_j+1}, v_{p_j+1}^{(j)},\dots,v_{m_j-p_j-1}^{(j)}, \underbrace{1,\dots,1}_{p_j+1}\},\ j=1,2. \tag{6.4}$$

It is noteworthy that the size of the j-th knot vector is m_j+1, with

$$m_j = n_j + p_j + 1. \tag{6.5}$$

Knot vectors $\mathbf{v}^{(1)}$ and $\mathbf{v}^{(2)}$ are two non-decreasing sequences of real numbers that can be interpreted as discrete collections of values of the dimensionless parameters u_1 and u_2, respectively. As the CPs, also the knot vectors components form a net. In the following sections, two main properties of B-spline basis functions will be exploited: the *local support property* and the *strong convex hull property*.

- **Local support property**. One basic property of the blending functions is the *local support property*: $N_{i_j,p_j}(u_j) = 0$ if u_j is outside the interval $\left[v_{i_j}^{(j)}, v_{i_j+p_j+1}^{(j)}\right[$. Therefore, it is evident that the product $N_{i_1,p_1}(u_1)N_{i_2,p_2}(u_2) = 0$ if (u_1,u_2) is outside the open rectangle $\left[v_{i_1}^{(1)}, v_{i_1+p_1+1}^{(1)}\right[\times \left[v_{i_2}^{(2)}, v_{i_2+p_2+1}^{(2)}\right[$, which represents the local support associated to the CP $\mathbf{P}_{i_1,i_2}$. Formally, the local support of the CP $\mathbf{P}_{i_1,i_2}$ can be defined as:

$$\mathrm{S}_{i_1,i_2} \coloneqq \left\{(u_1,u_2) : (u_1,u_2) \in \left[v_{i_1}^{(1)}, v_{i_1+p_1+1}^{(1)}\right[\times \left[v_{i_2}^{(2)}, v_{i_2+p_2+1}^{(2)}\right[\right\}. \tag{6.6}$$

- **Strong convex hull property**. If $(u_1,u_2) \in \left[v_i^{(1)}, v_{i+1}^{(1)}\right[\times \left[v_j^{(2)}, v_{j+1}^{(2)}\right[$ then $\mathbf{S}(u_1,u_2)$ is in the convex hull of CPs $\mathbf{P}_{i_1,i_2}$, with $i-p_1 \le i_1 \le i$ and $j-p_2 \le i_2 \le j$.

A deeper insight into the B-spline blending functions properties can be found in [171].

6.4 Problem Description

The goal of the design strategy is the maximisation of the first buckling load of multilayer VAT plates. The effectiveness of the MS2LOS is tested on two benchmarks: a square plate (benchmark 1, taken from [92]) and a quarter of square plate with a circular hole (benchmark 2). Both structures are subjected to in-plane compressive loads and their geometric parameters are illustrated in Fig. 6.1.

The main hypotheses [78] governing the behaviour of the VAT laminate at the macroscopic scale are listed here below.

- Each ply of the VAT laminate is made of the same material and the same thickness.
- The number of plies is kept unchanged during the optimisation process.
- The material behaviour is linear elastic.
- The VAT laminate is quasi-homogeneous (i.e. uncoupled and with the same behaviour in terms of normalised membrane and bending stiffness matrices) and fully orthotropic (both in membrane and bending) *point-wise*, i.e. these properties apply locally at each point of the structure;

The properties of the T300/5208 carbon-epoxy pre-preg strip, which constitute the tow of lamina, are reported in Table 6.1 for the sake of completeness. Of course, the technical constants of the lamina are taken from [92], while the PPs are calculated accordingly.

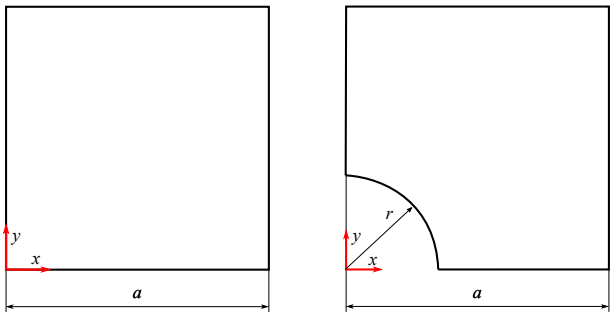

(a) (b)

Figure 6.1: Geometric parameters of (a) the square plate and (b) the square plate with a circular hole.

Technical constants		Polar parameters of $\mathbf{Q}$ [a]		Polar parameters of $\tilde{\mathbf{Q}}$ [b]	
E_1 [MPa]	181000.0	T_0 [MPa]	26878.6659	T [MPa]	5393.6268
E_2 [MPa]	10273.0	T_1 [MPa]	24738.3141	R [MPa]	1776.3732
G_{12} [MPa]	7170.5	R_0 [MPa]	19708.6659	Φ [deg]	90.0
ν_{12}	0.28	R_1 [MPa]	21436.2608		
ν_{23}	0.42	Φ_0 [deg]	0.0		
		Φ_1 [deg]	0.0		
Thickness					
h_{ply} [mm]	0.127				

[a] In-plane reduced stiffness matrix of the pre-preg strip.
[b] Out-of-plane shear stiffness matrix of the pre-preg strip.

Table 6.1: Material properties of the T300/5208 carbon-epoxy pre-preg strip.

6.5 First-level problem formulation

The FLP mathematical background essentially relies on the FSDT, as in the case of CSC, and on the use of B-spline surfaces theory. On the one hand, the FSDT allows for integrating the influence of the transverse shear stiffness on the physical responses of the VAT laminate. On the other hand, B-spline surfaces are used to describe the PPs distribution over the structure.
The use of B-spline surfaces to describe the PPs fields has a fundamental consequence: the anisotropy field description is completely unrelated from the mesh of the FE model. In fact, the design variables are not calculated at the centroid of the mesh elements as in the classical FE-based approaches [9, 10] but they are computed only at the B-spline surfaces CPs. This aspect leads to a strong reduction of the number of design variables. Moreover, as detailed in the following of this section, the use of B-spline entities also allows to reduce the number of optimisation constraints to be checked during the optimisation process. Therefore, the reduction of design variables and of the optimisation constraints allow to carry out the optimisation process with a reduced computational cost. In particular, the advantages related to the use of B-spline surfaces come from two fundamental properties: the *local support property* and the *strong convex-hull property*, see [171]. The way these properties are exploited is clarified in the following.

Without loss of generality, the following subsections focus on a meaningful design

problem: the maximisation of the first buckling factor of the VAT laminate subject to feasibility constraints on the PPs and to a requirement on the total thickness.

6.5.1 Mechanical design variables

Consider the constitutive law of the multilayer plate reported in Eq. (4.17). Under the hypotheses of quasi-homogeneous, fully orthotropic laminate (i.e. a laminate with $\mathbf{B}^* = \mathbf{O}$, $\mathbf{C}^* = \mathbf{O}$ and characterised by the same orthotropy type and direction for membrane and bending stiffness matrices): it can be proved that the overall number of independent mechanical design variables describing its mechanical response reduces to only three, i.e. the anisotropic moduli $R_{0K}^{A^*}$ and $R_1^{A^*}$ and the polar angle $\Phi_1^{A^*}$ (which represents the orientation of the main orthotropy axis) of the homogenised membrane stiffness matrix $\mathbf{A}^*$ [56, 57]. The description of the polar framework and its application in the context of the FSDT is reported in Sections 4.2, 4.3 respectively. For a deeper insight into these topics, the reader is addressed to [56, 57, 78].
For optimisation purposes, it is useful to introduce the dimensionless PPs:

$$\rho_0 \coloneqq \frac{R_{0K}^{A^*}}{R_0},\ \rho_1 \coloneqq \frac{R_1^{A^*}}{R_1},\ \phi_1 \coloneqq \frac{\Phi_1^{A^*}}{\pi/2}\ , \tag{6.7}$$

where R_0, R_1 and Φ_1 are taken from Table 6.1. The expression of the laminate stiffness matrices (together with their gradient) in terms of the dimensionless PPs is given in Appendix A. In the most general case, for a VAT composite, the three independent PPs vary point-wise over the structure. As stated beforehand, the variation of the generic PP ζ is expressed by means of a B-spline scalar function:

$$\zeta\left(u_1, u_2\right) = \sum_{i_1=0}^{n_1}\sum_{i_2=0}^{n_2} N_{i_1,p_1}(u_1) N_{i_2,p_2}(u_2)\zeta^{(i_1,i_2)},\ \zeta = \rho_0, \rho_1, \phi_1. \tag{6.8}$$

The dimensionless coordinates u_1 and u_2 can be arbitrarily defined: a natural choice is to relate them to the Cartesian coordinates of the laminate global frame:

$$u_1 = \frac{x}{a_x}\ , u_2 = \frac{y}{a_y}\ , \tag{6.9}$$

where a_j $(j = x, y)$ is the problem characteristic length along the j axis. In Eq. (6.8), $\zeta^{(i_1,i_2)}$ is the value of the dimensionless PP at the generic CP, whereas $N_{i_1,p_1}(u_1)$ and $N_{i_2,p_2}(u_2)$ are the B-spline blending functions computed at the dimensionless coordinates u_1 and u_2 respectively. An example of B-spline surfaces in the space of laminate PPs is shown in Fig. 6.2.

The integer parameters of the B-spline scalar function of Eq. (6.8) are set *a priori* and do not take part in the optimisation process. As done in [78], also the non-trivial knot-vector components appearing in Eq. (6.4) are set as evenly distributed in the interval $]0, 1[$ and are kept unchanged during the optimisation analysis. Therefore, the only design variables are the PPs defined at the CPs which can be grouped into the following vector:

$$\mathbf{x}^{\mathrm{T}} = \left\{\rho_0^{(0,0)}, \cdots, \rho_0^{(n_1,n_2)}, \rho_1^{(0,0)}, \cdots, \rho_1^{(n_1,n_2)}, \phi_1^{(0,0)}, \cdots, \phi_1^{(n_1,n_2)}\right\}\ . \tag{6.10}$$

In the most general case, the total number of design variables is equal to $3 \times (n_1 + 1) \times (n_2 + 1)$. Furthermore, the feasibility constraints, which arise from the combination of the layer orientations and positions within the stack [52], must be integrated into the

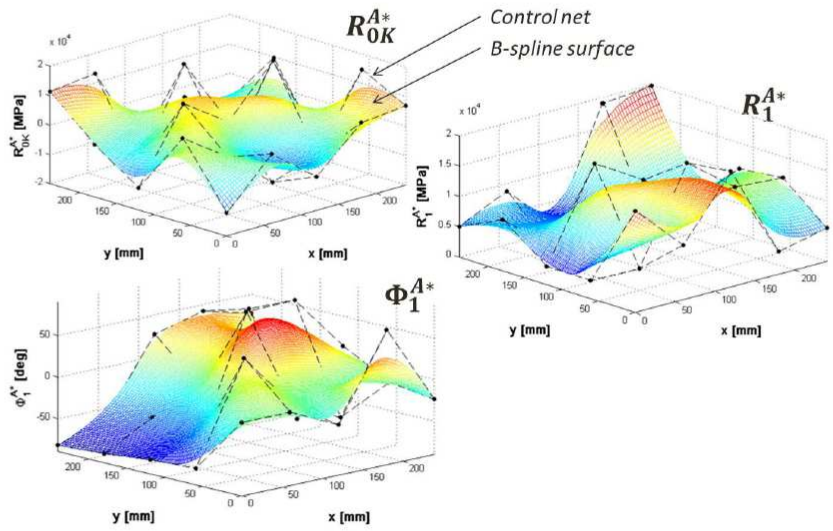

Figure 6.2: Example of B-spline surfaces in the space of laminate PPs taken from [5].

FLP formulation. Inasmuch as the laminate is quasi-homogeneous [52], it is sufficient to impose these constraints only for the PPs of matrix $\mathbf{A}^*$, i.e.

$$\begin{cases} -1 \leq \rho_0 \leq 1 \ , \\ 0 \leq \rho_1 \leq 1 \ , \\ 2\rho_1^2 - 1 - \rho_0 \leq 0 \ . \end{cases} \tag{6.11}$$

It is noteworthy that first and second inequalities of Eq. (6.11) can be taken into account as lower and upper bounds for the dimensionless anisotropic moduli, i.e. ρ_0 and ρ_1. Therefore, the expression of the resulting feasibility constraint on the laminate PPs, which must be considered for the generic CP, is:

$$g_{ij}(\mathbf{x}) = 2\left(\rho_1^{(i,j)}\right)^2 - 1 - \rho_0^{(i,j)} \leq 0 \ , i = 0, \cdots, n_1, \ j = 0, \cdots, n_2. \tag{6.12}$$

The strong convex-hull property of the B-spline blending functions ensures that, if the feasibility constraint of Eq. (6.12) is met on the CPs, it is satisfied for each point belonging to the B-spline surface (see [78] for more details). The feasibility constraint of Eq. (6.12) must be imposed in order to ensure that a feasible stack, satisfying the optimal PPs fields resulting from the FLP, could be found as a result of the SLP. The reader is addressed to [52] for a wide discussion on feasibility constraints in the PPs space.
From Eq. (6.12), it is evident that, in the most general case, the total number of feasibility constraints is equal to $(n_1 + 1) \times (n_2 + 1)$.

6.5.2 Mathematical statement of the problem

The FLP aims at determining the optimum distribution of the laminate PPs maximising the first buckling factor of the structure and satisfying, simultaneously, the feasibility constraints on the laminate PPs at each point of the plate. Consider the eigenvalue

buckling problem:

$$(\mathbf{K} + \lambda_k \mathbf{K}_\sigma)\, \boldsymbol{\psi_k} = \mathbf{0},\ \forall\ \boldsymbol{\psi_k} \neq \mathbf{0}, \tag{6.13}$$

where $\mathbf{K}$ is the stiffness matrix of the FE model, $\mathbf{K}_\sigma$ is the geometric stiffness matrix, λ_k is the k-th buckling factor and $\boldsymbol{\psi_k}$ is the k-th eigenvector associated to λ_k. Here, only the first buckling factor is computed, thus $k = 1$. In the following, the first buckling factor λ_1 is denoted as λ to simplify the nomenclature. Formally, the design problem can be stated as a CNLPP as:

$$\begin{aligned} &\min_{\mathbf{x}}\ -\lambda(x), \\ &\text{subject to:} \\ &\begin{cases} (\mathbf{K} + \lambda_k \mathbf{K}_\sigma)\, \boldsymbol{\psi_k} = \mathbf{0}, \\ h = \text{const.}\ , \\ g_{ij}(\mathbf{x}) \leq 0,\ i = 0, \cdots, n_1,\ j = 0, \cdots, n_2. \end{cases} \end{aligned} \tag{6.14}$$

The design space of the FLP, together with the type of each design variable, is detailed in Table 6.2. In Eq. (6.14) the overall thickness of the laminate h is kept constant.

Design variable	Type	Lower bound	Upper bound
ρ_0	continuous	-1.0	1.0
ρ_1	continuous	0.0	1.0
ϕ_1	continuous	-1.0	1.0

Table 6.2: Design space of the first-level problem.

In order to solve problem (6.14) by means of a suitable deterministic algorithm, the gradient of both the objective function and the constraints functions with respect to the design variables, i.e. the laminate dimensionless PPs at each CP, must be computed. The derivation of the gradient of the feasibility constraints of Eq. (6.12) is straightforward:

$$\begin{aligned} \frac{\partial g_{st}}{\partial \rho_0^{(i,j)}} &= \begin{cases} -1 & \text{if}\quad s = i,\ t = j, \\ 0 & \text{otherwise}, \end{cases} \\ \frac{\partial g_{st}}{\partial \rho_1^{(i,j)}} &= \begin{cases} 4\rho_1^{(i,j)} & \text{if}\quad s = i,\ t = j, \\ 0 & \text{otherwise}, \end{cases} \\ \frac{\partial g_{st}}{\partial \phi_1^{(i,j)}} &= 0. \end{aligned} \tag{6.15}$$

Conversely, the gradient of the k-th buckling factor requires a special attention. In order to derive its analytical expression, the local support property of the B-spline blending functions [171] as well as the adjoint method [172] are exploited. To this end, consider the following proposition.

Proposition 6.5.1. *Consider a deformable anisotropic plate subject to given external loads. Under the hypotheses of small generalised displacements and strains, the gradient of the k-th buckling factor λ_k reads:*

$$\begin{cases} \dfrac{\partial \lambda_k}{\partial \zeta^{(i,j)}} = \dfrac{\lambda_k}{w_k} \left[\displaystyle\sum_{e \in \mathrm{S}_{ij}} \frac{\partial \zeta_e}{\partial \zeta^{(i,j)}} \left(w_{ek}^* + \lambda_k \mathbf{s}_{ek}^{\mathrm{T}} \frac{\partial \mathbf{K}_{\mathrm{lam_e}}}{\partial \zeta_e} \boldsymbol{\varepsilon}_{0e} \right) + \boldsymbol{\mu}^{\mathrm{T}} \frac{\partial \mathbf{K}}{\partial \zeta^{(i,j)}} \mathbf{d}_0 \right],\ \zeta = \rho_0, \rho_1, \phi_1, \\ \mathbf{K}\boldsymbol{\mu} = -\lambda_k \boldsymbol{\eta}_k. \end{cases} \tag{6.16}$$

where $\boldsymbol{\mu}$ is the solution of the adjoint system.

The proof of proposition 6.5.1, the meaning of the quantities appearing in Eq. (6.16) and the pseudo-code of the algorithm used to compute the gradient of λ_k are provided in Appendix B.

Remark 6.5.1. *In Eq. (6.16), ζ_e represents the generic dimensionless PP of Eq. (6.8) evaluated at the element centroid, i.e. $\zeta_e = \zeta(u_{1e}, u_{2e})$, whilst, according to Eq. (6.8), its derivative reads:*

$$\frac{\partial \zeta_e}{\partial \zeta^{(i,j)}} = N_{i,p_1}(u_{1e}) N_{j,p_2}(u_{2e}). \tag{6.17}$$

Remark 6.5.2. *In Eq. (6.16), S_{ij} is the discretised version of the generic CP local support defined as:*

$$\mathrm{S}_{ij} \coloneqq \left\{ e : (u_{1e}, u_{2e}) \in \left[U_i^{(1)}, U_{i+p_1+1}^{(1)} \right[\times \left[U_j^{(2)}, U_{j+p_2+1}^{(2)} \right[\right\}. \tag{6.18}$$

The local support property of B-spline blending functions relates the control net, which affects the shape of the B-spline surface, to the mesh of the FE model through the definition of an influence zone for each CP, i.e. the so-called local support. Therefore the variation of the generic dimensionless PP assigned to a given CP influences only the elements belonging to the local support of such a CP. As discussed in [78], the size of the local support zone depends on the B-spline surface discrete parameters, i.e. the degrees of the blending functions and the number of CPs.

Remark 6.5.3. *In Eq. (6.16), $\mathbf{d}_0$ is the vector of the nodal generalised displacements, solution of the preliminary linear static analysis:*

$$\mathbf{K}\mathbf{d}_0 = \mathbf{f}_0, \tag{6.19}$$

where $\mathbf{f}_0$ is the vector of external nodal forces (of arbitrary value, generally a unit value is used). $\boldsymbol{\varepsilon}_{0e}$, $(e = 1, \cdots, N_e)$ is the vector of generalised strains of Eq. (4.18) evaluated for each element composing the FE model (the number of elements is N_e). The solution of Eq. (6.19) is used to compute the pre-stress state involved in the definition of the geometric stiffness matrix $\mathbf{K}_\sigma$. All details are provided in Appendix B.

6.5.3 Numerical strategy

Problem (6.14) is a non-convex CNLPP in the space of the laminate PPs. Its non-linearity is due, on the one hand, to the nature of the objective function, the buckling factor, which is a non-convex function with respect to the orthotropy orientation field. On the other hand, the complexity of such a problem is also due to the non-linear feasibility constraints imposed on the PPs of the plate, see Eq. (6.12).

For the resolution of problem (6.14) a hybrid optimisation tool called VISION (*VarIable Stiffness composItes Optimisation based on NURBS*), developed by Montemurro [5] and made by the union of the ERASMUS algorithm [5] and a general deterministic algorithm, is employed. VISION is available in both MATLAB and Python versions. The Python version has been further developed through the implementation of the objective function gradient in order to deal with problem (6.14) and is employed here. The Sequential Least Square Quadratic Programming (SLSQP) algorithm available in *Numpy* package, from the Python-based environment *Scipy*, has been used as a deterministic algorithm [173]. VISION is interfaced with the FE model of the VAT plate (used essentially to compute the physical/geometrical responses involved into the definition of objective function and constraint functions), see Fig. 6.3.

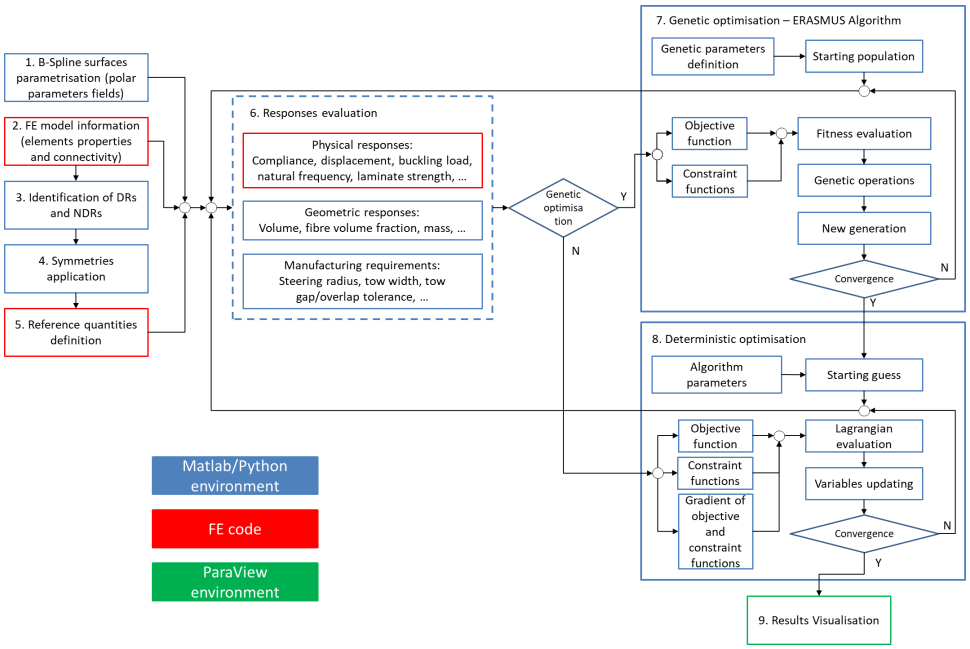

Figure 6.3: VISION flowchart[5].

The VISION tool is composed of three main phases: pre-processing phase (steps 1-5), optimisation solvers (steps 6-8) and post-processing phase (step 9). A synthetic description of each step is given here below.

1. *B-spline surfaces parametrisation.* During this phase the user must set the discrete parameters (number of CPs, degrees of the blending functions) tuning the shape of the B-spline surfaces representing the laminate PPs fields as well as the values of the non-trivial components of each knot-vector. The above quantities are just geometric parameters of the B-spline blending functions which are not included in the vector of design variables. If the user does not provide the knot-vector components, they are uniformly distributed in the interval $[0, 1]$.

2. *FE model information.* The FE model of the problem at hand must be properly prepared in the external FE code, in terms of both geometry and mesh of design regions (DRs) and non-design regions (NDRs). Once the mesh is generated, the elements belonging to DRs are selected and their data are passed to the MATLAB/PYTHON environment. For each element, the relevant information are: its identifier, the Cartesian coordinates of its centroid as well as its area (shell element) and volume (solid element).

3. *Identification of DRs and NDRs.* Not all the zones of the structure have to be optimised and this requirement can be fulfilled by forecasting proper NDRs within the FE model at specific locations. Therefore, including the PPs defined at all CPs (even those CPs whose local support falls within NDRs) among the design variables is useless. To this purpose, before launching the optimisation, a dedicated function checks all CPs local supports. Consider the local support of the generic CP S_{ij}: if the dimensionless coordinates (u_{1e}, u_{2e}) of at least one element centroid belonging to the DR are in S_{ij}, then the corresponding PPs defined at that CP are inserted in the

design variables array; otherwise, they are deleted from this array. The discarded PPs are set equal to their lamina counterparts for those CPs whose local support is the empty set.

4. *Symmetries Application.* Symmetries can be interpreted as variables saving from a computational viewpoint. Only independent CPs are effectively collected in the design variables array.

5. *Reference Quantities.* Geometrical, physical and manufacturing responses used to obtain dimensionless objective and constraint functions are set here. Their definition is not unique and the algorithm allows the external user to define the reference quantities. However, pre-set strategies can be selected for the most common problems (compliance minimisation, first buckling load maximisation, etc.).

6. *Responses evaluation.* The system responses involved into the definition of both objective function and constraint functions can be of different nature: geometrical, physical and technological. The user can implement some of them directly into the MATLAB/PYTHON environment (e.g. geometrical and technological requirements). For those responses requiring a FE analysis to be computed (e.g. buckling load, compliance, natural frequencies, etc.) an automatic interface between the optimisation algorithms (both meta-heuristics and deterministic) and the FE codes (both commercial and in-house codes) has been implemented into the VISION tool.

7. *Genetic optimisation.* During the first phase, solely the ERASMUS GA is interfaced with the FE model of the VAT composite: for each individual at each generation, a FE analysis is invoked for the evaluation of the physical responses. The FE model makes use of the design variables, given by the GA and elaborated by the MATLAB/PYTHON code, which generates the B-spline surfaces representing the dimensionless PPs fields. These fields are then projected over the FE model of the VAT plate in order to calculate the desired physical response as well as the feasibility constraint at each CP. At the end of the FE analysis, the GA elaborates the results provided by the FE model in order to execute the genetic operations. These operations are repeated until the GA meets the user-defined convergence criterion.

8. *Deterministic optimisation.* Due to the strong non-convex nature of the VAT design problem, the aim of the genetic calculation is to provide a potential sub-optimal point in the design space, which constitutes the initial guess for the subsequent phase, i.e. the local optimisation, where a suitable deterministic algorithm is interfaced with the same FE model of the VAT composite. In this case, the optimisation calculation is speed-up by giving explicitly the expression of the gradient of both constraint functions and objective function. The convergence of the optimiser is achieved when constraints are met (or barely met, i.e. the optimum solution is on the boundary of the search domain) and one of the following conditions occurs: (a) the predicted change of the objective function is lower than a prescribed tolerance (10^{-6}); (b) the norm of the gradient of the Lagrangian functional related to the problem at hand is very close to zero (10^{-6}); (c) the predicted change of design variables is lower than a prescribed threshold value (10^{-6}); (d) a maximum value of iterations (set by the user) has been attained. The upper bound on the iterations number is 250 for the benchmarks presented in this study.

9. *Results visualisation.* The optimised distribution of the laminate PPs can be converted in two different standard formats: IGS file (which can be easily imported in a

CAD environment) and VTK format. The latter can be exploited and manipulated into the ParaView® environment. In the benchmarks considered here, the VTK format has been chosen to visualise the PPs fields.

For each benchmark, two cases have been considered.

- *Case 1.* Only ϕ_1 varies over the structure, whilst ρ_0 and ρ_1 are considered uniformly distributed. In this case, the overall number of design variables for problem (6.14) is $2 + (n_1 + 1) \times (n_2 + 1)$. In this case, there is only one feasibility constraint on the laminate PPs to be checked.

- *Case 2.* This represents the most general case wherein ρ_0, ρ_1 and ϕ_1 vary over the structure. The overall number of design variables is $3 \times (n_1 + 1) \times (n_2 + 1)$, while the number of optimisation constraints is $(n_1 + 1) \times (n_2 + 1)$

Inasmuch as problem (6.14) is highly non-convex, the optimised solution strongly depends upon the choice of the initial guess $\mathbf{x}_0$. Here, the initial guess $\mathbf{x}_0$ is generated in three different ways. In the first case, $\mathbf{x}_0$ is null, which means that an isotropic initial guess is selected. In the the second case, $\mathbf{x}_0$ is the best individual resulting from the genetic optimisation performed by means of the ERASMUS algorithm [5]. In particular, the generic individual of the GA represents a potential solution for the problem at hand. In the most general case, the genotype of the individual for problem (6.14) is composed of $(n_1 + 1) \times (n_2 + 1)$ chromosomes with three genes coding the dimensionless PPs at each CP of the B-spline surface. In the third case, the initial guess is randomly generated.

It is noteworthy that, since problem (6.14) involves a requirement on the first buckling factor, the well-known mode switching phenomenon [174], typical of eigenvalue problems, can occur during the iterations of the optimisation process. For example, the mode switching phenomenon (together with the spurious mode phenomenon) affects topology optimisation [174] when considering eigenvalue problems (i.e. buckling or modal analyses). As far as topology optimisation problems involving requirements on critical buckling loads (or natural frequencies) are concerned, the most common numerical strategies available in the literature to deal with the mode switching issue have been integrated in a new topology optimisation method coupling NURBS hyper-surfaces with the classical Solid Isotropic Material with Penalisation (SIMP) method developed by Montemurro and coworkers [174–176]. In particular, in [174], dedicated numerical artefacts and guidelines to avoid the mode switching during the topology optimisation for problems involving modal analysis are provided.

Fortunately, in the case of VSCs the situation is not as complicated as in topology optimisation problems. In particular, only the buckling mode (eigenvector) associated to the lowest buckling factor (eigenvalue) is considered at each iteration during the optimisation. Therefore, if a mode switch occurs in between two iterations, in the next one, the correct buckling mode (i.e. that associated to the lowest eigenvalue) is considered (for the expression of the objective function and the related gradient). Moreover, a further check is introduced within the SLSQP algorithm to ensure that the lowest buckling factor of the structure continuously increases (and, thus, the merit function of problem (6.14) monotonically decreases) during iterations. Particularly, if the mode switching occurs and the value of the merit function of problem (6.14) at the current iteration is greater than that of the previous iteration, a new descendent direction is calculated in order to get a non-increasing value of the merit function along iterations.

Of course, a sound alternative could be to consider a different objective function involving a linear combination (i.e. a weighted sum) of the first N buckling factors, or

to introduce a suitable constraint on the imposed gap between two consecutive eigenvalues. Both strategies reveal effective for topology optimisation problems as discussed in [174]. However, for the test cases presented here, the simplified strategy discussed above is sufficient to correctly take into account for the mode switching phenomenon.

6.6 The finite element model for the optimisation

In order to assess the buckling factor and its gradient, an eigenvalue buckling analysis has to be carried out for the FE model of the VAT composite. The FE model is generated in ANSYS® environment by using SHELL181 elements, which have four nodes and six DOFs per node. The FE model is capable of updating the mechanical properties of each element of the mesh through the use of the PPs distributions at each iteration of the optimisation problem. The FE models of the benchmarks analysed here are shown in Fig. 6.4.

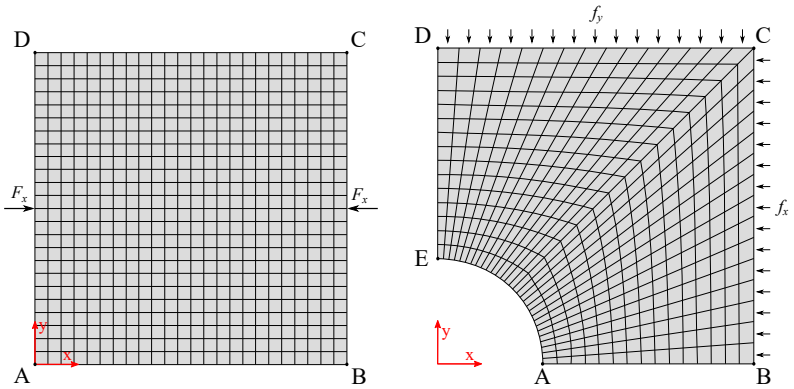

Figure 6.4: FE model and related BCs for (a) the square plate and (b) the square plate with a hole subject to bi-axial compression loads.

For each benchmark, the BCs are set as follows.

- *Benchmark 1* is a VAT composite square plate taken from the literature [92]. In this case, the plate is subjected to an uni-axial external compressive load F_x applied on nodes located at: $x = 0, y = a/2$ and $x = a, y = a/2$; see Fig. 6.4. In order to get a uniform displacement u_x for sides AD and BC as done in [92], constraint equations are imposed on nodes located at $x = 0, a$. The mesh size is chosen after a preliminary mesh sensitivity analysis on the convergence of the first buckling load, for the set of BCs reported in Table 6.3. It has been observed that a mesh having 12005 DOFs is sufficient to properly evaluate the first buckling load of the structure.

- *Benchmark 2* represents a quarter of a square plate with a hole subject to bi-axial compressive loads; The BCs on the generalised displacements are given in Table 6.3, while the uniform compressive forces per unit length, i.e. f_x and f_y, are applied on nodes located on sides BC and CD, respectively. Also in this case the mesh size is the result of a sensitivity analysis: an overall number of 2480 DOFs is sufficient to correctly assess the first buckling factor.

Benchmark 1		Benchmark 2	
Sides	geometric BCs	Sides	geometric BCs
AB, CD	$U_y = U_z = \theta_y = \theta_z = 0$	AB	$U_y = \theta_x = \theta_z = 0$
		CD	$U_x = U_z = 0$
BC, DA	$U_y = U_z = \theta_x = \theta_z = 0$	BC	$U_y = U_z = 0$
	$U_x(0,y) = U_x(0,a/2), U_x(a,y) = U_x(a,a/2) \quad \forall y \in [0, \frac{a}{2}[\cup]\frac{a}{2}, a]$	DE	$U_x = \theta_y = \theta_z = 0$

Table 6.3: BCs on generalised displacements for benchmarks 1 and 2.

It is noteworthy that a module composed of appropriate routines defining a general B-spline surface has been coded in Python (within the VISION tool) and interfaced with the FE model of the VAT plate. The following algorithm has been implemented to compute the local stiffness properties of each element of the FE model and to determine the buckling factor and its gradient.

Algorithm 1 Buckling analysis of VAT laminates through B-spline surfaces and polar parameters.

1: For a given set of dimensionless PPs defined at each CP, build the corresponding B-spline surfaces.
2: Discretise the plate into N_e elements.
3: Retrieve the Cartesian coordinates of the e-th element centroid, i.e. (x_e, y_e) and calculate the corresponding dimensionless coordinates (u_{1e}, u_{2e}) according to Eq. (6.9).
4: Determine the dimensionless PPs (and hence the Cartesian components of the laminate stiffness matrices) according to Eq. (6.8) and assign material properties to element e;
5: If $e < N_e$ set $e = e + 1$ and go to step 3, otherwise stop.
6: Execute Algorithm 2 (see B) for assessing the buckling factor and its gradient.

6.7 Numerical results

6.7.1 Benchmark 1: square plate subject to bi-axial compressive loads

The first benchmark refers to the geometry illustrated in Fig. 6.1(a) and it is used to assess the effectiveness of the MS2LOS by comparing the optimised solutions with those available in [92]. It is noteworthy that, since a quasi-homogeneous fully orthotropic laminate is considered, the feasible region, described by the inequality of Eq. (6.12), is smaller than that considered in [92]
The plate edge length is $a = 254$ mm, while its overall thickness is $h = 1.524$ mm. The BCs on the generalised displacements are given in Table 6.3. The value of the axial compressive loads applied to the VAT laminate nodes is equal to the first buckling load evaluated for a quasi-homogeneous isotropic laminate subject to the same BCs, which is equal to $F_x = F^{\text{cr}}_{x-\text{ISO}} = 2700.81$ N. As done in [92], results are reported in terms of the buckling load of the VAT plate normalised with respect to this value:

$$K_{\text{cr}} = F^{cr}_{x-\text{VAT}} / F^{\text{cr}}_{x-\text{ISO}} \tag{6.20}$$

Firstly, the results concerning Case 1 of Section 6.5.3 are presented (ϕ_1 variable over the structure and ρ_0 and ρ_1 uniformly distributed). The sensitivity of the optimised normalised buckling load K_{cr} to the size of the control net together with the number of iterations to get convergence are reported in Table 6.4, where a comparison with those

available in the literature [92] is also provided. The starting point (for each number of CPs) is the isotropic solution (i.e. $\rho_0 = \rho_1 = 0.0$), referred as ISO in the following. For each

	K_{cr}	Iterations
ISO	1.00	–
VAT 5×5, [92]	1.88	–
VAT 7×7, [92]	1.96	–
VAT 9×9, [92]	2.02	–
VAT 5×5 - *Case 1*	2.12 (+12.8%)	158
VAT 7×7 - *Case 1*	2.22 (+13.3%)	144
VAT 9×9 - *Case 1*	2.35 (+16.3%)	118

Table 6.4: Benchmark 1 - *Case 1*: sensitivity of the optimum normalised buckling load to the number of CPs (the percentages in parentheses indicate the improvements with respect to corresponding the literature solutions).

number of CPs, the optimal value of the dimensionless anisotropic moduli are reported in Table 6.5, while the optimal distribution of the polar angle $\Phi_1^{A^*}$ is illustrated in Fig. 6.5.

	ρ_0	ρ_1
VAT 5×5 - *Case 1*	0.73	0.93
VAT 7×7 - *Case 1*	0.81	0.95
VAT 9×9 - *Case 1*	0.80	0.95

Table 6.5: Benchmark 1 - *Case 1*: dimensionless anisotropic moduli for the optimised solutions.

The following considerations can be inferred from the analysis of these results.

- From Table 6.4, one can infer that the results obtained by means of the MS2LOS based on the polar formalism outperform those reported in the literature. When comparing results with the same CPs number, the increase of the normalised buckling factor varies between 12.8% (in the case of 25 CPs) and 16.3% (in the case of 81 CPs) with respect to the literature solution [92].
- Table 6.5 and Fig. 6.5 show that, even if the solutions with 49 CPs and 81 CPs are very close in terms of dimensionless anisotropic moduli values, the refined optimal distribution of the polar angle $\Phi_1^{A^*}$ for the case with a higher number of CPs brings to an increment of 5.86% of the normalised buckling load with respect to the case of a lower number of CPs.

As a consequence, a 7×7 control net has been chosed for the following optimisation analyses concerning benchmark 1. This choice represents the best compromise between computational costs and performances.

Two analyses are performed in the most general case (*Case 2* reported in Section 6.5.3) wherein ρ_0, ρ_1, and ϕ_1 vary over the structure, by considering two different starting points. In this case, the CNLPP is characterised by 147 design variables and 49 optimisation constraints. In particular, *Case 2a* makes use of a quasi-homogeneous isotropic solution as initial guess, while *Case 2b* considers, as starting point, a random-generated feasible set of PPs. It must be noticed that, for *Case 2b*, the random starting point has been selected as the best solution (in terms of initial value of the buckling load) among twenty different (feasible) PPs distributions generated randomly.

The normalised buckling load K_{cr} of the optimised solutions and the number of iterations to achieve convergence are reported in Table 6.6, where it is compared to that of the

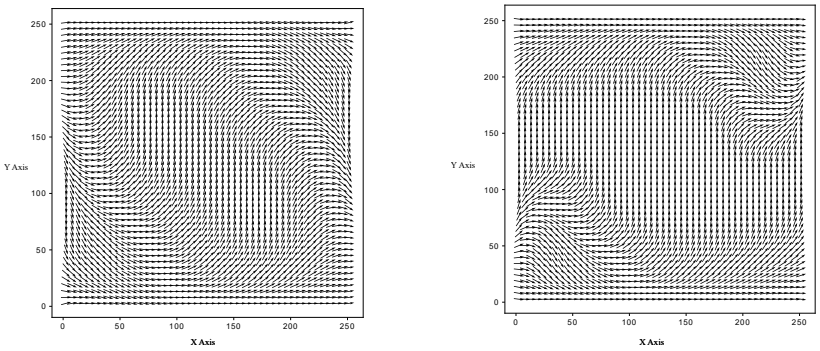

(a) VAT 5×5 (b) VAT 7×7

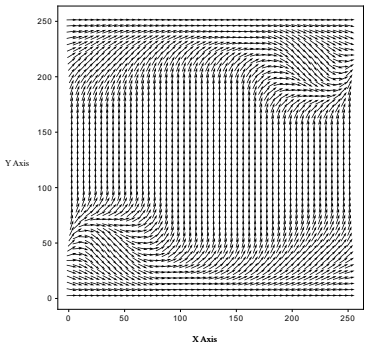

(c) VAT 9×9

Figure 6.5: Benchmark 1 - *Case 1*: optimal distribution of the polar angle $\Phi_1^{A^*}$.

quasi-homogeneous isotropic solution and to that of the corresponding *Case 1* solution of Table 6.4. The optimal PPs fields related to the optimised solutions *Case 2a* and *Case 2b* are illustrated in Figs. 6.6 and 6.7, respectively.

	K_{cr}	Iterations
ISO	1.00	–
VAT 7×7 - *Case 1*	2.22	144
VAT 7×7 - *Case 2a*	2.22	192
VAT 7×7 - *Case 2b*	2.30	166

Table 6.6: Benchmark 1 - *Case 2*: optimised solutions.

By looking at the distributions of Figs. 6.6 and 6.7 and by considering the results listed in Table 6.6, the following remarks can be done.

- As expected, the solutions obtained in *Case 2a* and *Case 2b* are different. Indeed, the buckling factor is a non-convex function in the PPs space, thus the optimised solution depends upon the choice of the initial guess.

- Table 6.6 shows that both optimised solutions are better than the reference one. The solution obtained in *Case 2a* (when the ISO solution is used as initial guess) has a normalised buckling load 2.22 times higher than that of the ISO solution. In this case, the optimised value of K_{cr} is identical to the one obtained in case *Case 1*, as

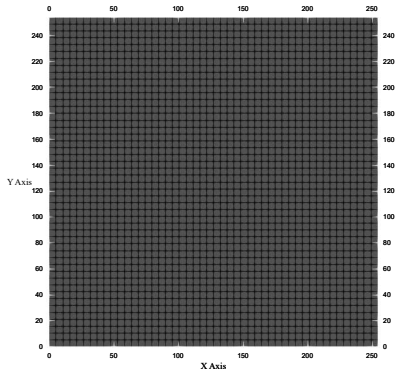

(a) $R_{0K}^{A^*} = 15964.02$ [MPa]

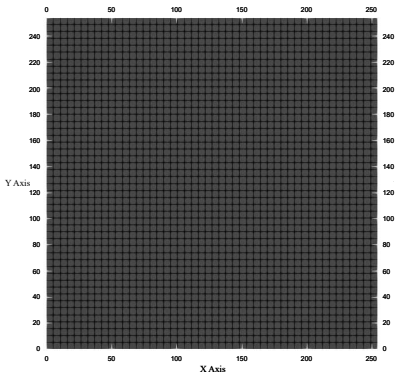

(b) $R_1^{A^*} = 20364.45$ [MPa]

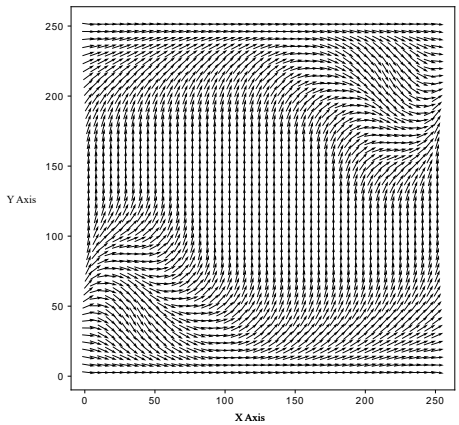

(c) $\Phi_1^{A^*}$

Figure 6.6: Benchmark 1 - *Case 2a*: optimal distribution of the PPs over the structure.

well as the distributions of $R_{0K}^{A^*}$, $R_1^{A^*}$ and $\Phi_1^{A^*}$ (compare results reported in Fig. 6.6 to those in Table 6.5 and Fig. 6.5).

- When the initial guess is randomly generated, the algorithm converges towards a different solution characterised by a normalised buckling load 2.30 times higher than the reference value. As it can been inferred from Fig. 6.7, the orthotropy type continuously changes over the structure because of the variation of the dimensionless polar moduli ρ_0 and ρ_1.

As a final remark, it must be highlighted that, although problem (6.14) is formulated in a smaller design space (when compared to that used in [92]), more efficient results (in terms of the first buckling factor) have been found in this Chapter. How is it possible? The reason is twofold.
Firstly, LPs are not as effective as PPs, which are tensor invariants, in describing the elastic symmetries of a tensor [4, 56–58, 78, 170]. Therefore, when PPs are used as design variables of the FLP, the optimisation algorithm has a direct control on the elastic symmetries of tensors and it is able to search for the optimum distribution of orthotropy type (by means of the polar moduli ρ_0 and ρ_1) and orientation (by means of the polar angle ϕ_1) maximising the first buckling factor of the VSC. Conversely, the optimisation algorithm has no control

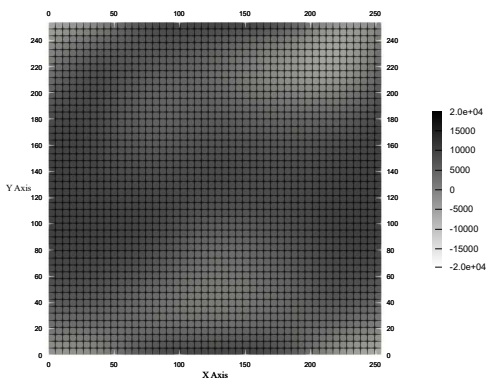

(a) $R_{0K}^{A^*}$ [MPa]

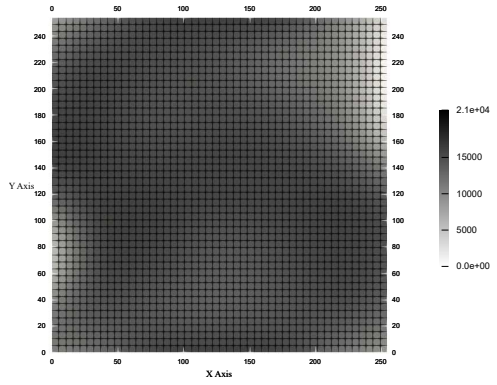

(b) $R_1^{A^*}$ [MPa]

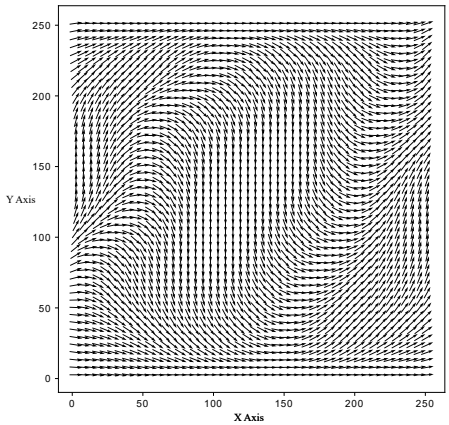

(c) $\Phi_1^{A^*}$

Figure 6.7: Benchmark 1 - *Case 2b*: optimal distribution of the PPs over the structure.

on the orthotropy type and orientation when LPs are used as design variables of the FLP as done in [92]. Accordingly, in this case the optimisation algorithm is, probably, trapped in a feasible local minimum characterised by a value of the first buckling factor lower than that characterising the local minimiser in the PPs space.
Secondly, as discussed in [4, 56–58, 78, 170], a thin (or moderately thick) VSC (but also a standard composite reinforced with straight fibres) show an "optimal" response (in terms of strain energy, buckling factor, strength, etc.) when the membrane and bending tensors tend to exhibit the same elastic behaviour. Therefore, using a quasi-homogeneous laminate with the same orthotropic behaviour in membrane and bending (i.e. $\mathbf{A}^* = \mathbf{D}^*$) helps in speeding up the convergence of the algorithm towards an efficient feasible local minimiser, i.e. a VSC configuration characterised by a very good value of the first buckling factor corresponding to an optimised membrane/bending behaviour.

6.7.2 Benchmark 2: square plate with a hole subject to bi-axial compressive loads

This second benchmark, taken from [4], refers to the geometry illustrated in Fig. 6.1(b). The values of the characteristic problem sizes are: $a = 90$ mm, $r = 30$ mm and the

plate thickness is $h = 3$ mm. The applied BCs are those listed in Table 6.3. The value of the bi-axial compressive loads applied to the VAT laminate middle plane corresponds to the buckling load of a quasi-homogeneous isotropic laminate (indicated as ISO in the following), which is equal to $f_x = f_y = f_{\text{ISO}}^{\text{cr}} = 118.78$ Nmm^{-1}.
For benchmark 2, a preliminary study on the convergence of the normalised buckling load K_{cr} to the control net size is done in order to determine the number of CPs to be used during optimisation. This sensitivity analysis has been conducted by considering that only ϕ_1 varies over the structure, whilst ρ_0 and ρ_1 are uniformly distributed. The starting point (for each number of CPs) is the ISO solution.

	K_{cr}	Iterations
ISO	1.00	–
VAT 4×4	1.66	28
VAT 5×5	1.67	46
VAT 6×6	1.79	37
VAT 7×7	1.79	83
VAT 8×8	1.80	90

Table 6.7: Benchmark 2 - Sensitivity of the normalised buckling load to the number of CPs.

The results of this sensitivity analysis are given in Table 6.7. It has been observed that the model with 6×6 CPs represents the best compromise between accuracy and computational costs. Therefore, this choice results in 38 design variables and one feasibility constraint for *Case 1* and 108 design variables and 36 feasibility constraints for *Case 2*.

- *Case 1* - Two analyses are performed in this case, by considering two different starting points. In particular, *Case 1a* makes use of the ISO solution as a starting point, whilst for *Case 1b* the initial guess is the best solution provided by the ERASMUS algorithm at the end of the genetic search. Table 6.8 lists the normalised buckling load of the ISO solution and of the ERASMUS initial guess in the optimised configurations together with the number of iterations to achieve convergence.

	K_{cr}	Iterations
ISO	1.00	–
ERASMUS - GA	2.29	–
Case 1a	1.79	37
Case 1b	3.23	57

Table 6.8: Benchmark 2 - *Case 1*: optimised solutions.

The values of the optimised dimensionless anisotropic moduli are reported in Table 6.9, whereas the optimal distributions of the polar angle $\Phi_1^{A^*}$ over the structure for *Case 1a* and *Case 1b* are illustrated in Fig. 6.8.

	ρ_0	ρ_1
Case 1a	−0.70	0.39
Case 1b	1.00	1.00

Table 6.9: Benchmark 2 - Case 1: dimensionless anisotropic moduli for the optimised solution.

From an analysis of the results reported in Tables 6.8 and 6.9 and by looking at the polar angle fields of Fig. 6.8, the following remarks can be inferred.

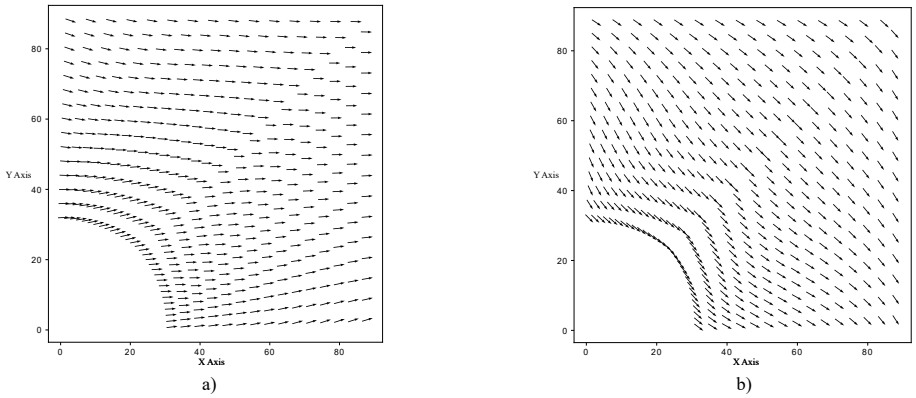

Figure 6.8: Benchmark 2: optimal distribution of the polar angle $\Phi_1^{A^*}$ over the structure for *Case 1a* (a) and *Case 1b* (b).

- The two optimisation calculations converge towards different local minima, showing, again, the non-convex nature of the problem at hand.
- Both the optimised solutions are better than the reference one. In particular, when the solution provided by the GA is used as initial guess, the normalised buckling load of the optimised solution is 3.23 times greater than the ISO solution and almost two times greater than that obtained by using the ISO solution as initial guess. Moreover, the optimised solution of *Case 1b* has a normalised buckling load which is about 41% greater than that of the initial guess resulting from the GA calculation.
- The solution of *Case 1a* is characterised by a special orthotropic behaviour with $K^{A^*} = 1$ because the optimised value of ρ_0 is negative. The main orthotropy axis direction is aligned with the direction of the x axis of the plate almost everywhere over the VAT laminate. Conversely, the solution of *Case 1b* shows a standard orthotropic behaviour characterised by a unit value of the dimensionless anisotropic moduli and by an angular field which follows the boundary of the hole.

- *Case 2* - This is the most general case where all the three dimensionless PPs vary over the structure. As in the first case, three different starting points have been considered corresponding to: (a) the ISO solution (*Case 2a*); (b) the best solution provided by the ERASMUS algorithm (*Case 2b*); (c) a feasible initial guess randomly generated (*Case 2c*). The normalised buckling load relative to all initial guess and the optimised solutions are reported in Table 6.10.

	K_{cr}	Iterations
ISO	1.00	–
RANDOM	1.02	–
ERASMUS- GA	2.44	–
Case 2a	3.29	232
Case 2b	3.29	99
Case 2c	3.29	86

Table 6.10: Benchmark 2 - Case 2: optimised solutions.

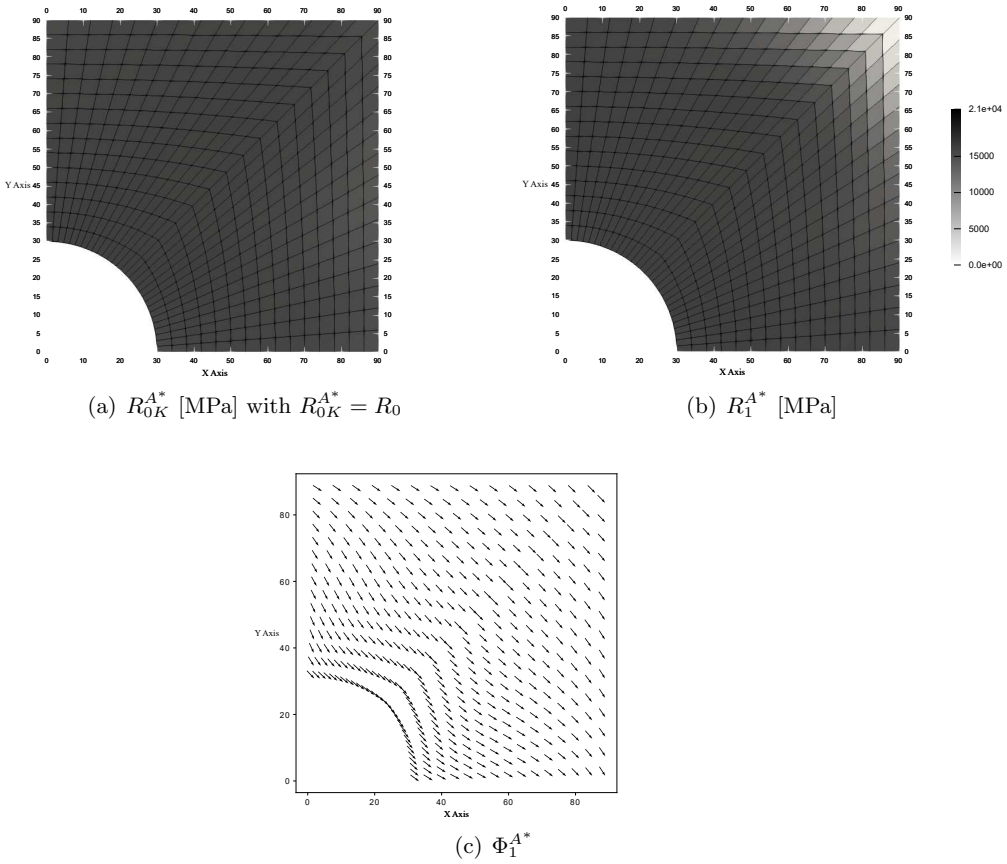

(a) $R_{0K}^{A^*}$ [MPa] with $R_{0K}^{A^*} = R_0$ (b) $R_1^{A^*}$ [MPa]

(c) $\Phi_1^{A^*}$

Figure 6.9: Benchmark 2 - Case 2: optimal distribution of the PPs over the structure.

As it can be immediately inferred from the analysis of these results, regardless of the initial guess, the optimiser converges towards the same local minimum. Accordingly, the optimal PPs fields are identical for each considered case and are illustrated in Fig. 6.9. In this case, the normalised buckling load of the optimised solution is increased of about 25.8% with respect to the solution found by the GA. Of course, the number of iterations to achieve convergence depends on the distance between the initial guess and the local minimum. It can be remarked that, also for benchmark 2, the point-wise variation of the anisotropic polar moduli over the structure does not necessarily imply a significant increase in the K_{cr} factor (the percentage difference between the two best solutions provided in Tables 6.8 and 6.10 is about 1.6%). This means that the influence of the point-wise variation of the main orthotropy axis orientation (related to the polar angle $\Phi_1^{A^*}$) on K_{cr} is predominant over that of the anisotropic moduli. In fact, when looking at the optimal PPs distributions shown in Fig. 6.9, one can notice that the anisotropic moduli are almost uniformly distributed over the plate (apart for a variation of the $R_1^{A^*}$ field near the upper right vertex of the plate). The optimised VAT laminate shows a standard orthotropic behaviour in each point.

Benchmark 2: effect of the loading condition on the optimised solution

The influence of the loading conditions on the optimised solutions is evaluated here. For the sake of brevity, the optimisation analyses have been performed only for the case of uniform dimensionless anisotropic moduli and point-wise variable normalised polar angle. Three values of the load ratio (LR := f_y/f_x) have been considered: 0 (i.e. only f_x is applied), 0.5 and 1. For each case, the isotropic solution has been considered as a starting guess.

The normalised buckling load of the optimised solutions, the optimised anisotropic moduli and the number of iterations are listed in Table 6.11, for each value of LR. The effect of LR on the optimal distribution of the polar angle $\Phi_1^{A^*}$ and on the first buckling mode shape are reported in Figs. 6.10 and 6.11, respectively.

LR	K_{cr}	ρ_0	ρ_1	Iterations
0	3.93	−1.0	0.0	64
0.5	2.08	−1.0	0.0	43
1.0	1.79	−0.70	0.39	37

Table 6.11: Effect of the loading conditions on the optimised solutions.

By looking at Figs. 6.10 and 6.11 and by considering the results listed in Table 6.11, the following remarks can be done.

- Each optimised solution is better than the ISO solution (for a given value of LR). The solution with LR = 0 presents the biggest improvement in the normalised buckling load.
- The optimised solutions with LR = 0 and LR = 0.5 have the same optimised anisotropic moduli and a quite similar distribution of the polar angle $\Phi_1^{A^*}$. These solutions represent a VAT laminate characterised by a square symmetry with the main orthotropy axes oriented at ±45 deg with respect to the local value of $\Phi_1^{A^*}$, see [56, 57].
- The LR = 1 case corresponds to the *Case 1a* reported in Table 6.9. As discussed beforehand, the optimisation algorithm stops into a local minima when the ISO solution is used as a starting guess. In this case a better result can be obtained by using the best individual provided by the ERASMUS code as a starting point.

6.8 Conclusions

In this Chapter the FLP formulation of the MS2LOS for VAT composites has been extended to deal with eigenvalue buckling problems. In particular, the main contribution consists of the derivation of the analytical form of the gradient of the buckling factor by taking advantage of the B-spline surface properties, which are used to represent the laminate PPs fields of the VAT composite. The considered design problem focuses on the maximisation of the first buckling load of a VAT laminate subject to feasibility constraints and geometrical requirements. The closed-form expression of the buckling factor gradient with respect to the design variables has been analytically derived by exploiting the properties of the B-spline blending functions. The algorithms required for the buckling factor gradient assessment have also been presented in this study: they ensure the minimum number of operations for the computation of the gradient in order to speed-up the

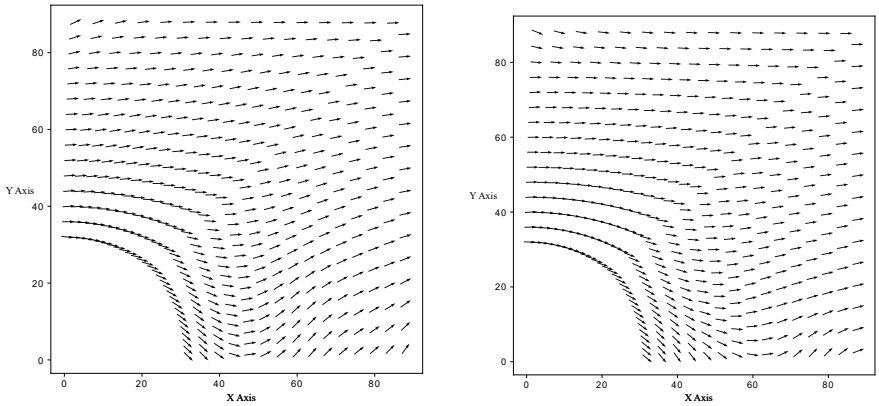

(a) LR = 0

(b) LR = 0.5

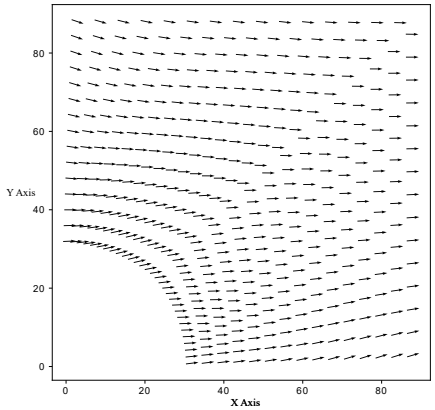

(c) LR = 1

Figure 6.10: Optimal distribution of the polar angle $\Phi_1^{A^*}$ over the structure for the optimised solution listed in Table 6.11.

optimisation process while guaranteeing a high accuracy.

Two test cases have been analysed to prove the effectiveness of the MS2LOS based on the polar formalism. The first benchmark problem, taken from the literature, has been considered to validate the performances of the optimised solutions resulting from the FLP of the MS2LOS through a comparison with those resulting from multi-level approaches based on LPs. The numerical results found here show that the optimised solutions provided by the MS2LOS based on the polar formalism outperform those presented in the literature: the improvement in the normalised buckling factor varies from 12.8% (when using a B-spline surface with 25 CPs to describe the polar angle distribution) to 16.3% (in the case of 81 CPs). In particular, the results presented in this study are very encouraging and show that a significant increase in the buckling strength of VAT composites can be obtained with respect to a reference quasi-homogeneous isotropic solution: up to 130% for benchmark 1 and up to 229% for benchmark 2. The advantages related to the use of B-spline surfaces and to the polar formalism in the context of the MS2LOS, presented in previous publications on the topic (i.e. a strong reduction of the computational costs when compared to FE-based approaches and the continuity of the PPs fields) are once again confirmed here. In addition, two important aspects of the MS2LOS based on the

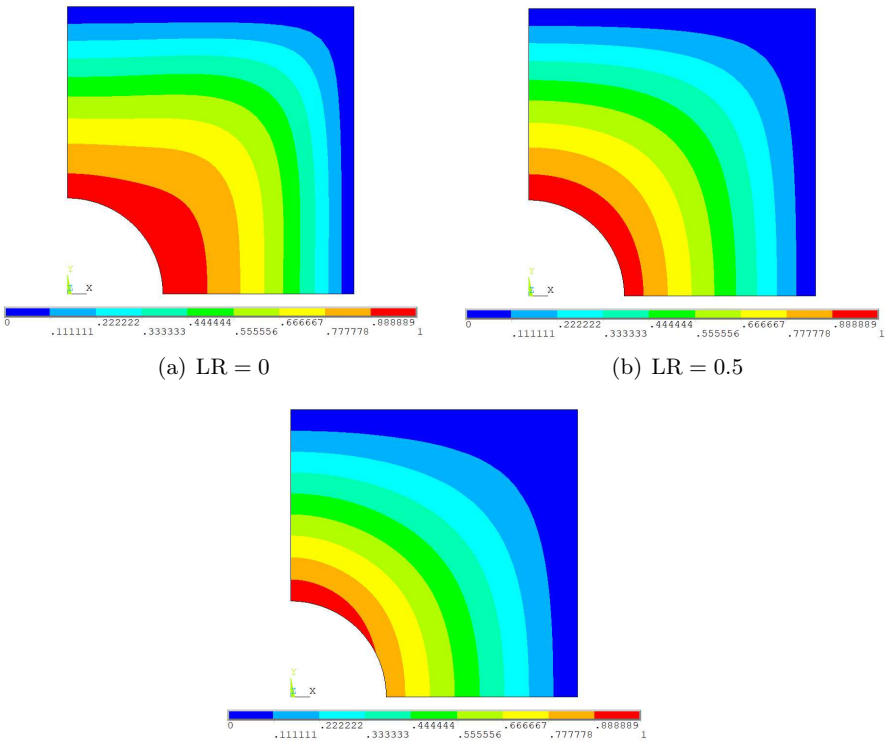

(a) LR = 0

(b) LR = 0.5

(c) LR = 1

Figure 6.11: Mode shape related to the first buckling load for the optimised solutions listed in Table 6.11.

polar formalism should be pointed out: (a) the effectiveness of the representation of the anisotropy based on PPs which allows determining locally the optimal symmetry group; (b) the absence of simplifying hypotheses either on the nature of the stack or on the kind of orthotropy of the laminate stiffness tensors during the FLP (unlike the approaches based on the use of LPs).

Regarding the prospects, some aspects of theoretical, numerical and technological nature deserve a particular attention. The optimisation strategy needs to be tested on more complex benchmarks, e.g. a representative stiffened panel extracted either from the wing or from the fuselage of an aircraft made of VAT composites. In addition, the design problem requires the formalisation of further technological constraints (e.g. gap and overlap between adjacent tows, tow width, the variation of the fibre volume fraction due to imperfections, etc.), related either to the AFP process or to the FFF+CFF technologies, in the FLP theoretical framework in order to get not only an optimised solution but also a manufacturable one. Research is ongoing on these aspects.

Chapter 7

Integration of the global-local modelling approach based on CUF within the MS2LOS

7.1 Introduction

In this Chapter, a modified version of the FLP of the MS2LOS is applied to a simplified wing-box model made of CSC. The aim is to integrate the global-local approach based on CUF discussed in Chapter 3 into the MS2LOS discussed in Chapters 5 and 6. The problem is formulated in terms of the least-weight design of the composite wing-box structure subject to design requirements related to buckling and first-ply failure. This last requirement is verified by using the global-local modelling approach involving a local layer-wise model based on CUF higher-order beam theories. The critical ZOI of the wing-box is identified by means of the tensorial laminate-level failure criterion presented in [60, 95]. In this Chapter, the work-flow of the MS2LOS has been modified in order to integrate the global-local modelling approach based on CUF and to determine feasible SSs satisfying the requirements of the problem at hand. In particular, there is no longer a clear distinction between FLP and SLP, but the two phases of the MS2LOS strongly interact during the optimisation process. More precisely, at the macroscopic scale the laminate behaviour is still described through the use of PPs, which constitute (together with the geometrical parameters) the design variables of the FLP. The solution search of the FLP is carried out through the GA ERASMUS. However, since a requirement on the first-ply failure index has been introduced in the problem formulation and since the most critical ZOI is modelled through a layer-wise FE model, for each individual representing the potential solution of the FLP, a nested genetic optimisation is carried out to find the optimal SS matching the values of the PPs corresponding to this individual and satisfying the requirement on the first-ply failure. The optimal stacking sequence, for each individual of the FLP, is searched in the domain of QT solutions [36, 37].
The Chapter is organised as follows: the problem description and the general work-flow of the design procedure are presented in Section 7.2. In Section 7.3, the mathematical formulation of the optimisation problem and the numerical strategy are detailed. The global FE model of the wing-box and the local 1D CUF model of the ZOI are described in Section 7.4, while the numerical results are discussed in Section 7.5. Finally, Section 7.6 is devoted to concluding remarks and prospects.

7.2 Problem Description

7.2.1 The benchmark structure

The benchmark considered here is a simplified wing-box model made of composite laminates.
The geometry of the structure, taken from [67], the boundary conditions (BCs) and the applied loads are illustrated in Fig. 7.1. The wing-box has a length $L = 3543$ mm, a width $W = 2240$ mm and a height $H = 381$ mm. The wing-box is clamped at $x = 0$ and four concentrated forces are applied at nodes located at $(x,\ y,\ z) = \left(L,\ i\frac{W}{3},\ \frac{H}{2}\right)$, $i = 0, 3$. The magnitudes of the forces are $F_1 = 360.04$ N, $F_2 = 751.55$ N, $F_3 = 751.55$ N and $F_4 = 1520.70$ N.

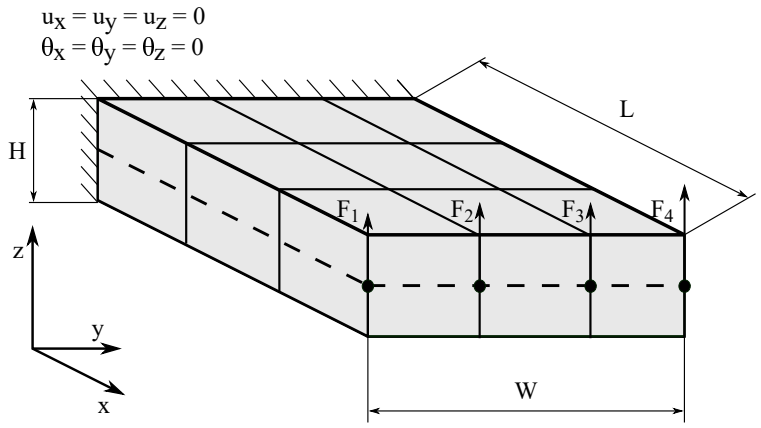

Figure 7.1: Geometry and BCs of the simplified wing-box taken from [67].

In the simplified wing-box, ribs, spars and stringers are replaced by continuous equally spaced composite plates with a pre-defined SS, i.e. $[45^\circ_{11}]_S$. All laminates are made of T300/N5208 graphite-epoxy pre-preg laminæ whose mechanical properties are reported in Table 7.1.

In this study, only dorsal and ventral panels are optimised. Conversely, the laminates constituting ribs, spars and stringers are kept unchanged during the optimisation process. For the sake of clarity, Fig. 7.2 shows the design and non-design regions of the wing box. The design region consists of six panels: three belonging to the dorsal region and three belonging to the ventral one.

As illustrated in Fig. 7.3, each panel of the design region is split into three sub-panels to check the design requirements related to the high-fidelity FE model generated for the most critical ZOI. As stated above, the high-fidelity FE model of the most critical ZOI relies on high-order 1D beam theories (layer-wise kinematics) within the CUF framework [130].

All the results presented in this study are compared to ones obtained for a reference configuration of the wing-box. In particular, the design region of the reference solution is composed of quasi-homogeneous isotropic laminates with a number of plies equal to 20: the total mass of the reference solutions is 261 kg.

Technical constants		PPs of $\mathbf{Q}^a$		PPs of $\tilde{\mathbf{Q}}^b$	
E_1 [MPa]	142000.0	T_0 [MPa]	22040.0	T [MPa]	5272.0
E_2 [MPa]	10300.0	T_1 [MPa]	19838.0	R [MPa]	1928.0
G_{12} [MPa]	7200.0	R_0 [MPa]	14840.0	Φ [deg]	90.0
ν_{12}	0.27	R_1 [MPa]	16550.0		
ν_{23}	0.42	Φ_0 [deg]	0.0		
		Φ_1 [deg]	0.0		

Engineering strengths		PPs of $\mathbf{G}_{\text{in}}{}^{\text{c}}$		PPs of $\mathbf{G}_{\text{out}}{}^{\text{d}}$ and $\mathbf{g}_{\text{in}}{}^{\text{e}}$	
X_t [MPa]	2280.0	Γ_0 [MPa]	7077.0	Γ [MPa]	8637
X_c [MPa]	1440.0	Γ_1 [MPa]	1312.0	Λ [MPa]	1647.0
Y_t [MPa]	57.0	Λ_0 [MPa]	3206.0	Ω [deg]	90.0
Y_c [MPa]	228.0	Λ_1 [MPa]	405.0		
Z_c [MPa]	57.0	Ω_0 [deg]	45.0	γ [MPa]	68.0
S_{23} [MPa]	40.0	Ω_1 [deg]	90.0	λ [MPa]	68.0
$S_{12} = S_{13}$ [MPa]	71.0		θ [MPa]	90.0	
Thickness:				$h_{\text{ply}} = 0.127$ [mm]	
Density:				$\rho = 1.578 \times 10^{-6}$ [Kg/mm^3]	

[a] In-plane reduced stiffness matrix.
[b] Out-of-plane shear stiffness matrix.
[c] In-plane reduced strength matrix.
[d] Out-of-plane strength matrix.
[e] In-plane strength vector.

Table 7.1: Mechanical properties of the T300/5208 carbon-epoxy pre-preg.

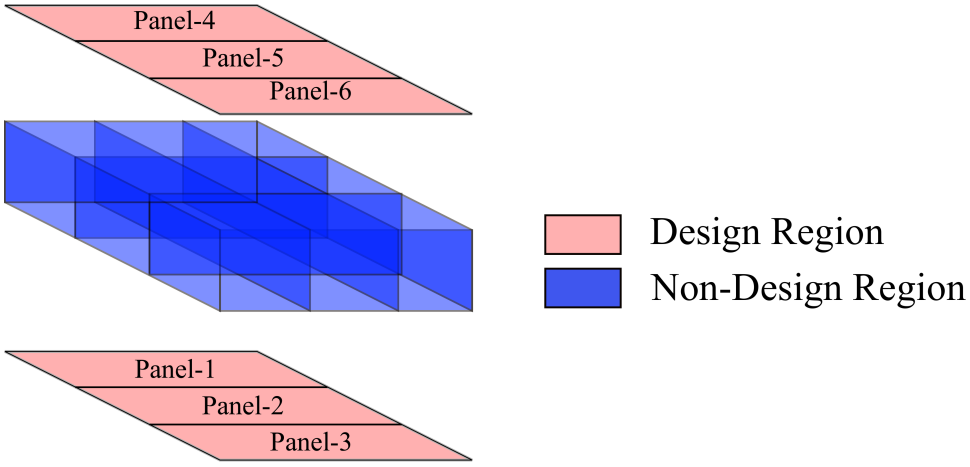

Figure 7.2: Design and non-design regions of the wing-box structure.

7.2.2 The modified MS2LOS

As stated above, the aim of this Chapter is to interface the MS2LOS with the global-local modelling approach based, on the one hand, on a standard FE code to generate the GFEM (to assess the global structural responses) and, on the other hand, on higher-order layer-

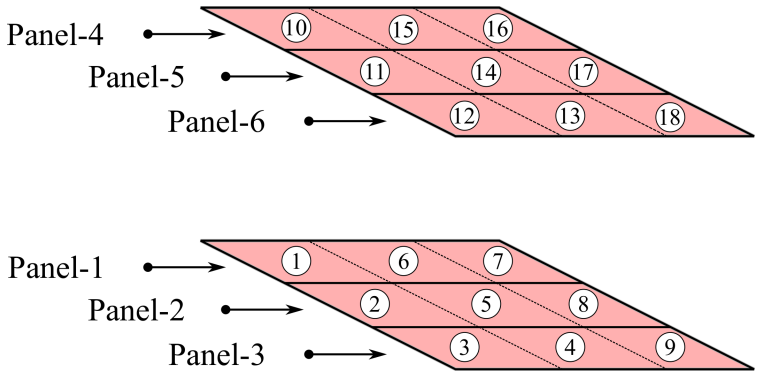

Figure 7.3: Sub-panels composing the design region of the wing-box

wise beam theories in the framework of CUF (to assess local design requirements). The reason is to accurately assess the local structural responses through the use of higher-order formulation to better characterise the mechanical behaviour of the most critical ZOI of the FE model overcoming, thus, the limitations of the FSDT on which the GFEM relies. The work-flow of the modified MS2LOS is illustrated in Fig. 7.4.

As stated above, the goal is to minimise the mass of the structure subject to the following design requirements: buckling factor, feasibility constraints on PPs of the laminates composing the wing-box, first-ply failure on the most critical regions. As illustrated in Fig. 7.4, the modified architecture of the MS2LOS is composed of two interdependent optimisation loops. The solution search for both loops is performed through the GA ERASMUS [5]. The outer loop represents the structural optimisation where both GFEM (built within ANSYS®) and LFEM (generated within CUF framework) are interfaced with ERASMUS. The inner loop represents the lay-up design of the SLP (this step is fully analytical, see Section 5.5), which is performed only for the most critical ZOI of the design region of the wing-box. In particular, during the outer loop, for each individual of each population, ERASMUS passes the vector of design variables $\mathbf{x}_{\text{out}}$ (see Section 7.3 for more details) to the GFEM, which is invoked to assess the mass of the wing-box, the first buckling factor and the LFI according to the formulation proposed by Catapano and Montemurro in [60, 95]. The LFI is then used to identify the most critical ZOI among the sub-panels constituting the design region of the wing-box, as shown in Fig. 7.3. It is noteworthy that the GFEM is generated by considering the definition of the laminates (constituting the wing-box) based on the PPs in the FSDT framework. Once the most critical panel of the wing-box is identified, the SLP is resolved on-the-fly to find, at least, one optimal SS meeting the current value of PPs and thickness (included in the vector of design variables $\mathbf{x}_{\text{out}}$, see Section 7.3) for the selected ZOI. It is noteworthy that the SS solutions of the SLP are searched in the space of QT solutions, as discussed in Sections 4.6 and 5.5. Once the optimal SS is found, it is passed to the LFEM based on layer-wise high-order beam theories to assess the ply failure index (the CUF environment is invoked to achieve this task). Finally, all requirements (from both GFEM and LFEM) are passed to ERASMUS (outer loop) to perform the genetic operations (selection, crossover, mutation, penalisation, elitism, etc.) until the convergence criterion is met.

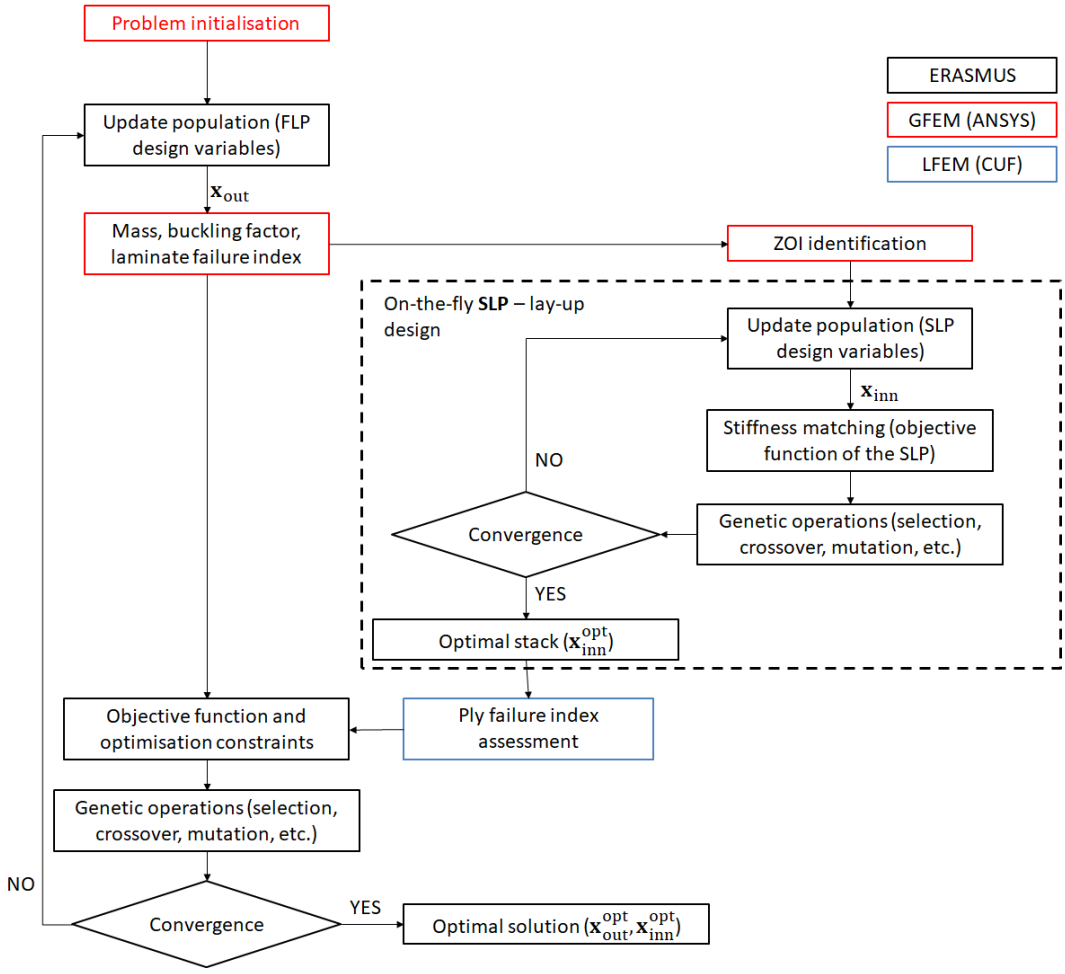

Figure 7.4: Work-flow of the modified MS2LOS.

7.3 Problem formulation

This Section is devoted to the problem formulation description by highlighting the main features (design variables, objective function, optimisation constraints) of both outer and inner loop of the process illustrated in Fig. 7.4.

7.3.1 Design variables of the outer optimisation loop

The outer optimisation loop focuses on the structural optimisation by considering the structural responses assessed through both GFEM and LFEM. Inasmuch as the local response of the structure, assessed by means of the LFEM, depends upon the macroscopic behaviour of the most critical ZOI extracted from the GFEM (this task is done via the evaluation of the LFI, as discussed in the following), and since the elastic and strength behaviours of the laminates composing the GFEM are described in the PPs space, the design variables of the outer loop are the laminate PPs and some geometric parameters (i.e. overall thickness and number of saturated groups of the QT solutions, as discussed in the following).

In particular, the laminates composing the design region of the wing-box are quasi-homogeneous and fully-orthotropic (both membrane and bending stiffness tensors). Therefore, the macroscopic behaviour of each laminate, in the FSDT framework, is uniquely described by three dimensionless PPs: ρ_0, ρ_1, ϕ_1, see Eq. (6.7). Moreover, the main direction of the orthotropy axis is assumed aligned with the x-axis of the wing-bow structure (see Fig. 7.1): accordingly, $\phi_1 = 0$ for each panel.
The variable change proposed by Izzi *et al.* [98] is used here to avoid the introduction of the feasibility constraint on the PPs within the problem formulation, unlike the strategy presented in Chapter 5. This approach consists of remapping over a unit square $[0,1] \times [0,1]$ the feasible domain of PPs identified by Eq. (5.10) through the following variables change:

$$(\alpha_0, \alpha_1) \coloneqq \left(\frac{\rho_0 - 1}{2\left(\rho_1^2 - 1\right)}, \rho_1 \right), \tag{7.1}$$

whose converse relation is

$$(\rho_0, \rho_1) = \left(1 + 2\alpha_0\left(\alpha_1^2 - 1\right), \alpha_1\right) \tag{7.2}$$

In this way, all the combinations of α_0 and α_1 automatically satisfy the feasibility conditions of Eq. (5.10), without the need of introducing explicit constraints into the problem formulation.
Two further geometric variables complete the set of design variables of the outer optimisation loop: the number of layers n_l and the number of saturated groups n_g for all the panels of the design regions. The number of layers n_l is needed to calculate the overall thickness of the laminate $h = n_l h_{\text{ply}}$, whilst the number of saturated group n_g is used within the inner optimisation loop (i.e. the on-the-fly resolution of the SLP for the most critical ZOI) to correctly select the family of QT solutions within the database generated via the algorithm described in [37]. Indeed, as explained in [37], the number of QT staks depends upon the combination of n_l and n_g.
The design variables of the outer optimisation loop are, thus, collected in the following vector:

$$\mathbf{x}_{\text{out}}^{\text{T}} \coloneqq \left(\rho_{0i}, \rho_{1i}, n_{li}, n_{gi}\right), \; i = 1, \ldots, n_p, \tag{7.3}$$

where $n_p = 6$ represents the number of panels composing the design region of Fig. 7.2.

7.3.2 Design variables of the inner optimisation loop

As discussed above, the inner optimisation loop, shown in Fig. 7.4, consists in solving on-the-fly the SLP by searching the solution in the database of QT stacks [37]. As discussed in Sections 4.6 and 5.5, QT SSs are closed form solutions that satisfy the requirements of membrane/bending uncoupling and homogeneity (membrane and bending normalised stiffness tensors are equal) regardless of the values of the orientation angles of the layers. Therefore, by means of a dedicated algorithm [37], it is possible to generate the database of QT solutions for a given pair of number of layers n_l and number of saturated groups n_g. This database was already available at the I2M laboratory as a result of the work by Garulli *et al.* [37].

Inasmuch as the number of QT solutions n_{sol} depends on the couple n_l, n_g, i.e. $n_{\text{sol}} = n_{\text{sol}}\left(n_l, n_g\right)$ it is useful to introduce a design variable related to the identifier ID_{sol} (i.e. an integer) that varies in the range $[1,\ n_{\text{sol}}\left(n_l, n_g\right)]$, which uniquely identifies the solution within the database for a given pair of number of layers and number of saturated groups.

Moreover, the orientation angle associated to each saturated group, i.e. θ_k, $k = 1, \ldots, n_g$ is also included within the design variables vector of the inner loop that reads:

$$\mathbf{x}_{\text{inn}}^{\text{T}} \coloneqq \left(\text{ID}_{\text{sol}},\ \theta_1, \ldots,\ \theta_{n_g}\right). \tag{7.4}$$

7.3.3 Objective function of the inner optimisation loop

Since the goal of the inner optimisation loop is to find, at least, one SS meeting the value of the PPs related to the current individual (of the generic population) of the outer loop, the objective function to be minimised is the function $I\left(f_i\left(\mathbf{x}_{\text{out}},\ \mathbf{x}_{\text{inn}}\right)\right)$ of Eq. (5.16). The expression of functions f_i, $(i = 1, \ldots, 6)$ is provided in Eq. (5.17). The SLP to be solved on-the-fly, for each individual of each population of the outer loop, can be formulated as an unconstrained non-linear programming problem (UNLPP) as:

$$\min_{\mathbf{x}_{\text{out}}} I\left(f_i\left(\mathbf{x}_{\text{out}},\ \mathbf{x}_{\text{inn}}\right)\right). \tag{7.5}$$

The properties of the SLP of Eq. (7.5) have been already discussed in Section 5.5. As discussed in Section 5.5, the GA ERASMUS is used to perform the solution search of problem (7.5). The genotype of the individual of the inner loop depends upon the value of the number of saturated groups n_g related to the current individual of the outer loop. In particular, the genotype of the generic individual of the inner optimisation loop is characterised by $n_g + 1$ genes: the first one codes the solution identifier ID_{sol}, whilst the remaining ones code the orientation angles of the n_g saturated groups. Each angle can take values in the interval $[-89,\ 90]$ deg with a step of 1 deg.

7.3.4 Objective function and optimisation constraints of the outer optimisation loop

The goal of the optimisation process illustrated in Fig. 7.4 is to minimise the mass of the wing-box that constitutes, thus, the merit function of the problem at hand. The mass of the wing-box reads:

$$M(\mathbf{x}_{\text{out}}) \coloneqq \rho_{\text{ply}} V(\mathbf{x}_{\text{out}}), \tag{7.6}$$

where $V(\mathbf{x}_{\text{out}})$ is the overall volume of the GFEM of the wing-box.

The first design requirement, to be included in the problem formulation, consists of a constraint on the first buckling factor λ of the structure. The constraint function reads:

$$g_1(\mathbf{x}_{\text{out}}) \coloneqq 1 - \lambda, \tag{7.7}$$

where the first buckling factor λ is the result of an eigenvalue buckling analysis conducted on the GFEM of the structure, i.e.

$$\left(\mathbf{K}_{\text{G}} + \lambda \mathbf{K}_{\sigma\text{G}}\right) \boldsymbol{\psi}_{\text{G}} = \mathbf{0}, \tag{7.8}$$

where $\mathbf{K}_{\text{G}}$ is the stiffness matrix of the GFEM, $\mathbf{K}_{\sigma\text{G}}$ is the geometric stiffness matrix of the GFEM, while $\boldsymbol{\psi}_{\text{G}}$ is the eigenvector related to the first buckling factor λ.
The second and third design requirements deal with the first-ply failure and delamination, respectively, which are assessed by checking a set of inequalities after carrying out a static analysis on the LFEM of the most critical ZOI. As discussed in Section 7.4, the most critical ZOI is identified and isolated by checking the local laminate failure index calculated from the laminate-level failure criterion presented in Section 4.4. Once the most critical ZOI

is identified, the LFEM is generated by using a high-order beam theory with a layer-wise kinematics in the CUF framework.

In particular, as discussed in Section 7.4, the LFEM is subjected to geometrical BCs, which are calculated from the results of a static analysis conducted on the GFEM (and opportunely transferred to the LFEM) as follows:

$$\mathbf{K}_{\mathrm{G}}\mathbf{u}_{\mathrm{G}} = \mathbf{f}_{\mathrm{G}}, \tag{7.9}$$

$$\mathbf{K}_{\mathrm{L}}\mathbf{u}_{\mathrm{L}} + \tilde{\mathbf{K}}_{\mathrm{L}}\tilde{\mathbf{u}}_{\mathrm{L}} = \mathbf{0}, \tag{7.10}$$

with

$$\tilde{\mathbf{u}}_{\mathrm{L}} \coloneqq \mathbf{P}\mathbf{u}_{\mathrm{G}}. \tag{7.11}$$

In Eq. (7.9), $\mathbf{u}_{\mathrm{G}}$ and $\mathbf{f}_{\mathrm{G}}$ are the vectors of generalised displacements and external forces applied to the GFEM, respectively. In Eq. (7.10), $\mathbf{u}_{\mathrm{L}}$ and $\tilde{\mathbf{u}}_{\mathrm{L}}$ are the unknown and imposed generalised displacements of the LFEM, whilst matrices $\mathbf{K}_{\mathrm{L}}$ and $\tilde{\mathbf{K}}_{\mathrm{L}}$ are the stiffness matrices of the LFEM after the application of the BCs of the Dirichlet type.
As stated above, the BCs applied to the LFEM in terms of generalised displacements $\tilde{\mathbf{u}}_{\mathrm{L}}$ on the LFEM boundary depend upon the results of a static analysis conducted on the GFEM $\mathbf{u}_{\mathrm{G}}$. The matrix $\mathbf{P}$ of Eq. (7.11) represents such transformation.

Once the results of the static analysis carried out on the LFEM are available, the first-ply failure is evaluated by using the Hashin's failure criteria for the prediction of ply failure [177] together with the mixed mode quadratic criteria to determine the onset of delamination [178]. All failure criteria considered in this study are assessed at the ply-level

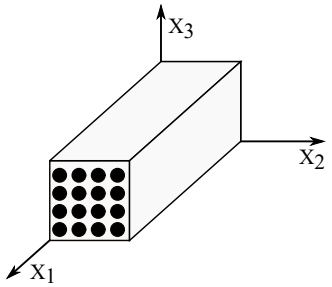

Figure 7.5: Local frame orientation for the assessment of first-ply failure and delamination related design requirements.

by considering the material coordinate system shown in Fig. 7.5. For the sake of clarity, the Hashin's failure criteria and the delamination criterion used in the formulation of the optimisation problem are briefly described here below.

- Hashin's failure criteria. This set of criteria is used to determine the first-ply failure based on the stress state and to determine the dominating failure mode at the ply-level. The inequalities to be checked (and corresponding to different failure modes for both fibre and matrix) are:

  1. Fibre Tension:

$$g_2(\mathbf{x}_{\mathrm{inn}}) \coloneqq \left(\frac{\sigma_{11}^2}{X_T}\right)^2 + \frac{\sigma_{12}^2 + \sigma_{13}^2}{S_{13}^2} - 1, \tag{7.12}$$

2. Fibre Compression:

$$g_3(\mathbf{x}_{\text{inn}}) \coloneqq \left(\frac{\sigma_{11}^2}{X_C}\right)^2 - 1, \tag{7.13}$$

3. Matrix Tension:

$$g_4(\mathbf{x}_{\text{inn}}) \coloneqq \frac{(\sigma_{22}+\sigma_{33})^2}{Y_T^2} + \frac{\sigma_{23}-\sigma_{22}\sigma_{33}}{S_{23}^2} + \frac{\sigma_{12}^2+\sigma_{13}^2}{S_{12}^2} - 1, \tag{7.14}$$

4. Matrix Compression:

$$g_5(\mathbf{x}_{\text{inn}}) \coloneqq \left[\left(\frac{Y_C}{2S_{23}}\right)^2 - 1\right]\left(\frac{\sigma_{22}+\sigma_{33}}{Y_C}\right) + \frac{(\sigma_{22}+\sigma_{33})^2}{4S_{23}^2} + \tag{7.15}$$

$$+ \frac{\sigma_{23}^2-\sigma_{22}\sigma_{33}}{S_{23}^2} + \frac{\sigma_{12}^2+\sigma_{13}^2}{S_{12}^2} - 1. \tag{7.16}$$

In the previous formulæ, σ_{ij} represents the generic component of the stress tensor in the material coordinate system. X and Y represent the material strength along x_1 and x_2 axes, respectively; the subscript T stands for tensile loading and C for compressive one. S_{ij} denotes the material shear strength in the plane $x_i - x_j$. Of course, if all the above expressions are lower than or equal to zero no failure occurs.

- Delamination onset criterion. The delamination onset is determined by means of the mixed mode quadratic criterion as:

$$g_6(\mathbf{x}_{\text{inn}}) \coloneqq \left(\frac{<\sigma_{33}>}{Z_T}\right)^2 + \left(\frac{\sigma_{23}}{S_{23}}\right)^2 + \left(\frac{\sigma_{13}}{S_{13}}\right)^2 - 1, \tag{7.17}$$

where $<\sigma_{33}> \coloneqq \max(0, \sigma_{33})$ is the transverse normal stress in the material coordinate system (which must be considered if and only if σ_{33} is positive, i.e. when it tends to separate adjacent plies). σ_{13} and σ_{23} are the transverse shear stresses, Z_T is the interlaminar normal strength while S_{13} and S_{23} are the transverse shear strengths. If the above expression is lower than or equal to zero no delamination occurs.

It is noteworthy that the above failure criteria require the assessment of the 3D stress field within each lamina. This task is achieved through local analysis of the ZOI by means of a layer-wise 1D CUF model, which accurately describe the stress field. The least-weight design of the wing-box structure can, now, be formulated as a CNLPP as follows:

$$\begin{aligned}
&\min_{\mathbf{x}_{\text{out}}} M(\mathbf{x}_{\text{out}}),\\
&\text{subject to:}\\
&\begin{cases}
\text{Eq. (7.8)}\\
\text{Eq. (7.9)}\\
\text{Eq. (7.10)}\\
\text{Eq. (7.5)}\\
g_1(\mathbf{x}_{\text{out}}) \le 0,\\
g_j(\mathbf{x}_{\text{inn}}) \le 0,\ j = 2,\dots,6.
\end{cases}
\end{aligned} \tag{7.18}$$

It is noteworthy that problem (7.18) is a non-standard non-convex CNLPP. The non-convexity is due, on the one hand, to the nature of the constraint functions involved in the problem formulation, and, on the other hand, on the strong coupling between global and local FE models (and, consequently, between the two loops constituting the whole optimisation process). In particular, according to the flow-chart illustrated in Fig. 7.4, the solution of the outer optimisation loop, i.e. $\mathbf{x}_{\text{out}}$ depends upon the solution of the SLP (inner optimisation loop), i.e. $\mathbf{x}_{\text{inn}}$, which is solved on-the-fly for each individual of the outer optimisation loop.

This dependency among the two set of variables is governed by a sort of strong coupling. One the one hand, the solution of the UNLPP of Eq. (7.5), i.e. the SLP of the inner loop, depends upon the current value of the design variable of the outer loop (related to the generic individual). On the other hand, the optimal solution of the outer loop must satisfy the optimization constraints g_j $(j = 2, \ldots, 6)$, which are evaluated on the LFEM, whose value depends upon the optimal solution of the inner loop.

Design variable	Type	Lower bound	Upper bound	Discretisation step
α_0	continuous	0.0	1.0	-
α_1	continuous	0.0	1.0	-
n_l	integer	13	30	1
n_g	integer	1	5	1

Table 7.2: Bounds on the design variables of the outer optimisation loop.

As stated in Section 7.2, the ERASMUS code [5] is used to carry out the solution search for both outer and inner optimisation loops. The bounds and the nature of the design variables involved in the outer loop are reported in Table 7.2, while the design variables of the inner loop have already been discussed in Section 7.3.3. The genotype of the generic individual of the outer optimisation loop is characterised by six chromosomes (one for each panel), each one composed of four genes, where each gene is related to a component of the design variables vector of the outer loop.

As shown in Fig. 7.4, the GA ERASMUS is coupled with the ANSYS FE commercial software to calculate the mass, the LFI distribution within the design region and the first buckling factor of the wing-box and with MUL2@GL code for check the ply-level failure modes of the most critical ZOI. Therefore, for each individual generated by the GA ERASMUS, at each iteration of the outer optimisation loop, three FE analyses are carried out: a static analysis (to assess the LFI distribution) and an eigenvalue buckling analysis on the GFEM of the wing-box structure and a static analysis on the LFEM of the ZOI to check the first-ply failure and delamination onset. The LFEM requires as input the SS of the sub-panel, which is not provided by the outer optimisation loop optimisation. Accordingly, a further local optimisation (inner loop) is necessary to determine the SS of the ZOI. To this purpose, the SLP of the MS2LOS is solved on-the-fly (for each individual of the outer loop) by means of the ERASMUS algorithm providing, in this way, the optimal SS in the space of QT solutions. Once the QT SS is obtained, the MUL2@GL code computes the design requirements related to the first-ply failure and to the delamination onset. These software are interfaced by means of a routine programmed in Python language.
At each iteration of the outer optimisation loop, the outputs are the value of the objective

function and of the constraints functions. ERASMUS elaborates the results provided by the FE analyses to perform the genetic operations. The outer loop is repeated until the user-defined convergence criterion is satisfied.

7.4 The finite element models

7.4.1 The global finite element model of the wing-box

As discussed above, two FE models of the wing-box structure are interfaced with the outer optimisation loop shown in Fig. 7.4: the GFEM of the whole wing-box and the LFEM of the most critical sub-panel belonging to the design region.
The FE model of the wing-box is automatically generated by means of an ad-hoc APDL script. The geometry and the mesh of the GFEM are opportunely parameterized and depend upon the input variables passed from ERASMUS to the APDL script. The mesh and the BCs of the GFEM are illustrated in Fig. 7.6. As far as BCs are concerned, $u_j = 0$, $\theta_j = 0$ $(j = x, y, z)$ is set on nodes located at $x = 0$, while four point loads are applied on the nodes located at $x = L$ as discussed in Section 7.2.
Two analyses are then executed on the GFEM: a static analysis to assess the LFI distribution and an eigenvalue buckling analysis to compute the first buckling factor of the structure.

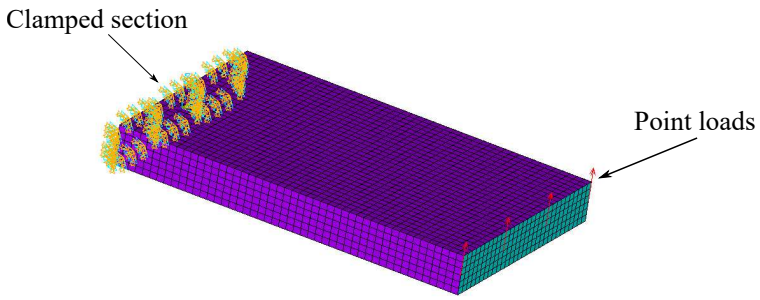

Figure 7.6: Mesh and BCs of the GFEM of the wing-box structure.

The mesh of the GFEM is composed of four-node ANSYS SHELL181 elements with six DOFs per node (FSDT framework using the implicit definition of the laminate constitutive matrices). A mesh convergence analysis, not reported here for the sake of synthesis, has been carried out to calibrate the mesh size in order to find a compromise between accuracy and computational costs. As a result of this sensitivity analysis, the element size has been set equal to 80 mm for an overall number of elements $N_{eG} = 4500$.

7.4.2 ZOI identification: the laminate-level failure criterion

The identification (and isolation) of the ZOI, which corresponds to one of the sub-panels constituting the design region of the wing-box, as shown in Fig. 7.3, is done by evaluating the local LFI according to the laminate-level failure criterion proposed by Catapano and Montemurro in [60, 95] and briefly discussed in Section 4.4. In particular, let Ω_{DR} be the set of elements constituting the design region. It is possible to define the maximum LFI as follows:

$$\mathrm{FI}_{\mathrm{lam,max}} \coloneqq \max_{e \in \Omega_{\mathrm{DR}}} \mathrm{FI}_{\mathrm{lam},e}, \tag{7.19}$$

where $\mathrm{FI}_{\mathrm{lam},e}$ is the LFI of Eq. (4.32) evaluated at the centroid of each element belonging to Ω_{DR}.
Let $e_{\max}$ be the ID of the element having the maximum LFI. Let $\Omega_{\mathrm{SP},j}$, $(j = 1, \ldots, 18)$ be the set of elements constituting the j-th sub-panel of the design region. Of course, $\Omega_{\mathrm{DR}} \Cup_{j=1,\ldots,18} \Omega_{\mathrm{SP},j}$. Finally, the most critical ZOI corresponds to the j-th sub-panel to which $e_{\max}$ belongs. Subsequently, this panel is extracted from the GFEM and meshed by using high-order 1D layer-wise elements as discussed in the following.

7.4.3 The local finite element model

The LFEM of the most critical ZOI is automatically generated by the Python interface after a post-processing phase of the results of the static analysis conducted on the GFEM. As discussed above, the LFI distribution is used to identify, isolate and extract the most-critical sub-panel of the design region of the wing-box, which constitutes the ZOI to be modelled via high-order theories. In particular, as illustrated in Fig. 7.7, the LFEM of the ZOI is composed of three high-order four-node beam elements (B4) belonging to the LE class. The beam cross-section is made of eight L9 sub-domains along the y-axis and one L9 sub-domain per ply along the z axis. BCs of the Dirichlet type are imposed on the LFEM boundary. In particular, the DOFs of the nodes located on the boundary of the most-critical sub-panel are recovered from the results of the static analysis performed on the GFEM and transferred to the LFEM. To correctly ensure the transfer of the BCs from the GFEM to the LFEM (which are characterised by different meshes and different element types) the DOFs evaluated at the nodes belonging to the skin of the sub-panel of the GFEM are interpolated and transferred to the nodes located on the boundary of the sub-domains of the cross-section of each beam element composing the LFEM (as shown in Fig. 7.7) according to Eq. (7.11). Finally, a static analysis is conducted on the LFEM to have an accurate assessment of the local stress field, which is of paramount importance to correctly predict the first-ply failure and the delamination onset according to the criteria of Eqs. (7.12) - (7.17). This is the main goal of the LFEM based on high-order beam elements developed in the CUF framework.

7.5 Numerical results

As stated in the introduction of this Chapter, the least-weight design problem of a composite wing-box structure is faced in this study. A modified version of the MS2LOS is employed to solve the problem and the global-local modelling approach based on higher-order layer-wise beam theories in the framework of CUF is used to locally verify the FI constraint of the critical ZOI of the wing-box during its optimisation. The aim is to optimise the stiffness/strength properties of the laminates constituting the wing-box while minimising its mass. The genetic parameters tuning the behaviour of the GA ERASMUS utilised to perform the solution search for both outer and inner loops of the optimisation strategy discussed in Section 7.2.2 are listed in Table 7.3.
Moreover, regarding the constraint-handling technique used in the outer loop, the ADP method has been considered [154]. For more details on the numerical techniques developed within the new version of ERASMUS and the meaning of the values of the different

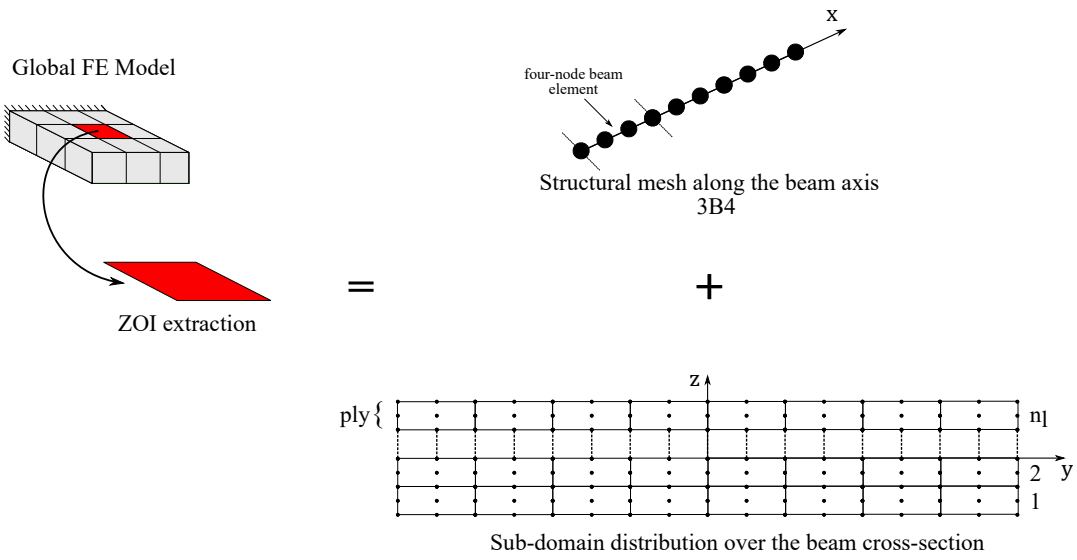

Figure 7.7: Layer-wise high-order LFEM.

Genetic parameters		
	Outer loop	Inner loop
N. of populations	1	1
N. of individuals	480	70
N. of generations	100	100
Crossover probability	0.85	0.85
Mutation probability	0.01	0.02
Selection operator	roulette-wheel	tournament selection
Elitism operator	active	active

Table 7.3: Genetic parameters of the GA ERASMUS for the outer and inner loops.

parameters tuning the algorithm the reader is addressed to [5].
Table 7.4 lists the mass of the optimised configuration with respect to the reference one, instead Table 7.5 reports the optimised set of the outer loop design variables for each panel of the wing-box design region.

	Mass $[kg]$	Mass reduction %
Reference solution	261	–
Optimised solution	234.05	10.33

Table 7.4: Mass of the reference and the optimised configurations of the wing-box.

Fig. 7.8 illustrates the value of the objective function for the best individual (within the population) vs. the number of generations: one can notice that the convergence towards the optimised configuration of the wing-box is achieved after 25 iterations of the outer loop.
The mode shape related to the first buckling load for both reference and optimised solutions

	ρ_0	ρ_1	n_l	n_g
Panel 1	0.77	0.91	16	3
Panel 2	0.85	0.58	13	3
Panel 3	0.46	0.08	14	3
Panel 4	0.43	0.14	21	2
Panel 5	0.21	0.32	23	3
Panel 6	−0.67	0.14	16	3

Table 7.5: Optimal value of the design variables of the outer optimisation loop (the dimensionless polar parameters are reported instead of the values of α_0 and α_1).

Outer loop	Inner loop
$\rho_0 = 0.77$	
$\rho_1 = 0.91$	$[2°/-16°/12°/2°/12°/2°/2°/-16°/$
$n_l = 16$	$-16°/2°/2°/12°/2°/12°/-16°/2°]$
$n_g = 3$	

Table 7.6: Optimal value of the design variables of both outer and inner loops of the ZOI (sub-panel 1 in Fig. 7.3).

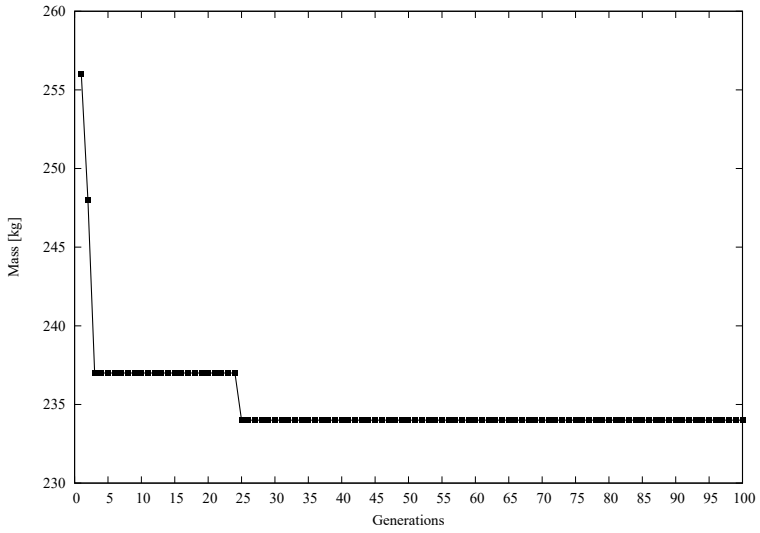

Figure 7.8: Mass vs. number of generations for the best individual during the optimisation process.

is shown in Fig. 7.9, whilst the distribution of the LFI over the elements constituting the design region of the wing-box structure is illustrated in Fig. 7.10 for both solutions. From the analysis of these results, it can be immediately inferred that the most critical zone of the design region is the sub-panel 1 belonging to panel 1, which is selected as a ZOI (the LFI gets the highest values for some elements belonging to this sub-panel). The optimal value of the design variables of the outer loop together with the optimal stacking sequence found at the end of the inner loop for the ZOI are reported in Table 7.6 and the polar diagrams of the homogenised stiffness matrices are depicted in Fig. 7.11 for

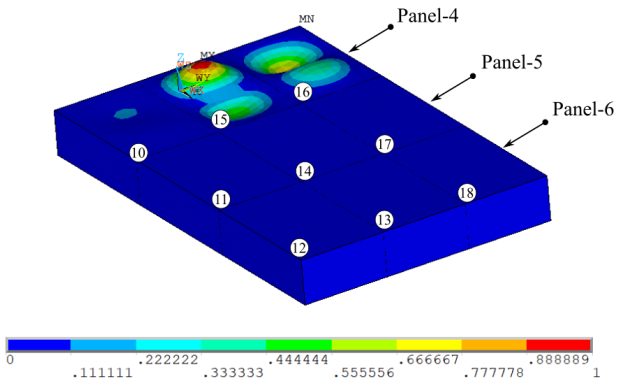

(a) $\lambda_{\text{ref}} = 1.029$

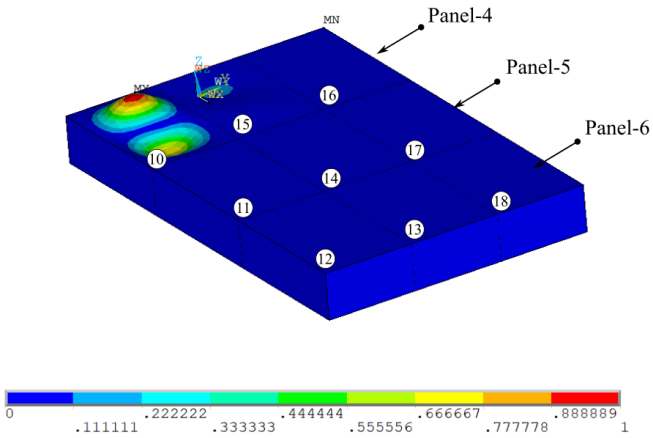

(b) $\lambda_{\text{opt}} = 1.034$

Figure 7.9: Mode shape related to the first buckling load for (a) reference solution and (b) optimised solution.

the best individual reported the in Table 7.6. The through-the-thickness variation of the in-plane stress field ($\sigma_{ij},\ i,j = x,y$) evaluated at the centre of the ZOI for the optimal stack provided in Table 7.6 is illustrated in Fig. 7.12. No out-plane stresses are represented here because they are negligible whit respect to the in-plane ones

The following remarks can be drawn from the analysis of these results. In terms of the first buckling load, the optimised solution is very close to the reference one and the local buckling occurs in sub-panel 10 of panel 4, whilst in the reference solution the local buckling occurs, essentially, in sub-panels 15 and 16, as illustrated in Fig. 7.9. As reported in Table 7.4, the optimised solution is 10.33% lighter than the reference one, which is a quite good achievement and demonstrates the effectiveness of this proposed approach in solving the least-weight design problem for the simplified composite wing-box considered in this study. As summarised in Table 7.5, each panel composing the design region is characterised by a standard orthotropic behaviour (with $K^{A^*} = 0$ because ρ_0 is positive), except panel 6, which shows the so-called "dog bone" orthotropy (i.e., with $K^{A^*} = 1$ because ρ_0 is negative). Figure 7.11 highlights two important aspects of the optimal stacking sequence characterising the ZOI: the solution is perfectly decoupled and homogeneous (thanks to the use of QT solutions), and it is totally orthotropic in membrane and bending (the

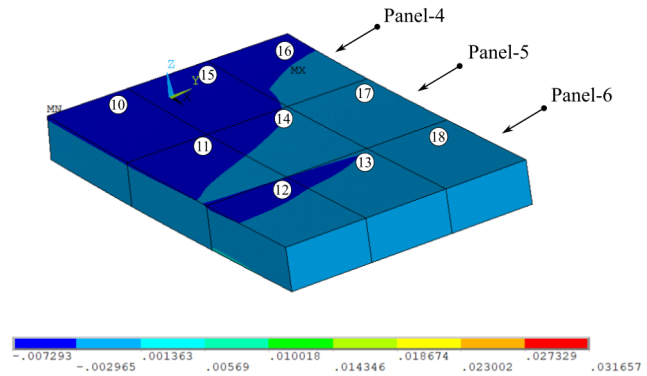

(a) Up view

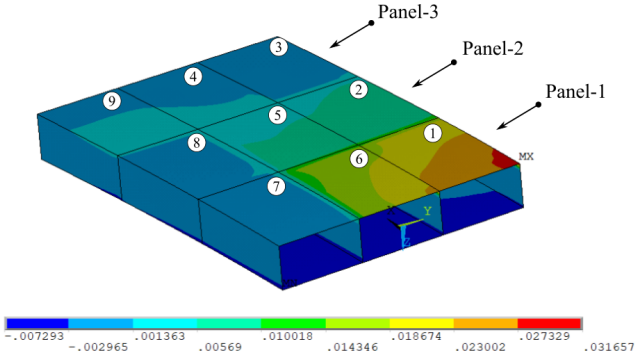

(b) Bottom view

Figure 7.10: Distribution of the LFI in the design region of the wing-box structure.

polar diagram is characterised by two axes of symmetry) with the main axis of orthotropy oriented at 0°. It is noteworthy that these properties have been obtained with a general QT stack which is neither symmetric nor balanced: this is due to the great potential behind the polar formalism in describing the elastic behaviour of laminates without using symplifying hypotheses on the nature of the stacks.
Finally, although the local analysis of the ZOI through the global-local modelling approach based on higher-order layer-wise beam theories allows describing the through-the-thickness variation of the stress field in a way more accurate than commercial FE codes, in the case study considered here, the optimal stack is not characterised by particular issues in term of neither first-ply failure nor delamination.

7.6 Conclusions

A modified version of the MS2LOS has been proposed in this chapter and has been applied to the least-weight design problem of a simplified composite wing-box structure subject to design requirements related to first buckling load, delamination and first-ply failure. The contribution of this work is to integrate the global-local approach based on CUF discussed in Chapter 3 into the MS2LOS discussed in Chapters 5 and 6 with major modifications

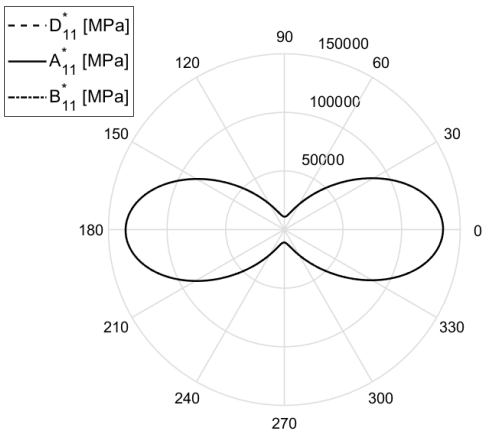

(a) First component of homogenised stiffness matrices $\mathbf{A}^*$, $\mathbf{B}^*$ and $\mathbf{D}^*$

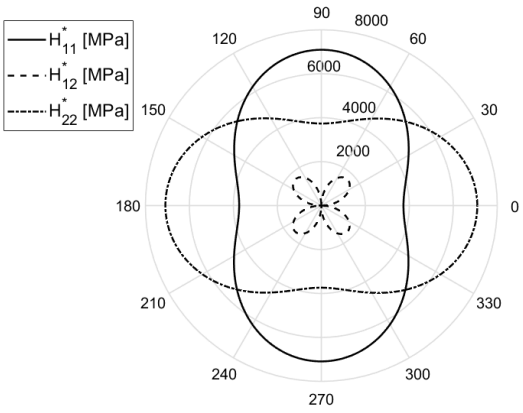

(b) Homogenised shear stiffness matrix $\mathbf{H}^*$

Figure 7.11: Homogenised stiffness matrices of the best individual reported in Tab.7.6.

on the overall architecture of the MS2LOS. In particular, the first-ply failure and the delamination requirements are verified by using the global-local modelling approach, based on the CUF framework, through a local layer-wise model whose kinematics relies on higher-order beam theories. In this work, the work-flow of the MS2LOS has been modified to integrate the global-local modelling approach; there is no longer a clear distinction between FLP and SLP because the two phases of the MS2LOS strongly interact during the optimisation process. At the macroscopic scale, the laminate behaviour is still described through the use of PPs, which constitute (together with the geometrical parameters) the design variables of the FLP. The solution search of the FLP is carried out through the GA ERASMUS. Instead, at the mesoscopic scale, since requirements on the first-ply failure index and on the delamination have been introduced in the problem formulation, and since the most critical ZOI is modelled through a layer-wise FE model, for each individual representing the potential solution of the FLP, a genetic optimisation is carried out to find,

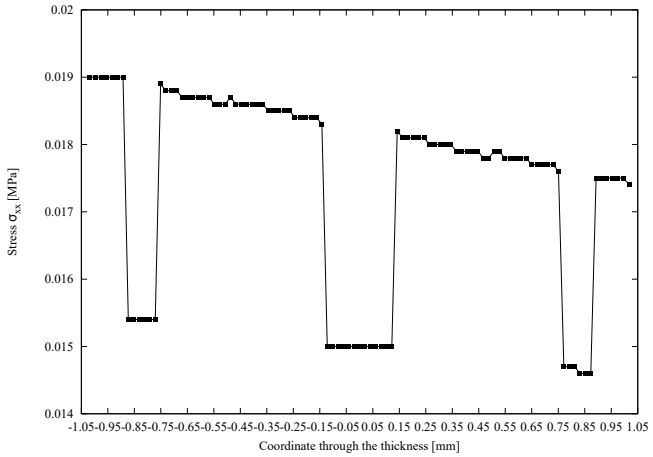

(a) σ_{xx}

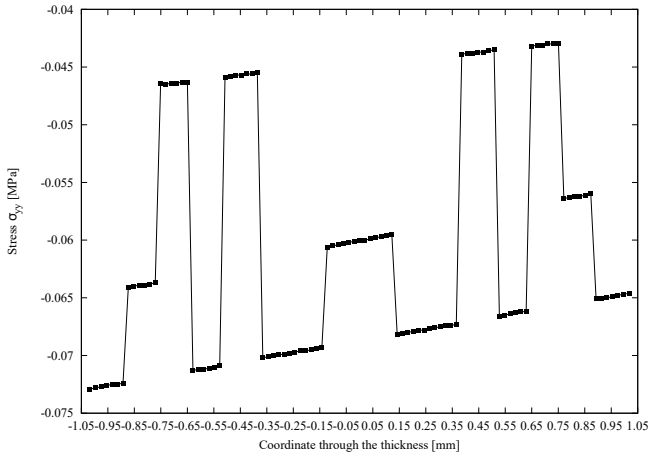

(b) σ_{yy}

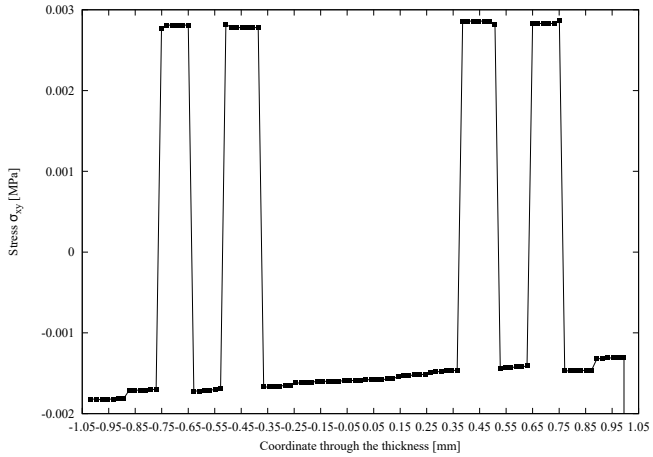

(c) σ_{xy}

Figure 7.12: Stress field through the thickness at the centre of the ZOI: (a) σ_{xx}, (b) σ_{yy}, (c) σ_{xy}.

by means of an on-the-fly resolution of the SLP, the optimal stack matching the values of the PPs corresponding to this individual and satisfying the requirements on the first-ply failure and on the delamination. In this case, the optimal stacking sequence is searched in the domain of QT solutions.
The optimised solution is 10.33% lighter than the reference one with an enhanced buckling strength, proving, thus, the effectiveness of the proposed approach. Further tests need to be set up to assess the effectiveness of the proposed methodology when dealing with design problems involving complex geometries and different load conditions, by integrating into the problem formulation more complex phenomena like post-buckling behaviour, damage mechanics, etc. The results obtained in this work represent just a first (encouraging) step to develop a general multi-scale optimisation approach to design complex composite structures: research is ongoing in this direction.

Chapter 8

Conclusions and prospects

The work carried out in this Thesis focuses on the development of a suitable global-local modelling approach, based on higher-order theories, which is integrated into the multi-scale two-level optimisation strategy (MS2LOS) for the optimal design of composite structures. This thesis is a Joint PhD Thesis and the work has been carried out at ENSAM in Bordeaux-Talence, under the supervision of Prof. M. Montemurro and Prof. J. Pailhès and at the Politecnico di Torino under the supervision of Prof. E. Carrera.
This work has been carried out in the context of the SMARTCOMPOSITE project, co-funded by the Nouvelle-Aquitaine region and by Politecnico di Torino, and it gives an original contribution in the development of a multi-scale design and optimisation strategy for composite structures integrating a global-local modelling strategy based on higher-order theories to correctly describe the physical responses involved at each problem scale.

8.1 General conclusions

Detailed conclusions and perspectives inherent to the topic of this Thesis are already discussed at the end of each Chapter. It would be redundant to give here all the details, thus, only the most relevant conclusions and perspectives will be briefly recalled. The literature survey of Chapter 2 has allowed picturing the state of the art on the main topics of the manuscript: the design methods for CSC and VSC structures and global-local modelling approaches for composites.
Bibliographic research on CSCs has shown that, despite the outstanding mechanical properties of this class of composite materials, the design problem requires a complex multi-scale formulation which leads to a huge amount of design variables. In the literature, this problem is faced making use of simplifying hypotheses and design guidelines to search for a feasible optimised solution. These simplification rules allow simplifying the optimisation problem but, on the other hand, the design space becomes extremely shrunk and, consequently, the solution search cannot converge toward true global optima. The same considerations of CSCs can be done for VCSs in the case of the design/optimisation problem, keeping in mind that the point-wise variation of the properties significantly complicates the resolution of the problem introducing more complex manufacturing constraints.
The difficulties of properly design/optimise at each relevant scale the properties of a CSC structure are faced in Chapter 5 by using MS2LOS to solve the least-weight design of a composite stiffened panel subject to requirements of different nature (geometrical, mechanical, technological, etc.). As discussed in the Chapter, the MS2LOS relies, on the one hand, on the utilisation of the PPs and on the framework of FSDT for describing the macroscopic behaviour of each laminate composing the panel and, on the other hand,

on a special genetic algorithm in order to perform the solution search for the considered problem. In addition, the design process is not submitted to restrictions: any parameter characterising the structure (at each relevant scale) is an optimisation variable; in fact, this allows searching for a true global minimum without making simplifying hypotheses. The optimum configurations found are non-conventional, and this is due to the use of the polar formalism to represent the macroscopic behaviour of the CSC structure, to the use of an evolutionary strategy together with the formulation of the problem, which is stated in the most general sense. The results obtained show that a significant weight saving can be obtained using the MS2LOS, which is up to 11.5% with respect to the reference structure with enhanced mechanical properties in terms of first buckling load (the percentage increment ranges from 9% to 9.5% depending on the considered optimum solution).
The end of the Chapter is devoted to a posteriori investigation of the quality of the optimum configurations by means of a high-order layer-wise FE model of the stiffened panel making use of elements with different kinematics and accuracy in the CUF framework. These theories are introduced in Chapter 3 and are employed in the global-local approach developed in this work. The quality investigation on the buckling loads of the reference and optimum configurations is done to figure out if is convenient or not a substitution of the FSDT with a high-order layer-wise FE model in the framework of MS2LOS. The idea is in fact to enhance the capabilities of the MS2LOS in the detection of complex phenomena that affect the composite materials (e.g. free edge stresses, delamination, etc.).
The results of this analysis show that the buckling load provided by the ANSYS FE model (which is built by using shell elements based on FSDT) is overestimated. The range of percentage differences is from $7.4\% - 7.9\%$ for optimum solutions to 14% for the reference configuration. The discrepancy is related to the calculation of the 3D stress field in each layer, which strongly affects the geometric stiffness matrix used to evaluate the first buckling load of the panel. In the case of CUF model, the more accurate description of the stress field allows a better evaluation of the geometric stiffness matrix and of the first buckling load of the panel consequently. Despite these discrepancies, classical shell elements based on FSDT can be reliably employed in the framework of the MS2LOS because they allow finding true optimum solutions, and they represent the best compromise in terms of both the number of DOFs and computational cost.
This last statement is confirmed by the bibliographic research on the multi-scale optimisation strategies for CSCs and VSCs where the response of the structures is evaluated through the classical theories (CLT and FSDT in the case of composites) due to their versatility and moderate computational cost. The use of CLT and FSDT brings trouble because composite material requires a detailed evaluation of stresses to detect complex failure mechanisms which can be only studied by means of solid FE models or high-order theories. On the other hand, from a computational perspective, a full 3D FE model or a FE model composed of elements based on high-order kinematic models for a large-size structure is prohibitive and above all for optimisation algorithms. In the literature, this problem is faced with the use of global-local approaches. The idea behind these strategies is to use 3D FE or elements based on high-order kinematic models only in the ZOIs of the model. In this way, it is possible to achieve the best compromise between accuracy and computational costs, especially when such models must be included in an intricate optimisation framework.
The need to have an optimisation strategy efficient and able to detect phenomena that cannot be studied by standard classical theories motivates the work done in this manuscript. In Chapter 3, the original global-local approach realised in this thesis is presented. This approach consists of a two-step procedure that is developed to accurately assess the stress

field in the ZOI of the structures. The first step of this methodology is dedicated to the static analysis of the GFEM, which is made of classical 1D/2D elements and is generated by means of commercial software (*MSc-Nastran* and *Abaqus CAE* in this case). After the identification of the ZOI, in the second step, the ZOI is analysed by using high order 1D theories to describe in detail the stress field. In the LFEM analysis, the geometrical BCs resulting from the GFEM are applied to the boundary of the transition zone surrounding the ZOI. Furthermore, the LFEM of this global-local approach is characterised by the use of higher-order layer-wise beam theories in the framework of CUF, which has proven to be very effective and efficient in evaluating complex stress and deformation states in composite structures which are already used in Chapter 5 for the investigation of the quality of the optimum configurations of the CSC stiffened panel. Two classes of assessments are proposed to evaluate the performances of the global-local approach developed in this work. The first-class shows that the proposed global-local modelling approach can compute accurate 3D stress fields within the ZOIs by significantly reducing the computational costs with respect to detailed LFEMs made of 3D solid elements. The second class of benchmarks is dedicated to the free-edge phenomenon in the composite structure. In particular, this phenomenon is characterised by extremely high peaks of interlaminar stress and cannot be detected by standard 1D/2D FE. The global-local approach has proven to be effective in the description of the inter-laminar stresses, which are often the cause of the failure onset in composites and motivates its integration in the MS2LOS. Before moving to the conclusions related to Chapter 7, where the integration of the global-local modelling approach based on layer-wise higher-order theories developed in Chapter 3 with the MS2LOS for CSC structures is presented, the optimisation of a particular class of VSC is faced in Chapter 6. The aim of the Chapter is to determine, at the macroscopic scale, the optimum distribution of the VAT laminate PPs to satisfy the requirements and to maximise the first buckling load of a VAT composite plate. The optimisation of VAT composite is much more complicated than the CSC and this Chapter looks for a possible integration of the global-local approach into the MS2LOS also for this class of materials. The main contribution consists of the derivation of the analytical form of the gradient of the buckling factor by taking advantage of the B-spline surface properties, which are used to represent the laminate PPs fields of the VAT composite. The closed-form expression of the buckling factor gradient with respect to the PPs has been analytically derived by exploiting the properties of the B-spline blending functions. The need for the search for the analytical expressions of the buckling factor derivatives is due to the necessity to speed up the optimisation process. Numerical derivatives could easily be calculated but they require multiple runs of the FE model, which cause an increase in the computational costs. Two meaningful benchmarks taken from the literature prove the effectiveness of the approach presented in this Chapter. In particular, the numerical results found here show that the optimised solutions provided by the MS2LOS based on the polar formalism outperform those presented in the literature showing a significant increase in the buckling strength of VAT composites. Furthermore two important aspects of the MS2LOS are highlighted in this Chapter: on the one hand, the effectiveness of the representation of the anisotropy based on PPs which allows determining locally the optimal symmetry group, and on the other hand, the absence of simplifying hypotheses either on the nature of the stack or on the kind of orthotropy of the laminate stiffness tensors during the FLP, unlike the other approaches based on the use of LPs in the literature.

Lastly, Chapter 7 represents a fundamental brick of the work carried out in this manuscript. In this Chapter, the integration of the global-local modelling approach based on layer-wise higher-order theories developed in Chapter 3 within the MS2LOS for CSC structures is

presented. A modified version of the MS2LOS has been proposed and has been applied to the least-weight design problem of a simplified composite wing-box structure subject to design requirements related to first buckling load, delamination and first-ply failure. The architecture of the MS2LOS has been modified to integrate the global-local approach, in fact, there is no longer a clear distinction between FLP and SLP because the two phases of the MS2LOS strongly interact during the optimisation process. As well explained in the Chapter, the global-local approach is used to verify the requirements on the first-ply failure index and on the delamination of the most critical ZOI. In fact, for each individual representing the potential solution, a genetic optimisation is carried out to find the optimal stack matching the values of the PPs corresponding to this individual. The solution is searched in the space of QT solutions without introducing simplifying hypotheses on the nature of the stacking sequence. The obtained optimised solution is 10.33% lighter than the reference one with an enhanced buckling strength, proving, thus, the effectiveness of the proposed approach. Even if the difficulties at the programming level increased, the proposed modified version of the MS2LOS integrating the global-local modelling approach represents a first step in the development of a general multi-scale optimisation approach.

8.2 Prospects

The topics covered in this thesis give many insights for future developments.
The global-local modelling approach developed in this work is a powerful tool to detect complex stress states in composite structures efficiently. This approach can be improved by searching for better integration with the commercial software minimising user interventions. It is also necessary to investigate the effectiveness of the approach using other criteria to isolate ZOIs (i.e. local buckling). This approach needs to be also extended for the VSCs in order to allow their optimisation with respect to local design requirements.
The results provided by the MS2LOS in the optimisation of the CSC stiffened panel and VAT composite plates prove the effectiveness and the robustness of the optimisation approach and provide confidence for further researches. Regarding these prospects, some aspects of theoretical, numerical and technological nature deserve particular attention. The optimisation strategy needs to be tested on more complex benchmarks, e.g. a representative stiffened panel extracted either from the wing or from the fuselage of an aircraft made of VAT composites. In particular, the design problem requires the formalisation of further technological constraints (e.g. gap and overlap between adjacent tows, tow width, the variation of the fibre volume fraction due to imperfections, etc.), related either to the AFP process or to the FFF+CFF technologies, in the FLP theoretical framework in order to get not only an optimised solution but also a manufacturable one.
The modified version of the MS2LOS with the integration of the global-local approach shows very great potential in the optimisation of the simplified composite wing-box structure. For this case, it needs to introduce new or multiple ZOI isolation criteria in order to increase the number of requirements which can be verified at the same time. Therefore, it is fundamental to employ this approach in to complex test cases representative of real-world engineering problems to assess the effectiveness of the proposed methodology with complex geometries and different load conditions, by integrating into the problem formulation more complex phenomena, like post-buckling behaviour and damage mechanics.

Chapter 9

Dissemination activity

Research articles published in international journals

- **G. A. Fiordilino**, M. I. Izzi, & M. Montemurro. *A general isogeometric polar approach for the optimisation of variable stiffness composites: Application to eigenvalue buckling problems.* Mechanics of Materials 153 (2021): 103574. www.doi.org/10.1016/j.mechmat.2020.103574
- E. Carrera, **G. A. Fiordilino**, M. Nagaraj, A. Pagani & M. Montemurro. *A global/local approach based on CUF for the accurate and efficient analysis of metallic and composite structures.* Engineering Structures 188 (2019): 188-201. www.doi.org/10.1016/j.engstruct.2019.03.016
- M. Montemurro, A. Pagani, **G. A. Fiordilino**, J. Pailhès & E. Carrera. *A general multi-scale two-level optimisation strategy for designing composite stiffened panels.* Composite Structures 201 (2018): 968-979. www.doi.org/10.1016/j.compstruct.2018.06.119

Presentations in international conferences

- **G. A. Fiordilino**, M.I. Izzi, M. Montemurro & J. Pailhès. *Buckling factor maximisation of variable angletow laminates: a general B-spline surface-based approach.* 7th ECCOMAS thematic conference on the mechanical response of composites, Girona, Spain, 2019.
- E. Carrera, A. Garcia de Miguel, **G. A. Fiordilino** & A. Pagani. *Global/local analysis of free-edge stresses in composite laminates.* AIAA Scitech 2019 Forum, San Diego, California, 2019.
- M. Montemurro, A. Pagani, **G. A. Fiordilino**, J. Pailhès & E. Carrera.*Simultaneous size/material optimisation and accurate analysis of composite stiffened panels.* 20th International Conference on Composite Structures, Paris, France, 2017.

Presentations in national conferences

- **G. A. Fiordilino**, A. Pagani, E. Carrera & M. Montemurro. *Global-local analysis of composite structures.* 21ème Journées Nationales sur les Composites, Bordeaux, France, 2019.

Appendix A

Analytical expression of the laminate stiffness matrices and of their gradient

Under the hypothesis of quasi-homogeneous laminate, i.e. $\mathbf{B}^* = \mathbf{0}$ and $\mathbf{A}^* = \mathbf{D}^*$, the expression of the homogenised membrane stiffness matrix in terms of the dimensionless PPs reads:

$$\mathbf{A}^* \coloneqq \mathbf{A}_\mathbf{0}^* + R_0\rho_0\mathbf{A}_\mathbf{1}^* + R_1\rho_1\mathbf{A}_\mathbf{2}^*, \tag{A.1}$$

where matrices $\mathbf{A}_\mathbf{0}^*$, $\mathbf{A}_\mathbf{1}^*$, $\mathbf{A}_\mathbf{2}^*$ are defined as

$$\begin{aligned}
\mathbf{A}_\mathbf{0}^* &\coloneqq \begin{bmatrix} T_0 + 2T_1 & -T_0 + 2T_1 & 0 \\ & T_0 + 2T_1 & 0 \\ \text{sym} & & T_0 \end{bmatrix}, \quad \mathbf{A}_\mathbf{1}^* \coloneqq \begin{bmatrix} c_4 & -c_4 & s_4 \\ & c_4 & -s_4 \\ \text{sym} & & -c_4 \end{bmatrix}, \\
\mathbf{A}_\mathbf{2}^* &\coloneqq \begin{bmatrix} 4c_2 & 0 & 2s_2 \\ & -4c_2 & 2s_2 \\ \text{sym} & & 0 \end{bmatrix},
\end{aligned} \tag{A.2}$$

with

$$c_2 = \cos(\pi\phi_1), \; s_2 = \sin(\pi\phi_1), \; c_4 = \cos(2\pi\phi_1), \; s_4 = \sin(2\pi\phi_1). \tag{A.3}$$

Similarly, matrix $\mathbf{H}^*$ can be decomposed as:

$$\mathbf{H}^* \coloneqq \mathbf{H}_\mathbf{0}^* + R\rho_1\mathbf{H}_\mathbf{1}^*, \tag{A.4}$$

where matrices $\mathbf{H}_\mathbf{0}^*$ and $\mathbf{H}_\mathbf{1}^*$ are defined as:

$$\mathbf{H}_\mathbf{0}^* \coloneqq \begin{bmatrix} T & 0 \\ \text{sym} & T \end{bmatrix}, \quad \mathbf{H}_\mathbf{1}^* \coloneqq \begin{bmatrix} c_2^{\mathrm{H}^*} & s_2^{\mathrm{H}^*} \\ \text{sym} & -c_2^{\mathrm{H}^*} \end{bmatrix}, \tag{A.5}$$

with

$$c_2^{\mathrm{H}^*} = \cos\left(2\Phi^{\mathrm{H}^*}\right), \; s_2^{\mathrm{H}^*} = \sin\left(2\Phi^{\mathrm{H}^*}\right), \; \Phi^{\mathrm{H}^*} = \Phi + \Phi_1 - \frac{\pi}{2}\phi_1. \tag{A.6}$$

It is noteworthy that the quantities T_0, T_1, T, R, Φ_1 and Φ, appearing in Eqs. (A.1)-(A.6), are the PPs of the pre-preg tow listed in Table 6.1.

Taking into account for the above expressions, the derivatives of matrices $\mathbf{A}^*$ and $\mathbf{H}^*$ read:

$$\begin{aligned}
&\frac{\partial \mathbf{A}^*}{\partial \rho_0} = R_0 \mathbf{A}_\mathbf{1}^*, \ \frac{\partial \mathbf{A}^*}{\partial \rho_1} = R_1 \mathbf{A}_\mathbf{2}^*, \\
&\frac{\partial \mathbf{A}^*}{\partial \phi_1} = 2\pi R_0 \rho_0 \begin{bmatrix} -s_4 & s_4 & c_4 \\ & -s_4 & -c_4 \\ \text{sym} & & s_4 \end{bmatrix} + \pi R_1 \rho_1 \begin{bmatrix} -4s_2 & 0 & 2c_2 \\ & 4s_2 & 2c_2 \\ \text{sym} & & 0 \end{bmatrix},
\end{aligned} \tag{A.7}$$

$$\begin{aligned}
&\frac{\partial \mathbf{H}^*}{\partial \rho_0} = \mathbf{0}, \ \frac{\partial \mathbf{H}^*}{\partial \rho_1} = R \mathbf{H}_\mathbf{1}^*, \\
&\frac{\partial \mathbf{H}^*}{\partial \phi_1} = -\pi R \rho_1 \begin{bmatrix} -s_2^{\mathrm{H}^*} & c_2^{\mathrm{H}^*} \\ \text{sym} & s_2^{\mathrm{H}^*} \end{bmatrix}.
\end{aligned} \tag{A.8}$$

Moreover, inasmuch as the quasi-homogeneity hypothesis holds, the derivatives of matrix $\mathbf{B}^*$ are null, while those of matrix $\mathbf{D}^*$ are equal to those of matrix $\mathbf{A}^*$. Finally, the gradient of the laminate stiffness matrix $\mathbf{K}_{\mathrm{lam}}$ of Eq. (4.17) with respect to the generic PP ζ reads:

$$\frac{\partial \mathbf{K}_{\mathrm{lam}}}{\partial \zeta} = \mathrm{diag}\left(\frac{\partial \mathbf{A}^*}{\partial \zeta}, \frac{\partial \mathbf{D}^*}{\partial \zeta}, \frac{\partial \mathbf{H}^*}{\partial \zeta} \right), \quad \zeta = \rho_0, \rho_1, \phi_1. \tag{A.9}$$

Appendix B

Buckling factor gradient

The details of the proof of Proposition 6.5.1 are given here below.

Proof. Inasmuch as external forces do not depend upon the laminate dimensionless PPs, the derivative of the right-hand side of Eq. (6.19) is

$$\frac{\partial \mathbf{f}_0}{\partial \zeta^{(i,j)}} = \mathbf{0}. \tag{B.1}$$

Consider, now, the following functional:

$$\mathcal{F} := \boldsymbol{\psi}_{\boldsymbol{k}}^{\mathrm{T}} \left(\mathbf{K} + \lambda_k \mathbf{K}_\sigma\right) \boldsymbol{\psi}_{\boldsymbol{k}} + \boldsymbol{\mu}^{\mathrm{T}} \left(\mathbf{K}\mathbf{d}_0 - \mathbf{f}_0\right) = 0, \text{ with : } \boldsymbol{\mu} \neq \mathbf{0}. \tag{B.2}$$

In the above equation, $\mathcal{F}$ is identically null because Eqs. (6.13) and (6.19) holds. Moreover, $\boldsymbol{\mu}$ is the arbitrarily defined *adjoint vector*. The derivative of Eq. (B.2) reads:

$$\begin{aligned} &\frac{\partial \boldsymbol{\psi}_{\boldsymbol{k}}^{\mathrm{T}}}{\partial \zeta^{(i,j)}} \left(\mathbf{K} + \lambda_k \mathbf{K}_\sigma\right) \boldsymbol{\psi}_{\boldsymbol{k}} + \boldsymbol{\psi}_{\boldsymbol{k}}^{\mathrm{T}} \left(\mathbf{K} + \lambda_k \mathbf{K}_\sigma\right) \frac{\partial \boldsymbol{\psi}_{\boldsymbol{k}}}{\partial \zeta^{(i,j)}} + \\ &+ \boldsymbol{\psi}_{\boldsymbol{k}}^{\mathrm{T}} \frac{\partial \left(\mathbf{K} + \lambda_k \mathbf{K}_\sigma\right)}{\partial \zeta^{(i,j)}} \boldsymbol{\psi}_{\boldsymbol{k}} + \boldsymbol{\mu}^{\mathrm{T}} \left(\frac{\partial \mathbf{K}}{\partial \zeta^{(i,j)}} \mathbf{d}_0 + \mathbf{K} \frac{\partial \mathbf{d}_0}{\partial \zeta^{(i,j)}}\right) = 0. \end{aligned} \tag{B.3}$$

The first two terms of Eq. (B.3) are identically null due to Eq. (6.13); thus Eq. (B.3) simplifies to:

$$\boldsymbol{\psi}_{\boldsymbol{k}}^{\mathrm{T}} \frac{\partial \mathbf{K}}{\partial \zeta^{(i,j)}} \boldsymbol{\psi}_{\boldsymbol{k}} + \lambda_k \boldsymbol{\psi}_{\boldsymbol{k}}^{\mathrm{T}} \frac{\partial \mathbf{K}_\sigma}{\partial \zeta^{(i,j)}} \boldsymbol{\psi}_{\boldsymbol{k}} + \frac{\partial \lambda_k}{\partial \zeta^{(i,j)}} \boldsymbol{\psi}_{\boldsymbol{k}}^{\mathrm{T}} \mathbf{K}_\sigma \boldsymbol{\psi}_{\boldsymbol{k}} + \boldsymbol{\mu}^{\mathrm{T}} \left(\frac{\partial \mathbf{K}}{\partial \zeta^{(i,j)}} \mathbf{d}_0 + \mathbf{K} \frac{\partial \mathbf{d}_0}{\partial \zeta^{(i,j)}}\right) = 0. \tag{B.4}$$

By multiplying both sides of Eq. (6.13) to $\boldsymbol{\psi}_{\boldsymbol{k}}^{\mathrm{T}}$ one obtains:

$$\boldsymbol{\psi}_{\boldsymbol{k}}^{\mathrm{T}} \mathbf{K}_\sigma \boldsymbol{\psi}_{\boldsymbol{k}} = -\frac{\boldsymbol{\psi}_{\boldsymbol{k}}^{\mathrm{T}} \mathbf{K} \boldsymbol{\psi}_{\boldsymbol{k}}}{\lambda_k} := -\frac{w_k}{\lambda_k}. \tag{B.5}$$

Therefore, by injecting the above formula in Eq. (B.4), the derivative of the k-th buckling factor reads:

$$\frac{\partial \lambda_k}{\partial \zeta^{(i,j)}} = \frac{\lambda_k}{w_k} \left(\boldsymbol{\psi}_{\boldsymbol{k}}^{\mathrm{T}} \frac{\partial \mathbf{K}}{\partial \zeta^{(i,j)}} \boldsymbol{\psi}_{\boldsymbol{k}} + \lambda_k \boldsymbol{\psi}_{\boldsymbol{k}}^{\mathrm{T}} \frac{\partial \mathbf{K}_\sigma}{\partial \zeta^{(i,j)}} \boldsymbol{\psi}_{\boldsymbol{k}} + \boldsymbol{\mu}^{\mathrm{T}} \frac{\partial \mathbf{K}}{\partial \zeta^{(i,j)}} \mathbf{d}_0 + \boldsymbol{\mu}^{\mathrm{T}} \mathbf{K} \frac{\partial \mathbf{d}_0}{\partial \zeta^{(i,j)}}\right). \tag{B.6}$$

As discussed in [10], the geometric stiffness matrix of the generic element can be expressed as:

$$\mathbf{K}_{\sigma e} = \sum_{i=1}^{8} r_{0ei} \overline{\mathbf{K}}_i, \tag{B.7}$$

where r_{0ei} is the i-th component of the vector of generalised forces per unit length of Eq. (4.18), for the generic element e, whilst $\overline{\mathbf{K}}_i$ are matrices that depend only of the geometry of the element. The expression of each $\overline{\mathbf{K}}_i$ is given in Appendix C. The vector of generalised forces per unit length $\mathbf{r}_{0e}$ is obtained as solution of the system (6.19), i.e.

$$\mathbf{r}_{0e} = \mathbf{K}_{\mathrm{lam_e}}\boldsymbol{\varepsilon}_{0e} = \mathbf{K}_{\mathrm{lam_e}}\mathbf{B}_e\mathbf{L}_e\mathbf{d}_0. \tag{B.8}$$

In Eq. (B.8), $\mathbf{K}_{\mathrm{lam_e}}$ is the laminate stiffness matrix of Eq. (4.18), computed for the generic element, while $\boldsymbol{\varepsilon}_{0e}$ is the vector of the generalised strains of the laminate middle plane. $\mathbf{B}_e$ is the product of the linear differential operator and the shape function matrix (see [133]) for element e, whilst $\mathbf{L}_e$ is the connectivity matrix of element e. Therefore, the geometric stiffness matrix of the structure $\mathbf{K}_\sigma$ can be expressed as:

$$\mathbf{K}_\sigma = \sum_{e=1}^{N_e} \mathbf{L}_e^{\mathrm{T}}\mathbf{K}_{\sigma e}\mathbf{L}_e = \sum_{e=1}^{N_e} \mathbf{L}_e^{\mathrm{T}} \sum_{i=1}^{8} r_{0ei}\overline{\mathbf{K}}_i\mathbf{L}_e. \tag{B.9}$$

Consider, now, the term $\boldsymbol{\psi}_{\boldsymbol{k}}^{\mathrm{T}} \dfrac{\partial \mathbf{K}_\sigma}{\partial \zeta^{(i,j)}} \boldsymbol{\psi}_{\boldsymbol{k}}$ in Eq. (B.6). By taking into account for Eq. (B.9), it reads:

$$\boldsymbol{\psi}_{\boldsymbol{k}}^{\mathrm{T}} \frac{\partial \mathbf{K}_\sigma}{\partial \zeta^{(i,j)}} \boldsymbol{\psi}_{\boldsymbol{k}} = \sum_{e=1}^{N_e} \boldsymbol{\psi}_{\boldsymbol{k}}^{\mathrm{T}}\mathbf{L}_e^{\mathrm{T}} \sum_{i=1}^{8} \frac{\partial r_{0ei}}{\partial \zeta^{(i,j)}} \overline{\mathbf{K}}_i\mathbf{L}_e\boldsymbol{\psi}_{\boldsymbol{k}}. \tag{B.10}$$

By introducing the following definition

$$\mathbf{s}_{ek}^{\mathrm{T}} \coloneqq \{\boldsymbol{\psi}_{ek}^{\mathrm{T}}\overline{\mathbf{K}}_1\boldsymbol{\psi}_{ek}, \cdots, \boldsymbol{\psi}_{ek}^{\mathrm{T}}\overline{\mathbf{K}}_8\boldsymbol{\psi}_{ek}\}, \text{ with : } \boldsymbol{\psi}_{ek} = \mathbf{L}_e\boldsymbol{\psi}_k, \tag{B.11}$$

Eq. (B.10) simplifies to:

$$\boldsymbol{\psi}_{\boldsymbol{k}}^{\mathrm{T}} \frac{\partial \mathbf{K}_\sigma}{\partial \zeta^{(i,j)}} \boldsymbol{\psi}_{\boldsymbol{k}} = \sum_{e=1}^{N_e} \mathbf{s}_{ek}^{\mathrm{T}} \frac{\partial \mathbf{r}_{0e}}{\partial \zeta^{(i,j)}}. \tag{B.12}$$

By injecting Eq. (B.8) into the above formula and by taking into account for the local support property of Eq. (6.18), one obtains:

$$\boldsymbol{\psi}_{\boldsymbol{k}}^{\mathrm{T}} \frac{\partial \mathbf{K}_\sigma}{\partial \zeta^{(i,j)}} \boldsymbol{\psi}_{\boldsymbol{k}} = \sum_{e \in \mathrm{S}_{ij}} \frac{\partial \zeta_e}{\partial \zeta^{(i,j)}} \mathbf{s}_{ek}^{\mathrm{T}} \frac{\partial \mathbf{K}_{\mathrm{lam_e}}}{\partial \zeta_e} \boldsymbol{\varepsilon}_{0e} + \boldsymbol{\eta}_k^{\mathrm{T}} \frac{\partial \mathbf{d}_0}{\partial \zeta^{(i,j)}}, \tag{B.13}$$

where $\dfrac{\partial \zeta_e}{\partial \zeta^{(i,j)}}$ represents the partial derivative of the generic dimensionless PP expressed through a B-spline scalar function, given in Eq. (6.17), whilst $\dfrac{\partial \mathbf{K}_{\mathrm{lam_e}}}{\partial \zeta_e}$ is the partial derivative of the laminate stiffness matrix with respect to the dimensionless PPs evaluated at the element centroid, whose expression is reported in Appendix A. In Eq. (B.13), the vector $\boldsymbol{\eta}_k$ is defined as:

$$\boldsymbol{\eta}_k^{\mathrm{T}} \coloneqq \sum_{e=1}^{N_e} \mathbf{s}_{ek}^{\mathrm{T}}\mathbf{K}_{\mathrm{lam_e}}\mathbf{B}_e\mathbf{L}_e. \tag{B.14}$$

Consider, now, the term $\boldsymbol{\psi}_{\boldsymbol{k}}^{\mathrm{T}} \dfrac{\partial \mathbf{K}}{\partial \zeta^{(i,j)}} \boldsymbol{\psi}_{\boldsymbol{k}}$ in Eq. (B.6). As discussed in [78], the partial derivative of the structure stiffness matrix reads:

$$\frac{\partial \mathbf{K}}{\partial \zeta^{(i,j)}} = \sum_{e \in \mathrm{S}_{ij}} \frac{\partial \zeta_e}{\partial \zeta^{(i,j)}} \mathbf{L}_e^{\mathrm{T}} \int_{A_e} \mathbf{B}_e^{\mathrm{T}} \frac{\partial \mathbf{K}_{\mathrm{lam_e}}}{\partial \zeta_e} \mathbf{B}_e \mathrm{d}S \; \mathbf{L}_e, \tag{B.15}$$

where A_e represents the area of the generic shell element. By injecting the above formula into the product $\boldsymbol{\psi}_{\boldsymbol{k}}^{\mathrm{T}} \dfrac{\partial \mathbf{K}}{\partial \zeta^{(i,j)}} \boldsymbol{\psi}_{\boldsymbol{k}}$, one obtains:

$$\boldsymbol{\psi}_{\boldsymbol{k}}^{\mathrm{T}} \frac{\partial \mathbf{K}}{\partial \zeta^{(i,j)}} \boldsymbol{\psi}_{\boldsymbol{k}} = \sum_{e \in \mathrm{S}_{ij}} \frac{\partial \zeta_e}{\partial \zeta^{(i,j)}} w_{ek}^*, \tag{B.16}$$

where w_{ek}^* is defined as

$$w_{ek}^* \coloneqq \boldsymbol{\psi}_{\boldsymbol{k}}^{\mathrm{T}} \mathbf{L}_e^{\mathrm{T}} \int_{A_e} \mathbf{B}_e^{\mathrm{T}} \frac{\partial \mathbf{K}_{\mathrm{lam_e}}}{\partial \zeta_e} \mathbf{B}_e \mathrm{d}S \; \mathbf{L}_e \boldsymbol{\psi}_{\boldsymbol{k}} = \int_{A_e} \boldsymbol{\varepsilon}_{ek}^{\mathrm{T}} \frac{\partial \mathbf{K}_{\mathrm{lam_e}}}{\partial \zeta_e} \boldsymbol{\varepsilon}_{ek} \mathrm{d}S. \tag{B.17}$$

In the above expression, $\boldsymbol{\varepsilon}_{ek}$ represents the vector of the generalised strains of element e for the k-th mode shape. By injecting Eqs. (B.13) and (B.16) in Eq. (B.6), one obtains

$$\frac{\partial \lambda_k}{\partial \zeta^{(i,j)}} = \frac{\lambda_k}{w_k} \left[\sum_{e \in \mathrm{S}_{ij}} \frac{\partial \zeta_e}{\partial \zeta^{(i,j)}} \left(w_{ek}^* + \lambda_k \mathbf{s}_{ek}^{\mathrm{T}} \frac{\partial \mathbf{K}_{\mathrm{lam_e}}}{\partial \zeta_e} \boldsymbol{\varepsilon}_{0e} \right) + \boldsymbol{\mu}^{\mathrm{T}} \frac{\partial \mathbf{K}}{\partial \zeta^{(i,j)}} \mathbf{d}_0 + \left(\boldsymbol{\mu}^{\mathrm{T}} \mathbf{K} + \lambda_k \boldsymbol{\eta}_k^{\mathrm{T}} \right) \frac{\partial \mathbf{d}_0}{\partial \zeta^{(i,j)}} \right]. \tag{B.18}$$

The adjoint vector $\boldsymbol{\mu}$ can be chosen in such a way that the term multiplying $\dfrac{\partial \mathbf{d}_0}{\partial \zeta^{(i,j)}}$ vanishes, i.e.

$$\mathbf{K} \boldsymbol{\mu} = -\lambda_k \boldsymbol{\eta}_k. \tag{B.19}$$

Finally, Eq. (6.16) can be easily got by injecting Eq. (B.19) into Eq. (B.18). This last passage concludes the proof. ■

It is noteworthy that the assessment of the k-th buckling factor gradient requires the resolution of three systems, i.e. Eq. (6.13), Eq. (6.19) and the adjoint system of Eq. (B.19). Therefore, for each iteration of the optimisation process, the following algorithm is invoked to carry out all the necessary steps for computing the gradient of λ_k.

Algorithm 2 Computation of the gradient of the k-th buckling factor.

1: Solve Eq. (6.19) and get $\mathbf{d}_0$, $\boldsymbol{\varepsilon}_{0e}$ and $\mathbf{r}_{0e}$, $\forall e$.
2: Build $\mathbf{K}_\sigma$ according to Eq. (B.9).
3: Solve Eq. (6.13) and get λ_k, $\boldsymbol{\psi}_k$, $\boldsymbol{\varepsilon}_{ek}$, $\forall e$ and $\forall k$.
4: Calculate w_k and w_{ek}^*, $\forall e$ and $\forall k$, according to Eqs. (B.5) and (B.17), respectively.
5: Calculate $\mathbf{s}_{ek}$ and $\boldsymbol{\eta}_k$, $\forall e$ and $\forall k$, from Eqs. (B.11) and (B.14), respectively.
6: Solve the adjoint system of Eq. (B.19); get $\boldsymbol{\mu}$.
7: Calculate $\dfrac{\partial \mathbf{K}}{\partial \zeta^{(i,j)}}$ from Eq. (B.15).
8: Calculate $\dfrac{\partial \lambda_k}{\partial \zeta^{(i,j)}}$ from the first of Eq. (6.16).

Appendix C

Expression of the element geometric stiffness matrix

The analytical expression of matrices $\overline{\mathbf{K}}_i$, $(i = 1, \cdots, 8)$, appearing in Eq. (B.7), is reported here below. In particular, the definition of the element geometric stiffness matrix, given in Eq. (B.7), is not the classical one used in commercial FE software, like ANSYS® [165]. However, unlike the classical definition of the element geometric stiffness matrix, Eq. (B.7) is really useful for determining a straightforward expression of the buckling factor derivative.
In the following, the algorithm for retrieving the expression of each matrix $\overline{\mathbf{K}}_i \in \mathbb{R}^{24\times 24}$ for a shell element with four nodes and six DOFs per node (like the SHELL181 ANSYS® shell element), whose kinematics is described in the framework of the FSDT, is presented. Of course, this algorithm must be executed off-line, i.e. before the optimisation process, once the element type has been selected.

Algorithm 3 Derivation of matrices $\overline{\mathbf{K}}_i$.

1: Build a FE model made of a single element.
2: Set arbitrary material properties for the element. The material properties should be conveniently set in order to obtain a diagonal laminate stiffness matrix $\mathbf{K}_{\text{lam}}$ (in order to avoid coupling effects).
3: Impose an elementary strain field ($\varepsilon_{0ei} \neq 0$, $\varepsilon_{0ej} = 0$, $j = 1, \cdots, 8$ and $j \neq i$) by using suitable BCs at the four nodes.
4: Solve Eq. (6.19) and activate the pre-stress option (in this way the commercial FE code builds $\mathbf{K}_{\sigma e}$ according to the usual definition [165]).
5: Get r_{0ei} and $\mathbf{K}_{\sigma e}$ from the FE software.
6: Calculate $\overline{\mathbf{K}}_i = \dfrac{\mathbf{K}_{\sigma e}}{r_{0ei}}$
7: If $i < 8$ set $i = i + 1$ and go to step 3, otherwise stop.

The expressions of $\overline{\mathbf{K}}_i$ for a square SHELL181 element of side L are provided here below. Each matrix $\overline{\mathbf{K}}_i$ is a symmetric partitioned matrix, composed of symmetric blocks, containing several null components. Therefore, only non-null terms are provided in the following:

$$\overline{\mathbf{K}}_1 = \frac{1}{8}\begin{bmatrix} \begin{bmatrix} \hat{\mathbf{A}}_1 & \hat{\mathbf{B}}_1 \\ \hat{\mathbf{B}}_1^{\mathrm{T}} & \hat{\mathbf{C}}_1 \end{bmatrix} & \begin{bmatrix} -\hat{\mathbf{A}}_1 & -\hat{\mathbf{B}}_1 \\ -\hat{\mathbf{B}}_1^{\mathrm{T}} & -\hat{\mathbf{C}}_1 \end{bmatrix} \\ \begin{bmatrix} -\hat{\mathbf{A}}_1 & -\hat{\mathbf{B}}_1 \\ -\hat{\mathbf{B}}_1^{\mathrm{T}} & -\hat{\mathbf{C}}_1 \end{bmatrix} & \begin{bmatrix} \hat{\mathbf{A}}_1 & \hat{\mathbf{B}}_1 \\ \hat{\mathbf{B}}_1^{\mathrm{T}} & \hat{\mathbf{C}}_1 \end{bmatrix} \end{bmatrix},$$
$$\text{with, } \hat{\mathbf{A}}_1 = \hat{\mathbf{A}}_1^{\mathrm{T}},\ \hat{\mathbf{C}}_1 = \hat{\mathbf{C}}_1^{\mathrm{T}}, \text{ and} \tag{C.1}$$
$$\hat{\mathrm{A}}_1^{(1,1)} = -3,\ \hat{\mathrm{A}}_1^{(1,2)} = -1,\ \hat{\mathrm{A}}_1^{(2,2)} = 1,\ \hat{\mathrm{A}}_1^{(3,3)} = 2,$$
$$\hat{\mathrm{B}}_1^{(1,1)} = 1,\ \hat{\mathrm{B}}_1^{(1,2)} = 1,\ \hat{\mathrm{B}}_1^{(2,1)} = -1,\ \hat{\mathrm{B}}_1^{(2,2)} = -1,\ \hat{\mathrm{B}}_1^{(3,3)} = -2,$$
$$\hat{\mathrm{C}}_1^{(1,1)} = -3,\ \hat{\mathrm{C}}_1^{(1,2)} = 1,\ \hat{\mathrm{C}}_1^{(2,2)} = 1,\ \hat{\mathrm{C}}_1^{(3,3)} = 2,$$

$$\overline{\mathbf{K}}_2 = \frac{1}{8}\begin{bmatrix} \begin{bmatrix} \hat{\mathbf{A}}_2 & \hat{\mathbf{B}}_2 \\ \hat{\mathbf{B}}_2^{\mathrm{T}} & \hat{\mathbf{C}}_2 \end{bmatrix} & \begin{bmatrix} -\hat{\mathbf{A}}_2 & -\hat{\mathbf{B}}_2 \\ -\hat{\mathbf{B}}_2^{\mathrm{T}} & -\hat{\mathbf{C}}_2 \end{bmatrix} \\ \begin{bmatrix} -\hat{\mathbf{A}}_2 & -\hat{\mathbf{B}}_2 \\ -\hat{\mathbf{B}}_2^{\mathrm{T}} & -\hat{\mathbf{C}}_2 \end{bmatrix} & \begin{bmatrix} \hat{\mathbf{A}}_2 & \hat{\mathbf{B}}_2 \\ \hat{\mathbf{B}}_2^{\mathrm{T}} & \hat{\mathbf{C}}_2 \end{bmatrix} \end{bmatrix},$$
$$\text{with, } \hat{\mathbf{A}}_2 = \hat{\mathbf{A}}_2^{\mathrm{T}},\ \hat{\mathbf{C}}_2 = \hat{\mathbf{C}}_2^{\mathrm{T}}, \text{ and} \tag{C.2}$$
$$\hat{\mathrm{A}}_2^{(1,1)} = 1,\ \hat{\mathrm{A}}_2^{(1,2)} = -1,\ \hat{\mathrm{A}}_2^{(2,2)} = -3,\ \hat{\mathrm{A}}_2^{(3,3)} = 2,$$
$$\hat{\mathrm{B}}_2^{(1,1)} = 1,\ \hat{\mathrm{B}}_2^{(1,2)} = 1,\ \hat{\mathrm{B}}_2^{(2,1)} = -1,\ \hat{\mathrm{B}}_2^{(2,2)} = -1,\ \hat{\mathrm{B}}_2^{(3,3)} = 2,$$
$$\hat{\mathrm{C}}_2^{(1,1)} = 1,\ \hat{\mathrm{C}}_2^{(1,2)} = 1,\ \hat{\mathrm{C}}_2^{(2,2)} = -3,\ \hat{\mathrm{C}}_2^{(3,3)} = 2,$$

$$\overline{\mathbf{K}}_3 = \frac{1}{2}\begin{bmatrix} \begin{bmatrix} \hat{\mathbf{A}}_3 & \mathbf{O} \\ \text{sym} & \hat{\mathbf{C}}_3 \end{bmatrix} & \begin{bmatrix} -\hat{\mathbf{A}}_3 & \mathbf{O} \\ \text{sym} & -\hat{\mathbf{C}}_3 \end{bmatrix} \\ \begin{bmatrix} -\hat{\mathbf{A}}_3 & \mathbf{O} \\ \text{sym} & -\hat{\mathbf{C}}_3 \end{bmatrix} & \begin{bmatrix} \hat{\mathbf{A}}_3 & \mathbf{O} \\ \text{sym} & \hat{\mathbf{C}}_3 \end{bmatrix} \end{bmatrix},$$
$$\text{with, } \hat{\mathbf{A}}_3 = \hat{\mathbf{A}}_3^{\mathrm{T}},\ \hat{\mathbf{C}}_3 = \hat{\mathbf{C}}_3^{\mathrm{T}}, \text{ and} \tag{C.3}$$
$$\hat{\mathrm{A}}_3^{(1,2)} = -1,\ \hat{\mathrm{A}}_3^{(3,3)} = 1,$$
$$\hat{\mathrm{C}}_3^{(1,2)} = -1,\ \hat{\mathrm{C}}_3^{(3,3)} = -1,$$

$$\overline{\mathbf{K}}_4 = \overline{\mathbf{K}}_5 = \overline{\mathbf{K}}_6 = \mathbf{O}, \tag{C.4}$$

$$\overline{\mathbf{K}}_7 = \frac{1}{72}\begin{bmatrix} \begin{bmatrix} -24\hat{\mathbf{K}}_7 - 12\hat{\mathbf{A}}_7 + 4\hat{\mathbf{C}}_7 & 24\hat{\mathbf{K}}_7 + 12\hat{\mathbf{B}}_7 + 2\hat{\mathbf{C}}_7 \\ 24\hat{\mathbf{K}}_7 - 12\hat{\mathbf{B}}_7 + 2\hat{\mathbf{C}}_7 & -24\hat{\mathbf{K}}_7 + 12\hat{\mathbf{A}}_7 + 4\hat{\mathbf{C}}_7 \end{bmatrix} & \begin{bmatrix} 12\hat{\mathbf{K}}_7 + 6\hat{\mathbf{B}}_7 + \hat{\mathbf{C}}_7 & -12\hat{\mathbf{K}}_7 - 6\hat{\mathbf{A}}_7 + 2\hat{\mathbf{C}}_7 \\ -12\hat{\mathbf{K}}_7 + 6\hat{\mathbf{A}}_7 + 2\hat{\mathbf{C}}_7 & 12\hat{\mathbf{K}}_7 - 6\hat{\mathbf{B}}_7 + \hat{\mathbf{C}}_7 \end{bmatrix} \\ \begin{bmatrix} 12\hat{\mathbf{K}}_7 - 6\hat{\mathbf{B}}_7 + \hat{\mathbf{C}}_7 & -12\hat{\mathbf{K}}_7 + 6\hat{\mathbf{A}}_7 + 2\hat{\mathbf{C}}_7 \\ -12\hat{\mathbf{K}}_7 - 6\hat{\mathbf{A}}_7 + 2\hat{\mathbf{C}}_7 & 12\hat{\mathbf{K}}_7 + 6\hat{\mathbf{B}}_7 + \hat{\mathbf{C}}_7 \end{bmatrix} & \begin{bmatrix} -24\hat{\mathbf{K}}_7 + 12\hat{\mathbf{A}}_7 + 4\hat{\mathbf{C}}_7 & 24\hat{\mathbf{K}}_7 - 12\hat{\mathbf{B}}_7 + 2\hat{\mathbf{C}}_7 \\ 24\hat{\mathbf{K}}_7 + 12\hat{\mathbf{B}}_7 + 2\hat{\mathbf{C}}_7 & -24\hat{\mathbf{K}}_7 - 12\hat{\mathbf{A}}_7 + 4\hat{\mathbf{C}}_7 \end{bmatrix} \end{bmatrix},$$
$$\text{with, } \hat{\mathbf{K}}_7 = \hat{\mathbf{K}}_7^{\mathrm{T}},\ \hat{\mathbf{A}}_7 = \hat{\mathbf{A}}_7^{\mathrm{T}},\ \hat{\mathbf{B}}_7 = -\hat{\mathbf{B}}_7^{\mathrm{T}},\ \hat{\mathbf{C}}_7 = \hat{\mathbf{C}}_7^{\mathrm{T}}, \text{ and} \tag{C.5}$$
$$\hat{\mathrm{K}}_7^{(1,3)} = 1,\ \hat{\mathrm{A}}_7^{(1,5)} = L,\ \hat{\mathrm{B}}_7^{(1,5)} = -\hat{\mathrm{B}}_7^{(5,1)} = -L,\ \hat{\mathrm{C}}_7^{(4,6)} = L^2,$$

$$\overline{\mathbf{K}}_8 = \frac{1}{72}\begin{bmatrix} -12\hat{\mathbf{K}}_8 + 6\hat{\mathbf{A}}_8 + 2\hat{\mathbf{C}}_8 \begin{bmatrix} 2\mathbf{I} & \mathbf{I} \\ \mathbf{I} & 2\mathbf{I} \end{bmatrix} & 12\hat{\mathbf{K}}_8 + 6\hat{\mathbf{B}}_8 + \hat{\mathbf{C}}_8 \begin{bmatrix} \mathbf{I} & 2\mathbf{I} \\ 2\mathbf{I} & \mathbf{I} \end{bmatrix} \\ 12\hat{\mathbf{K}}_8 - 6\hat{\mathbf{B}}_8 + \hat{\mathbf{C}}_8 \begin{bmatrix} \mathbf{I} & 2\mathbf{I} \\ 2\mathbf{I} & \mathbf{I} \end{bmatrix} & -12\hat{\mathbf{K}}_8 - 6\hat{\mathbf{A}}_8 + 2\hat{\mathbf{C}}_8 \begin{bmatrix} 2\mathbf{I} & \mathbf{I} \\ \mathbf{I} & 2\mathbf{I} \end{bmatrix} \end{bmatrix},$$

with, $\hat{\mathbf{K}}_8 = \hat{\mathbf{K}}_8^{\mathrm{T}},\ \hat{\mathbf{A}}_8 = \hat{\mathbf{A}}_8^{\mathrm{T}},\ \hat{\mathbf{B}}_8 = -\hat{\mathbf{B}}_8^{\mathrm{T}},\ \hat{\mathbf{C}}_8 = \hat{\mathbf{C}}_8^{\mathrm{T}}$, and

$\hat{\mathrm{K}}_8^{(2,3)} = 1,\ \hat{\mathrm{A}}_8^{(2,4)} = L,\ \hat{\mathrm{B}}_8^{(2,4)} = -\hat{\mathrm{B}}_8^{(4,2)} = L,\ \hat{\mathrm{C}}_8^{(5,6)} = L^2,$ (C.6)

Of course, the analytical form of matrices $\overline{\mathbf{K}}_i$ can be determined in the most general case of rectangular (or pseudo-rectangular) elements. These expressions are not reported here for the sake of brevity.

Bibliography

[1] B. Alemour, O. Badran, M. R. Hassan, A review of using conductive composite materials in solving lightening strike and ice accumulation problems in aviation, Journal of Aerospace Technology and Management 11 (2019).

[2] T. Garulli, Design and validation of fully-uncoupled multi-directional lay-ups to evaluate interlaminar fracture toughness, Ph.D. thesis, Bordeaux (2020).

[3] M. Montemurro, A. Catapano, A new multi-scale design methodology for the optimisation of variable stiffness composites (2017).

[4] M. Montemurro, A. Catapano, On the effective integration of manufacturability constraints within the multi-scale methodology for designing variable angle-tow laminates, Composite Structures 161 (2017) 145–159.

[5] M. Montemurro, A contribution to the development of design strategies for the optimisation of lightweight structures. HDR thesis, Université de Bordeaux, http://hdl.handle.net/10985/15155, Bordeaux, France, 2018.
URL http://hdl.handle.net/10985/15155

[6] M. Montemurro, A. Pagani, G. A. Fiordilino, J. Pailhès, E. Carrera, A general multi-scale two-level optimisation strategy for designing composite stiffened panels, Composite Structures 201 (2018) 968–979.

[7] M. I. Izzi, M. Montemurro, A. Catapano, J. Pailhès, A multi-scale two-level optimisation strategy integrating a global/local modelling approach for composite structures, Composite Structures 237 (2020) 111908.

[8] M. I. Izzi, M. Montemurro, A. Catapano, D. Fanteria, J. Pailhes, Multi-scale optimisation of thin-walled structures by considering a global/local modelling approach, Proceedings of the Institution of Mechanical Engineers, Part G: Journal of Aerospace Engineering (2020) 0954410020939338.

[9] S. Setoodeh, M. M. Abdalla, Z. Gürdal, Design of variable–stiffness laminates using lamination parameters, Composites Part B: Engineering 37 (4-5) (2006) 301–309.

[10] S. Setoodeh, M. M. Abdalla, S. T. IJsselmuiden, Z. Gürdal, Design of variable-stiffness composite panels for maximum buckling load, Composite structures 87 (1) (2009) 109–117.

[11] R. M. Jones, Mechanics of composite materials, McGraw-Hill, 1975.

[12] W. Lansing, W. Dwyer, R. Emerton, E. Ranalli, Application of fully stressed design procedures to wing and empennage structures, Journal of Aircraft 8 (9) (1971) 683–688.

[13] Y. Hirano, Optimum design of laminated plates under axial compression, AIAA Journal 17 (9) (1979) 1017–1019.

[14] J.-S. Moh, C. Hwu, Optimization for buckling of composite sandwich plates, AIAA journal 35 (5) (1997) 863–868.

[15] R. Spallino, G. Giambanco, S. Rizzo, A design algorithm for the optimization of laminated composite structures, Engineering Computations (1999).

[16] S. K. Ha, D.-J. Kim, T.-H. Sung, Optimum design of multi-ring composite flywheel rotor using a modified generalized plane strain assumption, International journal of mechanical sciences 43 (4) (2001) 993–1007.

[17] U. Topal, Ü. Uzman, Maximization of buckling load of laminated composite plates with central circular holes using mfd method, Structural and Multidisciplinary Optimization 35 (2) (2008) 131–139.

[18] D. Graesser, Z. Zabinsky, M. Tuttle, G. Kim, Designing laminated composites using random search techniques, Composite Structures 18 (4) (1991) 311–325.

[19] P. M. Sargent, D. O. Ige, N. R. Ball, Design of laminate composite layups using genetic algorithms, Engineering with computers 11 (2) (1995) 59–69.

[20] L.-r. Tsau, C.-h. Liu, A comparison between two optimization methods on the stacking sequence of fiber-reinforced composite laminate, Computers & structures 55 (3) (1995) 515–525.

[21] L.-R. Tsau, Y.-H. Chang, F.-L. Tsao, The design of optimal stacking sequence for laminated frp plates with inplane loading, Computers & structures 55 (4) (1995) 565–580.

[22] M. Walker, T. Reiss, S. Adali, P. Weaver, Application of mathematica to the optimal design of composite shells for improved buckling strength, Engineering Computations (1998).

[23] D. Sadagopan, R. Pitchumani, Application of genetic algorithms to optimal tailoring of composite materials, Composites Science and Technology 58 (3-4) (1998) 571–589.

[24] V. Savic, M. E. Tuttle, Z. B. Zabinsky, Optimization of composite i-sections using fiber angles as design variables, Composite Structures 53 (3) (2001) 265–277.

[25] P. Weaver, Designing composite structures: lay-up selection, Proceedings of the institution of mechanical engineers, Part G: journal of aerospace engineering 216 (2) (2002) 105–116.

[26] O. Erdal, F. O. Sonmez, Optimum design of composite laminates for maximum buckling load capacity using simulated annealing, Composite Structures 71 (1) (2005) 45–52.

[27] H. Ghiasi, D. Pasini, L. Lessard, Optimum stacking sequence design of composite materials part i: Constant stiffness design, Composite Structures 90 (1) (2009) 1–11. doi:https://doi.org/10.1016/j.compstruct.2009.01.006.
URL https://www.sciencedirect.com/science/article/pii/S026382230900018X

[28] F.-X. Irisarri, A. Lasseigne, F.-H. Leroy, R. Le Riche, Optimal design of laminated composite structures with ply drops using stacking sequence tables, Composite Structures 107 (2014) 559–569.

[29] S. Adali, V. Verijenko, M. Walker, Optimal laminate configurations with symmetric lay-ups for maximum postbuckling stiffness, Composites Engineering 4 (11) (1994) 1119–1127. doi:https://doi.org/10.1016/0961-9526(95)91286-P.
URL https://www.sciencedirect.com/science/article/pii/096195269591286P

[30] S. Adali, A. Richter, V. Verijenko, E. Summers, Optimal design of hybrid laminates with discrete ply angles for maximum buckling load and minimum cost, Composite Structures 32 (1) (1995) 409–415, eighth International Conference on Composite Structures. doi:https://doi.org/10.1016/0263-8223(95)00067-4.
URL https://www.sciencedirect.com/science/article/pii/0263822395000674

[31] R. L. Riche, R. T. Haftka, Optimization of laminate stacking sequence for buckling load maximization by genetic algorithm, AIAA journal 31 (5) (1993) 951–956.

[32] F. Aymerich, M. Serra, Optimization of laminate stacking sequence for maximum buckling load using the ant colony optimization (aco) metaheuristic, Composites Part A: Applied Science and Manufacturing 39 (2) (2008) 262–272. doi:https://doi.org/10.1016/j.compositesa.2007.10.011.
URL https://www.sciencedirect.com/science/article/pii/S1359835X07002357

[33] R. T. Haftka, J. L. Walsh, Stacking-sequence optimization for buckling of laminated plates by integer programming, AIAA journal 30 (3) (1992) 814–819.

[34] F.-X. Irisarri, D. H. Bassir, N. Carrere, J.-F. Maire, Multiobjective stacking sequence optimization for laminated composite structures, Composites Science and Technology 69 (7) (2009) 983–990. doi:https://doi.org/10.1016/j.compscitech.2009.01.011.
URL https://www.sciencedirect.com/science/article/pii/S0266353809000074

[35] U. S. D. of Defense, Laminate stacking sequence effects, In Composite Materials Handbook MIL-HDBK-17-3F 3 (2002) 5.68–5.71.

[36] P. Vannucci, G. Verchery, A special class of uncoupled and quasi-homogeneous laminates, Composites Science and Technology 61 (2001) 1465–1473.

[37] T. Garulli, A. Catapano, M. Montemurro, J. Jumel, D. Fanteria, Quasi-trivial stacking sequences for the design of thick laminates, Composite Structures 200 (2018) 614–623.

[38] T. Garulli, A. Catapano, M. Montemurro, J. Jumel, D. Fanteria, Quasi-trivial solutions for uncoupled, homogeneous and quasi-homogeneous laminates with high number of plies, ECCM VI, International Center for Numerical Methods in Engineering (CIMNE), GBR (2018) 255–265.

[39] M. Montemurro, A. Catapano, D. Doroszewski, A multi-scale approach for the simultaneous shape and material optimisation of sandwich panels with cellular core, Composites Part B: Engineering 91 (2016) 458–472.

[40] C. G. Diaconu, M. Sato, H. Sekine, Feasible region in general design space of lamination parameters for laminated composites, AIAA journal 40 (3) (2002) 559–565.

[41] C. Diaconu, M. Sato, H. Sekine, Layup optimization of symmetrically laminated thick plates for fundamental frequencies using lamination parameters, Structural and multidisciplinary Optimization 24 (4) (2002) 302–311.

[42] B. Liu, R. Haftka, P. Trompette, Maximization of buckling loads of composite panels using flexural lamination parameters, Structural and Multidisciplinary Optimization 26 (1) (2004) 28–36.

[43] M. Bloomfield, J. Herencia, P. Weaver, Optimisation of anisotropic composite plates incorporating non-conventional ply orientations, in: 49th AIAA/ASME/ASCE/AHS/ASC Structures, Structural Dynamics, and Materials Conference, 16th AIAA/ASME/AHS Adaptive Structures Conference, 10th AIAA Non-Deterministic Approaches Conference, 9th AIAA Gossamer Spacecraft Forum, 4th AIAA Multidisciplinary Design Optimization Specialists Conference, 2008, p. 1918.

[44] J. E. Herencia, P. M. Weaver, M. I. Friswell, Initial sizing optimisation of anisotropic composite panels with t-shaped stiffeners, Thin-Walled Structures 46 (4) (2008) 399–412.

[45] S. T. IJsselmuiden, M. M. Abdalla, Z. Gürdal, Implementation of strength-based failure criteria in the lamination parameter design space, AIAA journal 46 (7) (2008) 1826–1834.

[46] S. W. Tsai, E. M. Wu, A general theory of strength for anisotropic materials, Journal of composite materials 5 (1) (1971) 58–80.

[47] K. R. Bramsiepe, V. Handojo, Y. M. Meddaikar, M. Schulze, T. Klimmek, Loads and structural optimization process for composite long range transport aircraft configuration, in: 2018 Multidisciplinary Analysis and Optimization Conference, 2018, p. 3572.

[48] M. A. Albazzan, R. Harik, B. F. Tatting, Z. Gürdal, Efficient design optimization of nonconventional laminated composites using lamination parameters: A state of the art, Composite Structures 209 (2019) 362–374.

[49] G. Verchery, T. Vong, Une méthode d'aide graphique à la conception des séquences d'empilement dans les stratifiés, in: 5èmes Journées Nationales sur les Composites, Paris, 1986, pp. 267–280.

[50] P. Vannucci, G. Verchery, Stiffness design of laminates using the polar method, International Journal of Solids and Structures 38 (50-51) (2001) 9281–9294.

[51] P. Vannucci, Plane anisotropy by the polar method, Meccanica 40 (4-6) (2005) 437–454.

[52] P. Vannucci, A note on the elastic and geometric bounds for composite laminates, Journal of Elasticity 112 (2) (2013) 199–215.

[53] M. P. Scardaoni, M. Montemurro, Convex or non-convex? on the nature of the feasible domain of laminates, European Journal of Mechanics-A/Solids 85 (2021) 104112.

[54] A. Catapano, B. Desmorat, P. Vannucci, Invariant formulation of phenomenological failure criteria for orthotropic sheets and optimisation of their strength, Mathematical Methods in the Applied Sciences 35 (15) (2012) 1842–1858.

[55] M. Montemurro, A. Vincenti, P. Vannucci, Design of the elastic properties of laminates with a minimum number of plies, Mechanics of Composite Materials 48 (4) (2012) 369–390.

[56] M. Montemurro, An extension of the polar method to the first-order shear deformation theory of laminates, Composite Structures 127 (2015) 328–339.

[57] M. Montemurro, Corrigendum to" an extension of the polar method to the first-order shear deformation theory of laminates"[compos. struct. 127 (2015) 328-339] (2015).

[58] M. Montemurro, The polar analysis of the third-order shear deformation theory of laminates, Composite Structures 131 (2015) 775–789.

[59] A. Catapano, B. Desmorat, P. Vannucci, Stiffness and strength optimization of the anisotropy distribution for laminated structures, Journal of Optimization Theory and Applications 167 (1) (2015) 118–146.

[60] A. Catapano, M. Montemurro, On the correlation between stiffness and strength properties of anisotropic laminates, Mechanics of Advanced Materials and Structures 26 (8) (2019) 651–660.

[61] M. Montemurro, A. Vincenti, P. Vannucci, A two-level procedure for the global optimum design of composite modular structures - application to the design of an aircraft wing. part 1 : theoretical formulation, Journal of Optimization Theory and Applications 155 (1) (2012) 1–23.

[62] M. Montemurro, A. Vincenti, P. Vannucci, A two-level procedure for the global optimum design of composite modular structures - application to the design of an aircraft wing. part 2 : numerical aspects and examples, Journal of Optimization Theory and Applications 155 (1) (2012) 24–53.

[63] A. Catapano, M. Montemurro, A multi-scale approach for the optimum design of sandwich plates with honeycomb core. part i: homogenisation of core properties, Composite structures 118 (2014) 664–676.

[64] A. Catapano, M. Montemurro, A multi-scale approach for the optimum design of sandwich plates with honeycomb core. part ii: the optimisation strategy, Composite structures 118 (2014) 677–690.

[65] M. Montemurro, Y. Koutsawa, S. Belouettar, A. Vincenti, P. Vannucci, Design of damping properties of hybrid laminates through a global optimisation strategy, Composite Structures 94 (2012) 3309–3320.

[66] M. Montemurro, A. Vincenti, Y. Koutsawa, P. Vannucci, A two-level procedure for the global optimization of the damping behavior of composite laminated plates with elastomer patches, Journal of Vibration and Control 21 (9) (2015) 1778–1800.

[67] E. Panettieri, M. Montemurro, A. Catapano, Blending constraints for composite laminates in polar parameters space, Composites Part B: Engineering 168 (2019) 448–457.

[68] M. P. Scardaoni, M. Montemurro, A general global-local modelling framework for the deterministic optimisation of composite structures, Structural and Multidisciplinary Optimization 62 (2020) 1927–1949.

[69] M. P. Scardaoni, M. Montemurro, E. Panettieri, A. Catapano, New blending constraints and a stack-recovery strategy for the multi-scale design of composite laminates, Structural and Multidisciplinary Optimization 63 (2) (2021) 741–766.

[70] X. Wang, M. Jiang, Z. Zhou, J. Gou, D. Hui, 3d printing of polymer matrix composites: A review and prospective, Composites Part B: Engineering 110 (2017) 442 – 458.

[71] H. Ghiasi, K. Fayazbakhsh, D. Pasini, L. Lessard, Optimum stacking sequence design of composite materials part ii: Variable stiffness design, Composite Structures 93 (1) (2010) 1–13.

[72] H.-J. L. Dirk, C. Ward, K. D. Potter, The engineering aspects of automated prepreg layup: History, present and future, Composites Part B: Engineering 43 (3) (2012) 997–1009.

[73] B. C. Kim, K. Potter, P. M. Weaver, Continuous tow shearing for manufacturing variable angle tow composites, Composites Part A: Applied Science and Manufacturing 43 (8) (2012) 1347–1356.

[74] B. C. Kim, P. M. Weaver, K. Potter, Manufacturing characteristics of the continuous tow shearing method for manufacturing of variable angle tow composites, Composites Part A: Applied Science and Manufacturing 61 (2014) 141–151.

[75] M. A. Nik, K. Fayazbakhsh, D. Pasini, L. Lessard, Optimization of variable stiffness composites with embedded defects induced by automated fiber placement, Composite Structures 107 (2014) 160–166.

[76] A. W. Blom, C. S. Lopes, P. J. Kromwijk, Z. Gurdal, P. P. Camanho, A theoretical model to study the influence of tow-drop areas on the stiffness and strength of variable-stiffness laminates, Journal of composite materials 43 (5) (2009) 403–425.

[77] S. T. Peters, Handbook of composites, Springer Science & Business Media, 2013.

[78] M. Montemurro, A. Catapano, A general b-spline surfaces theoretical framework for optimisation of variable angle-tow laminates, Composite Structures 209 (2019) 561–578.

[79] M. W. Hyer, H. Lee, The use of curvilinear fiber format to improve buckling resistance of composite plates with central circular holes, Composite structures 18 (3) (1991) 239–261.

[80] M. W. Hyer, R. Charette, Use of curvilinear fiber format in composite structure design, AIAA journal 29 (6) (1991) 1011–1015.

[81] Z. Gürdal, R. Olmedo, In-plane response of laminates with spatially varying fiber orientations-variable stiffness concept, AIAA journal 31 (4) (1993) 751–758.

[82] S. Nagendra, S. Kodiyalam, J. Davis, V. Parthasarathy, Optimization of tow fiber paths for composite design, in: 36th Structures, Structural Dynamics and Materials Conference, 1995, p. 1275.

[83] D. Jegley, B. Tatting, Z. Gurdal, Optimization of elastically tailored tow-placed plates with holes, in: 44th AIAA/ASME/ASCE/AHS/ASC Structures, Structural Dynamics, and Materials Conference, 2003, p. 1420.

[84] Z. Gürdal, B. F. Tatting, C. Wu, Variable stiffness composite panels: effects of stiffness variation on the in-plane and buckling response, Composites Part A: Applied Science and Manufacturing 39 (5) (2008) 911–922.

[85] Z. Wu, P. M. Weaver, G. Raju, B. C. Kim, Buckling analysis and optimisation of variable angle tow composite plates, Thin-walled structures 60 (2012) 163–172.

[86] G. Raju, Z. Wu, B. C. Kim, P. M. Weaver, Prebuckling and buckling analysis of variable angle tow plates with general boundary conditions, Composite Structures 94 (9) (2012) 2961–2970.

[87] G. Raju, Z. Wu, P. M. Weaver, Postbuckling analysis of variable angle tow plates using differential quadrature method, Composite Structures 106 (2013) 74–84.

[88] B. H. Coburn, Z. Wu, P. M. Weaver, Buckling analysis of stiffened variable angle tow panels, Composite Structures 111 (2014) 259–270.

[89] M. A. Albazzan, R. Harik, B. F. Tatting, Z. Gürdal, Efficient design optimization of nonconventional laminated composites using lamination parameters: a state of the art, Composite Structures (2018).

[90] S. T. IJsselmuiden, M. M. Abdalla, Z. Gurdal, Optimization of variable-stiffness panels for maximum buckling load using lamination parameters, AIAA journal 48 (1) (2010) 134–143.

[91] A. Khani, S. T. IJsselmuiden, M. M. Abdalla, Z. Gürdal, Design of variable stiffness panels for maximum strength using lamination parameters, Composites Part B: Engineering 42 (3) (2011) 546–552.

[92] Z. Wu, G. Raju, P. M. Weaver, Framework for the buckling optimization of variable-angle tow composite plates, AIAA Journal 53 (12) (2015) 3788–3804.

[93] D. M. Peeters, S. Hesse, M. M. Abdalla, Stacking sequence optimisation of variable stiffness laminates with manufacturing constraints, Composite Structures 125 (2015) 596–604.

[94] M. Montemurro, A. Catapano, A new paradigm for the optimum design of variable angle tow laminates, in: Variational Analysis and Aerospace Engineering, Springer, 2016, pp. 375–400.

[95] A. Catapano, M. Montemurro, Strength optimisation of variable angle-tow composites through a laminate-level failure criterion, Journal of Optimization Theory and Applications 187 (2020) 683–706.
URL https://doi.org/10.1007/s10957-020-01750-6

[96] A. Jibawy, C. Julien, B. Desmorat, A. Vincenti, F. Léné, Hierarchical structural optimization of laminated plates using polar representation, International Journal of Solids and Structures 48 (18) (2011) 2576–2584.

[97] M. Miki, Y. Sugiyama, Optimum design of laminated composite plates using lamination parameters, AIAA journal 31 (5) (1993) 921–922.

[98] M. Izzi, A. Catapano, M. Montemurro, Strength and mass optimisation of variable stiffness composites in the polar parameters space, Structural and Multidisciplinary Optimisation (2021).

[99] I. Babuška, J. Chandra, J. E. Flaherty, Adaptive computational methods for partial differential equations, Vol. 16, Siam, 1983.

[100] B. Szabó, I. Babuška, Finite element analysis, Wiley, New York, 1991.

[101] K.-J. Bathe, Finite element procedures, Klaus-Jurgen Bathe, 2006.

[102] J. Fish, L. Pan, V. Belsky, S. Gomaa, Unstructured multigrid method for shells, International Journal for Numerical Methods in Engineering 39 (7) (1996) 1181–1197.

[103] N. Moës, J. Dolbow, T. Belytschko, A finite element method for crack growth without remeshing, International Journal for Numerical Methods in Engineering 46 (1) (1999) 131–150.

[104] J. Fish, The s-version of the finite element method, Computers & Structures 43 (3) (1992) 539–547.

[105] J. Fish, S. Markolefas, Adaptive s-method for linear elastostatics, Computer Methods in Applied Mechanics and Engineering 104 (3) (1993) 363–396.

[106] K. W. Shim, D. J. Monaghan, C. G. Armstrong, Mixed dimensional coupling in finite element stress analysis, Engineering with Computers 18 (3) (2002) 241–252.

[107] P. Blanco, R. Feijóo, S. Urquiza, A variational approach for coupling kinematically incompatible structural models, International Journal for Numerical Methods in Engineering 197 (17-18) (2008) 1577–1602.

[108] K. Mao, C. Sun, A refined global-local finite element analysis method, International Journal for Numerical Methods in Engineering 32 (1) (1991) 29–43.

[109] H. B. Dhia, Multiscale mechanical problems: the Arlequin method, Comptes Rendus de l'Academie des Sciences Series IIB Mechanics Physics Astronomy 12 (326) (1998) 899–904.

[110] H. Hu, S. Belouettar, M. Potier-Ferry, et al., Multi-scale modelling of sandwich structures using the Arlequin method part i: Linear modelling, Finite Elements in Analysis and Design 45 (1) (2008) 37–51.

[111] F. Biscani, G. Giunta, S. Belouettar, E. Carrera, H. Hu, Variable kinematic beam elements coupled via arlequin method, Composite Structures 93 (2) (2011) 697–708.

[112] R. J. Guyan, Reduction of stiffness and mass matrices, AIAA Journal 3 (2) (1965) 380–380.

[113] M. Nastran, Superelement user's guide, MSC. Software Corporation.–2001.–72 (2001).

[114] J. B. Ransom, N. F. Knight Jr, Global/local stress analysis of composite panels, Computers & Structures 37 (4) (1990) 375–395.

[115] R. K. Kapania, S. G. Haryadi, R. T. Haftka, Global/local analysis of composite plates with cutouts, Computational Mechanics 19 (5) (1997) 386–396.

[116] S. Haryadi, R. Kapania, R. Haftka, Global/local analysis of composite plates with cracks, Composites Part B: Engineering 29 (3) (1998) 271–276.

[117] D. Muheim Thompson, O. Hayden Griffin JR, 2-d to 3-d global/local finite element analysis of cross-ply composite laminates, Journal of Reinforced Plastics and Composites 9 (5) (1990) 492–502.

[118] P. Guidault, O. Allix, L. Champaney, J. Navarro, A two-scale approach with homogenization for the computation of cracked structures, Computers & Structures 85 (17) (2007) 1360–1371, computational Structures Technology. doi:https://doi.org/10.1016/j.compstruc.2006.08.085.
URL https://www.sciencedirect.com/science/article/pii/S0045794906003634

[119] M. Akterskaia, E. Jansen, S. Hühne, R. Rolfes, Efficient progressive failure analysis of multi-stringer stiffened composite panels through a two-way loose coupling global-local approach, Composite Structures 183 (2018) 137–145, in honor of Prof. Y. Narita. doi:https://doi.org/10.1016/j.compstruct.2017.02.011.
URL https://www.sciencedirect.com/science/article/pii/S0263822317303616

[120] P. Cresta, O. Allix, C. Rey, S. Guinard, Nonlinear localization strategies for domain decomposition methods: Application to post-buckling analyses, Computer Methods in Applied Mechanics and Engineering 196 (8) (2007) 1436–1446.

[121] E. Panettieri, M. Montemurro, D. Fanteria, F. Coccia, Multi-scale least-weight design of a wing-box through a global/local modelling approach, Journal of Optimization Theory and Applications (2020) 1–24.

[122] M. P. Scardaoni, M. Montemurro, E. Panettieri, Prandtlplane wing-box least-weight design: a multi-scale optimisation approach, Aerospace Science and Technology 106 (2020) 106156.

[123] E. Carrera, A. Pagani, M. Petrolo, Use of Lagrange multipliers to combine 1d variable kinematic finite elements, Computers & Structures 129 (2013) 194–206.

[124] E. Zappino, G. Li, A. Pagani, E. Carrera, Global-local analysis of laminated plates by node-dependent kinematic finite elements with variable esl/lw capabilities, Composite Structures 172 (2017) 1–14.

[125] E. Carrera, M. Filippi, P. Mahato, A. Pagani, Accurate static response of single-and multi-cell laminated box beams, Composite Structures 136 (2016) 372–383.

[126] E. Carrera, M. Cinefra, M. Petrolo, E. Zappino, Finite element analysis of structures through unified formulation, John Wiley & Sons, 2014.

[127] I. Kaleel, M. Petrolo, E. Carrera, Elastoplastic and progressive failure analysis of fiber-reinforced composites via an efficient nonlinear microscale model, Aerotecnica Missili & Spazio 97 (2) (2018) 103–110.

[128] E. Carrera, I. Kaleel, M. Petrolo, Elastoplastic analysis of compact and thin-walled structures using classical and refined beam finite element models, Mechanics of Advanced Materials and Structures (2017) 1–13.

[129] M. Petrolo, M. Nagaraj, I. Kaleel, E. Carrera, A global-local approach for the elastoplastic analysis of compact and thin-walled structures via refined models, Computers & Structures 206 (2018) 54–65.

[130] E. Carrera, G. Fiordilino, M. Nagaraj, A. Pagani, M. Montemurro, A global/local approach based on CUF for the accurate and efficient analysis of metallic and composite structures, Engineering Structures 188 (2019) 188–201.

[131] E. Carrera, G. Giunta, M. Petrolo, Beam structures: classical and advanced theories, John Wiley & Sons, 2011.

[132] E. Carrera, A. Pagani, Multi-line enhanced beam model for the analysis of laminated composite structures, Composites Part B: Engineering 57 (2014) 112–119.

[133] J. N. Reddy, Mechanics of laminated composite plates and shells. Theory and Analysis, 2nd Edition, CRC Press, 2004.

[134] A. Pagani, A. De Miguel, M. Petrolo, E. Carrera, Analysis of laminated beams via unified formulation and legendre polynomial expansions, Composite Structures 156 (2016) 78–92.

[135] M. NASTRAN, Reference manual, 2008, MSC Software Corporation (2008).

[136] J. J. Wijker, Mechanical vibrations in spacecraft design, Springer Science & Business Media, 2004.

[137] L. Liao, A study of inertia relief analysis, in: 52nd AIAA/ASME/ASCE/AHS/ASC Structures, Structural Dynamics and Materials Conference 19th AIAA/ASME/AHS Adaptive Structures Conference 13t, 2011, p. 2002.

[138] A. R. Barnett, T. W. Widrick, D. R. Ludwiczak, Closed-form static analysis with inertia relief and displacement-dependent loads using a msc/nastran dmap alter (1995).

[139] E. Carrera, M. Petrolo, Refined one-dimensional formulations for laminated structure analysis, AIAA Journal 50 (1) (2012) 176–189.

[140] E. Carrera, A. Garcia de Miguel, G. A. Fiordilino, A. Pagani, Global/local analysis of free-edge stresses in composite laminates, in: AIAA Scitech 2019 Forum, 2019, p. 1760.

[141] A. Wang, F. W. Crossman, Some new results on edge effect in symmetric composite laminates, Journal of Composite Materials 11 (1) (1977) 92–106.

[142] E. Martin, D. Leguillon, N. Carrère, A twofold strength and toughness criterion for the onset of free-edge shear delamination in angle-ply laminates, International journal of Solids and Structures 47 (9) (2010) 1297–1305.

[143] N. Saeedi, K. Sab, J.-F. Caron, Delaminated multilayered plates under uniaxial extension. part i: Analytical analysis using a layerwise stress approach, International Journal of Solids and Structures 49 (26) (2012) 3711–3726.

[144] A. de Miguel, A. Pagani, E. Carrera, Free-edge stress fields in generic laminated composites via higher-order kinematics, Composites Part B: Engineering 168 (2019) 375–386.

[145] L. Lagunegrand, T. Lorriot, R. Harry, H. Wargnier, J. Quenisset, Initiation of free-edge delamination in composite laminates, Composites Science and Technology 66 (10) (2006) 1315–1327.

[146] T. Lorriot, G. Marion, R. Harry, H. Wargnier, Onset of free-edge delamination in composite laminates under tensile loading, Composites Part B: Engineering 34 (5) (2003) 459–471.

[147] G. Verchery, Les invariants des tenseurs d'ordre 4 du type de l'élasticité, in: Mechanical behavior of anisotropic solids/comportment Méchanique des Solides Anisotropes, Springer, 1982, pp. 93–104.

[148] D. B. Adams, L. T. Watson, Z. Gürdal, C. M. Anderson-Cook, Genetic algorithm optimization and blending of composite laminates by locally reducing laminate thickness, Advances in Engineering Software 35 (1) (2004) 35–43.

[149] G. Raju, Z. Wu, P. Weaver, On further developments of feasible region of lamination parameters for symmetric composite laminates, in: 55th AIAA/ASMe/ASCE/AHS/SC structures, structural dynamics, and materials conference, 2014, p. 1374.

[150] T. Macquart, M. T. Bordogna, P. Lancelot, R. De Breuker, Derivation and application of blending constraints in lamination parameter space for composite optimisation, Composite Structures 135 (2016) 224–235.

[151] G. Caprino, I. C. Visconti, A note on specially orthotropic laminates, Journal of Composite Materials 16 (5) (1982) 395–399.

[152] P. Vannucci, G. Verchery, A special class of uncoupled and quasi-homogeneous laminates, Composites science and technology 61 (10) (2001) 1465–1473.

[153] M. Montemurro, M. Izzi, J. El-Yagoubi, D. Fanteria, An experimental validation of the effectiveness of quasi-trivial solutions for composite laminates, in: First International Conference on Mechanics of Advanced Materials and Structures, ITA, 2018.

[154] M. Montemurro, A. Vincenti, P. Vannucci, The automatic dynamic penalisation method (ADP) for handling constraints with genetic algorithms, Computer Methods in Applied Mechanics and Engineering 256 (2013) 70–87.

[155] M. Montemurro, Optimal design of advanced engineering modular systems through a new genetic approach, Ph.D. thesis, UPMC, Paris VI, France, http://tel.archives-ouvertes.fr/tel-00955533 (2012).

[156] M. Montemurro, H. Nasser, Y. Koutsawa, S. Belouettar, A. Vincenti, P. Vannucci, Identification of electromechanical properties of piezoelectric structures through evolutionary optimisation techniques, International Journal of Solids and Structures 49 (13) (2012) 1884–1892.

[157] A. Catapano, Stiffness and strength optimisation of the anisotropy distribution for laminated structures, Ph.D. thesis, UPMC, Paris VI, France, http://tel.archives-ouvertes.fr/tel-00952372 (2013).

[158] Y. Audoux, M. Montemurro, J. Pailhès, A metamodel based on non-uniform rational basis spline hyper-surfaces for optimisation of composite structures, Composite Structures (2020) 112439.

[159] Y. Audoux, M. Montemurro, J. Pailhès, Non-uniform rational basis spline hyper-surfaces for metamodelling, Computer Methods in Applied Mechanics and Engineering 364 (2020) 112918.

[160] L. Cappelli, M. Montemurro, F. Dau, L. Guillaumat, Multi-scale identification of the viscoelastic behaviour of composite materials through a non-destructive test, Mechanics of Materials 137 (2019) 103137.

[161] L. Cappelli, G. Balokas, M. Montemurro, F. Dau, L. Guillaumat, Multi-scale identification of the elastic properties variability for composite materials through a hybrid optimisation strategy, Composites Part B: Engineering 176 (2019) 107193.

[162] G. Bertolino, M. Montemurro, G. De Pasquale, Multi-scale shape optimisation of lattice structures: an evolutionary-based approach, International Journal on Interactive Design and Manufacturing (IJIDeM) 13 (4) (2019) 1565–1578.

[163] M. Montemurro, M. I. Izzi, J. El-Yagoubi, D. Fanteria, Least-weight composite plates with unconventional stacking sequences: design, analysis and experiments, Journal of Composite Materials 53 (16) (2019) 2209–2227.

[164] G. Costa, M. Montemurro, J. Pailhès, A general hybrid optimization strategy for curve fitting in the non-uniform rational basis spline framework, Journal of Optimization Theory and Applications 176 (1) (2018) 225–251.

[165] Ansys, ANSYS Mechanical APDL Basic Analysis Guide. Release 15.0, ANSYS, Inc., Southpointe, 275 Technology Drive, Canonsburg, PA 15317 (2013).

[166] A. Pagani, E. Carrera, Unified formulation of geometrically nonlinear refined beam theories, Mechanics of Advanced Materials and Structures 25 (1) (2018) 15–31.

[167] R. De Borst, M. A. Crisfield, J. J. Remmers, C. V. Verhoosel, Nonlinear finite element analysis of solids and structures, John Wiley & Sons, 2012.

[168] A. Catapano, M. Montemurro, J.-A. Balcou, E. Panettieri, Rapid prototyping of variable angle-tow composites, Aerotecnica Missili & Spazio 98 (4) (2019) 257–271.

[169] G. Fiordilino, M. Izzi, M. Montemurro, A general isogeometric polar approach for the optimisation of variable stiffness composites: Application to eigenvalue buckling problems, Mechanics of Materials 153 (2021) 103574.

[170] M. Montemurro, A. Catapano, Variational analysis and aerospace engineering: mathematical challenges for the aerospace of the future, in: Vol. 116 of Springer Optimization and Its Applications, Springer International Publishing, 2016.

[171] L. Piegl, W. Tiller, The NURBS book, Springer Science & Business Media, 2012.

[172] R. M. Errico, What is an adjoint model?, Bulletin of the American Meteorological Society 78 (11) (1997) 2577–2592.

[173] J. Nocedal, S. J. Wright, Numerical Optimization, 2nd Edition, Springer Verlag, 2006.

[174] G. Costa, M. Montemurro, Eigen-frequencies and harmonic responses in topology optimisation: A cad-compatible algorithm, Engineering Structures 214 (2020) 110602.

[175] G. Costa, M. Montemurro, J. Pailhès, A 2D topology optimisation algorithm in NURBS framework with geometric constraints, International Journal of Mechanics and Materials in Design 14 (4) (2018) 669–696.

[176] G. Costa, M. Montemurro, J. Pailhès, NURBS hyper-surfaces for 3D topology optimization problems, Mechanics of Advanced Materials and Structures (2019) 1–20.
URL https://doi.org/10.1080/15376494.2019.1582826

[177] Z. Hashin, Failure criteria for unidirectional fiber composites (1980).

[178] J. C. Brewer, P. A. Lagace, Quadratic stress criterion for initiation of delamination, Journal of composite materials 22 (12) (1988) 1141–1155.